Spectroscopic Study of Triplet Exciton Dynamics at the Hybrid Organic-Inorganic Interface

Jesse Allardice

Department of Physics

University of Cambridge

This dissertation is submitted for the degree of

Doctor of Philosophy in Physics

St. John's College

May 2020

Dedicated to...

David and Louise

Declaration

This thesis is the result of my own work and includes nothing which is the outcome of work done in collaboration except as declared in the Preface and specified in the text. It is not substantially the same as any that I have submitted, or, is being concurrently submitted for a degree or diploma or other qualification at the University of Cambridge or any other University or similar institution except as declared in the Preface and specified in the text. I further state that no substantial part of my thesis has already been submitted, or, is being concurrently submitted for any such degree, diploma or other qualification at the University of Cambridge or any other University or similar institution except as declared in the Preface and specified in the text. It does not exceed the prescribed word limit for the relevant Degree Committee.

Jesse Allardice

May 2020

Acknowledgements

Before admission to Cambridge, I had little to no idea what criteria I should be following for choosing a PhD program. When making this decision, there was one standout piece of advice I did receive: "Akshay Rao would be a good supervisor." I can now confirm that this was an extreme understatement. Akshay, you have been the supervisor every PhD student dreams of having. Every time supervisors have come up in discussion with other students, the conversation has ended with not so subtle hints of jealously in others' mouths. You have put so much of your time and energy into your students' futures, and have encouraged and enabled us to achieve the wildest of goals. I'd like to thank you and your family for giving so much to our little community.

I'd also like to thank my advisor, Neil Greenham. Thank you for the many deep discussions on theoretical rigour. Your attention to detail and patience in understanding any convoluted, misdirected point I made was greatly appreciated. As you have recently experienced the novelty of having technology in your home which is directly related to your own PhD, you have inspired me to hope that one day in the future the projects presented here will end up in action on my own home walls/roof.

To the many postdoctoral researchers I have had the pleasure to learn from, thank you. Particular thanks go to; Alex Cheminal, Murad Tayebjee, Hannah Stern, Victor Gray, Zhilong Zhang, and Naoyuki Nishimura. On many occasions when I had absolutely no idea what I was doing, your mentorship was a lifeboat in a stormy sea. At the risk of potentially pushing this metaphor a little far: I thank Nathaniel Davis for helping me get the experimental equivalent of sea legs, by showing me that chemistry is just a game of dangerous Lego.

I give special thanks to the team of scientists from Cambridge Photon Technology, Simon Dowland and Jurjen Winkel, for imparting their technical knowledge on me. Which of course was mixed with a healthy supply of great banter.

Of our collaborators from The University of Sheffield, I would especially like to thank Daniel Toolan and Michael Weir for undertaking the Photon Multiplier project with us. It has often been a confusing experimental journey, so your enthusiasm and insight were a significant factor in aiding us to reach so many of our goals.

To my friends and fellow cohort of PhD students with which I started this adventure; Arya Thampi, Ture Hinrichsen, Limeng Ni, Qifei Gu, Richard Chen, Raj Pandya, Hope Bretscher, Chanakarn Phansa, James Xiao, Edward Booker, Peter Budden, and Leah Weiss, thank you. I have an endless supply of amazing memories with you all. I am honoured to have spent this influential time with you.

To the Rao and Optoelectronics group as a whole, I am greatly appreciative to have been a part of this wonderful research community. I thank you all for your patience, help and encouragement. Without any one of you, my time at the Cavendish would be missing a crucial factor.

I am very grateful to my funders; St. John's College, The Cambridge Commonwealth Trust, and the Winton Programme for the Physics of Sustainability. I am especially thankful to Nalin Patel for his mentoring and support through the Winton programme.

James, Victor, Hope, Nipun, Soo Teck, Ture, Nate, and Sofia, thank you for undergoing the substantial task of proofreading and editing this dissertation. I am endlessly grateful and apologetic. As someone who has never been a confident writer, it has been helpful to know that you have my back. I'd particularly like to thank Caitlin Attenburrow, who with full knowledge of my ongoing battles with the English language, agreed to help turn this document into a dissertation.

Although the research requirements of a PhD are technically demanding, I have found that it is just as important a test of your ability to connect with people on a personal level. It is the strength of these relationships that keep motivation high and the ball rolling.

The St. John's College community had a larger part in catalysing these connections. To my close friends; Michael, Valerio, Kate, and Jessica, thank you for the many shenanigans and great company. Hope to see you all again soon once we make it back to the U.K. Though there are many people that make the college community an engaging, academic, and friendly home, I believe special thanks should go to Graduate Tutor Sue Colwell and the late Master Christopher Dobson.

To my lifelong friends Tim, Joe, Arthur and Robbie, sorry for leaving to the far side of the planet. All day, every day, wouldn't be enough time for all the adventures I want to have with you. The many wonderful shared experiences we have together have shown me what it is to be truly comfortable with others and myself. Time spent with you is the definition of time well spent.

With a statistical significance of at least a couple of sigma, it has been pointed out to me that I am lucky by nature. This is most certainly a selection or reporting bias by myself or others. However, there are a few cases in which I do feel incredibly fortunate. I don't know what to call it other than luck, that on my first day in the Cavendish I meet the most irradiant person ever. She was enthralling, gorgeous and doing a PhD in Physics, in the Maxwell… in the office opposite my own. I don't know if serendipity is enough to describe that particular collision of circumstances. Through friendship and partnership, Sofia Taylor has been the defining relationship of my time in Cambridge. Thank you for all the amazing times together, and being there when plans fell apart and I needed to hide under someone's desk. I can't wait to see where life takes us next.

Lastly, I would like to thank my family David, Louise, Georgia, Matthews and Allardices. From childhood to my current status as what could possibly be described as adulthood, the upbringing you have given me has been one of a kind. I am endlessly grateful for the opportunities you have given me. The enduring advantage of having a loving family such as ours is second to none.

Spectroscopic Study of Triplet Exciton Dynamics at the Hybrid Organic-Inorganic Interface

Jesse Allardice

The control and utilisation of spin-triplet excitons in organic semiconductors is highly sought after for the next generation of Optoelectronic applications. Of particular interest is the utilisation of these photoexcited states in the singlet-fission photon-multiplier and triplet-triplet annihilation upconversion processes. Singlet fission is an exciton multiplication process in organic molecules, in which a photogenerated spin-singlet exciton is rapidly and efficiently converted into two spin-triplet excitons. Conversely, triplet-triplet annihilation is essentially the same reaction operating in reverse. These processes offer two spectral management mechanisms to break the Shockley–Queisser limit by overcoming the thermalisation and absorption losses inherent to all single-junction photovoltaics. Such spectral management technologies have been predicted to increase the maximum possible efficiency of Si-based cells from 32 % to greater than 40 %, breaking the Shockley–Queisser limit.

Harnessing these processes would be facilitated if the energy of the triplet exciton could be efficiently interchanged with photons. However, utilising triplet excitons like this poses a significant challenge, as transitions between the ground state and triplet excited states typically have negligible mediation by photons. Transitions such as these are spin forbidden, and have a correspondingly weak oscillator strength. In this thesis, we investigate a promising method to overcome this impasse, using inorganic quantum dots (QDs) to efficiently convert between triplet excitons and photons. We develop a variety of novel hybrid organic-inorganic systems that perform singlet-fission photon-multiplication and triplet-triplet annihilation upconversion.

We find that in order to achieve efficient triplet transfer at the hybrid organic-inorganic interface, it is critical to engineer the surface of the QD with a triplet transfer ligand. The triplet transfer ligand facilitates transfer by acting as an intermediate excited state during the transfer process, encouraging the formation of an optimal solid-state morphology, and providing a weak adsorption site for rapid transfer to occur at. Among the many highlights, we develop a solid-state singlet-fission photon-multiplier with an exciton multiplication efficiency of ~190%, showing significant promise for real-world application. Additionally, advanced spectroscopic techniques and mathematic modelling are applied to gather an in-depth understanding of the impact of a variety of photophysical processes on operation under realistic working conditions. These results establish a variety of highly tuneable platforms to understand the triplet transfer process at the organic semiconductor and inorganic QD interface, providing clear design rules for new materials that perform spectral management.

Contents

List of Publications

(1) **Jesse R. Allardice**, Arya Thampi, Simon Dowland, James Xiao, Victor Gray, Zhilong Zhang, Peter Budden, Anthony J. Petty, Nathaniel J. L. K. Davis, Neil C. Greenham, John E. Anthony, and Akshay Rao. 2019. "Engineering Molecular Ligand Shells on Quantum Dots for Quantitative Harvesting of Triplet Excitons Generated by Singlet Fission." Journal of the American Chemical Society 141:12907–15.

(2) Victor Gray, **Jesse R. Allardice**, Zhilong Zhang, Simon Dowland, James Xiao, Anthony J. Petty, John E. Anthony, Neil C. Greenham, and Akshay Rao. 2020. "Direct vs Delayed Triplet Energy Transfer from Organic Semiconductors to Quantum Dots and Implications for Luminescent Harvesting of Triplet Excitons." ACS Nano 14(4):4224–34.

(3) **Jesse Allardice***, Victor Gray*, Simon Dowland*, Daniel T. W. Toolan, Michael P. Weir, James Xiao, Zhilong Zhang, Jurjen Winkel, Géraud Delport, Samuel D. Stranks, Anthony J. Petty II, John Anthony, Richard Friend, Anthony J. Ryan, Richard A. L. Jones, Neil C. Greenham, and Akshay Rao. "Efficient Harvesting of Triplet Excitons Generated from Singlet Fission in a Bulk Organic-Semiconductor/Quantum-Dot Blend."

In preparation

* These authors contributed equally

(4) **Jesse Allardice**, Nathaniel J. L. K. Davis, Victor Gray, Naoyuki Nishimura, Simon Dowland, Leah R. Weiss, James Xiao, Zhilong Zhang, Peter Budden, Anthony J. Petty II, John Anthony, Neil C. Greenham, and Akshay Rao. "Excited State Trapping and Ligand Shells with Annihilator Adsorption in a PbS QD Upconversion System."

In preparation

(5) Nathaniel J. L. K. Davis, **Jesse R. Allardice**, James Xiao, Anthony J. Petty, Neil C. Greenham, John E. Anthony, and Akshay Rao. 2018. "Singlet Fission and Triplet Transfer to PbS Quantum Dots in TIPS-Tetracene Carboxylic Acid Ligands." Journal of Physical Chemistry Letters 9(6):1454–60.

(6) Nathaniel J. L. K. Davis, **Jesse R. Allardice**, James Xiao, Arfa Karani, Tom C. Jellicoe, Akshay Rao, and Neil C. Greenham. 2019. "Improving the Photoluminescence Quantum Yields of Quantum Dot Films through a Donor/Acceptor System for near-IR LEDs." Materials Horizons 6(1):137–43.

(7) Naoyuki Nishimura, **Jesse R. Allardice**, James Xiao, Qifei Gu, Victor Gray, and Akshay Rao. 2019. “Photon Upconversion Utilizing Energy beyond the Band Gap of Crystalline Silicon with a Hybrid TES-ADT/PbS Quantum Dots System.” Chemical Science 10(18):4750–60.

(8) Naoyuki Nishimura, Victor Gray, **Jesse R. Allardice**, Zhilong Zhang, Anton Pershin, David Beljonne, and Akshay Rao. 2019. “Photon Upconversion from Near-Infrared to Blue Light with TIPS-Anthracene as an Efficient Triplet–Triplet Annihilator.” ACS Materials Letters 1(6):660–64.

(9) Jeffrey Gorman, Raj Pandya, **Jesse R. Allardice**, Michael B. Price, Timothy W. Schmidt, Richard H. Friend, Akshay Rao, and Nathaniel J. L. K. Davis. 2019. “Excimer Formation in Carboxylic Acid-Functionalized Perylene Diimides Attached to Silicon Dioxide Nanoparticles.” Journal of Physical Chemistry C 123(6):3433–40.

(10) Arelo O. A. Tanoh, Jack Alexander-Webber, James Xiao, Géraud Delport, Cyan A. Williams, Hope Bretscher, Nicolas Gauriot, **Jesse Allardice**, Raj Pandya, Ye Fan, Zhaojun Li, Silvia Vignolini, Samuel D. Stranks, Stephan Hofmann, and Akshay Rao. 2019. “Enhancing Photoluminescence and Mobilities in WS2 Monolayers with Oleic Acid Ligands.” Nano Letters 19(9):6299–6307.

List of Patents

(1) Davis, N. J., **Allardice, J. R.** & Rao, A. (2017). “A photon multiplying material”. United Kingdom Patent No. GB1720190.6. Retrieved from https://www.ipo.gov.uk/p-ipsum/Case/ApplicationNumber/GB1720190.6

(2) Rao, A., **Allardice, J. R.** & Davis, N. J. (2019). “A photon multiplying material”. International Application No. PCT/GB2018/053501. Retrieved from https://patentscope.wipo.int/search/en/detail.jsf?docId=WO2019110971&_cid=P21-K9M7MM-86560-1

List of Figures

List of Tables

Nomenclature

AM1.5G	air mass coefficient at 1.5 atmospheres thickness
AO	atomic orbital
B	magnetic field
CCD	charge-coupled device
FRET	Föster resonant energy transfer
fsTA	femtosecond transient absorption
FWHM	full width at half maximum
GSB	ground state bleach
HA	hexanoic acid
HOMO	highest occupied molecular orbital
ISC	inter-system crossing
LUMO	lowest unoccupied molecular orbital
MO	molecular orbital
nsTA	nanosecond transient absorption
OA	oleic acid
PIA	photoinduced absorption
PL	photoluminescence
PLQE	photoluminescence quantum efficiency
PV	photovoltaic

QD	quantum dot
Rub	rubrene or 5,6,11,12-tetraphenyltetracene
SANS	small-angle neutron scattering
SAXS	small-angle X-ray scattering
SE	stimulated emission
SET	singlet exciton transfer
SF	singlet exciton fission
SF-PM	singlet fission photon multiplicator
TA	transient absorption
TCSPC	time-correlated single photon counting
TEM	transmission electron microscopy
TET	triplet exciton transfer
TET-CA	6,11-bis-((triisopropylsilyl)ethynyl)tetracene-2-carboxylic acid
TIPS-Tc	5,12-bis-((triisopropylsilyl)ethynyl)tetracene
trPL	transient photoluminescence
TTA	triplet-triplet annihilation
TTA-UC	triplet-triplet annihilation upconverter
UCQE	upconversion quantum efficiency

Chapter 1

Introduction

"If we do not change course by 2020, we risk missing the point where we can avoid runaway climate change, with disastrous consequences for people and all the natural systems that sustain us." – UN Secretary-General António Guterres.

The global transition to sustainable energy sources is a key step in the progress towards climate change mitigation. The adoption of energy generation by photovoltaics is a solution to meeting the global energy demand during this transition. Increasing photovoltaics' energy generation efficiency has been pointed to as a productive method for increasing the most economically influential metric: dollars per Watt of energy generated.[1] Reduction of this metric is expected to be an effective means to accelerate the adoption of solar energy.[2] Progress towards this goal should therefore be of paramount concern for academia and industry, as institutions which ideally exist for the benefit of humanity.

This thesis aims to increase the energy generation efficiency of photovoltaic devices by implementing advanced spectra management. Spectral management structures utilising the carrier modulation processes: singlet exciton fission and triplet-triplet annihilation were developed and investigated. The photophysics of these systems was studied by spectroscopic techniques, such as ultrafast transient absorption. The combination of information from multiple sources led to the development of an increased picture of the relevant processes in these spectral management systems. New understanding of existing spectral management systems, demonstration of novel structures, and implications for future research discussed in this thesis deliver important progress towards increased photovoltaic efficiencies.

The Sun constantly irradiates the earth's surface with ~120000 TW of power, which far exceeds even the predicted ~30 TW of global energy consumption by the year 2050.[3,4] This 'effectively' unlimited source of sustainably energy has resulted in significant demand for photovoltaic technology, increasing at ~30% per year, making it the fastest-

growing electricity generation method.[5] However, the total installed solar energy generation capacity is still insufficient, accounting for only ~2% of the total global power consumption in 2017.[2,6] Increases to the power conversion efficiency of the photovoltaic modules is considered a promising strategy to encourage deployment of solar energy generation technologies at a global scale.

The photovoltaic industry has already made a substantial effort to optimise photovoltaic technologies, resulting in low manufacturing costs and high efficiencies. These developments have led to solar energy gaining a competitive advantage over fossil fuels as a power source. However, the dominate technology currently being deployed is single-junction, silicon-based cells. The power conversion efficiency of photovoltaics of this kind is approaching an upper limit of ~32% set by the Shockley–Queisser. Therefore, if a change in strategy is not implemented, there are thermodynamic considerations that will limit further technological progress. Rather than further engineering of this technology, all-new strategies are needed to drive photovoltaic deployment. Ironically, like many solutions to current physics problems, the alternative solution is not new at all: it was predicted long ago.

"[Singlet] exciton fission in the organic coating could provide two electron-hole pairs per absorbed photon… It is suggested that energy transfer from an organic coating of a semiconductor be used to produce electron-hole pairs in the latter." – D.L. Dexter, 1979.[7]

Spectral management strategies aim to efficiently use energy from a broader section of the solar spectrum. Strategies employing singlet fission and triplet-triplet annihilation have been proposed to scavenge more energy from high and low energy photons, respectively.[8–10] The singlet fission photon multiplier and triplet-triplet annihilation upconverter have been proposed as devices which utilise these aforementioned processes.[8,11] Both technologies rely on the conversion of energy between that stored by a spin-triplet exciton in an organic semiconductor and a photon. Proof of concept devices have been developed previously which utilise triplet exciton transfer at the interface of the organic semiconductor and inorganic quantum dots.[12–15]However, the development and optimisation of devices that can generate substantial improvements in power conversion efficiency is still underway.

Within the spectral management community ongoing research aims include; development of bulk solid-state architectures for the singlet fission photon multiplier and triplet-triplet annihilation upconverter, tuning of these architectures for coupling with silicon-based photovoltaics, and investigation of possible loss pathways and their mitigation for optimisation of singlet fission yield, triplet exciton transfer and triplet-

triplet. In this dissertation, we employ materials characterisation, spectroscopy and computational modelling in pursuit of these goals.

We begin this thesis with a summary of the relevant background knowledge and an overview of the current state of research in the literature. Next, we detail experimental and numerical methods. Subsequently, we report on three intertwined projects pursuing advanced spectral management for photovoltaics. Due to the interrelation of these projects, the knowledge gained from any one of them has enlightening implications for the other projects. In Chapters 4 and 5 we demonstrate bulk singlet fission photon multipliers with efficient singlet fission and triplet exciton transfer in solution-phase and solid-state systems, respectively. In both systems, we show that engineering the surface of the inorganic quantum dots with triplet transmitter ligands leads to increased triplet exciton transfer. The solution phase system is shown to meet previously unachieved goals of acceptable levels of parasitic quantum dot absorption and maintained it's singlet fission photon multiplication efficiency up to solar-equivalent fluences. In the solid-state system, we identify the formation of a trap state that limits singlet fission yield. The presence of this trap state is then controlled with QD nucleation sites and film fabrication methodology. Crucial to the development of an efficient solid-state singlet fission photon multiplier, we demonstrate a novel surface chemistry approach to mitigate phase separation in hybrid organic-inorganic quantum dot blends. This approach uses a chemically favourable ligand to encourage quantum dot dispersion within an organic host. Using familiar components Chapter 6 details the investigation of a solution-phase triplet-triplet annihilation upconversion system. Here, we find that attachment of the triplet transmitter ligand introduces a trap state on the quantum dots. These trap states are investigated in relation to triplet exciton transfer and it is indicated that they involve a surface state on the QD. The adsorption of annihilator molecules to the surface of the quantum dots is identified as a process aiding triplet exciton transfer. Each results chapter summarises the lessons learnt from the corresponding project, and in the final chapter, we suggest research directions for future work.

Chapter 2

Background and Theory

This chapter details the minimum required knowledge and technical vocabulary for the reader to have the most enjoyable understanding of the research. We begin with an overview of the electronic states and processes present in organic semiconductors, highlighting their interactions with photons and excited state processes.

Next, we familiarise the reader with inorganic quantum dots and their distinctive photophysical properties. The combination of these two classes of materials has led to fruitful research across the field of optoelectronics. The operation of these hybrid structures generally requires energy transfer at the organic-inorganic interface, which is discussed extensively in this thesis.

The third section of this chapter covers the history and principles of energy transfer at the hybrid interface. Finally, we identify possible uses for optoelectronic devices based on hybrid structures in relation to solar spectral management. The ultimate goal of this is increased efficiency of solar energy harvesting via commercially viable technologies.

For a more exhaustive discussion of these topics, the curious reader is directed to the excellent books “Electronic Processes in Organic Semiconductors” by A. Koehler and H. Baessler, and “Nanocrystal Quantum Dots” edited by V. Kilmov.[16,17] Theoretical frameworks relevant to a specific part of this thesis are detailed within the related chapter.

2.1 Photophysics of Organic Semiconductors

Many scientifically and sociologically important technologies, such as field effect transistors (FETs), photovoltaics (PVs), light emitting diodes (LEDs) and thermoelectric devices require semiconducting materials. A semiconducting material occurs when individual atoms are brought together forming structures as small as a few atoms or as large as entire crystals. Bringing together atoms is one way to generate semiconducting properties. These molecules generally consist of a covalently bonded structure of carbon and hydrogen atoms; and additional structural and electrical functionality is often introduced by the incorporation of atoms such as nitrogen, oxygen, fluorine and sulphur.

In this dissertation we focus on conjugated organic molecules possessing beneficial optical properties. Electromagnetic radiation interacts with the electronic transitions present in these molecules, resulting in the absorption and emission of photons near the visible part of the electromagnetic spectrum.[18] Because of this, conjugated organic molecules are incredibly useful for optoelectronic application. The electronic states associated with these transitions are composed of molecular orbitals, with electronic wavefunctions extending spatially over the covalent bonds within the molecule.

When conjugated organic molecules are combined in the solid state the resultant structures are commonly held together by a relatively weak intermolecular force. For example, monomolecular crystals are held together by '*van der Waals'* interactions. This weak coupling between molecules means that the bulk material's electronic properties are similar to that of the isolated molecules. Thus, an understanding of electronic states for individual molecules is sufficient to describe large amounts of electronic properties for multi-molecule material states such as crystals, liquids and concentrated solutions. With this in mind, the following sections build up an understanding of the electronic states for a single molecule.

2.1.1 Atomic and Molecular Orbitals

One way to understand the dominant physics relevant for the electronic states in conjugated organic molecules is to build up from the individual atomic orbital wavefunction. Atomic orbitals are the solutions to the time-independent Schrödinger equation for a single electron surrounding a positively charged nucleus, similar to hydrogen orbitals. A linear combination of these atomic orbitals can be used to form molecular orbitals, an approximate solution for the multi-nucleus Schrödinger equation.

Figure 2.1 illustrates carbon's atomic orbitals as a basis for the molecular orbitals of ethylene. This example demonstrates the origin of 'π-orbits', the condition for a molecule being conjugated. The atomic orbital electron configuration for an isolated ground state carbon atom is $1s^2 2s^2 2p^2$. Within the theory of atomic orbital hybridisation, bringing together two carbon atoms to form a double bond results in sp^2 hybridisation of each atom's atomic orbitals. For each carbon atom, this sp^2 hybridisation results in the creation of three coplanar, orthogonal and degenerate sp^2 orbitals, from the linear combination of one 2*s* orbital and two 2*p* orbitals.

The ethylene molecular orbitals are then found by taking a linear combination of these hybridised atomic orbitals for each carbon atom and the relevant hydrogen 1*s* orbitals. This leads to the two adjacent sp^2 orbitals, colinear to the bond axis, one from each C atom, mixing to form a σ bond. The σ bonds have electronic density in the space between the participating atoms. These bonds determine the structure of the molecule. Electrons participating in σ bonds are commonly very tightly bound, ~10 eV, relative to unoccupied orbitals or the vacuum.[19] The energy required to facilitate the transition of electrons from orbitals is generally beyond the scope of optical processes.

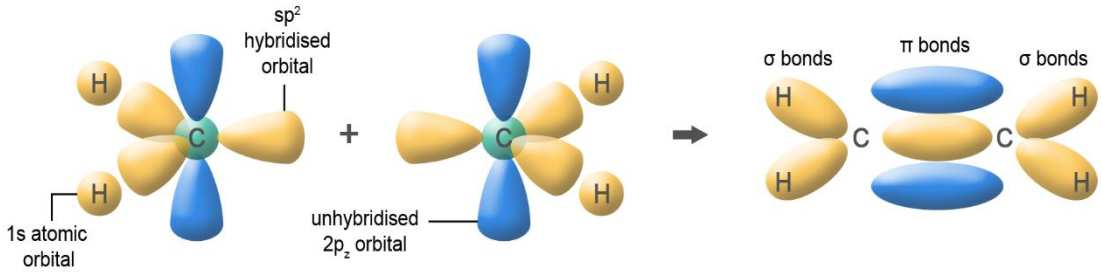

Figure 2.1: Schematic of the sp^2 hybridisation and bonding in ethylene. The electron density in the σ bonds is localised between participating atoms. The π bond's electron density is predominately above and below the sp^2 hybridisation plane. Adapted from a figure by Dr Sebastian Albert-Seifreid.

Other than the sp^2 orbitals, each carbon atom has a lone electron in the remaining p_z orbital. These orbitals mix resulting in a π bond, with electron density perpendicular to the bonding axis and hybridisation plane. These π bonding electrons have zero orbital strength in the hybridisation plane and instead have significant electron density situated above and below the plane. The π bonds lead to energetical unfavourable rotation around the bond axis, leading to more rigid structures. One of the key take away points from this example is that electrons in π bonds are commonly the most weakly bound in conjugated molecules. Therefore, understanding their properties is sufficient to explain low-energy physics of the molecules, such as the interaction with visible photons. For

example, π bonding electrons are responsible for the electrical and optical properties, which have been exploited for numerous applications.[19]

This methodology can be extended to molecules with many atoms, illustrated by Figure 2.2. A variety of theoretical methods exist for determining the solution for the many-nucleus system as a linear combination of atomic orbitals.[19–21] Here, we highlight some of the key features relevant to the presented results. The addition of further sp^2 hybridised carbon atoms to the bonding system can be interpreted as causing π orbitals to delocalise further, resulting in significantly spatially extended wavefunctions. For example benzene has sp^2 hybridisation of the in-plane atomic 2*p* atomic orbitals. The $2p_z$ orbitals, perpendicular to the bonding plane, form a π bonding system with a delocalised wavefunction extending over the entire carbon ring. This highlights an important characteristic of conjugated molecules, the electrons participating in the delocalised π bonding system have wavefunctions extending over many atoms. The electrons are no longer associated with a single atom and are instead a particle that experiences the effects of the entire molecule.

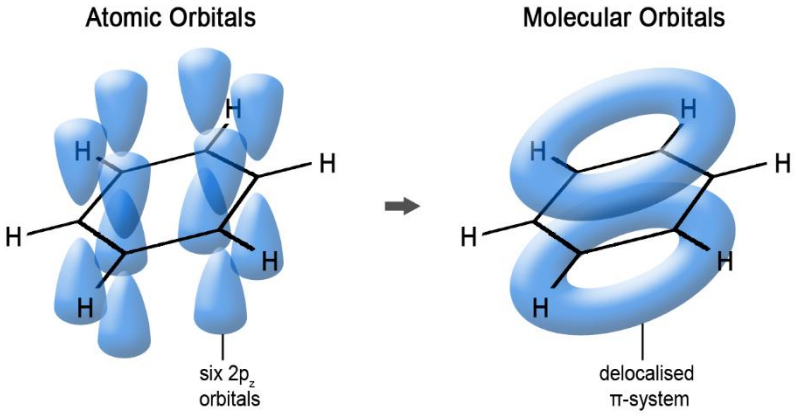

Figure 2.2: Schematic showing the delocalised molecular orbitals of benzene. The combination of six p_z atomic orbitals leads to the formation of a significantly delocalised π bonding system.

It is important to emphasise the distinction between molecular orbitals and complete electronic states of a molecule. Molecular orbitals are the one-electron wavefunctions for a particular molecule. Conversely, the full electronic states for a molecule are the solution to the many bodied quantum mechanics problem prescribed to the molecule and include the electron-electron interactions. The ground state of a many-electron system of the full molecule can be approximated as the progressive filling of the lowest energy molecular orbitals of the molecule with the required number of electrons. Within

this approximation the highest occupied molecular orbital (HOMO) and the lowest unoccupied molecular orbital (LUMO), can be used to calculate the optical transitions and electronic properties of the molecule. Differing energy and occupancy of these two states results in the semiconducting properties of conjugated organic molecules. The energy of the HOMO approximates the energy required to remove an electron from the molecule, or its 'ionisation potential'. The LUMO energy approximates the energy gained by adding an electron to the molecule, the 'electron affinity'. The energy difference between these two levels is the minimum amount for any pair of occupied and unoccupied orbitals. Excitation of an electron from the HOMO to the LUMO gives rise to the lowest energy optical transition of the molecule and thus determines the optical gap of the material. Excited charge carriers such as electrons and holes, generally occupy the LUMO and HOMO respectively, due to thermalisation.

2.1.2 Excitons

To fully describe the electronic processes in organic semiconductors, the use of theoretical frameworks describing the many-electron system, with explicit inclusion of electron-electron interactions are necessary. One example that demonstrates the limitations of molecular orbital description is the absorption of a photon. Absorption of a photon with equal to or above the optical gap can result in the excitation of an electron from the HOMO to the LUMO of a particular molecule. It is useful to treat the missing electron from HOMO as a spin 1/2, positively charged quasi-particle, termed a 'hole'. Molecular orbital approximations struggle to properly describe excited states such as this. Effects such as the relaxation of the nuclear coordinates and redistribution of the remaining electrons in the excited state, means the HOMO and LUMO are not ideal approximations of the excited hole and electron wavefunctions. In particular, these approximations do not account for the coulombic attraction between the electron and hole. This Coulombic attraction leads to a neutrally-charged bound-state quasi-particle, termed an 'exciton'. This excited state, named after 'excitation packets' was proposed by Frenkel to explain the optical absorption in crystalline materials and energy transfer from absorbing donor molecules to emissive accepter molecules with no electrical current.[22] In a simplified picture of the system, the coulombic attraction between this hole and the excited electron results in a reduction of the excited state energy relative to the difference between HOMO and LUMO energies. This difference is referred to as exciton binding energy.

In inorganic semiconductors, strong dielectric screening results in a reduced coulombic interaction between the electron and hole. Thus the associated binding energy of the

exciton is reduced to the order of 10s of meV.[23] Excitons in these systems are distinguished as 'Mott-Wannier excitons', since at room temperature there is readily enough thermal energy available to separate these excitons into free electron and hole charge carriers.[24] Additionally, these charge carries have wavefunctions that extend over volumes significantly larger than that of a crystal unit cell. Comparatively, the significantly lower dielectric constant typical of organic semiconductors, results in reduced screening of the electron-hole coulombic attraction. Thus, the exciton binding energy for these excitons, referred to as 'Frenkel excitons', is typically 100s of meV. The resultant excitons are strongly localised over a few molecules and not easily separated by external electric fields or thermal energy at room temperature. This use of the exciton as a description of the excited state is useful for understanding electronic transport properties of organic semiconductors.

Another situation where the molecular orbital treatment is not sufficient, is the consideration of the electron's spin. This is particularly important for understanding spin physics relevant to excitons. These excitons are two bound particles with spin-angular momentum. The combination of two spin 1/2 particles has well-established rules for the angular momentum of the exciton and leads to four eigenstates.[25] One of this eigenstates, referred to as the 'singlet state', has antiparallel spin for the electron and hole, thus has total spin of zero. The three remaining states, referred to as 'triplet states', have parallel spin for the electron and hole, and total spin angular momentum of 1 (in units of $\hbar$). This spin dependence of the exciton introduces a further energy dependence of the system due to the exchange interaction.[26] This exchange interaction separates the otherwise degenerate singlet and triplet states, resulting in the triplet state being lower in energy than the singlet state. This energy difference, termed the 'exchange energy', is generally independent of the delocalisation of the electron and hole.[27] The exchange energy has been experimentally found to be ~0.7 eV in conjugated polymer molecules.[26] The increased overlap of HOMO and LUMO results in an increased exchange energy in the case of polyacenes, relevant to the studies presented here.[27–29] Oligoacenes are experimentally found to have singlet triplet splitting about 1 eV independent of molecule size.[27] Excitons with spin wavefunction from one of the triplet states, referred to as 'triplet excitons', behave very differently from 'singlet excitons'. The triplet exciton's transport between molecules and interaction with photons is significantly different from that of the singlet exciton, as detailed in following sections. It is the unique properties and possible uses of the triplet exciton states that are of significant investigation in this dissertation.

2.1.3 Dynamic Processes in Organic Molecules

The research presented in this dissertation includes optical studies of the dynamic evolution of excited state populations in conjugated organic materials. Our use of conjugated organic molecules is motivated by their potential application in solar energy harvesting. As such, understanding their interaction with visible light is important. In this section we detail some of the principles that govern the optical processes occurring in conjugated organic materials that determine the excited state dynamics.

2.1.3.1 Radiative Transitions

To develop an understanding of organic molecules' interaction with electromagnetic radiation, we start with 'Fermi's golden rule'. Initially developed by Dirac from first-order time-dependent perturbation theory, it describes the transition rate from an initial state to a continuum of final states mediated by a perturbing interaction, such as interaction with a photon.[30] There many derivations of this expression, which are detailed in previous work.[19,31] In summary, begin with the initial and final eigenstates of the unperturbed time-independent Hamiltonian. The interactions of this system are described by an interaction Hamiltonian and treated as a perturbation of the original system. Perturbation theory then allows calculation of the eigenstates for the full Hamiltonian system by a Taylor series expansion in the time-evolution operator.[16] In this manner, it is possible to calculate the transition rate k_{if}, between an initial Ψ_i and final Ψ_f eigenstate of the unperturbed system, by the expression[16]

$$k_{if} = \frac{2\pi}{\hbar} \left| \langle \Psi_f | \widehat{H_I} | \Psi_i \rangle \right|^2 \rho(E_f) \,. \tag{2.1}$$

Here, $\widehat{H_I}$ is the interaction Hamiltonian and $\rho(E_f)$ is the density of the final state. When investigating the interaction with photons such as radiative transitions, the appropriate perturbation Hamiltonian is given by the electric dipole operator $\widehat{H_I} = e\hat{\boldsymbol{r}}$, where e is the fundamental charge and $\hat{\boldsymbol{r}}$ is the position operator.

The eigenstates to the time-independent Hamiltonian can be separated into three components; the electronic wavefunction $\Psi_{el}(\boldsymbol{r}, \boldsymbol{r_n})$ dependent on the electron's location $\boldsymbol{r}$ and nuclear coordinates $\boldsymbol{r_n}$, the vibrational wavefunction $\Psi_{vib}(\boldsymbol{r_n})$ and the spin wavefunction Ψ_{spin}, which depends on the spin of the electrons. The separation of the wavefunction into these three components ignores interactions between them. This

originates from the Born-Oppenheimer approximation which separates electronic and vibrational wavefunctions. Within this approximation the transition rate is given by

$$k_{if} = \frac{2\pi}{\hbar}\left|\langle \Psi_{el,f}\Psi_{vib,f}\Psi_{spin,f}\left|e\hat{\boldsymbol{r}}\right|\Psi_{el,i}\Psi_{vib,i}\Psi_{spin,i}\rangle\right|^2\rho(E_f) \quad (2.2)$$

The spin and vibrational wavefunctions have no dependence on $\boldsymbol{r}$, and so the transition rate can be simplified to

$$k_{if} = \frac{2\pi}{\hbar}\left|\langle \Psi_{el,f}\left|e\hat{r}\right|\Psi_{el,i}\rangle\right|^2\left|\langle \Psi_{vib,f}\left|\Psi_{vib,i}\rangle\right|^2\right|\langle \Psi_{spin,f}\left|\Psi_{spin,i}\rangle\right|^2\rho(E_f)\,, \quad (2.3)$$

with dependence only on the overlay of the initial and final states of the vibrational and spin wavefunction. Under these approximations, the photon mediated transition rate is the product of three factors. In the following section we demonstrate the selection rules for the photon mediated transition rate in terms of these three factors.

2.1.3.1.1 Electronic Factor

The first factor influencing the radiative transition rate is the $\left|\langle \Psi_{el,f}\left|e\hat{\boldsymbol{r}}\right|\Psi_{el,i}\rangle\right|$ term, commonly referred to as the 'transition dipole moment'. The dipole operator has odd parity, its sign flips under spatial inversion. Thus, if the initial and final state wavefunctions are of the same parity, the integrand as a whole has odd parity and thus the integral evaluated over all space is zero. Therefore its transition rate is zero. The transitions between states of the same parity, is referred to as 'symmetry forbidden'. For most molecules, their ground state wavefunction is of even parity and so photon absorption can only access excited states of odd parity. Excited states that have a symmetry forbidden transition with the ground state are commonly referred to as dark states. Symmetry of the wavefunctions aside, the strength of the transition increases with both the overlap of the initial and final wavefunction, and the spatial extent of the wavefunctions. Wavefunctions with higher delocalisation, such as in conjugated systems, lead to stronger photon interactions.

2.1.3.1.2 Vibrational factor

Within the Born-Oppenheimer approximation, vibrations refer to displacements of the nuclear coordinates. The energy of the molecule is dependent on the position of the nuclear coordinates interacting with the electronic wavefunctions in the electrons

bonding the molecule together. The electronic bonding determines the shape of the molecule, and results in the expectation value for the nuclear coordinates sits at the bottom of a local minimum in the potential energy surface. By a second order Taylor-series expansion about this local minimum, one can arrive at a paraboloid potential energy surface or, equivalently, a multi-dimensional harmonic oscillator potential. A quantum mechanical treatment of the oscillations in nuclear coordinates leads to sets of vibrational states that are evenly spaced in energy with associated vibrational wavefunctions for the molecule. A coordinate transform from nuclear coordinates to the normal mode coordinates Q_i is usually performed to emphasise collective motion of the couple oscillators. The potential energy surfaces associated with these normal modes are dependent on the electronic wavefunctions and so are different for excited electronic states. As Figure 2.3 illustrates, the potential energy surfaces of the excited state are generally shifted to a higher minimum energy and larger normal mode coordinates. This is consistent with the increased electronic energy and increased inter-nuclear distances in the excited states.

Returning to the radiative transition rate; it is transitions between these vibrational states that we are investigating. The factor $\left|\left\langle \Psi_{vib,f} \middle| \Psi_{vib,i} \right\rangle\right|^2$ is referred to as the 'Franck-Condon factor'. This factor illustrates that it is the overlap of initial and final vibrational wavefunctions that affects the radiative transition rate. The associated 'Franck-Condon principle', asserts that transitions between different electronic level's potential energy surfaces, occurs vertically, with no change in nuclear coordinates during the transition. For example, radiative excitation from the ground electronic and vibrational state, occurs to multiple vibrational energy levels within the excited electronic state (Figure 2.3). This is then followed by relaxation of the molecule to the lowest vibrational energy level within the excited electronic level, usually by the desperation of vibrational energy to the environment. Such vibrational relaxation processes occur on a picosecond timescale. This is significantly faster than the reverse radiative transition to the ground state that occurs on a nanoseconds timescale. As a result, the emission of photons predominately occurs from the lowest vibrational energy level of the excitation state to many of the excited vibrational energy levels of the ground state. The resultant pattern of photon absorption strength has clear peaks due to vibrational energy transitions. The emission of photon strengths is roughly a reflection of the absorption with respect to energy.

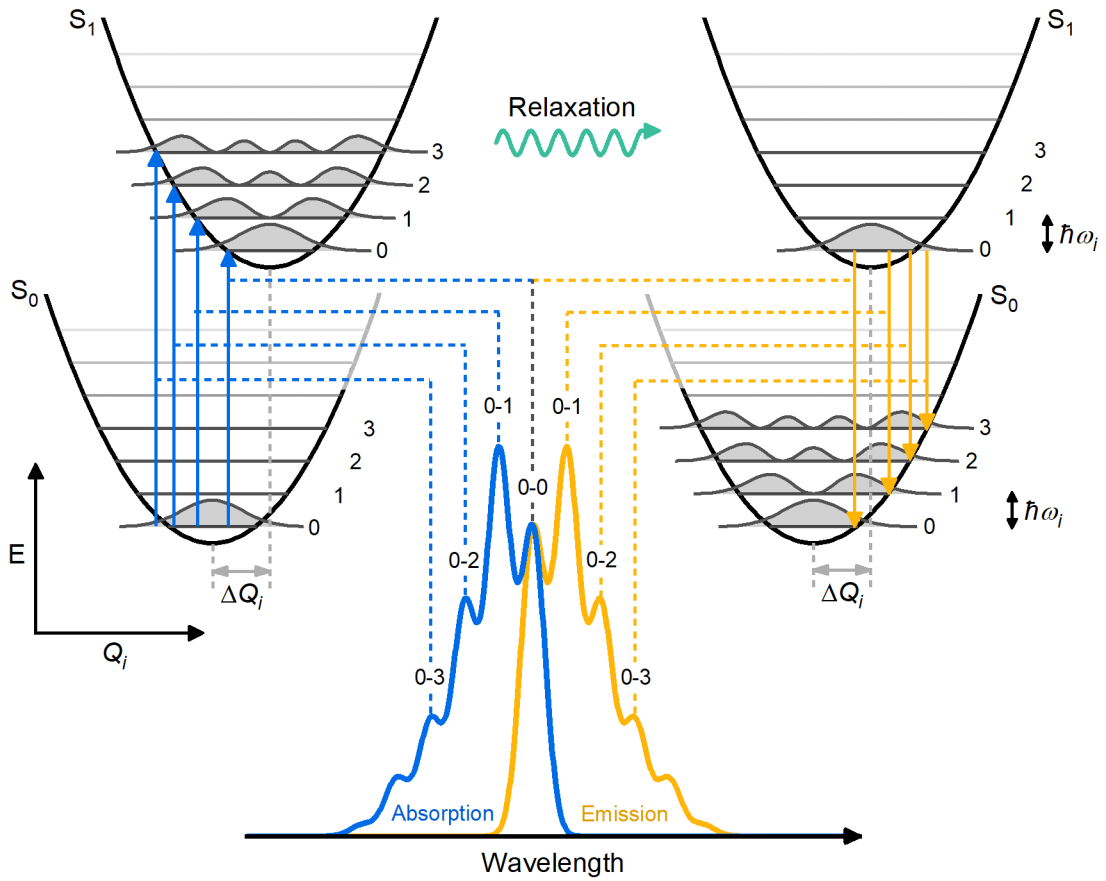

Figure 2.3: Schematic showing the absorption and emission of photons by an organic molecule. Absorption of photon from the ground state S_0, to the first excited, spin singlet, electronic state S_1. The vibrational levels for each electronic level are as labelled. After excitation to many of the excited vibrational energy levels in the excited electronic state, relaxation to lower vibrational energy levels occurs. This is followed by emission of photons by transition from the lowest vibrational energy level in the excited state to many of the excited vibrational energy levels in the ground electronic state. The correspondence between these transitions and the resultant absorption and emission spectrum is shown. Adapted from a figure by Dr Sebastian Albert-Seifried.

2.1.3.1.3 Spin factor

The remaining factor of consideration, influencing the radiative transition rate, is due to the spin of the initial and final state. The inner product $\left|\langle\Psi_{spin,f}|\Psi_{spin,i}\rangle\right|$ is one for identical initial and final spins states and zero for different initial and final spins states. As such, transitions between states with different spin are referred to as 'spin forbidden'. This asserts that radiative transitions from a spin singlet state to a spin triplet state is spin forbidden so is unlikely to occur. This selection rule is loosened where 'spin-

orbit coupling' is significant. Spin-orbit coupling is the interaction of the orbital angular momentum and the spin angular momentum of the molecule. This interaction mixes the singlet and triplet states, making some transitions allowed which would otherwise be spin forbidden. The strength of spin-orbit coupling increases with the atomic number of the atoms used in the molecule. As a result, photon mediated transition rates between singlet and triplet states are only significant in molecules containing heavy atoms. The ground state in organic molecules is commonly of singlet spin. Therefore, emission of a photon from a spin singlet excited state to the ground electronic state is spin allowed and referred to as 'fluorescence'. Emission from a spin triplet excited state is usually spin forbidden and referred to as 'phosphorescence'. The general term for the emission of a photon from an excited state is 'photoluminescence'.

2.1.3.2 Non-radiative Transitions

Having briefly surveyed the influences of radiative transitions in organic molecules, we now detail the principles of transition between energy levels not only mediated by interaction with a photon. Previously, we mentioned the relaxation between vibrational states within an electronic energy level. The excess vibrational energy is dissipated to the environment surrounding the molecule as heat. Due to the exchange of heat energy between molecules, this results in a Maxwell-Boltzmann distribution of the populations within the vibrations energy levels in a large sample of molecules.

Non-radiative transitions occur between vibrational energy levels from different electronic states. If spin of the total wavefunction is conserved during non-radiative transitions, the process is referred to as 'internal conversion' (Figure 2.4). When the spin of the wavefunction does change the process is 'intersystem crossing'. Similar to the radiative transitions, non-radiative transitions rates can be found by time-dependent perturbation theory. In this case the appropriate interaction Hamiltonian is the 'nuclear kinetic energy operator'. Transition rate from initial to final state is given by[16]

$$k_{if} = \frac{2\pi}{\hbar} \left| \left\langle \Psi_{el,f} \Psi_{spin,f} \Psi_{vib,f} \left| \frac{\partial}{\partial Q} \right| \Psi_{el,i} \Psi_{spin,i} \Psi_{vib,i} \right\rangle \right|^2 \rho(E_f) \,. \tag{2.4}$$

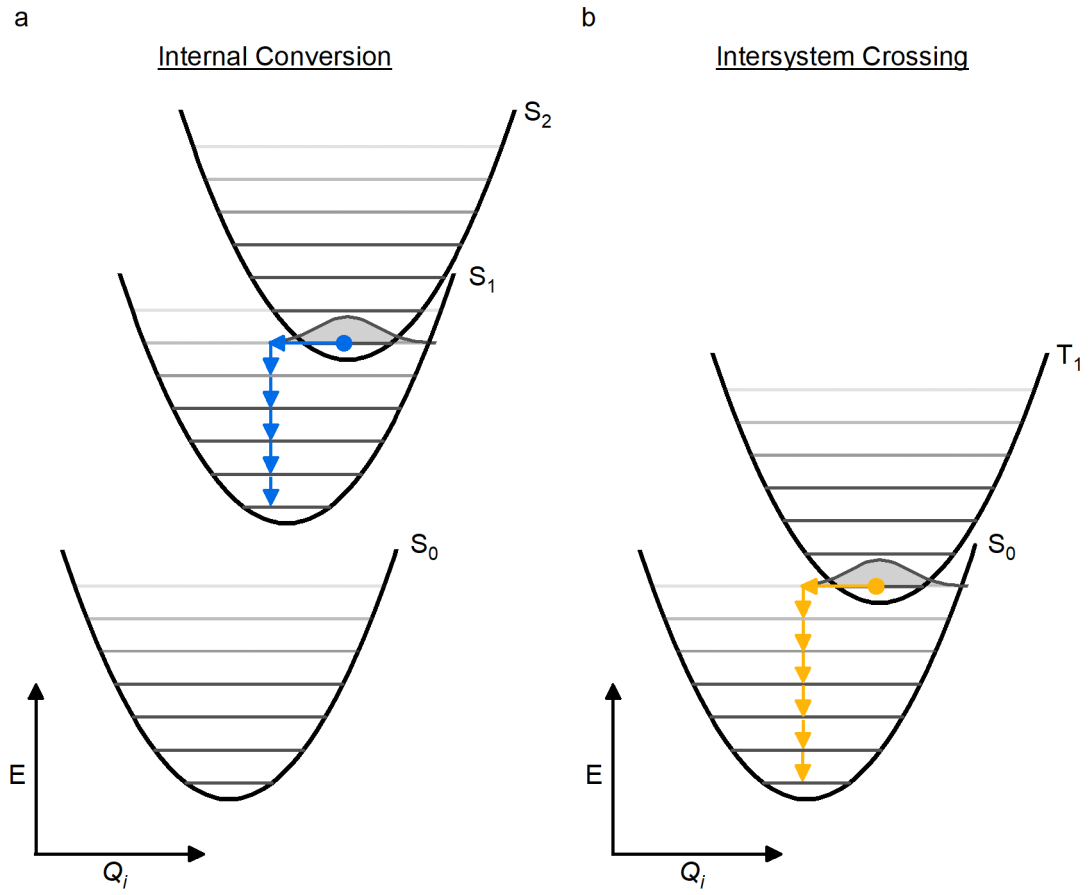

Figure 2.4: Schematic of non-radiative transitions followed by vibrational relaxation. a) Internal conversion between states of the same spin. b) Intersystem crossing between states of different spin. Adapted from a figure by Dr Ture Hinrichsen.

From this one can arrive at the expression

$$k_{if} = \frac{2\pi}{\hbar} J^2 F \rho(E_f) \,, \tag{2.5}$$

where $F = \left|\langle \Psi_{vib,f} | \Psi_{vib,i} \rangle\right|^2$ is the Franck-Condon factor mentioned previously and J contains the electronic coupling between the initial and final states. The Frack-Condon factor has an exponential relationship with the energy difference between the initial and final state.[32,33] This leads to a non-radiative transition rate of the form

$$k_{if} \propto \exp\left(-\gamma \frac{\Delta E}{\hbar \omega_M}\right), \tag{2.6}$$

where γ is dependent on the structure of the molecule and ω_M is the angular frequency of highest energy vibration of the final electronic state.[32,33]

This highlights the mediation of non-radiative transition by 'phonons': quasi-particles of vibrational energy. This expression known as 'energy gap law', has been shown to be in good agreement with experimental data and sufficiently describes many non-radiative processes.[34]

In many conjugated molecules, the highest energy mode is a stretching mode of the molecule and has energy of the ~200meV.[35,36] As a result, internal conversion between the many, closely packed, excited states to the 'band edge' state, of the same spin, occurs rapidly within ~100 ps (Figure 2.4a).[37,38] In contrast, the transition from the band edge state to the ground state has an energy difference of a few eV, and therefore proceeds significantly slower via a multi-phonon decay pathway.[39] Figure 2.4b illustrates an important case of non-radiative transition, the decay from the first excited triplet exciton state to the ground state (spin singlet). The initial, horizontal component of the transition is an example of intersystem crossing mediated by a weak spin orbit coupling. As a result, the transition rate is usually relatively slow. However, in the absence of fast radiative decay (spin forbidden transition) and reduced energy difference from the ground state, the non-radiative decay of the excited triplet state is generally the dominate decay pathway. [39] In absence of influencing factors, such as strong spin-orbits coupling, typically the first excited, spin triplet state has significantly longer lifetimes than the first excited, spin singlet state. This long lifetime makes them an incredibly useful 'energy carrier', with many applications as shown by results presented in this dissertation.

2.1.3.3 Singlet Fission and Triplet-Triplet Annihilation

In this section we introduce two processes occurring in conjugated organic materials important for understanding results in 'singlet fission' and 'triplet-triplet annihilation'. Singlet fission (SF) is an exciton multiplication process where a photoexcited spin singlet exciton is rapidly and efficiently converted into two spin triplet excitons. This is proceeded by the excited singlet state interacting with an adjacent molecule which is in the ground state and therefore requires a minimum amount of coupling between the two molecules. Polycrystalline films or concentrated solutions of a singlet fission capable

molecule are some examples with sufficient coupling for singlet fission to occur. Triplet-triplet annihilation (TTA) is effectively this reaction in reverse. Two spin triplet excitons 'annihilate' together to form one excited state spin singlet exciton and one spin singlet, ground state molecule. Other than the spin constraints, these processes are bound by energy conservation and so only occur if enthalpically allowed.

Singlet fission was first proposed by Singh et al. to explain the 'delayed' fluorescence in crystalline anthracene.[40] Specifically, when exciting with a photon energy twice that of the triplet exciton, they observed a novel triplet generation process. Critically, this triplet generation process had an activation energy incompatible with direct intersystem crossing. Singh et al. deduced that this triplet generation process could be both rapid and efficient. This was backed by the observation that this process, only occurring from a highly energetic singlet state, was out-competing internal conversion down to the band edge state. This was followed by significant research in the 1960-80s, which identified singlet fission occurring in variety of organic materials, including crystalline anthracene, tetracene.[41,42]

A important development in the understanding the singlet fission process was achieved by investigating the strengths of the 'prompt' and delayed fluorescence under the application of an external magnetic field.[43,44] These experiments were built on the already understood properties of TTA under an applied magnetic field.[45,46] They prompted the development of the first theoretical descriptions of the process.[47]

The experimental evidence of a rapid singlet fission process indicates that it is a spin allowed process. Within the model proposed by Merrifield and Johnson, singlet fission preferentially populates certain spin configurations of the triplet states.[45,47] Within this model the singlet fission produces a coupled triplet pair state ${}^1(TT)$ with pure spin singlet character, thus conserving angular momentum. The transition from excited singlet exciton to correlated triplet pair state is assumed to be fundamentally rapid, mediated by electrostatic interactions. The separation of the triplet pair to free triplets $T_1 + T_1$, is relatively slow and governed by spin decoherence, as well as spin-dependent and diffusion processes. This theoretical framework suggests the following reaction scheme for the singlet fission process

$$S_n + S_0 \rightleftarrows {}^1(TT) \rightleftarrows T_1 + T_1 \,. \tag{2.7}$$

Here S_n is the excited spin singlet state and S_0 is a ground state molecule. The main advantage of this description with two steps to the free triplets, is that it offers an

explanation for the observed magnetic field dependence of the steady state and transient fluorescence.

The expected dependence of steady state fluorescence for a singlet fission system is well established.[46] Via the Zeeman interaction, application of a magnetic field modifies the number of triplet pair states that can couple to the S_1 state shifting the equilibrium between singlets and triplets, described by equation (2.7).[48] This modulation of the singlet population can be detected by a change in the steady state fluorescence, photocurrent from a device, or levels of prompt and delayed transient fluorescence. Typically, this results in an increased fluorescence, under external field strengths of ~500 mT.[49] The rise at high fields is usually accompanied by a slight dip at low fields. The exact crossing between these two regimes is dependent on the material, usually occurring between 50 mT and 250 mT.

These magnetic field effects are not universally observed for all materials that undergo singlet fission. For example, the exact nature of the equilibrium between the singlet triplet pair and free triplets, can be heavily one sided for materials exhibiting exothermic singlet fission. In such cases, the change in singlet population due to the application of a magnetic field is low to undetectable. Thus, the absence of a magnetic field effect on the fluorescence does not rule out the presence of singlet fission occurring.[50]

The energy of the singlet exciton in relation to the twice the triplet exciton state's energy is important for determining whether singlet fission or triplet-triplet annihilation is the dominant process in an organic material. For singlet fission to be dominant, the energy of the singlet state is generally required to be at least twice that of triplet state. The opposite is true for triplet-triplet annihilation. These are basic guidelines and there are extra entropy considerations that should also be included.[51,52]

Additional energy considerations include the energetic accessibility of further excited triplet and singlet states, such as the following reactions

$$T_1 + T_1 \rightarrow T_n + S_0 \,,$$

$$S_1 + S_1 \rightarrow S_n + S_0 \,. \qquad \textit{(2.8)}$$

As competing channels with the singlet fission and preferred triplet-triplet annihilation process, these reactions are not generally desired. However, minimisation of bimolecular processes such as these has been achieved via engineering of the molecule structure.[53] Molecular design such as this offers a means to optimise the efficiency of either singlet fission or triplet-triplet annihilation.

Since the initial research interest in singlet fission in the 1970s, there has been a significant wave of new results in the past decade. These include experimental verification that materials with singlet fission efficiencies approaching 200% are indeed possible.[54] Organic material need not be in crystalline form, singlet fission can occur in the solution phase as well.[55,56]

Triplet-triplet annihilation has been shown to be significantly efficient in the solution phase.[57] The hypothesised coupled triplet pair state has been directly observed, along with its separation into free triplets. [55,56,58–61] Advances in ultrafast femtosecond spectroscopy have allowed the identification of vibronically coherent components of singlet fission on sub 500 fs timescales. The coupling of vibrionic and electronic degrees of freedom result in ultrafast generation of the triplet pair state.[58,59,62,63]

Lastly, there are now many increasingly complex theoretical descriptions of the singlet fission process that capture greater extents of the relevant physics.[48,62,64] For example, models can be used to explain the quantum beating present in delayed fluorescence as the coherent recombination of the triplets to regenerate the singlet state.

2.1.3.4 Excimers and Singlet Fission

The role of 'excimer' states in the singlet fission process is debated.[55,56,65,66] The term excimer refers to an 'excited dimer' state particular to a physically interacting pair of molecules rather than a chemically bonded dimer.[16] The excimer state is the result of the van-der-Waals interaction between adjacent molecules, leading to the splitting of the otherwise degenerate, singularly excited state on either molecule. In cases where the intermolecular distance is large or the relative orientation of the two dimers is such that the dipole-dipole interaction between molecules is weak, then this splitting can be small.

For 'amorphous' films, the highly disordered nature of the molecular packing can result in the mean splitting being smaller than the inhomogeneous broadening within the film. This situation is desired for devices such as organic light-emitting diodes and organic solar cells, as there is no low energy excimer state to 'trap' charge carriers. This situation can be engineered using synthetic or fabrication strategies. For example, the addition of bulky, sterically hindering side groups to the molecules, or use of a volatile, low-boiling point solvent for film processing, can result in high structural disorder. In Section 5.4, we investigate the use of a vacuum pressure to facilitate solvent evaporation for the fabrication control of disordered films. In films such as these, electronic states are

resemble isolated molecules with the inclusion of polarisation interactions within the solid.

In comparison, in the case of strong van-der-Waals interactions, the energy level splitting can be large, and excitation can result in significant reorientation of the interacting molecules. As a result, photoexcitation of the material leads to the occupation of excimer states that sit significantly lower (by at least 100 meV) than the first excited singlet state. Spin singlet excimer states can still have significant oscillator strength and thus can emit photons directly. However, excimer emission has spectral profiles that are usually exempt from any vibrational structure, and in comparison to the fluorescence are redshifted and have slower radiative decay rates.[67] These distinctions offer easily verifiable means for excimer identification.

In films of organic molecules, these two cases are not absolute. The random morphology present within amorphous films can result in varying degrees of these cases in parallel. For example, crystallographic faults in polycrystalline films or the boundary of ordered and amorphous domains are prone to creating sites that give rise to excimer fluorescence, even if the ideal crystal emits only monomer like fluorescence.[16] In technologically relevant materials such excimer states have been shown to act as traps, reducing device performance.[68] The role of excimer states has been interpreted by some as either an intermediate to or competing pathway with the singlet fission process. In Section 5.4 we investigate these possible explanations and the consequences for harvesting of triplets excitons generated by singlet fission. Smith, M.B. and Michl, J. have provided in-depth reviews of singlet fission materials.[27,54]

2.2 Photophysics of Inorganic Quantum Dots

Quantum dots (QDs) are nano-scale clusters of atoms, termed a nanocrystal, commonly made from inorganic materials. Quantum dots are an incredibly promising optoelectronic material due to a combination of unique properties.[69] These versatile semiconductors are solution processable and are synthesised at low temperatures relative to the energy intensive furnaces used for purification of inorganic crystalline semiconductor materials such as Si. Of particular note, inorganic quantum dots can be engineered to interact with light across the sun's spectrum and beyond into the infrared.[70]

2.2.1 Electronic States of Quantum Dots

Inorganic nanocrystals can be made significantly smaller than the spatial extent of the exciton excited states of the bulk semiconducting material. This parameter, commonly quantified by the 'Bohr radius' of the exciton, defines the average electron-hole separation of an exciton in bulk material. The process of restricting the excitons spatial extent within the nanocrystal, leads to a phenomenon referred to as 'quantum confinement'. Here, the energy bands of the bulk semiconductor are restricted to discrete energy levels in the nanocrystal. Consequentially quantum dots are considered as artificial atoms, due to their analogy with atomic orbitals and energy levels.

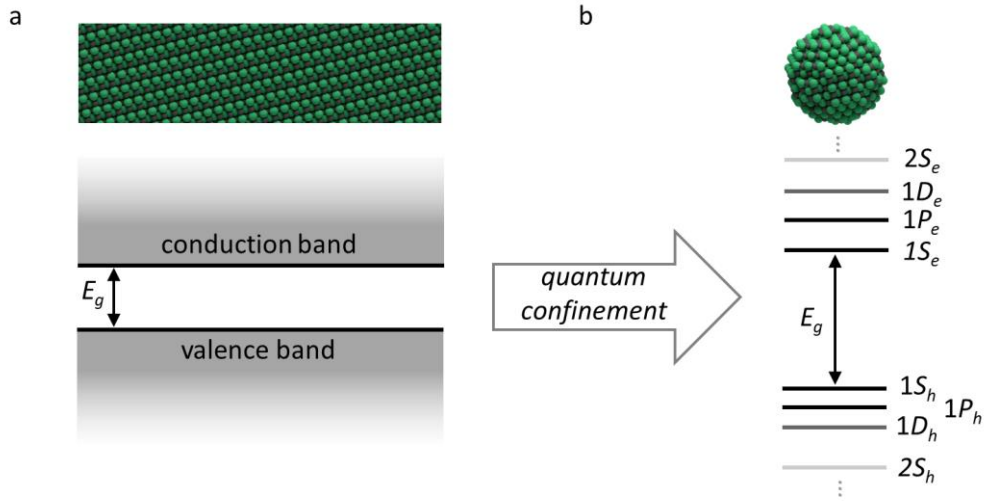

Figure 2.5: Effect of quantum confinement on the electronic states of nanocrystals. a) bulk material possessing conduction and valence bands. b) Nanocrystal with quantum confinement leading to quantised energies for the electrons (e) and holes (h). The quantum confinement results in an increased bandgap for smaller nanocrystals.

Approximation with the iconic quantum mechanics problem of a spherical infinite quantum well gives a qualitative picture of the electronic states in QDs. Within this framework, the available electronic states for the electron or hole are described by[17]

$$E_{l,n}^{e,h} = \frac{\hbar^2 \alpha_{l,n}^2}{2m_{e,h}a^2}. \tag{2.9}$$

Here $m_{e,h}$ is the effective mass of electron or hole, a is the radius of the nanocrystal, $\alpha_{l,n}$ is the *nth* root of the spherical Bessel function of order *l*. Similar to the principal and orbital quantum numbers of atoms, n is commonly assigned integer values, while l is given letters (S,P,D,…), for the naming of QD states (Figure 2.5). More complete

treatments of the quantum dot include the effects of band mixing and Coulomb interaction between electron and hole. Additionally, due to faceted crystal growth the nanocrystals are non-spherical. These limitations aside, this interpretation highlights the strong dependence of the energy levels on the size of the quantum dot. This relationship illustrates the route to 'bandgap' engineering with control of the nanocrystal size by synthesis. Nanocrystals that show an increased bandgap compare to that of the bulk material are said to exhibit the 'quantum size effect'.

2.2.2 Radiative Transitions

The radiative transition probability from the ground state, $|0\rangle$, to a particular electron-hole pair is given by dipole matrix element,[17]

$$P = \left|\langle \Psi_{e,h,p}| \, \boldsymbol{e} \cdot \hat{p} \, |0\rangle\right|^2 ,$$

(2.10)

where $\boldsymbol{e}$ is the polarisation vector of the light and $\hat{p}$ is the momentum operator. In the 'strong confinement' regime, where the electron and hole can be treated independently, the transition probability can be expressed in terms of the singlet particle states

$$P = |\langle \Psi_e| \, \boldsymbol{e} \cdot \hat{p} \, |\Psi_h\rangle|^2 .$$

(2.11)

Finally, assumption that the 'envelope functions' are slowly varying in terms of $\boldsymbol{r}$, such that the momentum operator acts only on the unity cell portion (u_{nk}) of the wavefunctions and in the spherical infinite well model yields

$$P = |\langle u_c| \, \boldsymbol{e} \cdot \hat{p} \, |u_v\rangle|^2 \, \delta_{n_e,n_h} \delta_{l_e,l_h} .$$

(2.12)

This highlights the simple selection rules for the radiative transitions to or from the ground state ($\Delta n = 0$ and $\Delta l = 0$). The participating electron and hole must have the same energy level n and angular moment l. The optical gap is therefore approximated by the sum of the $1S_e$ and $1S_h$ energies. Within this interpretation the optical gap of the QD is heavily dependent on the size of the nanocrystal. This leads to absorption and luminescent energies that are determined by nanocrystal size, which can be controlled by synthesis. Optical or electrical excitation to high energy states typically relax to band edge states ($1S_e$ electron and $1S_h$ hole) on a few to 10's of picosecond timescales.[71–73] In QDs this relaxation can be mediated by a variety of mechanism such as phonon

mediated relaxation (for weakly confined QDs) or electron-hole Auger relaxation (strongly confined QDs).

2.2.3 Surface Passivation and Ligands

The high surface to volume ratio of quantum dots, means a significant proportion of the atoms in the nanocrystal are close to the surface where defects commonly occur. The surface of these nanocrystals are normally 'capped' with organic aliphatic ligands that chemically bind to the inorganic's surface. These ligands stabilise the surface chemistry of the nanocrystal during growth and passivate surface defects.[69] Non-optimal ligand coverage can result in defect states at non-passivated atom sites on the nanocrystal surface, causing low energy states within the bandgap.[74] These and other trap states can induce non-radiative recombination of charge carrier pairs.[75,76] Critical to optoelectronic applications, surface traps and ligand choice can effect photoluminescent quantum efficiencies, recombination rates, excited state transfer and overall performance of QD devices.[77] The insulating, aliphatic ligands, that inorganic QDs are usually produced with, are often changed post-synthesis to shorter ligands, or removed completely to enhance excited state transfer in and out of the QDs.[78]

2.2.4 Quantum Dots in Films

One standing limitation is that when quantum dot films are fabricated, generally they lose properties that make isolated quantum dots so useful, such as in a colloidal suspension. This comes down to two dominate factors, reduced excitonic energy and aggregation assisted trapping. Generally, when made into films there is increased coupling between individual nanocrystals. In the case of strong coupling, the exciton energy can be reduced due to the leakage of electronic wavefunctions into adjacent nanocrystals, reducing the effective spatial confinement.[17] For example, this leads to red-shifting effects that a device designer would need to take into account to match the energy levels between a film of QDs and another material such as an electron acceptor.

Secondly, QDs on their own have an affinity to pack into close-packed structures such as face-centred-cubic or hexagonal-close-packed arrays of QDs. The sufficient interdot coupling can lead to excited state transfer between QDs.[78] When defected QDs are included in this aggregated quantum dot composite, they trap states that can affect the entire aggregate.[77] This leads to decreased excited state properties such as charge transport and photoluminescence yields.[75,76] This is also the case for co-dispersions of QDs with another material, such as a conjugated organic molecule. Co-dispersions

generally result in segregation into a QD aggregate and organic molecule phases.[79,80] Hybrid structures with homogeneously dispersed QDs within an organic molecular host are highly sought after for spectral management applications.[9]

2.2.5 Hybrid Devices with Conjugated Organics

Within this dissertation, we extensively use quantum dots in hybrid structures with conjugated organic molecules for their spin-mixing and energy tunability properties. The lead sulfide (PbS) nanocrystals used in this dissertation contain the heavy element Pb. As discussed in Section 2.1.3 the high atomic number of the atoms within the nanocrystals, leads to strong spin-orbit coupling. As a result, the pure spin singlet and spin triplet states are poor quantum numbers for the system, resulting in strong mixing of these states within the QD. It has previously been shown that these QDs are a useful means of converting between spin triplet excited states on organic molecules and absorbent/ luminescent states in the QD. It has been shown that triplet excitons injected from an organic material into a lead based QDs become luminescent.[13,81] The reverse process of photoexcitation of a lead based QD leading to triplet excitons on an adjacent organic molecule has also been demonstrated.[14] Critically, it is the ability to tune the bandgap of the QDs that allows the selection between these two processes. These processes are discussed further throughout the results of this dissertation.

2.3 Triplet Exciton Transfer

In this section we highlight the key principles governing triplet exciton transfer at the hybrid interaction between inorganic quantum dots and organic semiconductors. Here ‘transfer’ refers to the simultaneous ‘de-excitation’ of a donor ‘chromophore’ and excitation of an acceptor chromophore.

For systems with strong inter-molecular coupling energy transfer can be coherent, preserving phase information of the wavefunction from the donor to acceptor. Naturally occurring light-harvesting complexes are one system suggested to exhibit coherent transfer.[82] In conjugated organic molecules, transfer is commonly consistent with weak coupling and associated with incoherent transfer.[19] Here, electronic and vibrational dephasing leads to localisation of the exciton on a single chromophore and transport occurs via the diffusive hopping of the exciton between chromophores.

There are two commonly considered mechanisms for the transfer of excitons, Föster resonant energy transfer and Dexter transfer (Figure 2.6).[83,84] These processes are mediated by coulomb and exchange mechanisms respectively.

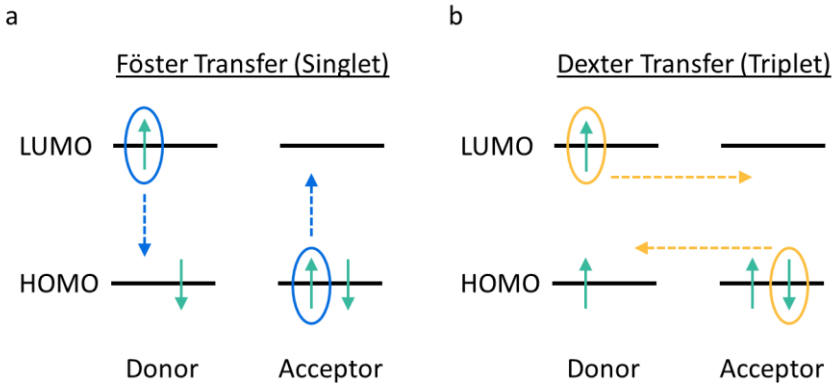

Figure 2.6: Schematic of Föster and Dexter energy transfer.
a) Föster transfer of a spin singlet exciton from donor to acceptor, mediated a 'virtual' photon. b) Dexter transfer of a spin singlet exciton from donor to acceptor, mediated the correlated transfer of two electrons. Adapted from a figure by Dr Mark Wilson

2.3.1 FRET

Föster resonant energy transfer (FRET) is mediated by a coupling of the electric dipoles of each chromophore.[83] As illustrated by Figure 2.6, FRET involves the transfer of a "virtual" photon, between donor and acceptor, resembling the emission of a photon from the donor and subsequent absorption by the accepter. By the use of the point-dipole approximation where the spatial extent of donor and accepter are neglected, the FRET transition rate has been show to follow,[16]

$$k_{FRET} \propto \frac{f_D f_A}{R^6} J \,. \tag{2.13}$$

Here, f_D and f_A are the oscillator strengths of the donor and accepter chromophores respectively, R is their separation and J is the overlap integral of normalised emission and absorption spectrum of donor and accepter respectively.

The dependence on oscillator strength of the donor and acceptor is critical to determining which states can participating in FRET. For example, triplet excited states, which have a spin disallowed transition to the spin singlet ground state, have a correspondingly weak oscillator strength. Therefore, triplet excited states do not

undergo appreciable FRET. In comparison, singlet excited states are spin-allowed, and FRET is their dominate transfer mechanism. FRET has a strong distance dependence ($k_{FRET} \propto R^{-6}$), meaning that transfer is only efficient for conjugated organic chromophore couplings less than a few nanometres in separation.[85]

2.3.2 Dexter

In the cases of excited states with low oscillator strength, Dexter transfer is far more significant. As illustrated by Figure 2.6, the process can be interpreted as the correlated exchange of two electrons that does not require a change of any electron's spin. Spin triplet excited states predominately undergo Dexter transfer. Spin singlet excited states can also undergo Dexter transfer, however, FRET is generally the dominant mechanism as Dexter is a shorter-range interaction than FRET. Within the spherically-symmetric particle approximation the Dexter transition rate follows, [16]

$$k_{DET} \propto e^{-2R/L} J \,, \tag{2.14}$$

where R is the spatial separation of the donor and accepter and L is the average radial extent of donor and acceptor states. There is again dependence on the spectral overlap integral J, however, there is no dependence on the associated oscillator strengths. This results in the ability of states with disallowed transitions to the ground state such as triplet excitons, to participate in energy transfer via Dexter transfer. Dexter transfer requires significant overlap of donor and acceptor wavefunctions, quantified by the exponential decay with donor-acceptor separation. Generally it is only, appreciable for transfer between neighbouring molecules or other ~1 nm separations.[85]

Comparing transfer mechanisms, Föster for singlet excitons and Dexter for triplet excitons, one could conclude that singlet excitons form the dominate excited state energy carriers, due to the higher transfer rate for FRET relative to Dexter transfer. However, the lifetime of triplet excitons is generally significantly longer, such that triplet excitons have longer to make multiple transfers before decay to the ground state. As a result, the mean diffusion length of triplet excitons can be substantial and lead to significant amounts of energy transfer.

2.3.3 Transfer at the Hybrid Organic-Inorganic Interface

In this section we look at the long history of devices utilising energy transfer at the hybrid organic semiconductor and inorganic quantum dot interface. We highlight their use in a

variety of optoelectronic applications; from photovoltaics, singlet fission sensitised photovoltaics, to the their more recent use in spectral management applications. Critical to the research of this dissertation, we expand on the relationship between the energy tunability of the QDs and energy level matching with organic semiconductors.

The combination of many parallel fields of research intermingling has led to the proposal of both singlet-fission photon-multiplier and triplet-triplet annihilation upconversion, devices. The progression to this point takes root in the QD/organic PV field, as one of the initial inorganic QD and organic semiconductor hybrid structures. For the best part of two decades, QDs were investigated for use in hybrid PV devices with organic semiconductors. Over this period the field saw many milestones, from the first demonstration of charge separation at the interface of organic polymers and CdSe QDs, to full photovoltaic devices with ~3 % power conversion efficiency in 2012.[86,87] As illustrated by Figure 2.7a, key lessons from this research were that the 'type-2 heterojunction' between QD and organic could result in ultrafast charge transfer and separation, as well as the use of hybrid structures in general for optoelectronic applications.[88]

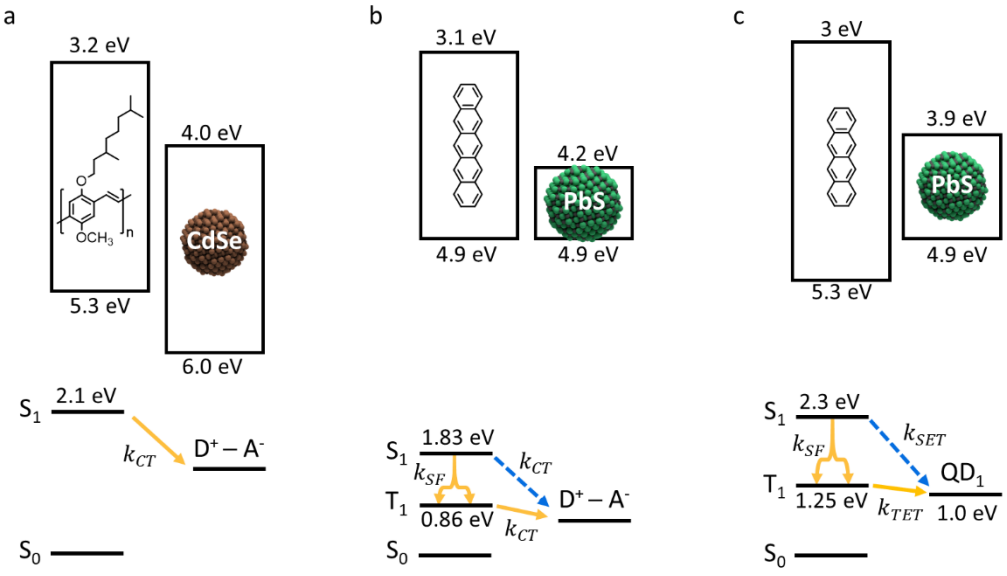

Figure 2.7: Schematic of the relevant energy levels at organic-inorganic interfaces. The HOMO and LUMO energy levels (top) and corresponding Jablonski energy diagrams (bottom) for a variety of hybrid structures. a) Organic polymer-QD photovoltaic device. b) Singlet fission sensitised QD photovoltaic device. c) Singlet-fission photon multiplier device.

Meanwhile, there were developments in using singlet fission in 'fullerene' based devices. The demonstration of triplet exciton transfer in pentacene/fullerene type-2 heterojunctions, was an influential discovery.[89] Crucially, this showed the enhanced

quantum efficiency possible using singlet fission in pentacene, an exothermic singlet fission material - one of the first successful application relevant uses. This work called attention to the use of external magnetic fields to identify the contribution of singlet fission generated triplets to overall performance. This was followed by renewed interest in singlet fission and lead to spectroscopic identification of the triplet transfer dynamics, showing that singlet fission was occurring rapidly within 200 fs after photoexcitation.[90]

Parallel to this was the influential development of singlet-fission sensitised infrared quantum dot solar cells.[91] This type-2 heterojunction demonstrated the first combination of an organic singlet fission material and inorganic quantum dot, a structure similar to that which forms the bulk of the work report in this dissertation (Figure 2.7b). The key development achieved by this structure is the charge dissociation of triplet excitons generated by singlet fission at the QD/organic interface.

Many different combinations of organic singlet fission triplet donors and acceptors of both organic molecules and inorganic QDs were tested in these early reports of charge transfer. The dependence of the triplet exciton dissociation on the alignment of energy levels in the two materials was extensively mapped.[92] This research climaxed with the development of singlet fission based organic photovoltaic devices with external quantum efficiency greater than 100%.[93] This measure of how many chargers are captured per incident photon, is typically limited to 100%. Notable efficient utilisation of a singlet fission material for charge multiplication allowed researchers to achieve an efficiency above this limit, cementing the value of singlet fission for improving solar energy harvesting. However, these devices have a considerable limitation, this particular use of singlet fission allowed a doubling of the extracted photocurrent but at half the voltage. These competing effects result in little to no, net improvement in power conversion efficiency with respect to a traditional organic singlet junction cell.

The next step along our technological road map is the harvesting of entire triplet excitons, rather than charge separation of an electron and hole. The transfer of triplet excitons generated by singlet fission were demonstrated to transfer from organic singlet fission molecules and inorganic QDs, in bi-layers of the structures.[12,94] Critical to this triplet exciton transfer is the alignment of the QD energy levels relative to the electronic level within the organic molecules. As illustrated by Figure 2.7c, to inhibit singlet exciton dissociation, a type-1 heterojunction was employed. Additionally, the energy of the QD bandgap needed not to be greater than the triplet exciton energy. The key benefit of this triplet exciton transfer, over charge separation, was that the triplet exciton once inside the QD resulted in excited state emission identical to the pure QD

photoluminescence. This was attributed to the high spin-orbit coupling within the QD allowing for the usually spin-forbidden triplet state to become emissive.

Other than the significant milestone of showing this harvesting of triplet excitons, researchers identified Dexter transfer as the likely transfer mechanism for triplet excitons between an organic molecule and QD, as illustrated in Figure 2.8a. The key indicator of this being that the transfer efficiencies had exponential dependence on the donor-acceptor separation, as determined by the length of the aliphatic ligands surrounding the QD. With short enough ligands, the triplet transfer efficiency increased towards unity. However, the synthesised QDs with long aliphatic oleic acid ligands showed little transfer, highlighting the need for engineering of the QD ligand shell. This particular method for controlling triplet transfer rates has the drawback that QD films with shorter ligands typically suffer from reduced photoluminescence quantum efficiency due to aggregation assisted interdot transfer and trapping, as discussed in Section 2.2.4. Again, these works employ the effect of external magnetic fields applied to the devices to confirm the dominance of triplet exciton transfer over singlet transfer. As illustrated by Figure 2.8b, they observed a shift in the equilibrium between singlet excitons on the organic and QD excitons with the application of a ~0.5 T magnetic field. This was identified by an increase in fluorescence from the organic at high fields, as expected for material undergoing singlet fission. In contrast, the photoluminescence from the QD followed a corresponding reduction, consistent with a state populated by the triplet excitons generated by singlet fission.

With inspiration from this work, Huang et al. investigated the possibility of utilising this process in reverse, transferring excitons from QD to the triplet state of an organic molecule.[14] By adjusting the materials so that the QD exciton was higher in energy than the organic's triplet exciton, they demonstrated that such a process is possible and further illustrated the use of the generated triplet excitons for triplet-triplet annihilation photon upconversion in the solution phase.

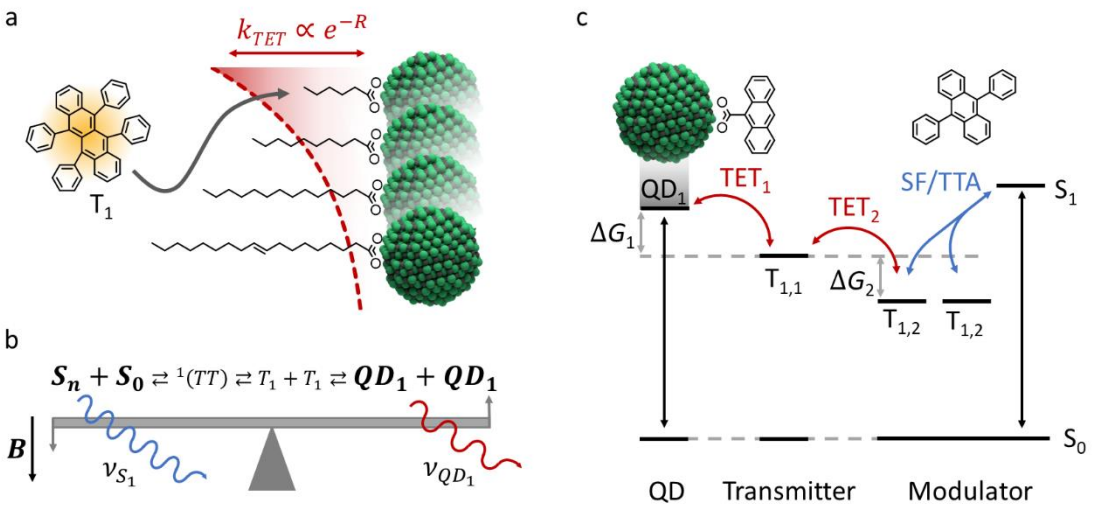

Figure 2.8: Triplet exciton transfer at the hybrid organic-inorganic QD interface.
a) Illustration of the triplet exciton transfer at the hybrid organic-inorganic QD interface, mediate by the Dexter transfer mechanism. b) Visual analogy of the equilibrium between singlet excitons on the organic and excitons on the QD. Application of a ~0.5 T external magnetic field shifts the equilibrium towards the singlet exciton population (singlet heavy). This shift in population is reflected in the photoluminescence from these states. c) Schematic of a generalised photo modulator. Interconversion between one high energy and two low energy photons is mediated by the QD, triplet transmitter, and triplet modulator.

After photoexcitation of the QD, Huang et al. identified delayed fluorescence from organic rubrene molecules and found it to be well described by triplet bi-molecular decay regenerating the singlet exciton. The researchers additionally introduced a novel strategy involving the use of an electronically active triplet 'transmitter' ligand attached to the surface of the QDs, as opposed to the usual high bandgap aliphatic ligands. This strategy relied on the rapid exciton transfer from the CdSe QD to the transmitter ligand, followed by a secondary transfer step to the 9,10-Diphenylanthracene in solution surrounding the QD (Figure 2.8c). Though the upconversion efficient was relatively low, ~0.01 %, the developments described by the researchers in this work inspire a significant amount of the strategies deployed in this dissertation.

Further investigations showed that the diffusion mediated transfer followed a Stern-Volmer like quenching dependence on the concentration of the accepter molecules. Also, the bi-molecular transfer rate was heavily dependent on the moment of excess energy between QD exciton and organic triplet exciton energy.[95] Marcus-Hush theory is pointed to as an appropriate theoretical framework to understand the role of this driving energy in the transfer process, with recent experiments supporting this assignment.[96,97] The use of phenyl spacer units between the triplet transmitter chromophore and the QD

core showed that the reverse triplet transfer process also follows an exponential dependence on the separation between donor and acceptor, assigned as Dexter transfer.[96]

Triplet transmitter ligands are attached to the QDs post synthesis by solution ligand exchange.[98] This ligand exchange has been shown to introduce additional states other than the QD exciton and organic triplet state.[97–99] The role of these states, which have been described as 'surface bound', is still under debate. In the literature there are many proposed assignments for these states, such as a charge transfer intermediate state, an electronic state on the surface of the QD near the ligand, or as a trap state introduced by poor passivation of the QDs surface.[97–99]

Based on these developments we present a general scheme for 'photon modulation', for use in SF-PM and TTA-UC (Figure 2.8c). Here, the interconversion between one high energy and two low energy photons is determined by the relative Gibbs free energy of the QD exciton, triplet transmitter, and triplet and singlet states of the 'triplet modulator'. In this scheme the QD acts as a spin-mixing component, allowing the conversion between photons and exciton state which can transfer with the transmitter ligand. Triplet excitons can additionally transfer between this transmitter state and the triplet state of the triplet modulator. This triplet modulator is a generalisation of the singlet fission or triplet-triplet annihilation materials, which performs one of these processes based on the Gibbs driving energy between the singlet exciton and two triplet excitons. Choice of materials dictates the direction photon modulation occurs.

There has been progress towards solid state implementations of triplet-triplet annihilation, with substantial efficiencies being reached.[100,101] However, these devices have been limited to bi-layer architectures and as a result suffer from relatively low absorption in the few mono-layer thicknesses of the QDs. In solid-state bilayer films the Dexter transfer dependence on the length of the aliphatic ligands surrounding the quantum dots was shown to have an upper limit.[101] As illustrated by Figure 2.8a the transfer of the triplet exciton between organic and QD was consistent with an exponential dependence on the acceptor donor separation. However, the increased dielectric constant, for more tightly packed QDs with a shorter ligand, results in little gain in transfer rate for ligands shorter than a six-carbon chain.

Singlet fission photon multiplier relies on lessons learnt here, to efficiently harvest triplet excitons from an organic singlet fission molecule to a QD. Triplet-triplet annihilation upconversion pulls on the developed knowledge base for the transfer from the QD to organic molecules. Efficient implementation of processes requires

understanding of the many technical breakthroughs described here. Details of the utilisation of these processes for spectral management are detailed further in Section 2.4.

2.3.4 Dynamics of Diffusion Mediated Transfer

In this section we detail the theoretical framework used to describe the energy transfer at a spherical interface. In the results section of this dissertation this approximation is regularly used to describe the triplet transfer between an inorganic QD and surrounding organic molecules.

2.3.4.1 Diffusion Limited Transfer

Following the methodology of Collins and Kimdall, we describe the kinetic theory for reaction rates between two species.[102] The kinetic theory of colloid coagulation as a diffusion controlled process using Fick's law of diffusion was originally developed by Smoluchowski.[103,104] This formalises the assumption that the reaction of two species sets up a concentration gradient of one species of particles surrounding the other and this concentration gradient results in the net flow rate of particles a described by Fick's law of diffusion. Specifically, Fick's law of diffusion in partial differential equation (PDE) form

$$\frac{\partial c}{\partial t} = D\nabla^2 c \,, \tag{2.15}$$

is solved for the concentration of the diffusing species $c(r,t)$, in spherical coordinates with the boundary condition on the surface of a sphere radius R, that $c(r = R) = 0$ for all $t \geq 0$. Along with the initial condition that a uniform concentration yields

$$c(r,0) = \begin{cases} c_0 \,, r > R \\ 0 \,, r \leq R \end{cases}. \tag{2.16}$$

This sphere represents the effective distance at which the two species can react. Simultaneous diffusion of both species is accounted for by D being the sum of the individual diffusion coefficients. Figure 2.9 illustrates the effect these constraints have on the resulting reactant concentration profile and resulting reaction flux.

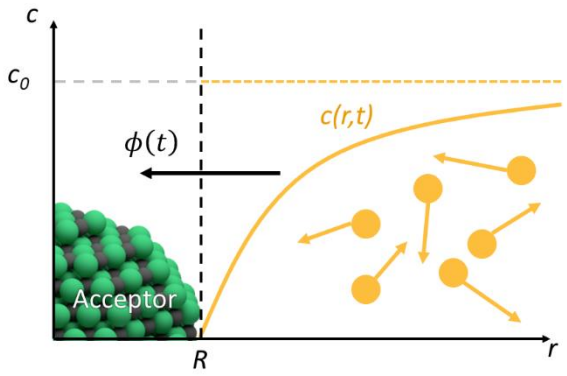

Figure 2.9: Illustration of the concentration profile for a instantaneous reaction.
The concentration of the diffusing reactant, surrounding the reaction site, is zero at the sphere's boundary ($r = R$).

The solution to this PDE and associated boundary condition is

$$c(r,t) = c_0\left[1 - \frac{R}{r}erfc\left(\frac{r-R}{\sqrt{4Dt}}\right)\right].$$

(2.17)

Where the complementary error function is defined as

$$erfc(x) = \frac{2}{\sqrt{\pi}}\int_z^\infty e^{-z^2}dz\,.$$

(2.18)

Of particular importance, the particle flux across the boundary at $r = R$ is given by

$$\phi = 4\pi R^2 D\left(\frac{\partial c}{\partial t}\right)_{r=R}.$$

(2.19)

Substitution of equation (2.17) for $c(r,t)$ into this expression yields

$$\phi = 4\pi RDc_0\left(1 + \frac{R}{\sqrt{\pi Dt}}\right).$$

(2.20)

This expression defines the rate of loss of the diffusing species due to reaction with the other species. In many cases, the time-dependant term is small and is neglected, yielding

$$\phi \approx 4\pi RDc_0 \,.$$

(2.21)

Sveshnioff showed that this theory extends to the case of ordinary bimolecular reactions in connection to florescence quenching in liquid solutions.[105]

2.3.4.2 Finite Reaction Rate

Collins and Kimball modified this theory by assuming that the probability that particle A (first species) reacts with particle B (second species) is proportional to the probability that particle A is between $r = R$ and $r = R + \Delta R$, where ΔR is infinitesimally small. The equivalent expression of the particle flux is

$$\phi = k4\pi R^2 c(R) \,,$$

(2.22)

where k, the 'reaction velocity', determines the specific reaction rate.[102] Figure 2.10 illustrates the effect these constraints have on the resulting reactant concentration profile and resulting reaction flux. In particular, this finite reaction velocity leads to a finite concentration of the reactant at the reaction boundary. This is analogous to there being a finite probability for the reactant to 'bounce' of the reaction boundary without reacting.

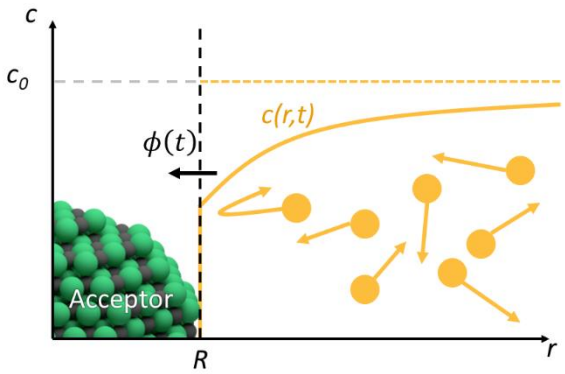

Figure 2.10: Illustration of the concentration profile for a kinetically limited reaction. The concentration of the diffusing reactant surrounding the reaction site, is non-zero at the spheres boundary $(r = R)$.

Combining equation (2.22) with the boundary condition described by equation (2.19) yields

$$c(R) = \frac{D}{k}\left(\frac{\partial c}{\partial r}\right)_{r=R}.$$

(2.23)

Letting $\gamma = \frac{D}{k}$ give

$$c(R) = \gamma\left(\frac{\partial c}{\partial r}\right)_{r=R}$$

(2.24)

The solution to this boundary condition and equation (2.15) is

$$\frac{c(r)}{c_0} = 1 - \frac{R-\beta}{r}\left[erfc\left(\frac{r-R}{\sqrt{4Dt}}\right) + \exp\left(\frac{Dt}{\beta^2} + \frac{r-R}{\beta}\right) erfc\left(\frac{\sqrt{Dt}}{\beta} + \frac{r-R}{\sqrt{4Dt}}\right)\right],$$

(2.25)

with $\frac{1}{\beta} = \frac{1}{\gamma} + \frac{1}{R}$. From equation (2.19), the flux across the boundary is

$$\phi = 4\pi D c_0\left[R - \beta + \frac{(R-\beta)^2}{\beta}\exp\left(\frac{Dt}{\beta^2}\right) erfc\left(\frac{\sqrt{Dt}}{\beta}\right)\right]$$

(2.26)

This has Taylor series expansion about $\frac{1}{t} = 0$ equal to

$$\phi = 4\pi D c_0 (R-\beta)\left[1 + \frac{R-\beta}{\sqrt{\pi Dt}}\left(1 - \frac{\beta^2}{2Dt} + \cdots\right)\right],$$

(2.27)

and so the flux to zeroth order in $1/\sqrt{t}$ is[106]

$$\phi = 4\pi D c_0 (R-\beta) = 4\pi D R c_0\left(\frac{R}{R + \frac{D}{k}}\right).$$

(2.28)

This expression has two regimes of particular interest. In the small *k* limit the particle flux approaches

$$\phi \to 4\pi R^2 k c_0.$$

(2.29)

In such cases the reaction is described as being purely 'kinetic limited'. However, in the large *k* limit the flux becomes

$$\phi \rightarrow 4\pi DRc_0 \,, \tag{2.30}$$

and we regain the expression for the purely 'diffusion limited' reaction rate described earlier. In the general case the reaction velocity determines the transition between these two limiting cases.

2.4 Advanced Spectral Management

In this final introductory section, we detail the development of photovoltaic (PV) energy conversion systems and spectral management as a necessary method for improving conversion efficiencies. Single junction cells, such as polycrystalline silicon PVs, are the most widely deployed type of device.[5] These are PVs in which a single 'p-n junction' is used to generate and separate electrical charges. The doped semiconductors in these PVs have a single absorption onset energy, associated with their electronic bandgap. The polycrystalline silicon PV is an iconic example of a single junction PV that exemplifies the advantages and disadvantages of the technology. The Shockley-Queisser limit sets a theoretical limit for the maximum power conversion efficiency possible in a single junction cell based on thermodynamic considerations. As illustrated by Figure 2.11, the main energy loss mechanisms in a Si-PV are either the incident photon being below the band gap of the material (and hence not absorbed), or an inability to extract the generated charges and thermalisation losses. This wavelength dependence illustrates that the single junction cells are very efficient in a narrow incident photon energy range above the material's bandgap. However, when the entire, broad, solar spectrum is considered the overall efficiency is significantly lower. The Shockley-Queisser limit for a silicon solar cell with a band gap of $\sim$ 1.1 eV, is ~33%.[107] Industrial progress towards reaching this efficiency has saturated at roughly 26.7%.[108] Single junction PVs, such as these are referred to as 'first generation' PV. They are thick and made from expensive, high purity semiconductors.[5]

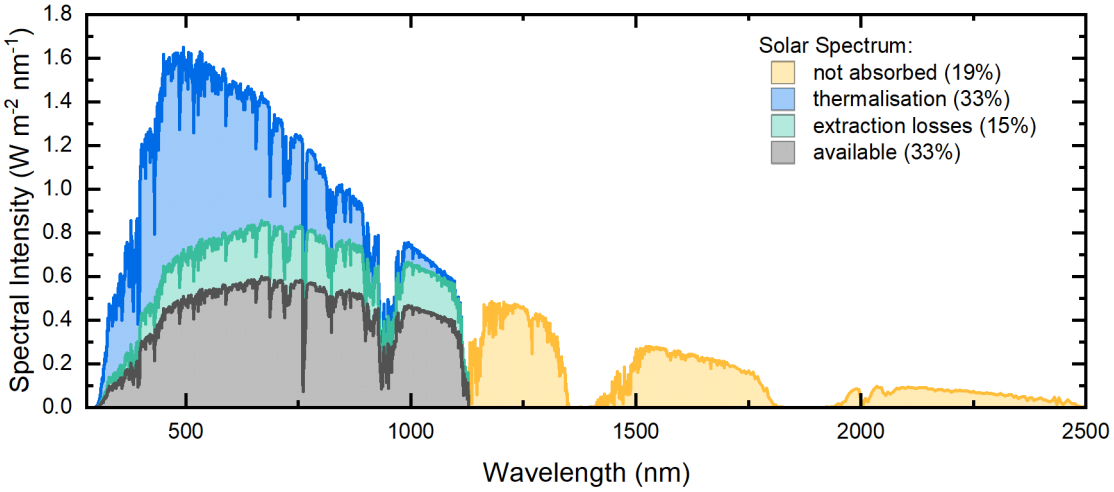

Figure 2.11: Solar spectrum with the key energy losses for a single junction Si-PV. Data taken from NREL resources,[109] figure adapted from Semonin et al.[110]

The 'second generation' PV are distinguished by being made from thin-film fabrication techniques. Such devices have 'active' layers which are in the 10s of nanometre - 10s of micrometre range, significantly thinner than first generation Si wafers of 100s of micrometres. Light management techniques are generally employed to ensure sufficient absorption within such small active layer thicknesses.[10] Of the second generation technologies, gallium arsenide based devices have shown considerable promise, with power conversion efficiency of 29.1%.[111] These single junction devices are the closest to reaching their respective Shockley-Queisser limit, ~32% in this case.[10]

This leads us to the aim of improving power conversion efficiency via spectral management strategies. Here, we define spectral management as the optimisation of how optoelectronic devices interact with the entire solar spectrum. Such techniques are required to reach 'third generation' PV cells, which are defined as those which overcome the Shockley-Queisser limit for singlet junction cells. There are a variety of proposed means to achieve such devices.

'Multijunction' or 'Tandem cells' are one such structure, where a collection of single junction PVs with semiconductors of bandgaps across the solar spectrum are stacked together. Each cell is electronically connected in serial or parallel to each. Under optimised conditions, the best tandem cells, based on a GaInAs/GaInP/ GaAs/AlGaInAs/AlGaInP, have reached 38.8 %.[112] However, manufacturing costs of the complex structure are very high, limiting the possible commercial applications.

A recently developed, promising alternative is perovskite-silicon tandem. This structure promises significantly lower fabrication costs and has reached considerably high power conversion efficiency of 29.1 %, overtaking the value for single junction silicon cell.[108] Though this research direction is developing substantially, tandem cells suffer from suboptimal performance under lighting conditions different to that which they are optimised for (usually a spectrum such as AM1.5G). The voltage or current matching criteria imposed by the electrical connection of the constituent cells limits achievable power conversion efficiency under real world conditions.[11]

Singlet-fission sensitised silicon PVs are a recent advancement that has significant potential as a means to break the Shockley-Queisser limit.[113] This report demonstrated the utilisation of triplet excitons by harvesting in a silicon photovoltaic after generation by singlet fission in an organic material. Such a process has long been predicted as a means to increase power conversion efficiencies.[7] However, these bi-layer, tetracene/silicon structures are limited by the use of elaborate interlayers. Such an approach, while promising, requires a change in cell design and thus has the added challenge of integration into existing PV manufacturing systems. Furthermore, the organic layers are thin, typically limited to <100 nm by the triplet diffusion length, resulting in <20 % photon absorption.[113] This limits the thickness of the singlet fission sensitizer and the related efficiency gains.

In this dissertation we focus on singlet fission photon multiplication and triplet-triplet annihilation upconversion as alternative methods to improve power conversion efficiency without significant altercation of the already well tuned Si-PV.

2.4.1 The Singlet Fission Photon Multiplier

The singlet fission photon multiplier (SF-PM) device offers a mechanism to break the Shockley-Queisser limit by overcoming the thermalisation losses inherent to all single junction photovoltaics. This is one of the most promising methods to harness the singlet fission process. The absorption of high-energy photons in a thin SF-PM layer on top of a Si-PV, results in a photoexcited singlet exciton which subsequently undergoes rapid and efficient singlet fission to form two triplet excitons (Figure 2.12a).[11,49] This is followed by efficient harvesting of the triplet excitons by a homogeneous dispersion of quantum dots within the singlet fission material. After transfer to the QDs, the excitons then recombine radiatively. Thereby, for every high-energy photon absorbed by the SF-PM, a pair of low energy photons is emitted that can then be captured in conventional silicon photovoltaic. The low bandgap quantum dots can absorb photons across a wide range

of photon energies and so they are maintained at a low density within the SF-PM to minimise absorption. Other than this parasitic absorption by the QDs, mid-energy photos pass through SF-PM and are absorbed and by the Si-PV. The absorbed photons by the Si-PV are then converted to electricity.

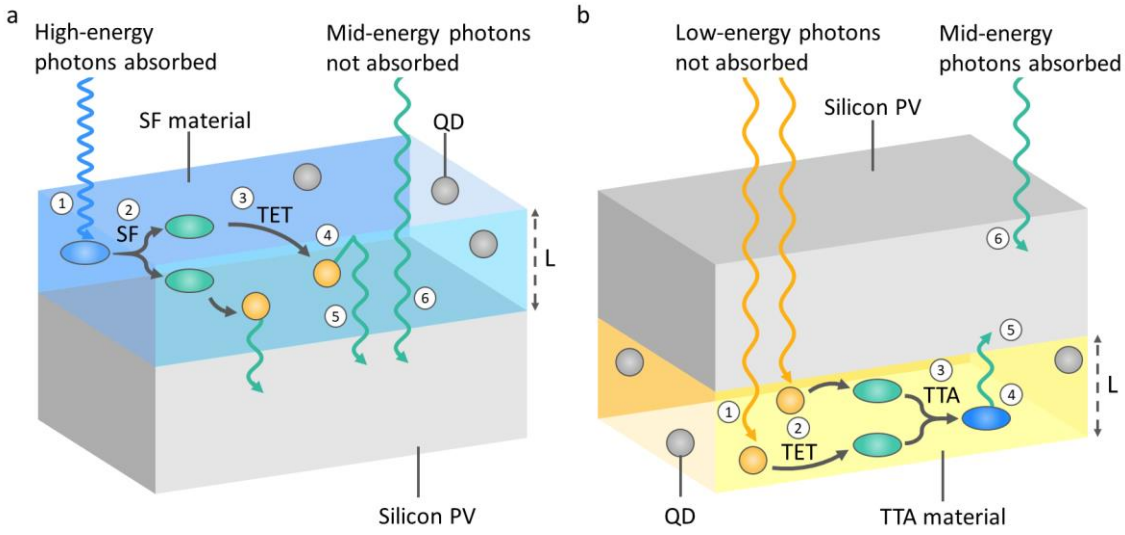

Figure 2.12: Schematic of SF-PM and TTA-UC films.
a) Bulk SF-PM system, with illustration showing the operation separated into constituent steps. 1) Absorption of high-energy photon in the SF host material. 2) Singlet fission process. 3) Triplet exciton transfer to the QDs distributed within the SF host. 4) Emission of low energy photons from QDs and (5) optical coupling where a significant fraction of the emitted photons are absorbed by the conventional Si-PV. 6) Mid energy photos pass through SF-PM and are absorbed by the Si-PV. b) Bulk TTA-UC system, with illustration showing the operation separated into constituent steps. 1) Low energy photon not absorbed by the Si-PV and are absorbed in the TTA host material. 2) Triplet exciton transfer from the QDs, distributed within the TTA host. 3) Triplet-triplet annihilation in the TTA host. 4) Emission of mid energy photons from TTA material. 5) Optical coupling where a significant fraction of the emitted photons are absorbed by the conventional PV device. 6) Mid energy photos absorbed by the Si-PV as usual. SF-PM illustration adapted from the schematic proposed by Rao and Friend.[9]

With these factors accounted for, the efficiency of a SF-PM as a function of the absorbed photon's wavelength can be separated into its constituent parts[81]

$$\eta_{SF-PM}(\lambda) = \left(\alpha_{QD}(\lambda) + \alpha_{SF}(\lambda)\eta_{SF}\eta_{TET}\right)\eta_{QD}\eta_{OC}\,. \tag{2.31}$$

Here, η_{SF} is the efficiency of the triplet generation in the per photon absorbed in the singlet fission material, ideally 200 %. η_{TET} is the fraction of generated triplets that transfer to the quantum dot. η_{QD} is the photoluminescent quantum efficiency of the quantum dots. η_{OC} is the optical coupling factor, the fraction of photons emitted by the

QD that are absorbed by the underlying PV cell. $\alpha_{QD}(\lambda)$ and $\alpha_{SF}(\lambda)$ are the fraction of the absorbed photons which are absorbed by the quantum dots and singlet fission material respectively. Equation (2.31) shows that for a SF downconverter to achieve high efficiencies each step in the down conversion process needs to be understood and optimised. An important factor in the operation of this device is the optical bandgap of the QD. The optical bandgap of the QD must be larger than the bandgap of silicon (Eg = 1.1 eV), such that its photoluminescence can be absorbed by the Si-PV.[114]

In a recent report the potential benefits of the SF-PM were investigated and it was found that incorporation with the best Si-PV devices, currently with a power conversion efficiency of 26.7%, could be improved to 32.5%. This value refers to 'optimistic' system parameters and a power conversion efficiency of 29.0 % is more achievable. This calculation relates to what the authors refer to as a 'realistic' SF-PM, defined as follows; there is less than 5% parasitic absorption by the QDs, there is negligible self-absorption by the QDs, the singlet fission yield is 200 %, the product of $\eta_{TET}\eta_{QD}\eta_{OC}$ is greater than 85%, and the singlet fission process results in entropic gain of 100 meV. Additionally, the authors calculate the photon escape cone for QD emission as less than 10%, based on a singlet fission material with a refraction index of 1.7. This results in η_{OC} > 90 % and can be improved by dielectric nanostructures. As a result, the optical coupling factor in Equation (2.31) is often omitted. These calculations suggests that an efficient SF-PM device could result in as much as a 22% relative improvement of the underlying Si-PV.

2.4.2 The Triplet-Triplet Annihilation Upconverter

The triplet-triplet annihilation upconverter (TTA-UC) device offers a mechanism to break the Shockley-Queisser limit by overcoming the sub-bandgap absorption losses inherent to all single junction photovoltaics. As illustrated by Figure 2.12b, the absorption of mid to high energy photons by the conventional Si-PV continues as usual. However, low energy photons not absorbed by the silicon pass straight through and are absorbed by a homogeneous dispersion of quantum dots within the triplet annihilator material.

Photoexcitation of the QD is followed by triplet exciton transfer to the organic material, where pairs of triplet excitons annihilate to form singlet excitons. The mid-energy photons from the organic's fluorescence are then optically coupled into the Si-PV. With this arrangement, it is imperative that the QD bandgap is less than that of silicon (1.1 eV). The organics' fluorescence is ideally greater than this, so that silicon can absorb the emitted photons. With these factors accounted for, the efficiency of a TTA-UC per absorbed photon can be separated into its constituent parts,[115]

$$\eta_{TTA-UC} = \eta_{ISC}\eta_{TET}\eta_{TTA}\eta_{FL}\eta_{OC} \cdot$$

(2.32)

Here, η_{ISC} is the intersystem cross efficiency from the photoexcited singlet state to a triplet state. η_{TET} is the triplet transfer efficiency from inorganic QD to organic triplet annihilator. η_{TTA} is the quantum efficiency of triplet-triplet annihilation to the singlet state in the organic. η_{FL} is the fluorescence quantum efficiency from the organic's singlet state. η_{OC} is the optical coupling factor, the fraction of photons emitted by the QD that are absorbed by the underlying PV cell. The efficiency of η_{TTA} is limited to 50 %, due to the requirement of two triplets to create one singlet exciton. The refractive index of the organic components of the TTA-UC, will be very similar to that of the SF-PM. Therefore, the optical coupling factor will be greater than 90 % and is often omitted.

The TTA-UC system has many similar constraints as the SF-PM system. The aggregation of QDs within the organic host must be low. It is ideal if the system is of bulk form, so that it is as optically dense enough. The QD's parasitic and self-absorption must be kept to a minimum as to not interfere with the of upconversion fluorescence. Finally, they share a need for readily achievable manufacturing conditions, which can be easily incorporated into existing Si-PV fabrication. The TTA-UC system has the additional constraint that the triplet-triplet annihilation efficiencies under solar fluence. If these conditions can be meet then there is the possibility of reaching the predicted thermodynamic limit of ~39% power conversion efficiency when coupled with Si-PV.[115] An 18% relative improvement is on par with that offered by the SF-PM device.

Ultimately, these two systems could be combined, SF-PM on top and TTA-UP below a conventional Si-PV. Under the naive assumption that these relative improvements would be additive, a 40% relative improvement in power conversion efficiency could be achieved. This improvement would be technologically, economically and environmentally significant on a global scale.

Chapter 3

Methods

In this chapter we detail the sample preparation methods, subsequent spectroscopic measurements and analysis techniques included within this dissertation. The organic material 6,11-bis-((triisopropylsilyl)ethynyl)tetracene-2-carboxylic acid, referred to as TET-CA, was synthesized by collaborators from the University of Kentucky under the supervision of Prof. John E Anthony. The singlet fission material 5,12-bis-((triisopropylsilyl)ethynyl)tetracene, referred to as TIPS-Tc, was obtained from Ark Pharm. All other chemicals were purchased from Sigma-Aldrich and used as delivered. The synthesis of PbS QDs was carried out by Dr James Xiao and Dr Zhilong Zhang. PbS QD ligand exchange with either TET-CA or hexanoic acid was performed either by Dr Nathaniel J. L. K. Davis, Dr Victor Gray, Dr James Xiao, Dr Zhilong Zhang and the by the author himself. Solution samples were prepared by Dr Victor Gray, Dr Simon Dowland and the author himself. All film samples were prepared by Dr Simon Dowland. Electron microscopy (Chapter 5) was performed by Dr James Xiao. Certain UV-Vis absorption spectroscopy measurements were performed by Dr James Xiao and Dr Simon Dowland, as indicated in the text. Photoluminescence quantum efficiency measurements were performed either under the supervision of Dr Simon Dowland (Chapter 4), by Dr Simon Dowland (Chapter 5) or in collaboration with Dr Nathaniel J. L. K. Davis (Chapter 6). Certain transient absorption measurements were carried out in liaison with Dr Arya Thampi (Chapter 4) and Dr Victor Gray (Chapter 5). Certain time-correlated single photon counting measurements were performed in liaison with Dr Victor Gray (Chapter 5). The transient photoluminescence mapping was performed with Dr Géraud Delport. The spectroscopic measurement of triplet sensitisation in solution was carried out by Peter Budden. Sample characterisation by X-ray and Neutron scattering measurements were obtained by Dr Daniel T. W. Toolan and Dr Michael P. Weir from the Department Chemistry and the Department of Physics and Astronomy, respectively, at The University of Sheffield. All other experiments were performed in the Optoelectronics Group, Cavendish Laboratory, University of Cambridge by the author.

3.1 Sample Preparation

3.1.1 Quantum Dots

The synthesis of PbS QDs by James Xiao and Zhilong Zhang was carried out following a previously reported method with minor modifications.[116] Briefly, 0.45 g of PbO, 7 g of oleic acid and 10 g of 1-octadecene were degassed at 110 °C for 2 hours in a three-neck flask. The reaction flask was subsequently flushed with nitrogen and its temperature dropped to 95 °C.

3.1.2 Ligand Exchange

The 6,11-bis-((triisopropylsilyl)ethynyl)tetracene-2-carboxylic acid ligands, referred to as TET-CA, were synthesized by our collaborators from the University of Kentucky following previously described methods.[98] The ligand exchange of the as-synthesised QDs with oleic acid ligands was performed in a nitrogen-filled glovebox. The PbS QD stock solution was diluted to ~20 mg mL^{-1} and a volume of 1 mL was used for the ligand exchange procedure. A volume of 0.2 mL of the TET-CA solution, at 10 mg mL^{-1} dissolved in tetrahydrofuran, was added to the PbS QD solution, and the mixture was stirred for at least 1 h. The PbS-TET-CA QDs were then extracted by adding acetone (4.8 mL) to the mixture followed by centrifugation. The supernatant was discarded and the precipitated QDs were re-dispersed in toluene (1 mL). The PbS-TET-CA QDs were further purified using a minimum of six repeated dispersion/precipitation/centrifugation cycles until the wash solution contained no TET-CA. The use of these QDs to produce the solutions and films studied in this dissertation is detailed as needed in each chapter respectively.

3.2 Steady-State Spectroscopy

3.2.1 UV-Vis Absorption

The measurement of a sample's absorption and photoluminescence require many of the same basic optical components. They both require a light source to act as an excitation beam, which can be either of a discrete wavelength or continuum wavelengths. Typically, a particular wavelength is then selected from this excitation source; for example, with a monochromator or a bandpass filter. This prepared beam is then directed to the sample. In an absorption measurement the transmitted beam, of

intensity $I(\lambda)$, is directed towards a detector; for example, a charge-coupled device (CCD) or photomultiplier tube. With the use of a reference measurement $I_0(\lambda)$, without the sample in place, the percentage of incident photon which are absorbed by the sample, $a(\lambda) = 1 - I(\lambda)/I_0(\lambda)$, referred to as the absorption of the sample, can be calculated. From the absorption of the sample, the absorbance can be calculated according to

$$a(\lambda) = 1 - 10^{-A(\lambda)} .$$

(3.1)

The attenuation coefficient is then given by absorbance per unit length of the material in question. In this dissertation the reported absorbance spectra were measured using a Shimadzu UV3600Plus spectrometer with attached integrating sphere.

3.2.2 Photoluminescence

To investigate the photoluminescence (PL), optics are used to collection the photons emitted by the sample after excitation. The collected light is filtered based on wavelength, typically with a monochromator or long-pass filters. These are predominantly to remove light from the excitation beam. The emitted light is then directed onto a photodetector. Two experimental setups were used to collect photoluminescence emission spectra in this dissertation: a free-space optics setup using an Andor Kymera 328i Spectrometer and a commercially available Edinburgh Instruments FLS 980 fluorometer.

The free-space optics setup uses a bank of temperature and current controlled laser diodes, purchased from Thorlabs, able to generate stable 515, 532, 658, 750 and 920 nm laser beams. After attenuation to the desired intensity, the selected laser beam was focused onto the sample cuvettes. PL emitted from the sample was collected and focused into a Andor Kymera 328i Spectrometer and the spectra were recorded using either a Si-CCD detector (Andor iDus 420) for the visible region, or a InGaAs detector (Andor, Dus InGaAs 490) for the NIR region. This apparatus has the benefit of offering very fine adjustment and control of incident laser power and a high detector sensitivity.

In comparison, the fluorometer setup has the advantage of measuring with fine increments both the excitation and emission wavelength dependence of the photoluminescence. In this dissertation photoluminescence excitation and emission spectra were obtained using a Edinburgh Instruments FLS 980 fluorometer. The

excitation and emission slit widths were both set to 2 nm bandwidth. The excitation beams were incident at 52 degrees relative to the normal direction of the sample.

3.2.3 Photoluminescence Quantum Efficiency

Photoluminescence quantum efficiency (PLQE) is the number of photons emitted from a molecule per photon absorbed. Unless specified otherwise, PLQE measurements reported in this dissertation were made following the procedure of de Mello et al.[117] Briefly, this method involves the comparison of the photocounts for the PL and excitation source under three measurement conditions, using a detector connected by fibre optics to a 'integrating sphere'. The first condition records the spectrally resolved photocounts for the excitation beam entering an empty integrating sphere. The remaining conditions require the measurement of the photocounts, using a sample inside the integrating sphere, with and without the excitation beam incident on the sample. Combination of these spectra allows the estimation of the PLQE for the sample. Again, photoexcitation was achieved with a variety of temperature and current controlled laser diodes. The attenuated beam of selected wavelength was aligned through a small hole onto samples suspended in a Spectralon-coated integrating sphere (Newport 819C-SL-5.3) modified with a custom baffle extension. Light from the experiment was collected using an optical fibre connected to a Andor Kymera 328i Spectrograph and spectra recorded using the same detectors as the photoluminescence spectra in the previous section.

3.2.4 Magnetic Dependent Photoluminescence

Magnetic field dependent PL measurements were performed using the free-space optics PL setup mentioned earlier, but placing the sample within the poles of an electromagnet Following a previously reported procedure, different magnetic field strengths were achieved by using a Keithley 2400 variable voltage source, connected to a current amplifier, to drive the electromagnet.[118] The magnetic field between the poles (at the sample position) was calibrated to the applied voltage by a Gauss-meter. When measuring the PL in the near IR region, a RG1000 long pass filter (Schott) and a PL950 long pass filter (Thorlabs) were used if appropriate for the particular sample. These were placed in front of the entrance to the spectrometer to remove laser scatter and higher order peaks from the grating. After averaging over multiple sweeps of the magnetic field and integration of the spectra, the percentage change relative to the spectrum under

zero applied field strength was calculated as follows. For each pixel (with corresponding wavelength) on the detector, the change in the PL,

$$\Delta PL(B,\lambda) = PL\,(B,\lambda) - PL_B(0,\lambda)\,, \tag{3.2}$$

was calculated as a function of the field strength. $PL_B(0,\lambda)$ is the measured PL spectrum at wavelength λ under zero applied magnetic field. The field strengths were sampled in a non-sequential order, reducing the effect of film degradation and any hysteresis in the sample's magnetic field dependence. The fractional change in PL at each wavelength is given by

$$\gamma(B,\lambda) = \frac{\Delta PL(B,\lambda)}{PL_B(0,\lambda)} = \frac{PL\,(B,\lambda) - PL_B(0,\lambda)}{PL_B(0,\lambda)}\,.$$

Here we have the spectral variation of the magnetic field dependence. This is then averaged over a specific wavelength range to determine a particular species' magnetic field dependent PL.

3.3 Transient Photoluminescence Spectroscopy

3.3.1 Time-Correlated Single Photon Counting

Large sections of this dissertation deal with investigation of the dynamics of excited states. Transient photoluminescence techniques offer valuable insights into the subset of excited states which are photoluminescent. Time-correlated single photon counting (TCSPC) was used during this work to measure the time dependence of photoluminescence. TCSPC systems work by measuring the time interval between the arrival of single photons and a trigger pulse from the laser exciting the sample. By sampling multiple detection events, a statistical distribution of the time between excitation and emission is built up. This is then interpretable as the time dependence of the PL from the material of interest. In this dissertation samples were excited with a pulsed supercontinuum laser (Fianum Whitelase SC-400-4, 6 ps pulse length) at a variable repetition rate, 0.2-1 MHz. The pump wavelength is set to either 535 or 650 nm (full-width at half-maximum 10 nm) with dielectric filters (Thorlabs). Pump scatter from the laser excitation within the photoluminescence collection path to the detector, was removed with an absorptive 1000 nm long-pass filter (Thorlabs). The infrared

photoluminescence is focused and detected by a single-photon avalanche photodiode based on InGaAs/InP (MPD-InGaAs-SPAD).

3.3.2 TCSPC Microscopy

Transient photoluminescence techniques readily lead themselves to combination with microscopy methods. Such methods allow the extraction of the excited state dynamics spatially over the sample. Providing a vales source of data for detailing spatial variations, defeats, or excited state diffusion, within samples. In Chapter 5, the confocal time-resolved photoluminescence images of the samples were measured using a commercially available confocal microscope setup (PicoQuant, MicroTime 200). Samples were excited with a 405 nm pulsed laser diode (PDL 828-S“SEPIA II”, PicoQuant, pulsed width of ~100 ps). The excitation beam was focused directly onto the sample’s surface with an air objective with optical parameters 100x and 0.8 NA. The excitation intensity was set to 25 $W.cm^{-2}$. The repetition rates were set to 2 MHz, leading to an excitation fluence of 50 $\mu J.cm^{-2}$. The photoluminescence signal was separated from the excitation light (405 nm) using a dichroic mirror (Z405RDC, Chroma), while a 550 ± 40 nm bandpass filter was used to select the fluorescence signal from the TIPS-Tc. The fluorescence was then focused onto a photomultiplier detector assembly (PMA Hybrid from Picoquant, a time resolution of 100 ps) through a pinhole (50µm).

3.3.3 Time-Gated Photoluminescence

Lastly, a time-gated photoluminescence setup was used to collect time-resolved PL spectra. This apparatus utilises an intensified charge-coupled device (ICCD) to generate broadband, extremely sensitive, time-resolved PL spectra. Briefly, a ‘gated’ electric field selects specific time periods, relative to a ‘trigger’ linked to the excitation source, over which photo-generated electrons in the system are extracted to the detector. Subsequently a ‘micro channel plate’ is used to amplify the electrical signal and transfer it to a phosphor layer. The gated photon signal from the phosphor layer is then detected by a CCD.

The excitation pulse is generated in a TOPAS optical amplifier, pumped with the output from a Spectra-Physics Solstice Ace Ti:Sapphire amplifier (1 kHz). The amplifier offers pulsed excitation across the visible and near IR region. The collected PL from the sample is focused into the slits of a Shamrock 303i Andor spectrometer coupled to a ICCD (iStar DH740 Andor). This apparatus has the significant advantage, over the previously mentioned setups, of being ‘intrinsically’ spectrally resolved and offering wide temporal

range from 2 ns (the measured temporal resolution) to milliseconds (limited by the repetition rate of the laser source).

3.4 Transient Absorption Spectroscopy

Transient Absorption (TA) spectroscopy is well established and incredibly useful technique for monitoring photoinduced reactions in materials and is the dominate experimental technique used in this dissertation. As is common in this research field, TA is actually a measurement of the transient transmission. The materials that are typically studied, such as conjugated organics, have relatively small changes in refractive index from photoexcitation. Therefore, such effects are neglected and the changes in the transmitted signal are attributed to changes in absorption. As illustrated by Figure 3.1, TA is a 'two-pulse', referred to as 'pump-probe', measurement which can illuminate the excited state dynamics within a material on femtosecond timescales. The pump is a temporal short laser pulse which generates photoexcitations within the material of study, at some reference $t = t_0$. At a predetermined time $t = t_0 + \tau$, the probe pulse interacts with the same sample region as the pump. This probe pulse is also a temporal short laser pulse; however, the probe is usually a broadband laser pulse, such that multiple wavelengths are probed at once. This broadband probe pulse is typically generated via non-linear optical processes such as 'white light generation' and 'super continuum generation'. Typically, the pump and probe beams are set to intercept the sample at a relative polarisation described as the magic angle ($\cos^{-1}\left(1/\sqrt{3}\right) = 54.7°$). At this relative polarisation angle, the measured transient transmission signal is independent of the samples dipole orientation.[119] In some cases, a third 'reference' pulse is used to reduce noise caused by fluctuations of the probe pulse.

The time difference between pump and probe τ is introduced by a mechanical delay, or electrically triggered for lower time resolution experiments. To measure the transient transmission the pump pulse is modulated either electrically or mechanically with a 'chopper'. This modulation of the pump allows the measurement of the transmission of the probe pulse in the unperturbed, no pump case ($T_{pump\ off}$) and in the perturbed, with pump case ($T_{pump\ on}$).

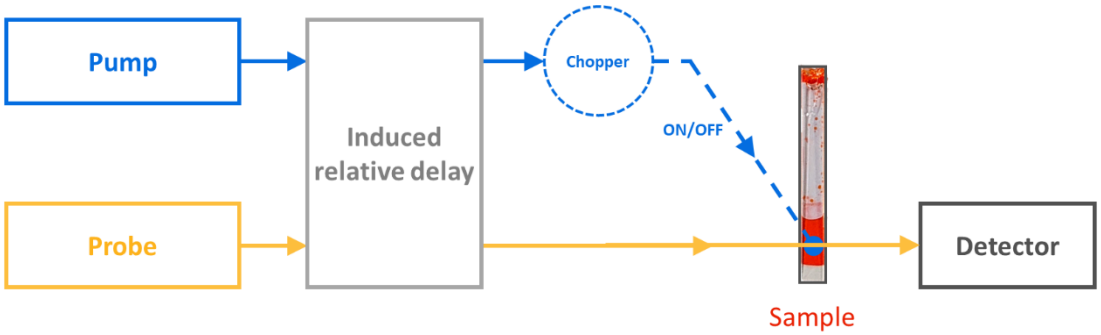

Figure 3.1: Schematic of the pump-probe apparatus used in this work.

The TA signal is then calculated by the fractional differential transmission,

$$\frac{\Delta T}{T} = \frac{T_{pump\ on} - T_{pump\ off}}{T_{pump\ off}}, \tag{3.3}$$

where T is the transmitted intensity of the probe beam. Figure 3.2 illustrates the separation of the typical transient transmission signal for an organic material, into its constituent components. These include features such as the 'Ground State Bleach', 'Stimulated Emission' and 'Photoinduced Absorption'. The origin and nature of these features are as follows:

- The Ground State Bleach (GSB) feature is a positive signal as measured by differential transmission, which roughly overlaps with the ground state absorption spectrum. This change in transmission is caused by the pump pulse exciting species from the ground state to an excited state. This is followed by the probe pulse experiencing a reduced absorption due to the decreased population of the ground state. The reduced absorption leads to an increased transmission and positive differential transmission.
- The Stimulated Emission (SE) is also a positive signal as measured by differential transmission, which roughly overlaps with the steady state photoluminescence spectrum. Here, the probe photon perturbs the electric field of an excited state resulting in stimulated emission of a photon, which is indistinguishable from the probe pulse. The increased number of photons in the probe pulse leads to an increased differential transmission.
- Photoinduced Absorption (PIA) is a negative signal as measured by differential transmission. This feature results from the newly accessed absorptive transition that occurs from the excited states accessed by the pump pulse. This increase in absorption results in a decreased differential transmission.

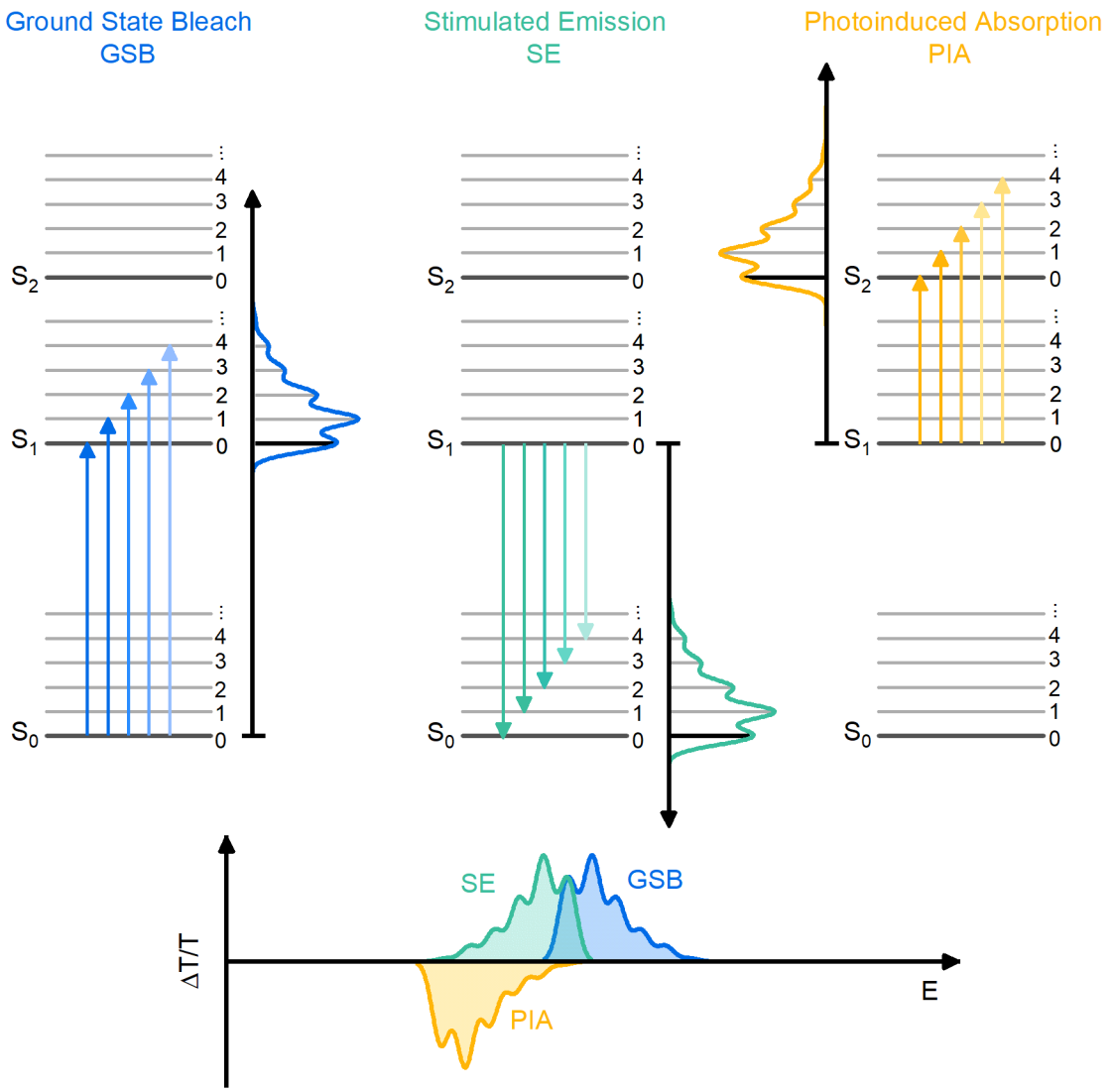

Figure 3.2: Illustration of the typical transient absorption features and the associated transitions. The ground state bleach (blue) results from the depletion of the ground state by the pump pulse exciting a fraction of electronic states to some higher energy state. The reduced population of the ground state leads to a positive $\Delta T/T$ signal. The stimulated emission (green) results from the emission from photons from the excited electronic population in S_1. This emission is stimulated by the probe pulse and results in a positive $\Delta T/T$ signal. The photoinduced absorption (orange) results from the absorption of the probe pulse by the excited state population, in S_1 for example, and leads to a negative $\Delta T/T$ signal. Adapted from a figure by Dr Simon Gélinas.

The measured TA signal strength for each spectral component is proportional to the population of the electronic states associated with each radiative transition. This list of TA features is not exhaustive, there are other processes that can lead to changes in differential transmission such as changes in refractive index, electroabsorption and

others. The transient transmission signals for inorganic QDs has the same components GSB, SE and PIA. However, in QDs these typically do not display transitions with strong vibrational character.

The transient absorption spectra reported in this dissertation were recorded on two different experimental apparatus. Each apparatus allowed for investigation over a different time delay range, one over femtosecond timescales (200 fs - 2 ns) and one over nanosecond timescales (1 ns- 300 μs).

3.4.1 Femtosecond Apparatus

The femtosecond transient absorption (fsTA) experiments are performed using an Yb based amplifying system, Light Conversion PHAROS, with 400 μJ per pulse at 1030 nm at repetition rate of 38 kHz. The laser output is modified using a 4 mm YAG substrate to produce the probe beam from 520 to 950 nm. Using a narrow-band optical parametric oscillator system (ORPHEUS- LYRA, Light conversion) with 1030 nm seed, the pump beam is generated (full-width at half-maximum 250 fs). The probe pulse is delayed using a computer-controlled mechanical delay-stage (Newport) and the on-off pump pulses are generated by means of a mechanical chopper (Thorlabs) before incidence with the sample. The pump and probe beams are focused to sizes 250x250 μm and 80x80 μm respectively, at the sample position. The probe pulse transmitted through the sample is collected using a silicon line scan camera (AViiVA EM2/EM4) with a visible monochromator with 550 nm blazed grating.

3.4.2 Nanosecond Apparatus

For nanosecond transient absorption (ns-TA) measurements, a LEUKOS Disco 1 UV Low timing jitter supercontinuum laser (STM-1-UV) is used to generate the probe. This laser produces pulses with a temporal breadth below 1 ns from 200-2400 nm and has an electronically controlled delay relative to the pump. The pump is generated at the desired wavelength using a TOPAS optical amplifier pumped by 800 nm 100 fs pulses from the Spectra-Physics Solstice Ace Ti:Sapphire amplifier at 1 kHz. The probe is split by a 50% reflectance beam splitter to create a reference. The pump and probe beams are overlapped on the sample adjacent to the reference beam. This reference is used to account for any shot-to-shot variation in transmission. The probe and reference beams are then focused into an imaging spectrograph (Andor, Shamrock SR 303i) and detected using a pair of linear image sensors (Hamamatsu, G11608) driven and read out at the full laser repetition rate by a custom-built board from Stresing Entwicklungsburo. In all

measurements, every second pump shot is omitted using a mechanical chopper for short-time measurements. The average fractional differential transmission (ΔT/T) of the probe is calculated for each time delay once 1000 shots have been collected.

3.5 Numerical Methods

In this section we detail the numerical methods used for decomposing the spectroscopy data collected in this work. A significant proportion of spectroscopic data can typically be mathematically characterised as two-dimensional functions, with wavelength as one of the independent variables. The remaining independent variable is often time. The measured signal strength at each time can be expressed as a linear combination of a set of linearly independent 'spectral components' which are functions of the wavelength. As demonstrated by Figure 3.3, each spectral component has an associated magnitude as each time point. For data with discrete wavelength and time points, this is mathematical equivalent to the matric multiplication

$$A_{t\times w} = K_{t\times i}S_{i\times w}. \tag{3.4}$$

$k_{t,i}$ is a matrix entry containing the amplitude at m^{th} timepoint, for the i^{th} spectrum of S (Figure 3.3). The i^{th} spectrum of S is the i^{th} row of $S_{i\times w}$. This does not explicitly account for effects that cause the shifting of spectral features as a function of the other independent variable, such as relaxation and electroabsorption. The elements of the product matrix $A_{t\times w}$ are typically the direct experimental observable, and it is the determination of the kinetics (K) and spectra (S) that is desired. Here, we refer to this process as decomposition. In this work we use two forms of decomposition, either spectral target analysis or global analysis. Spectral target analysis is achieved using linear regression and global analysis is achieved using a genetic algorithm.

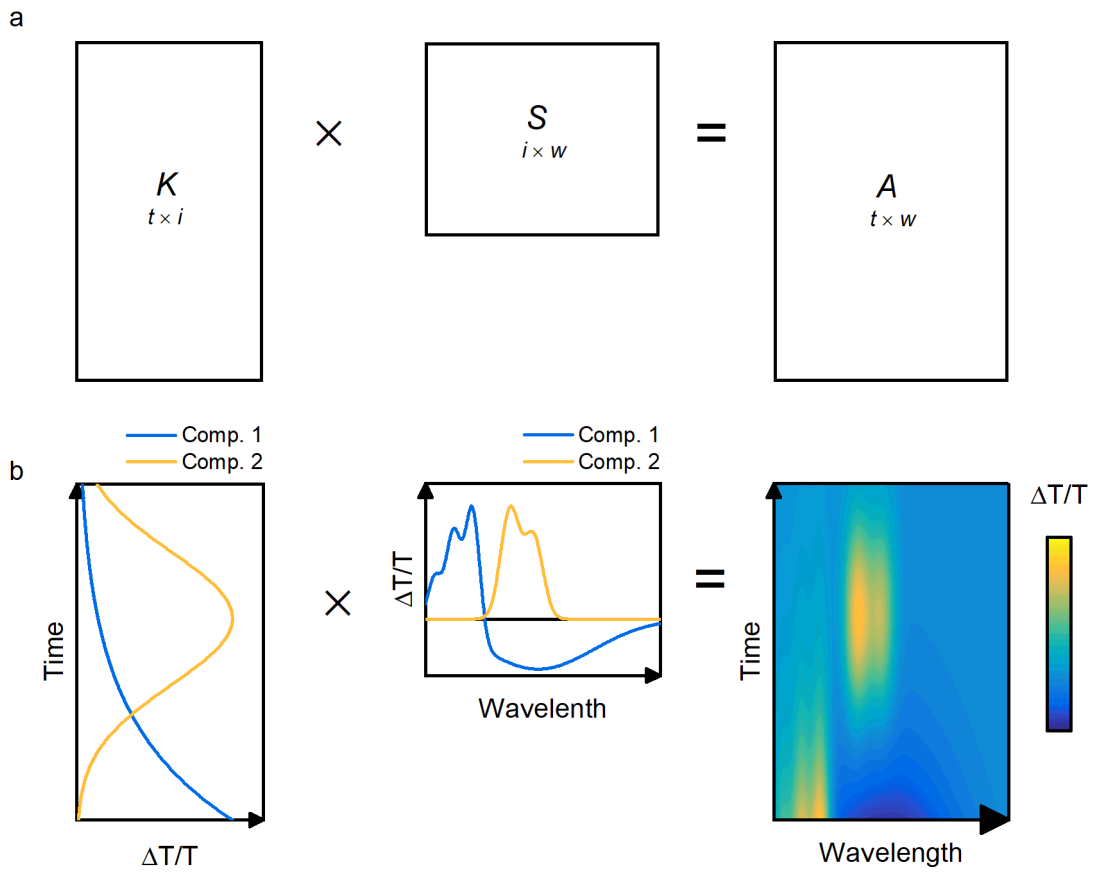

Figure 3.3: Schematic of the matrix and spectral decomposition used in this work.
a) Illustration of the matrix decomposition of the matrix A into its components matrices K and S.
b) Illustration of the spectral decomposition of the TA measaurement into its spectral and kinetic components.Adapted from a figure by Dr Ture Hinrichsen.

3.5.1 Spectral Target Analysis

If the spectra present in the measurement are known, the proportion of each spectrum present at every time point can be calculated via linear regression in order to perform spectral target analysis. This usually requires a separate measurement to verify the individual spectra. In certain cases, it is useful to reframe this problem in the context of linear regression, which is equivalent to the previous decomposition with the inclusion of a spectrum representing a constant offset (which can we set to zero if desired). The linear relation is of the form

$$Y = X\beta \,,$$

(3.5)

with,

$$Y = A^T; \beta = \begin{bmatrix} \beta_{01} & \beta_{02} & \cdots & \beta_{0m} \\ \beta_{11} & \beta_{12} & \cdots & \beta_{1m} \\ \vdots & \vdots & \ddots & \vdots \\ \beta_{i1} & \beta_{i2} & \cdots & \beta_{im} \end{bmatrix} = \begin{bmatrix} \boldsymbol{\beta_0} \\ K^T \end{bmatrix}; X = \begin{bmatrix} 1 & X_{11} & \cdots & X_{1i} \\ 1 & X_{21} & \cdots & X_{2i} \\ \vdots & \vdots & \ddots & \vdots \\ 1 & X_{n1} & \cdots & X_{ni} \end{bmatrix} = [\mathbf{1} \quad S^T] \,.$$

(3.6)

This system is solved using the Moore-Penrose pseudoinverse of the X matrix,

$$\beta = X^+ Y \,,$$

(3.7)

which leads to a solution for β by least squares fitting. From this, the strength of each spectra at each time point can be found.

3.5.2 Genetic Algorithm

In the case when not all the spectra present in a measurement are explicitly know, global analysis is used to determine the known spectral components. Global analysis of the spectral data is achieved using a genetic algorithm described previously.[120,121] The numerical algorithm was originally developed and written by Dr Simon Gelinas.

The genetic algorithm is an evolutionary algorithm used to simultaneously determine the present spectral components and their kinetics. A full description of this algorithm can be found elsewhere.[120,121] Briefly, this algorithm initiates by producing a large 'population' of candidate spectra. It then compares these spectra and kinetic amplitudes to the measured dataset, and quantifies their fitness by residual sum of squares with additional penalties for non-physical values. The 'fittest' spectra are then chosen using a tournament method, to 'breed' the next generation of candidates. The population of the next generation is computed using Gaussian-function masks of random parameters, with additional small fluctuations added to imitate random mutation. The algorithm returns the spectra and associated kinetics with the highest fitness when the top achieved fitness saturates with respect to additional generations

.

Chapter 4

Solution Phase Singlet-Fission Photon-Multiplier

A key goal of the singlet fission community is the development of a realistic singlet-fission photon-multiplier (SF-PM) technology. This goal is motivated by bold claims, that such a process could increase the efficiency of the best Si cells from 26.7% to 32.5%, thus breaking the Shockley–Queisser limit. However, these predictions had remained untestable, without the demonstration of such an SF-PM process occurring in a bulk system. That changed with our recent demonstration of a novel solution-phase SF-PM consisting of a blend of a highly soluble singlet fission material, and lead sulphide (PbS) QDs covered in triplet transmitter ligands.[122] Specifically, QDs covered in 6,11-bis-((triisopropylsilyl)ethynyl)tetracene-2-carboxylic acid ligands, referred to as TET-CA, were dispersed in toluene solution with 5,12-bis-((triisopropylsilyl)ethynyl)tetracene referred to as TIPS-Tc.[123] Here we detail the investigation of this model system TIPS-Tc:PbS-TET-CA, which shows efficient harvesting of triplet exciton generated by singlet fission.

We begin this chapter by introducing the materials and their basic properties. Subsequently, we use a range of steady-state measurements to quantify the performance of the TIPS-Tc:PbS-TET-CA system. We show that the system absorbs >95% of incident photons within the singlet fission material to generate singlet excitons. These excitons then undergo efficient singlet fission in the solution phase (135±5%) before quantitative harvesting of the triplet excitons (95±5%), via the TET-CA ligand, to a low concentration of QD acceptors, followed by the emission of IR photons. We find that in order to achieve efficient triplet harvesting it is critical to engineer the surface of the QD with the triplet transfer ligand TET-CA, analogous to recent work with QD-organic based up-conversion systems.[96] In the next section we use time-resolved measurements, combined with analytical modelling, to study the dynamics and mechanism of the triplet harvesting process. Critically we find that bi-molecular decay of triplet excitons is a major loss pathway which can be controlled via tuning the concentration of QD

acceptors. This bi-molecular decay is linked to reduced performance of the SF-PM system under steady-state operation at high incident irradiance. Fortunately, we demonstrate that under solar-equivalent fluences it is possible to efficiently harvest triplet excitons in a bulk system with a low concentration of QDs, maintaining sufficiently low QD parasitic absorption for realistic coupling to a Si PV cell. Furthermore we established design rules for such processes.[11]

In the last section, we investigate the limiting factors for the triplet transfer process. We find that triplet transfer from the TIPS-Tc to the PbS-TET-CA QDs is kinetically limited by the surface density of the TET-CA ligand. Of importance to future SF-PM design rules, we note that the current transfer mechanism is nearing its maximal rate and that further improvements will require strategies beyond that offered by a single monolayer of TET-CA ligands.

These results establish the solution-based SF-PM system as a simple and highly tuneable platform to understand the dynamics of triplet energy transfer (TET) process between organic semiconductors and QDs, one that can provide clear design rules for new materials. The wide applicability of these design rules is highlighted in the subsequent chapter which focuses on a solid-state implementation of an SF-PM system.

Content in this chapter is adapted from the resulting publication "Engineering Molecular Ligand Shells on Quantum Dots for Quantitative Harvesting of Triplet Excitons Generated by Singlet Fission".[122] *Found at https://pubs.acs.org/doi/10.1021/jacs.9b06584. The work is reproduced with permission from the publisher. Permission for further reuse must be obtained from the publisher.*
This publication is the result of collaboration with Arya Thampi[a], Simon Dowland[a], James Xiao[a], Victor Gray[a,d], Zhilong Zhang[a], Peter Budden[a], Anthony J. Petty II[b], Nathaniel J. L. K. Davis[c,a], Neil C. Greenham[a], John E. Anthony[b] and Akshay Rao[a]

[a]Cavendish Laboratory, University of Cambridge, J. J. Thomson Avenue, Cambridge, CB3 0HE, UK.
[b]Center for Applied Energy Research, University of Kentucky, Research Park Dr., Lexington KY 40511, USA.
[c]The MacDiarmid Institute for Advanced Materials and Nanotechnology, The Dodd-Walls Centre for Photonic and Quantum Technologies, School of Chemical and Physical Sciences, Victoria University of Wellington, Wellington 6140, NZ.
[d]Department of Chemistry, Ångström Laboratory, Uppsala University, Box 532, SE-751 20 Uppsala, Sweden.

4.1 Background and Motivation

The quest to increase the efficiency of solar energy harvesting has been a major scientific challenge since the invention of the photovoltaic cell (PV).[124] Single junction cells made from semiconductors such as silicon and GaAs have been well optimised and attain very high efficiencies of 26.7% and 29.1% respectively.[108,111] However, the efficiency of all single-junction cells is fundamentally capped by the Shockley-Queisser limit.[107] There is thus a need to develop technologies that can overcome these fundamental limits to the efficiency of single-junction cells.

Singlet fission is an exciton multiplication process occurring in a variety of organic semiconductor materials.[54,125] Here, one photogenerated spin-0 singlet exciton is converted to two spin-1 triplet excitons via a spin-allowed mechanism. Shortly after the discovery of the singlet exciton fission process (1968),[42,126–128] it was proposed as a route to break the Shockley–Queisser limit (1979) by reducing the energy lost by thermalisation of photoexcited charge carriers with excess energy above the bandgap.[7] However, while there has been a larger effort in recent years to develop new singlet fission molecules and understand the fundamental photophysics of the process, there have only been a few studies of how to harvest the triplet excitons generated via fission to improve the efficiency of inorganic PV cells, such as Si cells.[129–132]

One of the most promising methods to harness fission is to harvest the energy of the fission generated triplets via luminescence.[49] In such a scheme, each high energy photon absorbed by the singlet fission materials would lead to the formation of two triplet excitons via fission which would then be converted to two low energy photons, to be absorbed by a conventional inorganic PV cells, thus doubling the photocurrent from the high energy part of the solar spectrum. This scheme, termed a singlet fission photon multiplier (SF-PM), has been described recently and its potential effect on cell efficiencies calculated.[11] It was shown that it could increase the efficiency of the best Si PV cells available today from 26.7% to 32.5%, thus breaking through the Shockley–Queisser limit for the silicon bandgap. The SF-PM is also technologically attractive as it does not require modification of the underlying inorganic PV, but rather can be coated on top of it.

Since triplet excitons are dark states, due to their spin-forbidden return to the ground state, they are extremely poor photon emitters.[54] Hence, a key breakthrough was the demonstration of the transfer of triplet excitons to inorganic quantum dots (QDs), where

the excitations become bright and can recombine to emit photons.[12,94] This discovery also led to the study of the reverse process, the transfer of energy from QDs to the triplet state of organic semiconductors, for application in upconversion and triplet sensitisation to drive photochemical reactions.[14,133] Numerous studies have focused on the role of the ligand on the QD in facilitating or hindering the transfer of excited states to the organic semiconductor.[96,134,135] These ligands both passivate surface defects and provide the QDs with colloidal stability. The transfer dependence on the length of the ligands indicated a Dexter-like transfer mechanism, with shorter ligands providing more efficient transfer as the ligands serve as a tunnelling barrier.[101,136] Until the developments detailed here, there had been no equivalent studies looking at transfer of triplet exciton into QDs in bulk systems , the basis of the proposed SF-PM technologies. The two previous reports of triplet transfer to QDs considered bilayer systems containing layers of organic and QDs on top of each other. [12,94] The confined and bilayer nature of these systems meant that triplets formed via fission are always close to an interface with the QDs and hence have ample opportunity to tunnel across the ligands. However, such a scheme does not provide sufficient light absorption as to be of any practical use. In a useful SF-PM, the singlet fission material must be present in sufficient quantity to harvest most of the incident photons (>95%) and at the same time, the QDs must be present in a low concentration so as to minimise parasitic loss via absorption of solar photons by QDs. For a realistic SF-PM to operate as desired, it has been estimated the parasitic absorption must be <5%.[11] Previously, no such bulk system had yet been demonstrated, and the dynamics of the triplet transfer process to the QDs in such a system remained unexplored.

4.2 Sample Preparation

The synthesis of PbS QDs with oleic acid ligands (OA) and subsequent ligand exchange with either TET-CA or hexanoic acid (HA) was carried out using an adaptation of previously reported methods.[137] Solutions of PbS-OA or PbS-TET-CA QDs at varying concentrations (up to 100 mg mL^{-1}) and TIPS-Tc (200 mg mL^{-1}) were dispersed in toluene and dispensed into cuvettes under a nitrogen atmosphere.

Cuvettes of three varying thicknesses were used during optical measurements. For experiments requiring a fixed and accurate path length, 1 mm pathlength Hellma absorption quartz cuvettes were used. However, these cuvette's relatively long optical

pathlength results in solutions which are incredibly optically dense in the visible region and thus effectively no visible light can be transmitted. Even in situations where transmission is not important, the amount of material required is excessive.

To reduce the path length, in-house made cuvettes were used when possible (Figure 7.1). Cuvettes with roughly 100 µm path lengths were created by stacking a 100 µm thick polyvinyl chloride sheet, stencilled with a cavity, between two glass cover slides. Edges were sealed with a 2-part quick-dry epoxy (Araldite 2-part epoxy adhesive). The advantage of this particular sized cuvette is that the solution inside is of high enough optical density for reliable QD PLQE values to be achieved with excitation across the visible range. However, to achieve an SF-PM with low parasitic QD absorption (560-1200 nm), cuvettes with no PVC spacer were used during subsequent absorption measurements. These samples have a gap for solutions on the order of 10 µm, as determined from comparison of absorbance values with a TIPS-Tc reference solution.

4.3 Steady-State Optical Characterisation

We begin the characterisation of the solution-phase TIPS-Tc:PbS-TET-CA system by investigating its steady-state optical properties. Figure 4.1c shows the absorption and emission spectra of TIPS-Tc, TET-CA, PbS QDs with the native OA ligands (PbS-OA) and those modified with TET-CA via ligand exchange (PbS-TET-CA), dissolved in toluene. Attachment of the TET-CA ligand after multiple wash cycles in acetone is confirmed via UV-Vis absorption measurements, where the TET-CA absorbance peaks are visible on top of the PbS QD absorbance. The absorption of TIPS-Tc, TET-CA and PbS-TET-CA show clear vibrionic structure. The 0-0 vibrionic peak of TIPS-Tc at 535 nm gives an S_1 energy of 2.32 eV, while the TET-CA 0-0 peak at 545 nm (2.28 eV) indicates a 40 meV redshift on the addition of the carboxylic acid functional group. The triplet energy of TIPS-Tc is expected to be 1.2 eV,[123] meaning that singlet fission in TIPS-Tc is endothermic.

The PbS QDs are tuned such that their bandgap, as measured from the excitonic absorption peak at ~ 1180 nm (~ 1.05 eV), is below the triplet energy of TIPS-Tc (~ 1.2 eV), making it energetically favourable to accept triplets from TIPS-Tc.[12] The Stokes-shifted PbS QD photoluminescence peak is at ~ 1350 nm (~ 0.92 eV). TIPS-Tc is a well-studied singlet fission material, which has been shown to efficiently undergo fission in highly concentrated solutions (>200 mg/mL) with a fission yield of 120 ± 10%.[66,123]

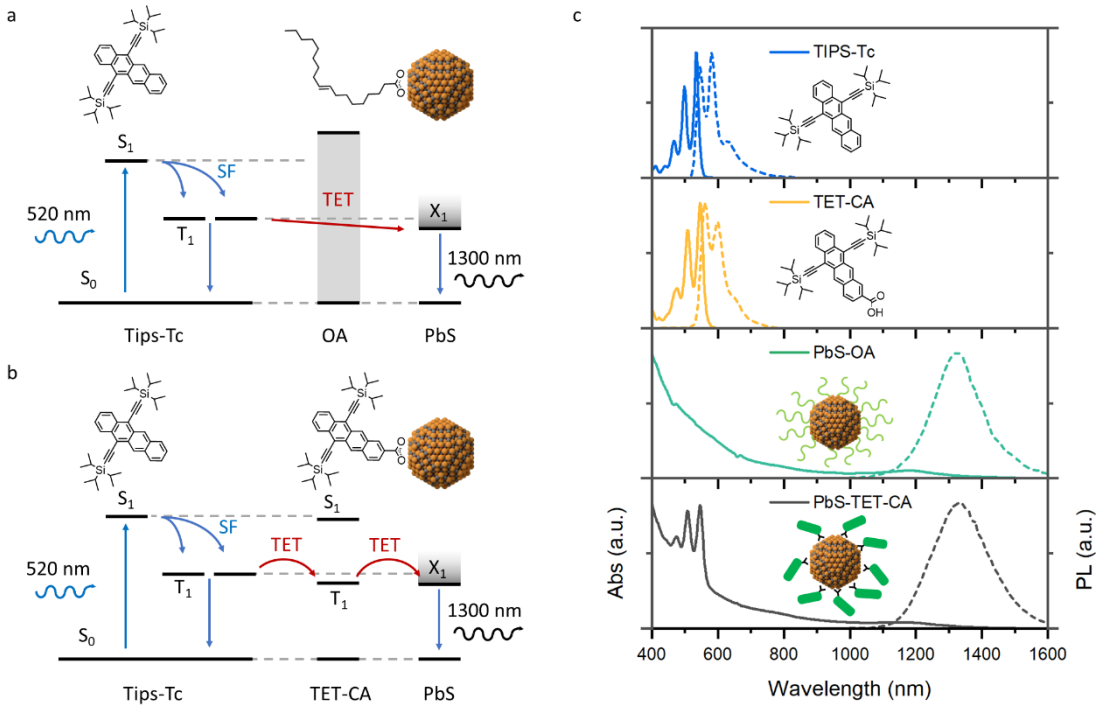

Figure 4.1: Schematic of the solution phase SF-PM system.
TIPS-Tc, TET-CA and PbS QDs act as the singlet fission material, transmitter, and emitter respectively in this hybrid photon multiplier system. (a, b) Schematics of the photon multiplication process. The TIPS-Tc molecules absorb high-energy visible photons, producing a photoexcited singlet state S_1, which then interacts with a different ground-state molecule to undergo singlet fission, forming two excited triplet molecules. (a) The high-bandgap carboxylic acid inhibits the TIPS-Tc triplets from getting close enough to the PbS QDs for triplet energy transfer (TET) to occur. (b) The TET-CA molecules bound to the PbS QDs surface are populated via TET from the TIPS-Tc, bringing the triplets in close contact with the PbS QDs and thus mediating TET to the PbS QDs. (c) The absorbance (solid line) and emission (dashed line) spectra of Tips-Tc (blue/top), TET-CA (orange/top-mid), PbS-OA QDs (green/bottom-mid) and PbS-TET-CA QDs (black/bottom). Reproduced with permission from the ACS publications.[122]

The TET-CA ligand is designed to act as a triplet transmitter ligand, whose triplet energy is chosen to lie above the bandgap of the QDs and slightly below that of the TIPS-Tc fission material, due to the conjugation of the COOH group which slightly lowers the energy levels in comparison to TIPS-Tc. As illustrated in Figure 4.1a, transfer of a triplet between TIPS-Tc and the PbS-OA QD would have to occur over a large distance. The oleic acid ligands act as a tunnelling barrier, resulting in a large Dexter transfer distance and thus reducing the rate of transfer.[12,94] In contrast, with the TET-CA ligand acting as a transmitter, the triplet exciton can first transfer to the ligand. After this initial triplet transfer, the Dexter transfer distance into the PbS QD has been significantly decreased

compared to transfer through either OA or HA.[96] Additionally, while the triplet exciton is located on the transmitter ligand it is in close proximity to the QD for an extended period of time. The increased interaction time, relative to the collisional interactions between triplet excitons on the TIPS-Tc molecules and the QDs covered with aliphatic ligands, leads to a higher triplet transfer rate.

Estimation of the number of ligands attached to the surface of a quantum dot is experimentally challenging and can be achieved with techniques such as DOSY NMR.[138] Here, when estimating the molar mass of PbS-OA, we include the mass of 130 oleic acid ligands attached to the surface of each QD.[139] From TEM measurements done in previous work, we estimate a QD core diameter of 3.4 ± 0.3 nm.[137] By modelling the QD as spherical with the same density as bulk PbS of 7.6 g/cm^3, with 130 oleic acid ligands per QD, we calculate a molar mass of (13 ± 2) x 10^4 g/mol.[140] We use this value when converting between grams and moles of PbS quantum dots. There are more sophisticated methods in the literature that take into account non-stoichiometric ratios of Pb and S. However, we leave the exploration of these methods to future work.[141]

4.3.1 Molar Attenuation Coefficients

In order to determine useful optical properties of the SF-PM system, it is necessary to measure the molar attenuation coefficients for the various components across the Vis-NIR range. For example, knowledge of the molar attenuation coefficients allows calculation of the relative absorption of photons to each component of the SF-PM. The absorbance spectra were measured using 1mm pathlength cuvettes with dilute solutions of TIPS-Tc, PbS-OA and PbS-TET-CA (2 mg/mL) in toluene. Starting from the known mass concentrations, the absorbance spectra, and molar masses, we estimate the molar attenuation coefficient via the Beer-Lambert law in the form

$$\epsilon = \frac{A \cdot M}{l \cdot \rho}, \tag{4.1}$$

where ϵ is the molar attenuation coefficient, A is the absorbance, l is the path length, M is the molar mass and ρ is the mass concentration. The obtained molar and mass attenuation spectra are shown in Figure 4.2 a and b. In particular, the molar attenuation coefficients at 515 nm for TIPS-Tc, PbS-OA and PbS-TET-CA were found to be 2.4×10^4, 2.6×10^5, and 3.5×10^5 $Lmol^{-1}cm^{-1}$, respectively (Figure 4.2). Knowledge of these attenuation coefficients is necessary to calculate the exciton multiplication factors for the SF-PMs from photoluminescent quantum efficiency values (see Section 4.3.3).

From the molar attenuation coefficients of TIPS-Tc and the QDs, we calculate the fraction of absorbed photons for each component as a function of wavelength. The fraction of absorbed photons by the ith component, $\alpha_i(\lambda)$, is related to the concentration of the individual components $[i]$ and molar attenuation coefficients $\epsilon_i(\lambda)$ by

$$\alpha_i(\lambda) = \frac{\epsilon_i(\lambda)[i]}{\sum_j \epsilon_j(\lambda)[j]}. \quad (4.2)$$

Figure 4.2b shows the fraction of photons absorbed by the TIPS-Tc molecules in a solution of TIPS-Tc (200 mg/mL) and PbS-TET-CA (100 mg/mL). By exciting at wavelengths shorter than 560 nm, we can predominately excite the TIPS-Tc, ever for this SF-PM with the highest concentration of PbS-TET-CA QDs in the range investigated.

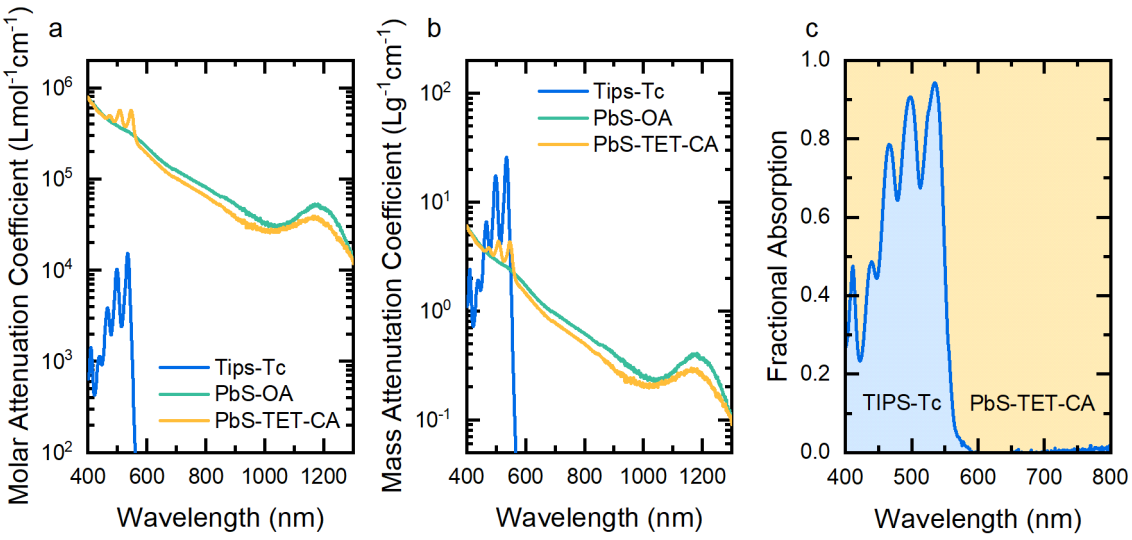

Figure 4.2: Comparison of SF-PM components attenuation coefficients.
Molar (a) and mass (b) attenuation coefficients of TIPS-Tc, PbS-OA QDs and PbS-TET-CA QDs. c) Predicted fractional absorption of the TIPS-Tc (blue area) and PbS-TET-CA (orange area) in a solution of TIPS-Tc (200 mg/mL) and PbS-TET-CA (100 mg/mL). Reproduced with permission from the ACS publications.[122]

The molar attenuation coefficient allows calculation of δ_P, the light penetration depth by

$$\delta_P = \frac{M}{\epsilon \rho \ln(10)}.$$

(4.3)

For TIPS-Tc (200 mg/mL) under 535 nm excitation, the measured molar attenuation coefficient is $\epsilon = 15200\ L\ mol^{-1}cm^{-1}$. Thus, for a 200 mg/mL concentration of pristine TIPS-Tc we calculate a penetration depth of 0.86 µm. SF-PM solutions on the order of a few microns thick are therefore necessary to absorb a sufficient fraction of the incident irradiance to be of use to real-world applications. We detailing the required dimensions in the following section.

Following the addition of PbS-TET-CA QDs, this light penetration depth is expected to decrease due to an increased attenuation coefficient. The subsequent analysis relies on the effective excitation density calculated using this penetration depth. Changes in the penetration depth with QD concentration will result in differences in the effective excitation density. However, over the QD concentration range investigated in this work, we calculate a reduction in the penetration depth by at most 6% (Figure 7.2). Therefore, for the current investigation, we assume the corresponding effect on the excitation density to be negligible.

4.3.2 Calculation of the QD Parasitic Absorption

Absorption of light directly to QDs is considered parasitic as the exciton multiplication step is absent, resulting in sub-optimal performance of the underlying PV. This parasitic absorption has the largest effect at wavelengths below the bandgap of the singlet fission material, where the QDs have non-negligible absorption and are the exclusive absorbing material in the SF-PM (Figure 4.2).

An upper limit for this parasitic absorption in a 'realistic' SF-PM implementation has been suggested to be 5%, with the condition that the SF-PM still be optically dense enough for the singlet fission material's absorption to be 95%.[11] Figure 4.3a shows the measured absorbance spectrum for a solution of TIPS-Tc (200 mg/mL) and PbS-TET-CA QDs (50 mg/mL) in an in-house made micro cuvette. A linear regression fit of this spectrum and the measured attenuation spectra reveals that the path length of the cuvette is 15 ± 2 µm. Hence we illustrate that it is possible to achieve pathlengths on the micron scale and that the absorbance in our SF-PM is two orders of magnitude higher in the singlet fission material (535 nm) than in the parasitic QD absorption range (>560 nm). As shown by the liquid crystal display community, there exist methods for producing solutions as thin as 2 µm; we leave it to future work to demonstrate a solution

SF-PM with such a low thickness.[142,143] However, we calculate that a 2.5 µm thick SF-PM solution would absorb 95% of the light at the TIPS-Tc absorption peak while maintaining the QD parasitic absorption (>560 nm) less than 5% (Figure 4.3b). Thus, it fullfills the absorption criteria for a proposed "realistic" SF-PM.[11]

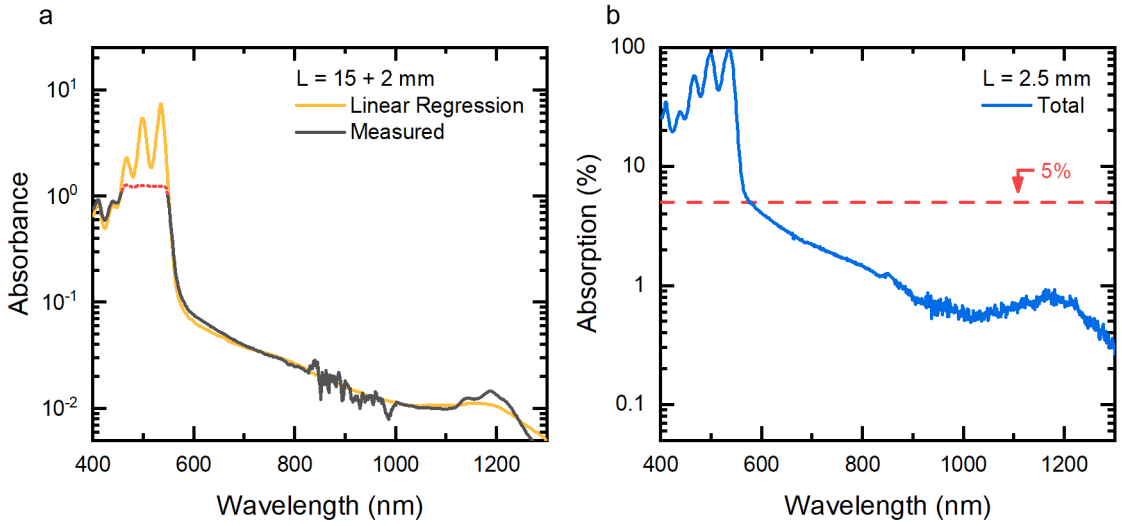

Figure 4.3: Calculation of the parasitic QD absorption.
a) Measured absorbance of a SF-PM solution (black curve) with 200 mg/mL of TIPS-Tc and 50 mg/mL of PbS-TET-CA QDs. Due to the extremely high absorption at the TIPS-Tc absorption peak and the limited sensitivity of the measurement, the true value for the TIPS-Tc absorbance peak is not captured (red dashed line). The measured attenuation spectra of TIPS-Tc and PbS-TET-CA, combined at the appropriate concentration, were fitted, by linear regression, to the valid region of the measured absorbance spectrum (orange curve). From the attenuation coefficient of the solution, we calculate the thickness of this "micro cuvette" as 15 ± 2 µm. b) Using the attenuation spectra for TIPS-Tc and PbS-TET-CA we calculate the attenuation spectrum for a 2.5 µm thick, TIPS-Tc (200 mg/mL) and PbS-TET-CA (50 mg/mL), singlet fission photon multiplier solution. From this, we calculate the percentage absorption for this PM solution. The horizontal dashed red line indicated 5 % photon absorption. Reproduced with permission from the ACS publications.[122]

4.3.3 Photoluminescence and Quantum Efficiency

We perform a qualitative evaluation of the SF-PM system by measuring IR-detected photoluminescence excitation spectra. Figure 4.4 shows the photoluminescence (PL) excitation spectrum of a solution of PbS-OA QDs in toluene (50 mg/mL), along with the comparable excitation scans for blends of TIPS-Tc (200 mg/mL) and QDs with various ligands. To allow comparison, the spectra have been normalised to their value under 700 nm excitation.[12] The excitation spectrum of PbS-OA has a decreasing emission

intensity with longer wavelength, following the absorbance of the QDs across this region. At wavelengths longer than 600 nm, where only the QDs are absorbing, all solutions follow the same trend. However, at wavelengths shorter than 600 nm the concentrated TIPS-Tc, with orders of magnitude higher absorption, is absorbing most of the light (Figure 4.3) and so the IR PL from the solution is an indication of the amount of exciton transfer from TIPS-Tc to the QDs. Compared to PbS-OA on its own, the TIPS-Tc:PbS-TET-CA solution shows an increase in the IR PL for wavelengths where the TIPS-Tc is absorbing, with the PL excitation peaks matching with TIPS-Tc absorption peaks, indicating a high exciton transfer efficiency. In contrast, blends of TIPS-Tc and PbS QDs without the TET-CA ligand (either OA or HA ligands) show a significant drop in IR PL for excitation below 550 nm, with dips that match with the absorption peaks of TIPS-Tc. This drop in IR PL shows that for these solutions the energy transfer from TIPS-Tc to the QDs is inefficient.

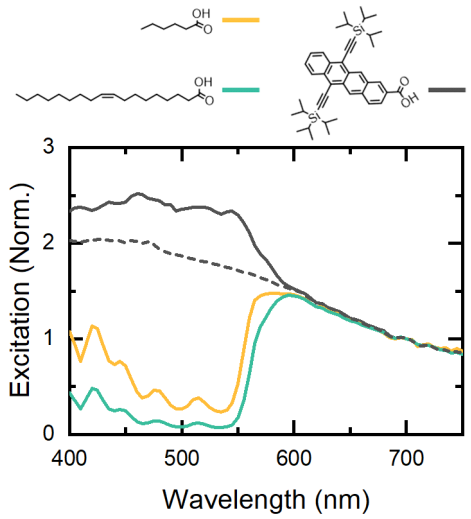

Figure 4.4: Detection of exciton transfer by photoluminescent excitation spectra.
PbS QD PL excitation spectra for solutions of TIPS-Tc (200 mg/mL) and 1.05 eV PbS QDs (50 mg/mL) with OA (green), HA (yellow) TET-CA (grey) ligands, along with PbS-OA QDs on their own (dashed). The excitation spectra are normalised to the value at 700 nm, where only the QD is absorbing. Reproduced with permission from the ACS publications.[122]

For quantitative evaluation of the SF-PM system, we use IR PLQE measurements on a series of solutions with varying QD concentrations. Table 7.1 and Figure 4.5 detail the PLQE values for the PbS QD emission in the TIPS-Tc:QD solutions excited at either 515 nm, which excites both TIPS-Tc and QD, or 658 nm, which selectively excites the QDs. For TIPS-Tc:PbS-TET-CA solutions the peak PLQE occurs at a QD concentration of 50 mg/mL, with 18.2% IR PLQE (515 nm excitation), while the intrinsic PLQE of the QD

in the same solution was found to be 14.6% (658 nm excitation). The increased PLQE value when the TIPS-Tc is predominately excited, relative to excitation of only the QDs, indicates efficient exciton multiplication via the singlet fission process and triplet exciton transfer to the PbS-TET-CA QDs.

The IR PLQE of a photon multiplier $\eta_{PM}(\lambda)$ for excitation at wavelength λ, with singlet fission donor and emissive QD acceptor components, can be expressed as[12]

$$\eta_{PM}(\lambda) = \eta_{QD}\frac{\mu_{QD}(\lambda) + \eta_{EMF}\mu_{Tc}(\lambda)}{\mu_{QD}(\lambda) + \mu_{Tc}(\lambda)},$$

(4.4)

where η_{QD} is the intrinsic PLQE of the QD, μ_i is the attenuation coefficient, base 10, of the ith component and η_{EMF} is the exciton multiplication factor. The exciton multiplication factor characterises the total exciton transfer from the donor to acceptor. In principle, the excitons that are transferred can be of spin-singlet and spin-triplet nature. However, by the end of this chapter, we systematically show that triplet exciton transfer is the dominate process occurring in the TIPS-Tc:PbS-TET-CA solutions and there is negligible singlet exciton transfer.

For comparison, the expected IR PLQE of the SF-PM solutions without exciton transfer is given by[12]

$$\eta_{k_{Tr=0}}(\lambda) = \eta_{QD}\frac{\mu_{QD}(\lambda)}{\mu_{QD}(\lambda) + \mu_{Tc}(\lambda)}\ .$$

(4.5)

The measured molar attenuation coefficients and the intrinsic QDs PLQE are combined to calculate the IR PLQE for the “no transfer case” in the SF-PM and is compared to the measured values (Figure 4.5). The calculated IR PLQEs for the “no transfer case” illustrates the minimum amount of IR PL that should be observed in the solutions. Hence, values higher than this level, like those observed for the TIPS-Tc:PbS-TET-CA solutions, indicate exciton transfer from the TIPS-Tc to the PbS QDs. The TIPS-Tc:PbS-OA solutions show little deviation from this lower limit, supplying additional evidence that the OA ligand inhibits exciton transfer between the TIPS-Tc and the PbS QDs.

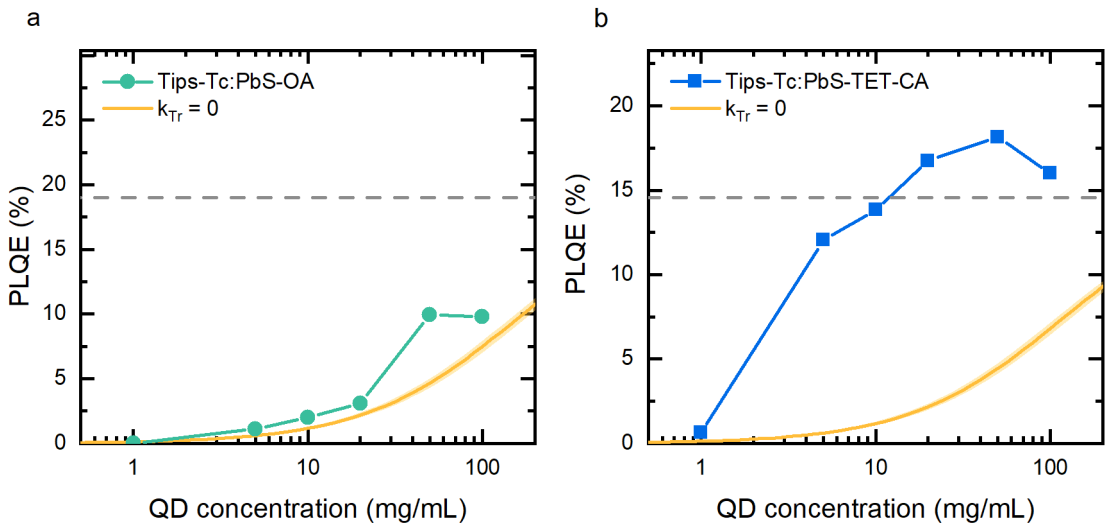

Figure 4.5: IR PLQE of values for TIPS-Tc:QD solutions.
TIPS-Tc (200 mg/mL) with (a) PbS-OA and (b) PbS-TET-CA solutions, under 515 nm excitation. The horizontal grey dashed lines indicate the intrinsic IR PLQE of the QDs, measured under 658 nm excitation. The yellow lines indicate the expected PLQE for the solution due to photon absorption directly to the QDs (no exciton transfer). The IR PLQE with 515 nm excitation were measured under 5 mW/cm² fluence. Reproduced with permission from the ACS publications.[122]

Alternatively, the exciton multiplication factor η_{EMF} can be explicitly calculated from[12]

$$\eta_{EMF}(\lambda) = \frac{1}{\mu_{Tc}(\lambda)}\left(\frac{\eta_{PM}(\lambda)}{\eta_{QD}}\left(\mu_{QD}(\lambda) + \mu_{Tc}(\lambda)\right) - \mu_{QD}(\lambda)\right). \quad (4.6)$$

η_{EMF} gives the number of excitons transferred to the PbS QDs per photon absorbed in the TIPS-Tc, in terms of the intrinsic QD IR PLQE (658 nm excitation), the SF-PM IR PLQE (excitation at λ) and the attenuation coefficients of the TIPS-Tc and QDs. Using equation (4.6), the measured molar absorption coefficients and IR PLQE values when the SF-PM solutions were excited at 515 nm and 658 nm, we calculate the exciton multiplication factor, η_{EMF}, as shown in Figure 4.6. Here we have quantitative proof of singlet fission photon multiplication, as we observe values of exciton transfer above 100% for concentrations greater than ~10 mg/mL of PbS-TET-CA QDs. In this system, exciton multiplication greater than 100% indicate that efficient singlet fission and triplet transfer are the dominate processes leading the QD emission.

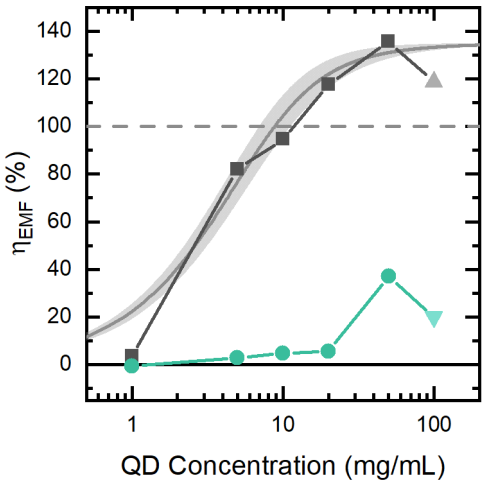

Figure 4.6: Quantification of the exciton multiplication factor.
Exciton multiplication factor for transfer from TIPS-Tc to PbS-OA (green circles) and PbS-TET-CA (black squares) in solutions with varying concentrations together with TIPS-Tc (200 mg/mL), under 515 nm 5 mW/cm^2 excitation. The horizontal grey dashed line indicates the point at which 100% excitation transfer occurs. The values for 100 mg/mL QD concentration have been highlighted as outliers due to self-absorption losses. The triplet exciton transfer efficiency, η_{TET}, calculated with the kinetic parameters derived from the nsTA (details in Section 4.5.2) is scaled by a singlet fission efficiency, $\eta_{SF} = 1.35 \pm 0.05$, to match with the values obtained by PLQE measurements for PbS-TET-CA (grey, with 95% confidence bounds). Reproduced with permission from the ACS publications.[122]

In Section 4.5, we develop a kinetic model to describe the transfer of triplet excitons from the TIPS-Tc to the PbS-TET-CA QDs. Without going into detail, we calculate the triplet transfer efficiency, η_{TET}, as a function of the PbS-TET-CA QD concentration, at the laser fluence used in the IR PLQE measurements. Multiplication of this TET efficiency with a singlet fission yield of $\eta_{SF} = 135 \pm 5\%$ gives reasonable agreement with the observed values for the exciton multiplication factor, $\eta_{EMF} = \eta_{SF}\eta_{TET}$, obtained from the PLQE data (Figure 4.6, grey curve). This value for the singlet fission yield agrees with previous predictions obtained by measurement of triplet sensitised transient absorption spectra and is the default value used for the remainder of this investigation.[123]

The measured exciton multiplication factor, η_{EMF}, for the PbS-OA system is low for all QD concentrations, indicating poor exciton transfer. Changing the QD ligand to HA does result in slightly increased IR PL when the TIPS-Tc is absorbing (Figure 4.4). This trend agrees with the HA ligand resulting in higher exciton transfer than the longer OA ligand due to HA having a shorter Dexter transfer distance.[12,94,101] However, the TET-CA ligand greatly outperforms the shorter HA ligands.

The observed drop in the IR PLQE values for 100 mg/mL QD concentration is assigned to self-absorption losses because of the high QD concentrations, and is therefore highlighted as an outlier (Figure 4.6). The drop in IR PLQE aligns with a red shifting of the QD's PL peak, a sign of self-absorption (Figure 7.3).[144]

4.3.4 Magnetic Field Dependent PL

We use magnetic field dependent PL measurements to confirm that the TIPS-Tc system is harvesting triplet excitons generated via singlet fission (Figure 4.7).[12] With excitation at 515 nm, the TIPS-Tc singlet emission (550-750 nm) shows an increased intensity on application of high magnetic fields (>0.3 T), as expected for a material undergoing singlet fission (Figure 4.7). Conversely, the PbS-TET-CA QDs' IR PL shows a corresponding decrease, indicating that the excited QD states are the result of triplets generated by singlet fission, transferred from the TIPS-Tc.[12,118] Direct excitation of the PbS-TET-CA QD with 658 nm laser light results in no observed magnetic dependence (for fields less than 0.5 T), similar to previous observations.[12,118]

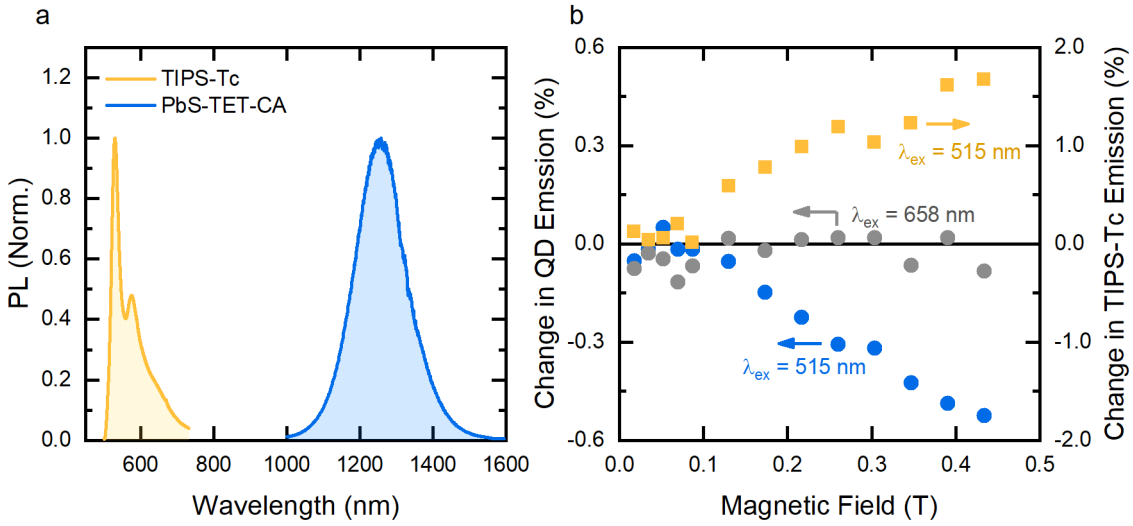

Figure 4.7: Magnetic dependent PL from TIPS-Tc:PbS-TET-CA solution.
a) TIPS-Tc (orange curve) and PbS-TET-CA QD (blue curve), normalised PL emission spectra of a TIPS-Tc:PbS-TET-CA solution (100:50 mg/mL), under 515 nm excitation, at zero applied field. b) Percentage change in the QD and TIPS-Tc PL, for a solution of TIPS-Tc:PbS-TET-CA solution (200:100 mg/mL). QD (blue circles) and TIPS-Tc (orange squares) emission resulting from excitation with 515 nm laser light. Direct excitation of the QD, with 658 nm (grey circle).

4.4 Triplet Harvesting Dynamics

In this section we delve into the dynamics of the triplet harvesting process occurring in the SF-PM solutions, beginning with the transient photoluminescence of the PbS QDs. Along with the increased steady-state PLQE, we measure higher levels of long-lived transient PL signal for TIPS-Tc:PbS-TET-CA solutions compared to TIPS-Tc:PbS-OA when excited at 530 nm, as shown in Figure 4.8. The longer-lived PL signal indicates that the triplet exciton transfer is occurring on timescales comparable to or slower than the decay of the excited QD states. Due to the long lifetime of the QDs compared to the fixed repetition rate (1 MHz) used to photoexcite the system, a significant population of excited TIPS-Tc and QD states remain present when the next pump laser pulse interacts with the system. The effect of this accumulation of excited state is most apparent by the high PL counts before time zero. These pre-time zero detector counts should not be confused with background detector counts due to ambient conditions and the electronic noise in the detector. Figure 4.8a shows the measured background counts for an equivalent detection period are indeed significantly lower than these pre-time zero values. To make this point as clear as possible we take the mean value of the background detector counts and remove it from the PL kinetics (Figure 4.8b). The pre-time zero PL counts remain clear.

We use a bi-exponential decay in the presence of periodic excitation in the form

$$y(t) = Ae^{-t/\tau_1} + Be^{-t/\tau_2} + \frac{B}{e^{T/\tau_2} - 1} \tag{4.7}$$

to fit the decay of the QD PL (see Appendix B for a detailed derivation). The short τ_1 time constant component is a parameterisation of the non-linear recombination occurring in the QD, due possibly to an Auger recombination, while the longer τ_2 time constant is the decay constant for excited QD states. Fitting to the IR transient PL is achieved by least-square fitting as shown in Figure 4.8b and the parameters shown in Table 4.1. When the SF-PM solutions are excited at 530 nm, where TIPS-Tc's absorption is dominant, we extract a decay constant of 1.30±0.01 µs for the PbS-OA quantum dots, compared to 22.0 ±0.7 µs for the PbS-TET-CA QDs. The value for PbS-OA QDs is in agreement with previous reports for PbS-OA QDs alone in toluene; however, the PbS-TET-CA value is significantly longer.[134] The extended PL decay constant suggests the TIPS-Tc triplet excited states are being harvested by the PbS-TET-CAQDs (10 mg/mL) with a time constant of roughly 20 µs.

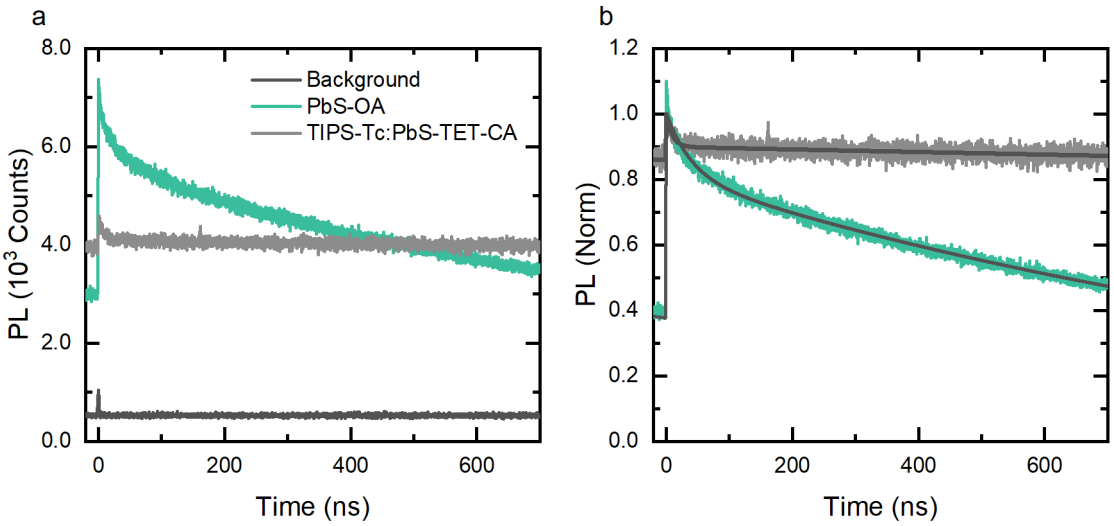

Figure 4.8: a) Transient near-infrared photoluminescence from TIPS-Tc:QD solutions. a) PL counts for 10 mg/mL PbS-OA NCs (green) and PbS-TET-CA QDs (grey) in toluene with 100 mg/mL TIPS-Tc, under excitation with 530 nm 300 pJ/cm², 1 MHz repetition rate pump pulse. The black curve is the counts collected from the ambient background for the same collection time without any sample present in the beam path. b) PL kinetics normalised to the maximum value after removal of a fixed constant representative of contributions to camera counts from ambient conditions. The laser pump timing has been aligned with t = 0 ns, and thus counts before this time are residual counts from all previous pump pulse. The fits to the transient kinetics (black) follow a parameterisation with a bi-exponential function, where the slower exponential decay is summed over all previous pump pulses, representing an exponential decay in a periodically driven system. Reproduced with permission from the ACS publications.[122]

Sample	τ_1 (ns)	τ_2 (µs)
PbS	40 ± 1	1.300 ± 0.005
TIPS-Tc:PbS-TET-CA	10 ± 1	22 ± 0.7

Table 4.1: Transient near-infrared photoluminescence fitting parameters. Fitting parameters for 10 mg/mL PbS-OA NCs and PbS-TET-CA QDs in toluene with 100 mg/mL TIPS-Tc, under excitation with 530 nm 300 pJ/cm², 1 MHz repetition rate pump pulse.

4.4.1 Building a Kinetic Model

With the knowledge that singlet fission photon multiplication is occurring in the SF-PM solutions of TIPS-Tc:PbS-TET-CA, we now seek a possible kinetic model to understand the dynamics of such a process. By taking the basic kinetic scheme for singlet fission and including a variety of interactions with a PbS-TET-CA QD we arrive at the kinetic scheme shown in Figure 4.9.[123] These interactions include singlet exciton transfer (SET) from the TIPS-Tc (k_{SET}) and TET-CA (k_{LSET}) to the QD excited state *X₁*; triplet exciton transfer (TET) in either direction between TIPS-Tc and TET-CA ($k_{\pm TET_1}$), TET-CA and the PbS QD ($k_{\pm TET_2}$) or directly between TIPS-Tc and the PbS QD ($k_{\pm TET}$). The decay channels include TIPS-Tc singlet radiative and non-radiative decay (k_{S_r} and $k_{S_{nr}}$); PbS QD radiative and non-radiative decay (k_{X_r} and $k_{X_{nr}}$) and TIPS-Tc excimer, TIPS-Tc triplet, TET-CA triplet monomeric decay (k_E, k_T and k_{LT}). Critically we take care to include TIPS-Tc triplet bi-molecular decay via the k_{TTA} rate. Many of these processes have been shown to occur previously.[98,123] However, this is not an exhaustive list of the possible processes.[66]

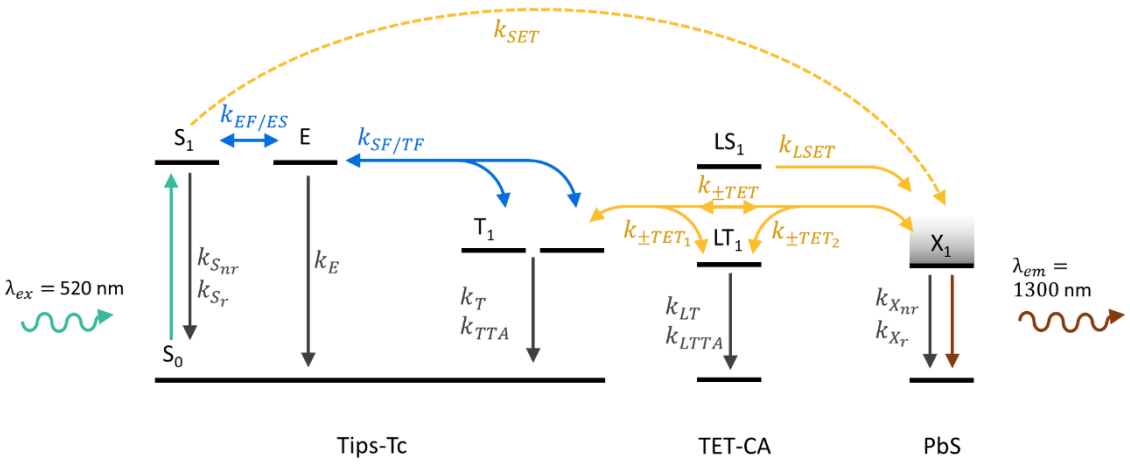

Figure 4.9: Kinetic scheme illustrating the relevant photophysical processes. This model includes an extensive list of the possible excited state processes that could occur in a solution of TIPS-Tc and PbS QD with TET-CA ligand. Reproduced with permission from the ACS publications.[122]

Analysis of the above scheme leads to the following system of differential equations:

$$\frac{dS_1}{dt} = -\left(k_{S_{nr}} + k_{S_r} + k_{SET}\right)S_1 - k_{EF}S_0S_1 + k_{ES}E + I(\lambda)\alpha_{Tc}(\lambda)\,,$$

$$\frac{dE}{dt} = k_{EF}S_0S_1 + k_{TF}T_1^2 - (k_{E,r} + k_{E,nr} + k_{ES} + k_{SF})E \,,$$

$$\frac{dT_1}{dt} = 2k_{SF}E + k_{-TET_1}LT_1 + k_{-TET}X_1 - (k_T + k_{TET_1} + k_{TET})T_1 - (k_{TTA} + 2k_{TF})T_1^2 \,,$$

$$\frac{dLS_1}{dt} = -k_{LS}SL_1 - k_{LSET}SL_1 + I(\lambda)\alpha_L(\lambda) \,,$$

$$\frac{dLT_1}{dt} = k_{TET_1}T_1 + k_{-TET_2}X_1 - (k_{LT} + k_{-TET_1} + k_{TET_2})LT_1 - k_{TTLA}LT_1^2 \,,$$

$$\frac{dX_1}{dt} = -\frac{dX_0}{dt} = k_{SET}S_1 + k_{TET_2}LT_1 + k_{TET}T_1 + k_{LSET}SL_1 - \left(k_{X_{nr}} + k_{X_r} + k_{-TET_2} + k_{-TET}\right)X_1 + I(\lambda)\alpha_{QD}(\lambda) \,.$$

(4.8)

Where S_0, S_1, E, T_1, LS_1, LT_1, X_0 and X_1 are respectively the density of the TIPS-Tc ground state, TIPS-Tc first excited singlet state, TIPS-Tc excimer state, TIPS-Tc triplet state, TET-CA first excited singlet state, TET-CA triplet state, PbS QD ground state and PbS QD excited state. $I(\lambda)$ is the density of photons absorbed by the sample as a function of the excitation wavelength λ and α_i is the fraction absorbed by the *ith* component.

In previous work, it has been shown that the TIPS-Tc singlet decays within 100 ps in concentrated solutions.[66,123] SET from TIPS-Tc to the PbS QD can occur during this initial decay of the singlet or from singlets regenerated via triplet-triplet annihilation (TTA) in the TIPS-Tc. However, these two processes can be distinguished via their characteristic fluence dependence. SET from the initial photoexcited singlet exciton will occur at a constant efficiency determined by the branching ratio, $k_{SET}/(k_{S_{nr}} + k_{S_r} + k_{SET} + k_{EF}S_0)$, at all fluences. However, SET from TTA generated singlets will happen after 100 ps and will increase superlinearly with fluence, significant populations of excited singlet excitons only being regenerated at high fluences. Later in Section 4.4.2, we show that SET from the photon generated singlet is not efficient in this system (< 5%) and so the dominant process occurring at low incident fluences for the TIPS-Tc singlet is singlet fission.

We simplify the above kinetic scheme by applying the following constraints on the triplet transfer and singlet fission processes. The QD bandgap has been chosen such that it is lower than the TIPS-Tc and TET-CA triplet energies, making TET from the TIPS-Tc and

TET-CA to the PbS QD energetically favourable over the reverse process. The singlet fission process is negligibly affected by the addition of the QDs, production of the singlet via TTA is excluded and SET from the TIPS-Tc singlet is inefficient. Exciton transfer is proceeding after singlet fission has occurred, meaning singlet fission can be treated as a unidirectional process that instantaneously produces triplets with a yield of η_{SF}. Triplet transfer from the TIPS-Tc to the TET-CA ligand is slow compared to transfer from the TET-CA ligand to the PbS QD, meaning k_{TET_2} is not the rate-limiting step and so there is negligible population of the TET-CA triplet state during the transfer step. Any photogenerated singlet excitons on the TET-CA ligand are transferred with unity efficiency to the PbS QD. This unity efficiency for singlet transfer is justified by the effective equivalence of the measured IR PLQE values of the PbS-TET-CA QDs when excited at wavelengths where the TET-CA and QD absorb (515 nm) and where only the QD absorbs (658 nm), 14.2% and 14.6% respectively. In previous studies, singlet fission has been reported to occur on the surface of PbS QDs in the TET-CA ligands; we do not observe this with the QDs used in this work and assign the difference to a lower TET-CA surface coverage resulting in weaker TET-CA and TET-CA interactions.[137] Finally, we consider the population of PbS QDs excited states as a weak perturbation of the QD ground state population and so treat X_0 as a constant. Under these simplifications, the kinetic model, as shown by Figure 4.10, can be expressed as three separable efficiencies, η_{SF}, η_{TET} and η_{QD}, described by the following system of equations:

$$\frac{dT_1}{dt} = \eta_{SF} I(\lambda)\alpha_{Tc}(\lambda) - (k_T + k_{TET}X_0)T_1 - k_2 T_1^2 \,,$$

$$\frac{dX_1}{dt} = k_{TET}X_0 T_1 - \left(k_{X_{nr}} + k_{X_r}\right)X_1 + I(\lambda)\alpha_{QD+L}(\lambda) \,. \qquad \textit{(4.9)}$$

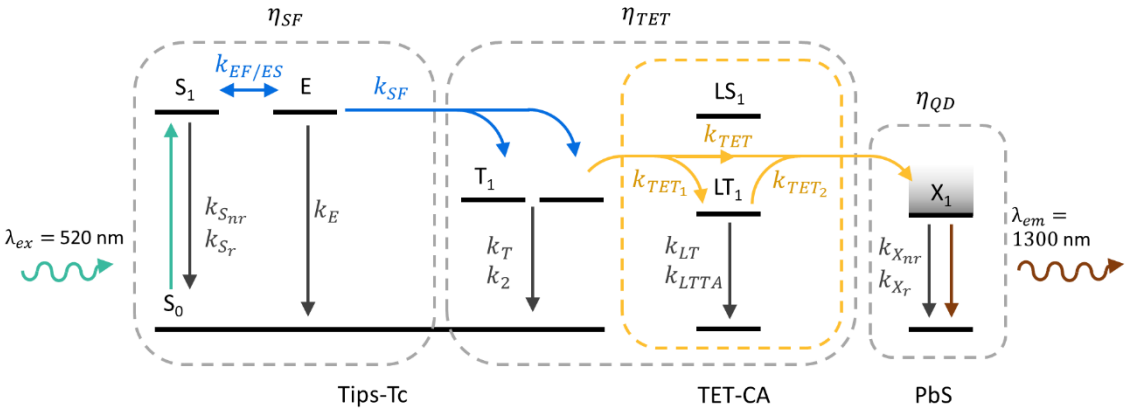

Figure 4.10: Kinetic scheme illustrating the simplified array of photophysical processes. The singlet fission and triplet transfer processes are assumed to be unidirectional. Reproduced with permission from the ACS publications.[122]

In a related piece of work that we leave to the reader for further investigation, we loosen the unidirectional constraints on the kinetic model described here.[97] This extra layer of complexity reveals insightful design rules regarding the exact energy offset that is required between the SF materials triplet energy, triplet transmitter triplet energy and the bandgap of the QD. However, the advanced analysis is consistent with the model described here for this particular system.

4.4.2 Femtosecond Transient Absorption

To evaluate the ultrafast excited-sate dynamics of TIPS-Tc in the presence of PbS QDs, femtosecond transient absorption spectra were measured (Figure 4.11 and Figure 4.12). In concentrated solutions of TIPS-Tc (200 mg/mL), with and without PbS-TET-CA (50 mg/mL), we observe a loss of the singlet and rise of triplet features within 100 ps after excitation.[66,123] The TIPS-Tc singlet exciton is identified by the clear stimulated emission (SE), positive peak at ~570 nm and broad photoinduced absorption (PIA), from ~600 nm to ~900 nm. These features decay over the course of 100 ps after photo exciton, concurrently with the growth of the TIPS-Tc triplet PIA (negative peak at ~850 nm).

We apply the genetic algorithm to deconvolve the femtosecond transient absorption map into kinetics and spectra for the TIPS-Tc singlet and triplet excitons (subplots c and d in Figures 4.14 and 4.15). For both the TIPS-Tc, with and without PbS-TET-CA QDs, the genetic algorithm successfully extracts kinetics that shows the decay of an initial species,

the singlet exciton, concurrent with the rise of a second species, the triplet exciton. The extracted spectra show features that agree with the SE and PIA of the singlet and triplet PIA signals assigned earlier. Because of the strong absorption of the QDs, the probe pulse is significantly weaker in the TIPS-Tc:PbS-TET-CA solution at shorter wavelengths. This results in worse probe statistics at wavelengths below 700 nm compared with spectra of TIPS-Tc on its own. As a result, the spectral features like the TIPS-Tc's singlet stimulated emission (580 nm) and PIA (650 nm) appear weaker as they have been masked by experimental noise. However, the singlet and triplet features in the range of 700-950 nm are still clear and allow for spectral deconvolution of the two species.

Comparing the decay of the singlet exciton's PIA at 860 nm, with and without the PbS QDs, reveals no significant difference in the fission kinetics (Figure 4.12b). Upon kinetic fitting with a mono-exponential decay (capturing the singlet decay) and constant offset (residual signal due to the triplet state), we find singlet decay constants in the range 70-80 ps (Table 4.2).

After the TIPS-Tc singlet exciton decays, the subsequent triplet spectrum with PIA peak at 850 nm is present at similar signal strengths as the pristine TIPS-Tc solution. This is observed from the genetic algorithm's deconvolution and the raw TA signal at times after 200 ps in Figure 4.12b, indicating that singlet fission occurs with similar yields with the PbS-TET-CA QDs present. The insignificant change in singlet decay rate and similar intensities of the subsequent PIA spectrum, with and without the Pbs-TET-CA, indicates that there is no effect on the singlet fission process.

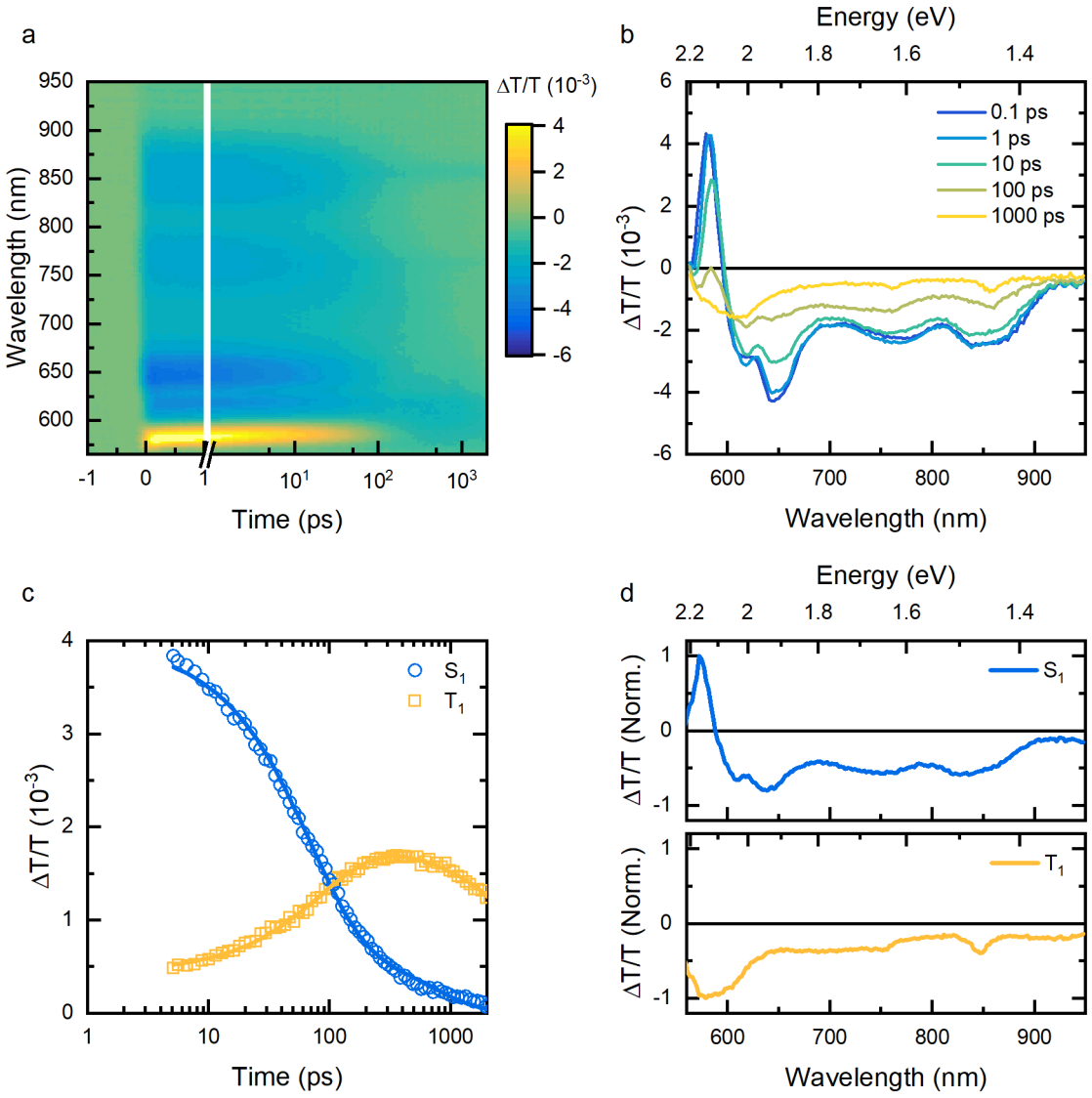

Figure 4.11: Identification of singlet fission in TIPS-Tc solutions.
Picosecond transient absorption map (a) and spectra (b) of ~100 µm thick TIPS-Tc solution (200 mg/mL). The sample was excited with a 15 µJ/cm² pulse centred at 535 nm. We decompose the fsTA map into two kinetics (c) and spectra (d) in a global analysis using the genetic algorithm. The kinetics were fitted with a bi-exponential function to give a guide to the eye. We assign the spectra to the singlet (initial state) and triplet (subsequent state).[123] *Reproduced with permission from the ACS publications.*[122]

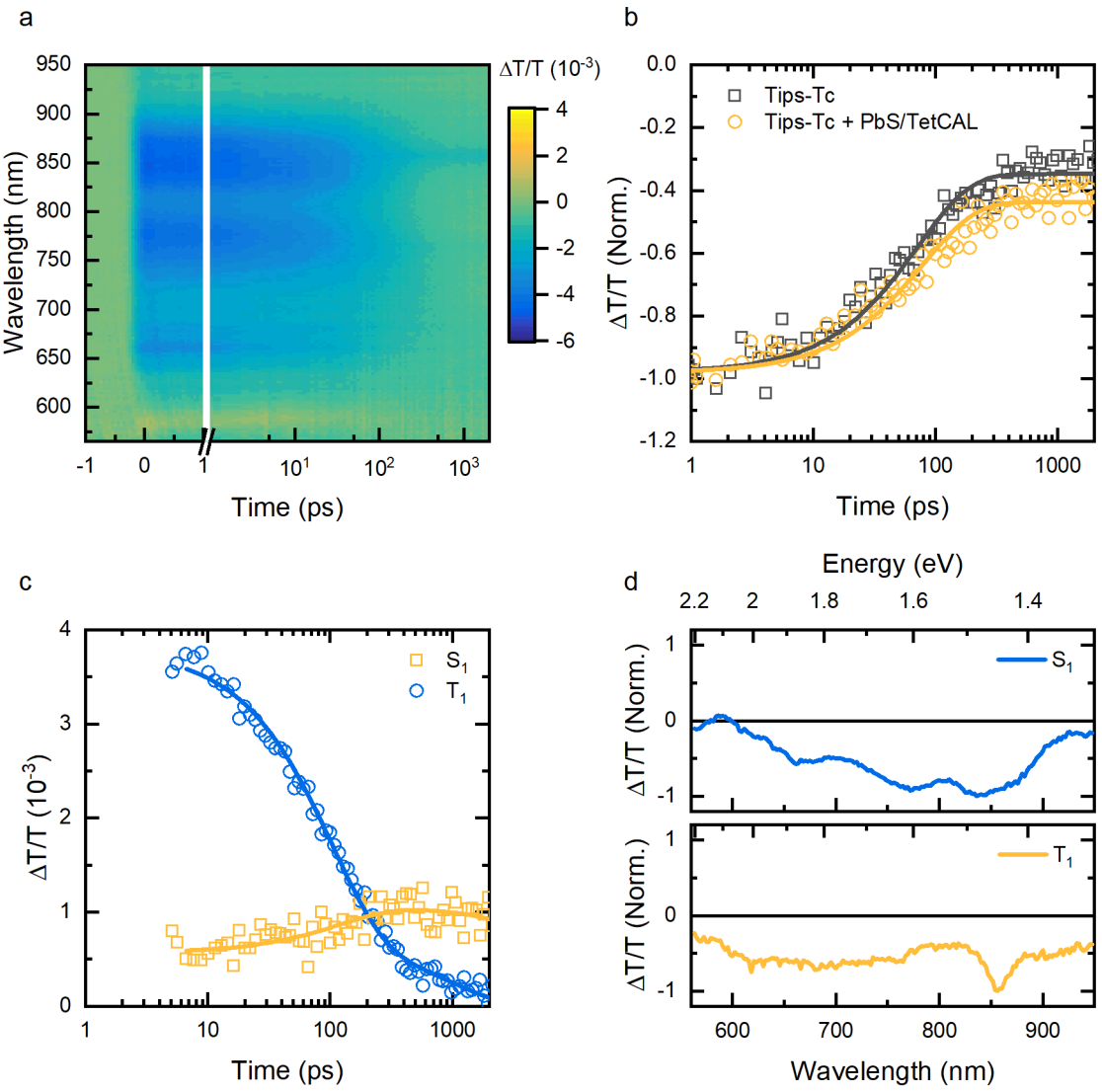

Figure 4.12: Identification of singlet fission in TIPS-Tc:PbS-TET-CA solutions.
a) Picosecond transient absorption map of ~100 µm thick TIPS-Tc:PbS-TET-CA (200:50 mg/mL) solution excited with a 15 µJ/cm^2 pulse centred at 535 nm. b) Comparison of the signal strength at 860 nm between TIPS-Tc and TIPS-Tc:PbS-TET-CA. The kinetic fitting is achieved using an exponential decay (capturing the singlet decay) with constant offset (residual signal due to the excimer state). We decompose the fsTA map into two kinetics (c) and spectra (d) using the genetic algorithm. The kinetics were fitted with a bi-exponential function to give a guide to the eye. We assign the spectra to the singlet (initial state) and triplet (subsequent state). Reproduced with permission from the ACS publications.[122]

Solution	Time Constant (ps)
TIPS-Tc	71 ± 4
TIPS-Tc:PbS-TET-CA	78 ± 6

Table 4.2: psTA fitted time constant for the decay of the TIPS-Tc singlet PIA. Decay rate obtained by fitting an exponential decay with offset to the fsTA kinetics at 860 nm. Samples excited with 535 nm, fs pulses at 15 μJ/cm^2.

4.4.2.1 Ruling out Singlet Exciton Transfer

Due to the similarity of the TIPS-Tc singlet decay with and without the PbS QDs present, it appears that singlet exciton transfer to the QD does not compete with the singlet fission. Here, we attempt to quantify just how little (or if any) singlet exciton transfer is occurring. As shown in Section 4.4.1 the TIPS-Tc singlet decay rate for solutions of TIPS-Tc k_1, and TIPS-Tc:PbS-TET-CA k_2, can be simplified to

$$k_1 = k_{S_r} + k_{S_{nr}} + k_{EF}S_0 \,, \tag{4.10}$$

$$k_2 = k_{S_r} + k_{S_{nr}} + k_{EF}S_0 + k_{SET} \,. \tag{4.11}$$

From this set of equations, the efficiency of singlet exciton transfer can be expressed as

$$\eta_{SET} = \frac{k_{SET}}{k_{S_r} + k_{S_{nr}} + k_{EF}S_0 + k_{SET}} = \frac{k_2 - k_1}{k_2} \,, \tag{4.12}$$

with uncertainty given by $\Delta\eta_{SET} = \left(\frac{k_1}{k_2}\right)\left(\frac{\Delta k_1}{k_1} + \frac{\Delta k_1}{k_1}\right)$. From the fitted fsTA TIPS-Tc singlet decay rates we find, $k_1 = 14.1 \pm 0.8\, ns^{-1}$ and $k_2 = 12.8 \pm 1.0\, ns^{-1}$. Therefore, the efficiency of SET in a solution of TIPS-Tc (200 mg/mL) and PbS-TET-CA (50 mg/mL) is $\eta_{SET} = -0.10 \pm 0.15$. This indicates an upper bound on singlet exciton transfer efficiency from the initially excited TIPS-Tc singlet to the PbS-TET-CA QDs at 5%.

The indication of a negligible single exciton transfer efficiency is corroborated by the observation that no spectral features could be assigned to changes in the population of excited QD states. PbS QD excited states result in broad PIA features in the 550-950 nm range.[137] As we see no significant growth of these QD features in the first 2 ns after

photoexcitation, any excited state population in the QDs within this time period is a result of direct photoexcitation. In summary, the transfer that has been observed in steady-state experiments is not the result of singlet exciton transfer but, as the most reasonable alternative, triplet exciton transfer on timescales greater than 2 ns.

4.4.3 Nanosecond Transient Absorption

To investigate the full decay dynamics of the excited states in TIPS-Tc and PbS-TET-CA, nanosecond transient absorption (nsTA) spectra were measured. We begin our discussion of the solution-phase singlet fission multiplication dynamics by probing the components individually. First, we characterise the nanosecond dynamics of the singlet fission material TIPS-Tc. The TIPS-Tc system has been studied previously and the fission dynamics investigated, allowing identification of the nsTA spectral components with ease. We build upon this previous work by quantifying the triplet decay dynamics.

4.4.3.1 TIPS-Tc Fluence Dependence

After femtosecond pulse excitation at 535 nm, of solutions of concentrated pristine TIPS-Tc, we observe long-lived (>10 μs) triplet excitons as identified by the triplet PIA features (Figure 4.13a), which is consistent with previous literature.[123] We identify the TIPS-Tc triplet excitons by the two photoinduced absorption (PIA) peaks at 840-850 and 960-970 nm.[66,123] Additionally, we identify a broad PIA feature across the probe range, identified as an excimer state, decaying within 10 ns.[66,123] The decay of TIPS-Tc triplets display significant fluence dependence, indicating bi-molecular recombination as a significant decay channel for the excited triplet states (Figure 4.13b).

To accurately identify the transfer of triplet excitons from the TIPS-Tc to the PbS-TET-CA QDs we seek a kinetic model to describe the triplet decay in TIPS-Tc alone. The decay of TIPS-Tc triplet density after generation by singlet fission can be expressed as[57]

$$\frac{d[T]}{dt} = -k_1[T] - k_2[T]^2 \,. \tag{4.13}$$

The strength of the measured TIPS-Tc triplet photo induced absorption at 840-850 nm is proportional to the total number of triplets present, $\frac{\Delta T}{T} \propto \int_V [T]\, dV$. We assume a uniform triplet density in the volume of integration described by the area and penetration depth of the pump beam. This assumption leads to a linear relationship

between the measured triplet PIA strength and the TIPS-Tc triplet density, $\frac{\Delta T}{T} = \chi[T]$. Thus, we find

$$\frac{d(\Delta T/T)}{dt} = -k_1(\Delta T/T) - k'_2(\Delta T/T)^2 ,$$

(4.14)

where $k'_2 = k_2/\chi$. We find χ by measurement of the pump beam area and power, singlet fission yield (135%), and absorbance of TIPS-Tc (giving the 535 nm laser penetration depth). The analytical solution to this differential equation is

$$\left(\frac{\Delta T}{T}\right)(t) = \left(\frac{\Delta T}{T}\right)_0 \frac{1-\beta}{\exp(k_1 t) - \beta},$$

(4.15)

with $\beta = \alpha/(k_1 + \alpha)$, and $\alpha = k'_2\left(\frac{\Delta T}{T}\right)_0$. Globally fitting this analytical function to multiple triplet decay kinetics at a range of fluences allows determination of the mono and bi-molecular decay rates (Figure 4.13 and Table 7.2). From the decay rates the fraction of triplets that decay mono-molecularly, f_1, and bi-molecularly, f_2, can be found using the following,[57]

$$f_1 = \frac{\beta - 1}{\beta}\ln(1-\beta) ,$$

(4.16)

$$f_2 = 1 - f_1 = 1 - \frac{\beta - 1}{\beta}\ln(1-\beta) .$$

(4.17)

We find that at the pump fluences achievable in this nsTA experiment, the fraction of triplet decaying bi-molecularly is between 0.5 – 1, within uncertainty (Table 7.2). Most triplets are decaying bi-molecularly even at the lowest measurable fluences.

Global fitting of multiple nsTA kinetics (at varying laser fluences) with equation (4.15), following previously reported methods for fitting triplet decay dynamics, allows extraction of monomolecular and bi-molecular triplet decay rates of 5.6 ± 5.1 $(ms)^{-1}$ and (7.6 ± 0.3) x 10^{-23} cm^3ns^{-1}, respectively (Table 7.2).[145]

The significant uncertainty on the mono-molecular decay rate indicates that we have not fully resolved the intrinsic decay of the triplet states. Given the uncertainty in the extracted values, comparison of the decay rate shows at most 40% of triplets decay

mono-molecularly at the lowest laser fluence used (21 µJ/cm^2), the rest decaying via bi-molecular channels.

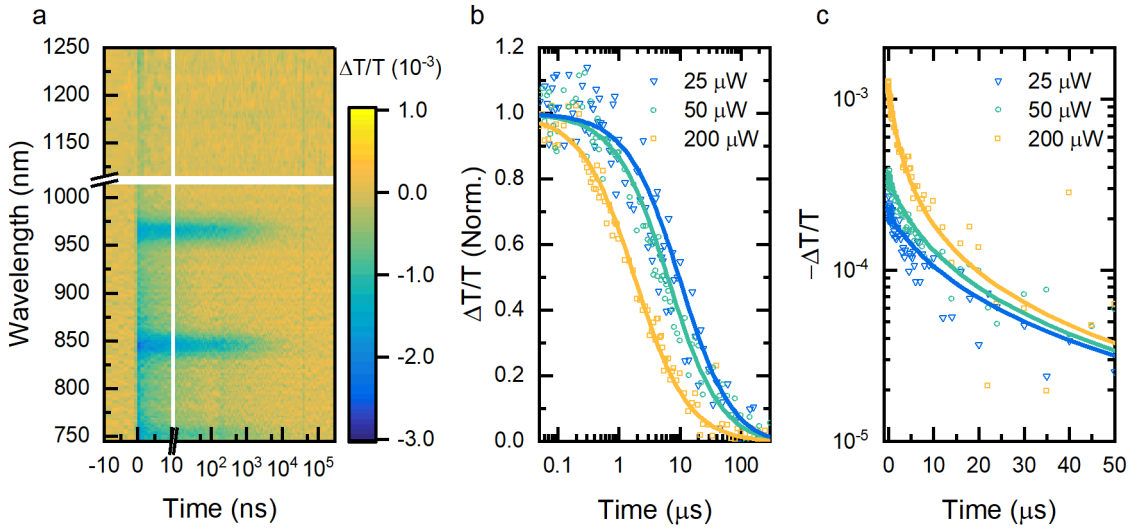

Figure 4.13: Triplet bi-molecular decay for TIPS-Tc in solution.
a) Nanosecond transient absorption map of ~100 µm thick TIPS-Tc solution (200 mg/mL). The sample was excited with a 168 µJ/cm^2 pulse centred at 535 nm. The normalised (b) and raw (c) nsTA signal strength at 840-850 nm for fluences from 25-200 µW (21-168 µJ/cm^2). Kinetics were fitted globally with an analytical function for a bi-molecular decay process. Reproduced with permission from the ACS publications.[122]

4.4.3.2 QD Transient Absorption

Following the study of TIPS-Tc, we investigate the PbS-OA and PbS-TET-CA QD dynamics on their own. After excitation at 535 nm of either QD, we observe nsTA features with microsecond lifetimes (Figure 4.14). Characteristic of PbS QDs of the particular bandgap used in this work, we detect a positive signal at 950-1200 nm, which is assigned to a ground state bleach (GSB) from QD excited states.[94] The excitonic excited state has photoinduced absorption features from 700-950 nm.

The time constant extracted by global fitting for the decay of the PbS-TET-CA GSB is 1900 ± 40 ns, in agreement with the IR TCSPC measurement for the IR photoluminescence lifetime of PbS-TET-CA. In comparison to the PbS-OA QDs, we observe an additional species upon excitation at 535 nm for the PbS-TET-CA QDs, identified by the time variation of the area normalised spectra. The time constant of 68 ± 5 ns is extracted for this additional PIA feature, when exciting PbS-TET-CA at 535 nm.

We assign this PIA present to excitations on the TET-CA ligand because of direct excitation from the pump pulse.

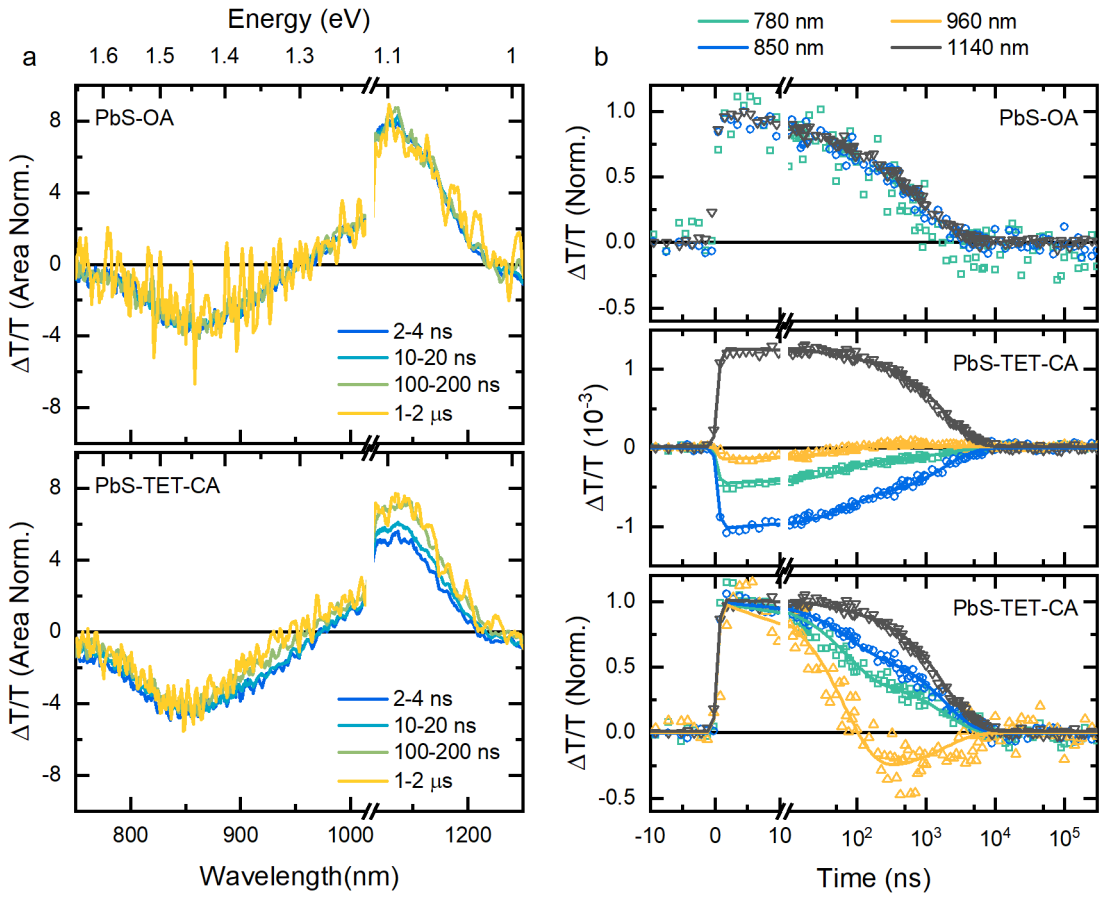

Figure 4.14: nsTA of PbS-OA and PbS-TET-CA QDs in solution.
a) Average nanosecond transient absorption spectra for ~100 micron thick PbS-OA and PbS-TET-CA solutions (10 mg/mL). The samples were excited with a 42 μJ/cm² pulse centred at 535 nm. b) Corresponding transient absorption kinetics across the probe range. The PbS-TET-CA kinetics were fitted with bi-exponential functions. Reproduced with permission from the ACS publications.[122]

4.4.3.3 QD Concentration Dependence

Having characterised the individual components, we sequentially investigated the transition from pure TIPS-Tc to a solution with a significantly high concentration of PbS-TET-CA QDs. From this, we detail the effects of the PbS-TET-CA concentration on the triplet harvesting dynamics. As we have already shown that PbS-OA QDs do not allow triplet transfer from TIPS-Tc, we limit the scope of the current nsTA investigation into

the TIPS-Tc:PbS-OA solutions to a small number of benchmark measurements. For these TIPS-Tc:PbS QD solutions, after femtosecond pulse excitation at 535 nm, we observe initial nsTA spectra that contain both TIPS-Tc triplet and excited state QD features in the NIR probe region (750-1250 nm) (Figures 4.18 and 4.19). In the presence of either PbS-OA or PbS-TET-CA at QD concentrations from 0 - 100 mg/mL, we observe no effect on the generation of triplets via singlet fission in TIPS-Tc, evident by the similar initial nsTA intensity of the triplet PIA features at 850 and 980 nm. Most notably, on the addition of more concentrated PbS QDs, a positive signal at 950-1200 nm (present from early times) increases in magnitude. We assign this feature to the combination of photoexcited and triplet transfer induced QD states leading to a GSB of the QD. The early time strength of this signal increases with QD concentration due to the increasing fraction of 535 nm pump photons absorbed by the QDs.

For both QDs types, at early times the negative nsTA feature corresponding to the TIPS-Tc excimer PIA overlaps with the GSB and PIA of the QDs (Figure 4.15a). The decay of this negative feature produces an apparent rise in the positive QD GSB signals which overlap in the 1140-1160 nm region (Figure 4.15b). This rise in signal is thus not associated with a change in QD population. At 10 ns after photoexcitation, the PbS-OA and PbS-TET-CA GSB signals are of similar intensities, indicating similar initial populations of excited QDs in both systems. We assign this initial TA signal to the fraction of photons that directly excite the QDs with the 535 nm pump pulse. After the initial direct excitation of the PbS-OA QDs, we observe a decay in the excited QD signal characterised by a 1.8 ± 0.1 µs decay constant. In comparison, the solution with PbS-TET-CA QDs (100 mg/mL) shows a significantly longer 5.1 ± 0.2 µs decay constant for the QDs. It is longer than its intrinsic 1.90 ± 0.05 µs lifetime (Figure 4.14). The increase in time constant is consistent with delayed triplet transfer to the QDs and is thus consistent with the obtained TrPL data. Comparison of the transient absorption kinetics of the TIPS-Tc triplet PIA at 840-850 nm, in solutions by itself, along with PbS-OA and PbS-TET-CA QDs, allows insights of the triplet harvesting dynamics. The key features to note are the reduced lifetime of the TIPS-Tc triplet due to quenching from the PbS-TET-CA QDs.

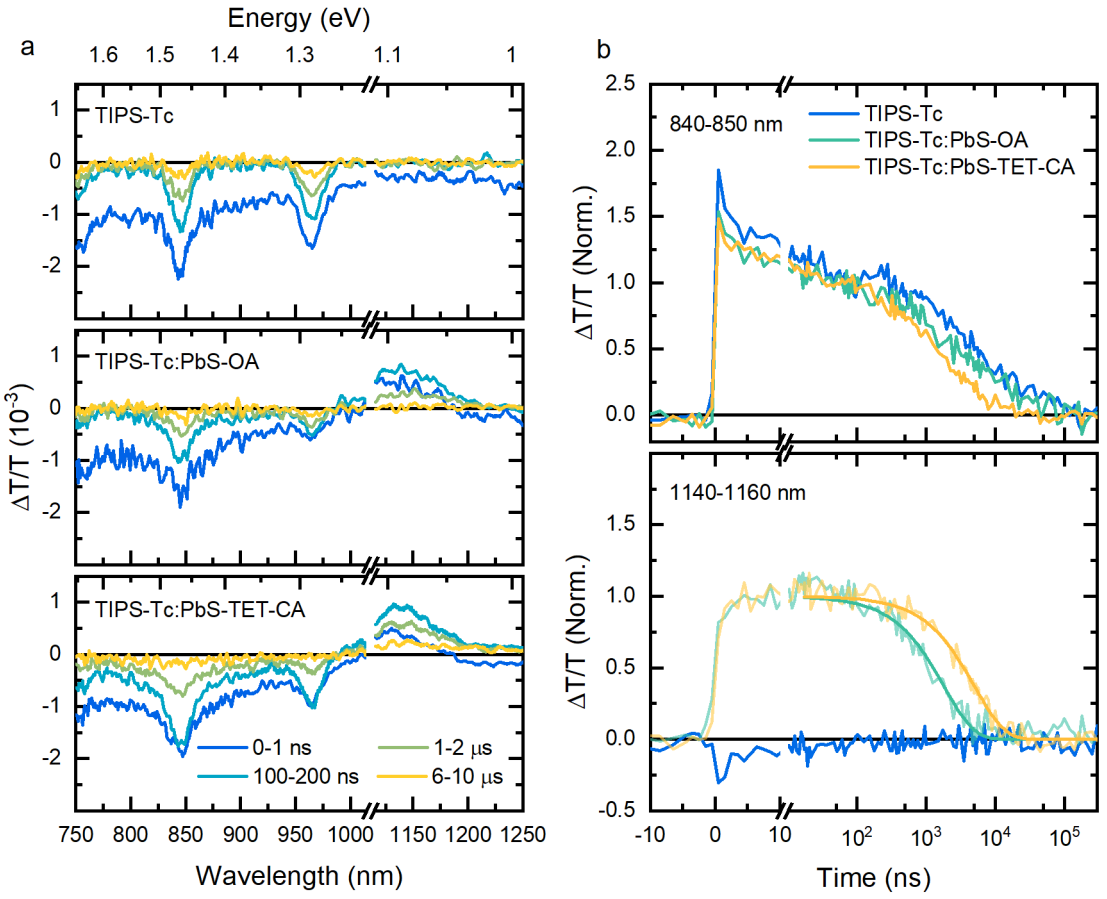

Figure 4.15: nsTA spectra and kinetics for TIPS-Tc:QD solutions.
a) Average nanosecond transient absorption spectra for ~100 micron thick TIPS-Tc (200 mg/mL), PbS-OA (100 mg/mL) with TIPS-Tc (200 mg/mL) and PbS-TET-CA (100 mg/mL) with TIPS-Tc (200 mg/mL) solutions. The samples were excited with a 168 µJ/cm^2 pulse centred at 535 nm. b) Normalised nsTA kinetics under 535 nm excitation (40 µJ/cm^2), at the TIPS-Tc triplet PIA (840-850 nm) and the PbS QD GSB (1140-1160 nm). The QD GSB signals have been fitted with a mono-exponential decay. The PbS-OA and PbS-TET-CA QDs are found to decay with a 1.8 ± 0.1 and 5.1 ± 0.2 µs decay constant, respectively. The 1140-1160 nm kinetic for TIPS-Tc has been scaled by the same normalised factor as for TIPS-Tc:PbS-TET-CA . Reproduced with permission from the ACS publications.[122]

4.4.3.4 Removal of Initial QD Population

To clarify the transfer of the TIPS-Tc triplets to the PbS-TET-CA QDs, nsTA difference maps were calculated.[146] In the following, we detail how the nsTA difference maps for the TIPS-Tc:PbS-TET-CA blends were calculated.

The difference nsTA maps contain information about excited QDs resulting from transfer, without contribution from directly excited PbS-TET-CA QDs. For example, Figure 4.16b shows the averaged spectra for PbS-TET-CA (10 mg/mL) and PbS-TET-CA (100 mg/mL) with TIPS-Tc (200 mg/mL), over the time range 100-200 ns normalised to the QD's GSB strength. Here it is clear that the difference between the two spectra can be assigned to the additional TIPS-Tc triplet PIA peaks at ~850 and ~960 nm in the TIPS-Tc:PbS-TET-CA solution. This overlay illustrates that the spectra of the SF-PM solution can be decomposed into its individual components. Extending this to include the individual component's kinetics allows the illumination of the differences resulting from triplet exciton transfer.

Earlier we showed that there is no transfer to the QDs within the first 2 ns. Here we extend that range to claim that there is no significant difference in the QD dynamics within the first 100 ns with or without the TIPS-Tc present (Figure 4.16a). Therefore, the initial TA signals showing QD features before 100 ns are due to direct photoexcitation.

We take the difference of the transient absorption maps for the TIPS-Tc:PbS_TET-CA mixtures relative to the PbS-TET-CA QDs on their own. We assume that any QD GSB that is present initially (but after the singlet PIA in the same region has decayed) is due to direct excitation from the 535 nm pump. Thus, their transient absorption map will be identical to that of PbS-TET-CA on its own under 535 nm excitation, and can therefore be removed from the transient absorption data of interest. To find this initial population of QDs that are directly excited we take the QD GSB kinetics averaged in the region 1120-1160 nm for the QDs on their own and scale it such that the value in the time range 20-40 ns agrees with the GSB signal in the mixtures (Figure 4.16a). This method assumes that no excitations are transferred before 20 ns. This can be justified since the triplet signatures do not decay significantly within 100 ns and so no significant amount of triplet excitons could have transferred before this time (Figure 4.16b).

Figure 4.16c shows the obtained scaling factors, indicative of the relative initial QD excited state population, as a function of the PbS-TET-CA QD concentration. The proportion of incident photons in the pump beam (535 nm), absorbed by the QDs, increases with the QD concentration as it becomes the dominate absorbing species. It will then reach a saturation point where there is no more photons for the QDs to absorb. The observed trend in initial QD excited state population is consistent with the increased fractional absorption of QDs.

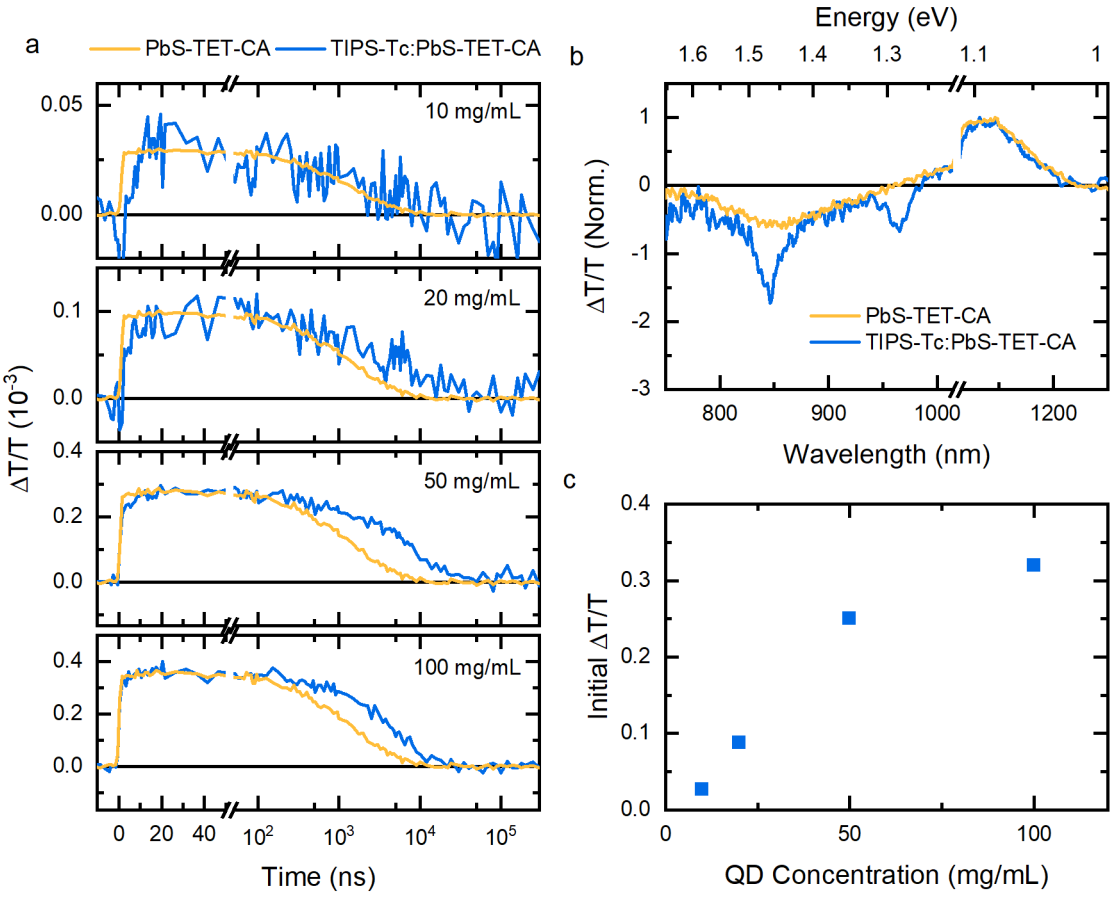

Figure 4.16: Removal of directly photoexcited QD populations.
a) Nanosecond transient absorption kinetics at 1140-1160 nm for solutions of TIPS-Tc (200 mg/mL) and PbS-TET-CA at varying concentrations under 42 µJ/cm² 535 nm excitation (black curves). Subsequently, the 1140-1160 nm kinetic for PbS-TET-CA alone (10 mg/mL), under the same excitation, is scaled such that they overlap during the time period 20-40 ns. b) Corresponding nanosecond transient absorption spectra for PbS-TET-CA (10 mg/mL) and PbS-TET-CA (100 mg/mL) with TIPS-Tc (200 mg/mL), averaged over 100-200 ns and normalised to the QD's GSB strength. The difference between the two spectra matches the spectral features of the TIPS-Tc triplet spectrum, indicating that at this time the only species present are the excited QD state and the TIPS-Tc triplet state. c) The scaling factors used to overlay the initial PbS-TET-CA GSB signal with the signal present in the solution SF-PM samples. Reproduced with permission from the ACS publications.[122]

The process of removing the nsTA components that correspond to the photoexcited QD states, clarifies the triplet harvesting dynamics. On inspection of the nsTA difference kinetics shown in Figure 4.17, the loss of the TIPS-Tc triplets correspond to a rise in the QD GSB. The strength of the QD GSB that grows in after 100 ns is seen to increase with the concentration of the QDs, consistent with a Stern-Volmer like transfer dynamics.

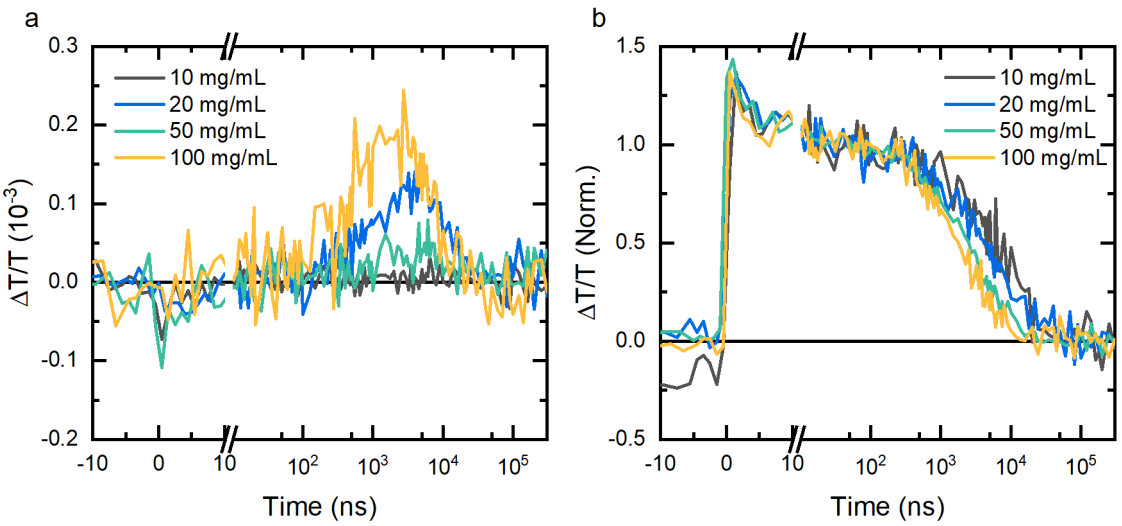

Figure 4.17: nsTA difference kinetics for TIPS-Tc:PbS-TET-CA solutions.
nsTA difference kinetics at the PbS QD GSB, 1140-1160 nm (a) and TIPS-Tc triplet PIA 860-850 nm (b) (relative PbS-TET-CA QDs) for solutions of concentrated TIPS-Tc (200 mg/mL), with varying concentrations of PbS-TET-CA QDs (10-100 mg/mL), with a 535 nm pump at 42 μJ/cm². Reproduced with permission from the ACS publications.[122]

4.4.3.5 Triplet Exciton Transfer

Quantifying the triplet transfer dynamics requires a means of extracting a triplet exciton population from the nsTA difference maps, a challenging process due to the multiple overlapping spectral features. Using linear regression, the kinetics of the TIPS-Tc triplet were isolated from the signatures of the other species, for the TIPS-Tc:PbSTET-CA solutions. Isolating the triplet dynamics requires reference spectra for the TIPS-Tc triplet, TIPS-Tc excimer and the PbS QD excited state. The TIPS-Tc triplet spectrum was taken as the nsTA spectrum at 1 μs after excitation of a solution of purely concentrated TIPS-Tc. This triplet spectrum was used as a reference in the genetic algorithm of the TIPS-Tc nsTA map and the fitted remaining spectral component assigned to the TIPS-Tc excimer spectrum. The spectrum for the PbS-TET-CA excited QD state was referenced as the spectrum measured 400 ns after photoexcitation of a solution of PbS-TET-CA under 535 nm excitation. These reference spectra, shown in Figure 4.18a, are used to reconstruct the observed nsTA difference maps via linear regression, solving for the kinetics associated with these spectra. The kinetic for the TIPS-Tc triplet population show a clear lifetime quenching with increased QD concentration (Figure 4.18b).

Subsequently, we use the following kinetic model to describe the transfer of triplets from the TIPS-Tc to the PbS-TET-CA QDs

$$\frac{dT_1}{dt} = -k_1 T_1 - k_2 T_1^2 \,,$$

(4.18)

where T_1 is the triplet density produced via singlet fission with an efficiency η_{SF}. k_1 and k_2 are the mono-molecular and bi-molecular decay rate for TIPS-Tc triplets. We approximate the triplet bi-molecular decay rate as constant with respect to changes in the QD concentration. This relies on the QDs having little effect on the volume which the triplets occupy and the triplet diffusion constant. Using the bimolecular triplet decay rate obtained for pristine TIPS-Tc as a fixed input parameter, we fit equation (4.15), an analytical solution for the 2nd order rate equation (Figure 4.18b), and extract the mono-molecular decay rate as a function of PbS-TET-CA QD concentration (Figure 4.18c). We find a reasonable agreement with a linear relationship between the triplet mono-molecular decay rate and QD acceptor consistent with Stern-Volmer quenching. This suggests fitting of the following function

$$k_1 = k_T + \gamma_{TET} X_0 \,,$$

(4.19)

where X_0 is the density of excited QD states, k_T is the intrinsic decay rate for TIPS-Tc triplet and γ_{TET} is the bi-molecular triplet transfer rate to the PbS-TET-CA QDs. We assume that the concentration of QDs in the ground state is equivalent to the concentration of QDs in this case as we are in a low excitation regime. Applying this Stern-Volmer-like quenching model, we extract a bi-molecular triplet transfer rate of γ_{TET} = 0.0039 ± 0.0001 $(mg/mL)^{-1}\mu s^{-1}$ ($5.1 \times 10^8 \pm 0.1 \times 10^8$ $M^{-1}s^{-1}$) and an intrinsic triplet lifetime of τ_T = 250 ± 180 µs.[145]

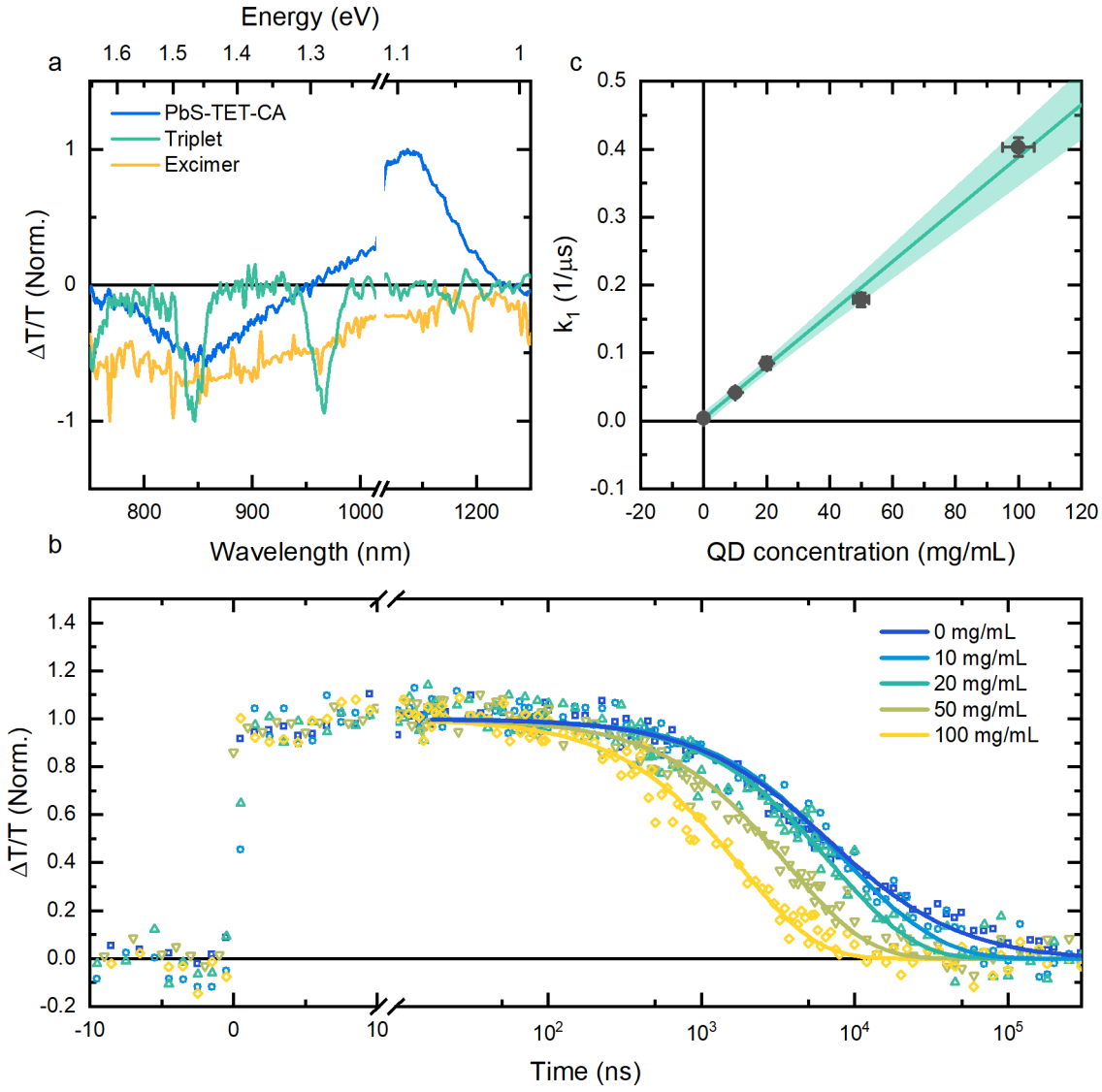

Figure 4.18: Parameterising triplet transfer in TIPS-Tc:PbS-TET-CA solutions.
a) Normalised nanosecond transient absorption spectra used to deconvolve the TIPS-Tc with PbS-TET-CA nanosecond transient absorbed difference maps. The PbS-TET-CA spectrum (blue) is its spectrum 100-200 ns after 535 nm excitation. The excimer (orange) and triplet (green) spectra were obtained using the genetic algorithm on nanosecond transient absorption of TIPS-Tc (200 mg/mL) under 535 nm pulsed excitation. b) Normalised TIPS-Tc triplet spectral component found from deconvolution via linear regression of the corresponding nsTA difference map, for a variety of PbS-TET-CA QD concentrations from 0 to 100 mg/mL, 42 μJ/cm^2 excitation. Triplet decay kinetics were fitted globally with (4.15). The bi-molecular decay rate was fixed as the value obtained for TIPS-Tc on its own. c) The fitted mono-molecular TIPS-Tc triplet decay rate as a function of PbS-TET-CA QD concentration (black dots), with error bars representing 95% confidence bounds from the fitting of the triplet decay kinetics. Linear fit (green line).

From previous diffusivity measurements and estimates of the interaction distance and the molar mass of the QD, we predict a bi-molecular transfer rate of 0.085 $(mg/mL)^{-1}\,\mu s^{-1}$, which is higher than the 0.0039 ± 0.0001 $(mg/mL)^{-1}\,\mu s^{-1}$ ($5.1x10^8 \pm 0.1x10^8\ M^{-1}\,s^{-1}$) obtained from the quenching of the triplet PIA. However, the data were well described by a Stern-Volmer-like quenching. This discrepancy of measured and estimated transfer rate indicates that not every collision between a triplet exciton on a TIPS-Tc molecule and the surface of the PbS-TET-CA QD results in a successful triplet transfer event. Possible explanations include non-uniform coverage of the TET-CA ligand over the surface of the PbS QD or residual OA ligands inducing steric hindrance. We expand on this in Section 4.6 by including a finite triplet transfer velocity from the TIPS-Tc triplet state to the PbS-TET-CA QDs.

Figure 4.19 shows the key triplet decay parameters extracted from the fitting of the TIPS-Tc triplet dynamics for the various individual TIPS-Tc:PbS-TET-CA solutions. For comparison, we show the predicted triplet decay parameters based on the extracted bi-molecular triplet transfer rate of 0.0039 ± 0.0001 $(mg/mL)^{-1}\mu s^{-1}$. We observe a decrease in the proportion of TIPS-Tc triplets decaying via bi-molecular channels, f_2, as the PbS-TET-CA QD concentration increases. This corresponds to an increased proportion of triplets decaying via mono-molecular channels, f_1, due to higher rates of triplet quenching resultant from triplet transfer.

The branching ratio $k_{TET}/(k_{TET} + k_T)$ quantifies the triplet transfer efficiency in the low fluence regime where bi-molecular triplet decay is non-existent (Figure 4.19c). Here we see at concentrations as low as 10 mg/mL, there is greater than 90% triplet transfer (within uncertainty) to the PbS-TET-CA QDs. For the 50 mg/mL solution of PbS-TET-CA QDs we calculate a triplet exciton transfer efficiency of $\eta_{TET} = 95\ \pm 5\ \%$, approaching 100% at higher QD concentration (Figure 4.19).

However, even at the lowest fluence measured, triplet extraction in the transient measurements is reduced due to the bi-molecular decay of TIPS-Tc triplet excitons. At the finite fluence used for the transient absorption measurements of 42 $\mu J/cm^2$, the transfer efficiency must be corrected by the mono-molecular decay fraction, f_1 (Figure 4.19d). At this fluence, the lowest obtainable within experimental limitations, the transient triplet transfer efficiency is capped at ~80%. From the simulation of the expected transient triplet transfer efficiency using the extracted triplet kinetic parameters k_T, γ_{TET} and k_2, at lower measurement fluences we would expect to see the triplet transfer efficiency rise and approach the low fluence regime's value.

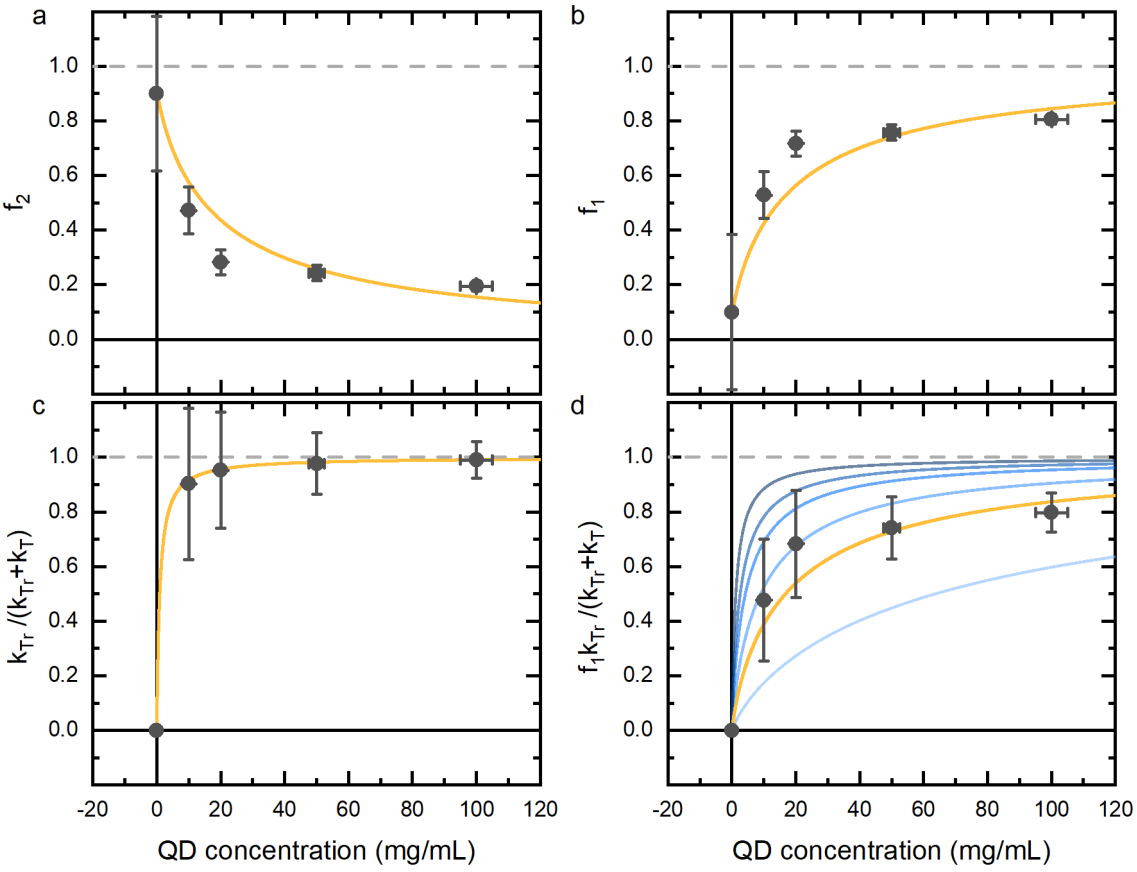

Figure 4.19: Investigation of the nsTA fitting parameters for TIPS-Tc:PbS-TET-CA solutions. Fitting is achieved for the TIPS-Tc triplet PIA (840-850 nm) of TIPS-Tc (200 mg/mL) and varying concentrations of PbS-TET-CA QDs (0-100 mg/mL), excited at 535 nm with 42 µJ/cm^2 (50 µW). (black circles) The fraction of TIPS-Tc triplet excitons that decay bi-molecularly (a), mono-molecularly (b), mono-molecular branching ratio (c) and the fraction of triplet excitons that are quenched by transfer to the PbS-TET-CA QDs (d), as functions of PbS-TET-CA QD concentration. Error bars are calculated via propagation of uncertainties arising from the 95% confidence bounds for the fitted parameters. From the bi-molecular TIPS-Tc triplet and PbS-TET-CA QD transfer rate, 0.0039 ± 0.0001 (mg/mL)$^{-1}$µs^{-1}, we calculate the same parameters in a-d, as continuous functions of the QD concentration, for the pump power used in the nanosecond transient absorption experiment (50 µW) (red lines). Using the obtained triplet transfer and decay parameters we simulate the fraction of triplet excitons that are quenched by transfer to the PbS-TET-CA QDs as functions of PbS-TET-CA QD concentration, for pump powers 1, 5, 10, 25, 200 µW (dark to light blue lines). Transient absorption signals at these lower pump powers are beyond our current experimentally reachable signal-to-noise. At simulated, low pump powers, the fraction of triplets transferred to the PbS-TET-CA QDs trends to 100%, for a QD concentration of 50 mg/mL. Reproduced with permission from the ACS publications.[122]

4.4.3.6 Simulation of Quantum Dot Dynamics

From the obtained TIPS-Tc triplet transfer and decay parameters, along with the intrinsic PbS-TET-CA QD excited-state lifetime, we have all parameters for the differential equations that describe the triplet and QD time-dependent populations after singlet fission:

$$\frac{dT_1}{dt} = -(k_T + k_{TET}X_0)T_1 - k_2T_1^2 \,, \tag{4.20}$$

$$\frac{dX_1}{dt} = k_{TET}X_0T_1 - k_XX_1 \,. \tag{4.21}$$

The equation for the triplet population has an analytical solution as described earlier. The solution for $T_1(t)$ can be substituted into the differential equation for the QD population (4.21). There exists an analytical solution to the aforementioned differential equation in terms of hypergeometric functions. However, to avoid the complexities of dealing with these intricate functions, we solve for the time-dependent QD population using numerical techniques. To illustrate the effect of bi-molecular TIPS-Tc triplet decay we simulate the triplet and QD populations with and without bi-molecular decay (Figure 4.20 a and b). Comparison of the simulated triplet dynamics illustrates how influential the bi-molecular decay of triplets is on the resulting kinetics. It begs the question, how effective is the measurement at detecting the triplet transfer? In particular, what is the reduction in sensitivity to the PbS QD excited state population due to the bi-molecular decay of triplet exciton under the current measurement conditions? To quantify this, we calculate the simulated QD excited state population due to transfer with and without triplet bi-molecular decay (Figure 4.20c). The subtle reduction in the QD excited state population because of triplet bi-molecular decay indicates that in this case there would be little to gain by arduously measuring the system at lower fluences.

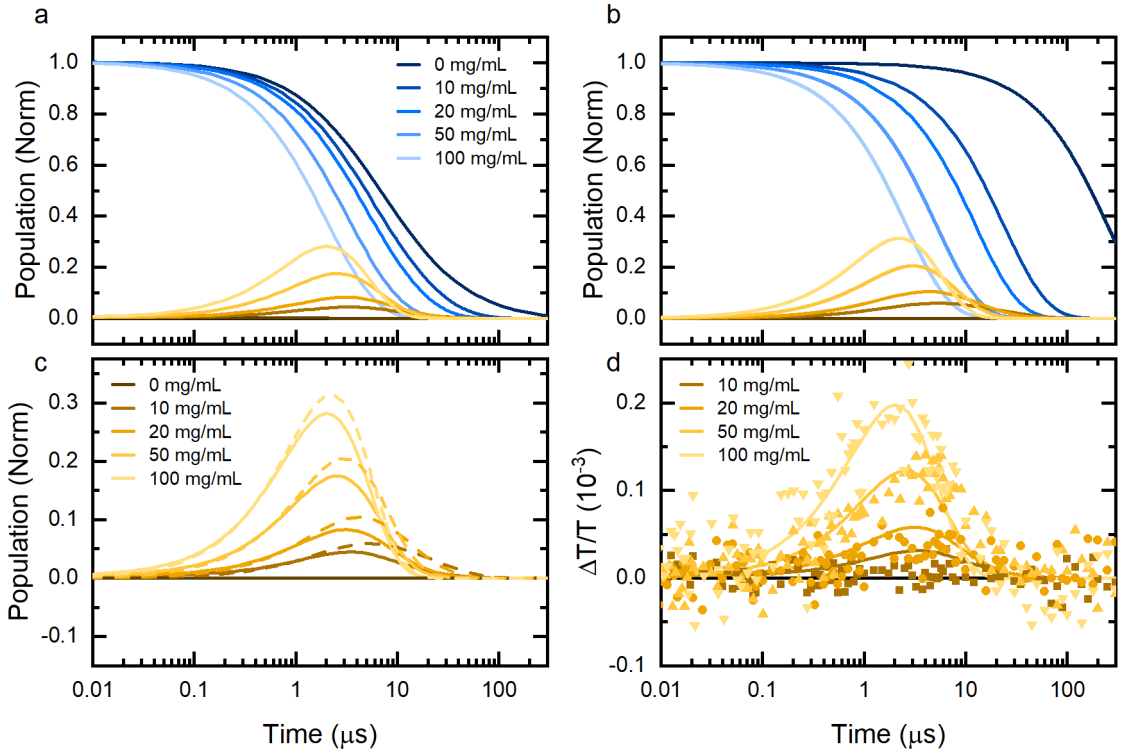

Figure 4.20: Comparison of QD excited state population resulting from transfer. Simulation of the triplet (blue) and QD populations (orange) with and without bi-molecular decay (a and b) for the varying concentration of PbS-TET-CA QDs. Simulated populations are calculated using the experimentally obtained kinetic parameters and excitation of 535 nm 42 μJ/cm². c) Comparison of the predicted QD population with (solid lines) and without (dashed lines) triplet bi-molecular decay. d) Predicted QD populations (with all parameters included) scaled to overlay with the measured nanosecond transient absorption difference kinetics at the PbS-TET-CA QD GSB (1140-1160 nm). Reproduced with permission from the ACS publications.[122]

We measure the fluence dependence for the TIPS-Tc:PbS-TET-CA (200:100 mg/mL) system to confirm consistency of the obtained kinetic model. As expected, a higher pump fluence results in a higher QD population, along with a faster triplet decay due to increased bi-molecular decay (Figure 4.21 a and b). Simulated QD population dynamics for the 200 μW pump power relative to the lower 50 μW pump power is in reasonable agreement with the observed dot GSB dynamics (Figure 4.21c). However, the simulated triplet population for the 200 μW kinetic does not decay as rapidly as the measured TA kinetic, which could indicate that the TIPS-Tc triplet bi-molecular recombination rate is higher in samples with high QD loading compared to TIPS-Tc on its own. We leave this effect to future work for investigation.

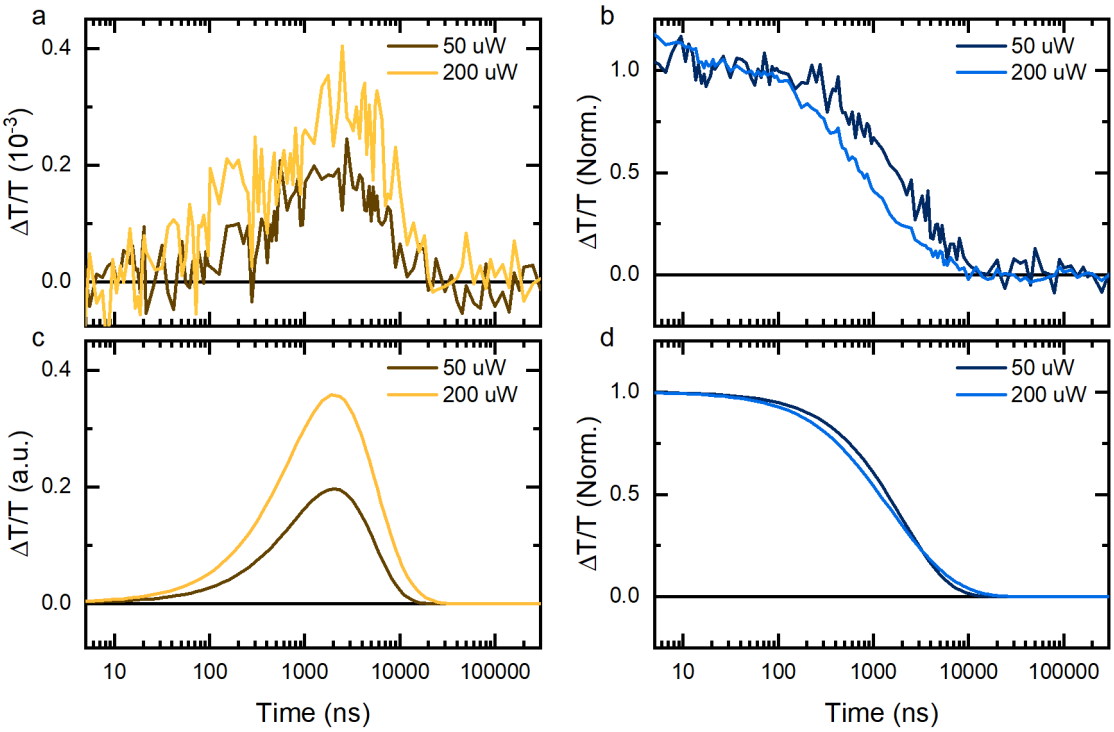

Figure 4.21: Fluence dependence of triplet transfer dynamics in TIPS-Tc:PbS-TET-CA solutions. Difference kinetics for (a) the PbS-TET-CA QD GSB (1140-1160 nm) and (b) TIPS-Tc triplet PIA (840-850 nm) for TIPS-Tc (200 mg/mL) with PbS-TET-CA (100 mg/mL) excited at 42 (black) and 168 (red) μJ/cm^2. The corresponding simulated QD (c) and triplet (d) populations. Reproduced with permission from the ACS publications.[122]

In summary, we observed triplet transfer dynamics where:

- The loss of TIPS-Tc triplet excitons corresponds with a rise in PbS QD excited state population. This is consistent with transfer from the TIPS-Tc triplet exciton to the PbS-TET-CA QDs.
- The strength of the QD GSB that grows in after 100 ns and the rate of TIPS-Tc triplet exciton mono-molecular decay is proportional with the concentration of the QDs, consistent with Stern-Volmer quenching.
- Based on the extracted intrinsic PbS-TET-CA QD lifetime and triplet transfer rate, simulated dynamics for the decay of the triplet excitons and the excited state QDs are calculated. Figure 4.22 shows these kinetics are consistent with the TIPS-Tc triplet difference PIA signal and the QD GSB signal (1140-1160 nm).
- Agreement with the two species model described by equations (4.20) and (4.21) suggests that the transfer of triplet excitons from the TET-CA molecules into the

QD is not rate-limiting. However, this step should still be seen as critically important for the transfer process.

Unexpectedly the nsTA data suggest that triplet exciton transfer in TIPS-Tc:PbS-TET-CA solutions is significantly hindered by bi-molecular decay of the TIPS-Tc triplets, presenting a concern for the versatility of this SF-PM to operate in real-world conditions under solar irradiance.

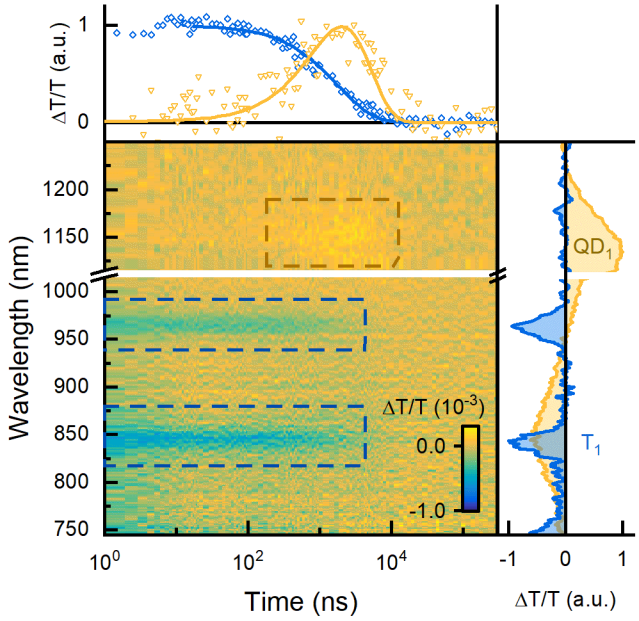

Figure 4.22: Summary of pump-probe spectroscopy for TIPS-Tc:PbS-TET-CA solutions. nsTA difference map for a solution of TIPS-Tc (200mg/mL) and PbS-TET-CA QDs (100 mg/mL), under 535 nm 40 μJ/cm² excitation. The PbS-TET-CA and TIPS-Tc triplet TA spectra used for decomposition by linear regression are shown (right inset). The strengths of TIPS-Tc triplet PIA signal (from linear regression) and the PbS-TET-CA QD GSB (1140-1160 nm) are shown with an overlaid simulation of the population (top inset). Reproduced with permission from the ACS publications.[122]

4.5 Steady-State Operation

Now that we have characterised the triplet harvesting dynamics in the TIPS-Tc:PbS-TET-CA solutions, we return our focus to the steady-state operation of this SF-PM system. In particular, we investigate the effect that triplet bimolecular decay in the SF material has

on performance under “real world” conditions. With the knowledge that the triplet exciton transfer efficiency is fluence dependent, we begin this section by calculating the fraction of the AM1.5G spectrum that TIPS-Tc can absorb. AM1.5G is a commonly used solar reference spectrum for the testing and certification of PV cells;it is a reasonable standard for the expected “real world” conditions that a SF-PM will face.

In the absence of using a solar simulation lamp, we take the publicly available spectral data and calculate the equivalent photon flux (Figure 4.23b).[109] We assume that an ideal SF-PM will absorb all photons with energy above the SF materials bandgap and none below. By integration of AM1.5G spectrum from 280 nm to 560 nm we find the TIPS-Tc solar-equivalent photon flux is 3.67×10^{20} photons $s^{-1}m^{-2}$. Under 532 nm laser excitation this equates to a fluence of 13700 $\mu W/cm^2$.

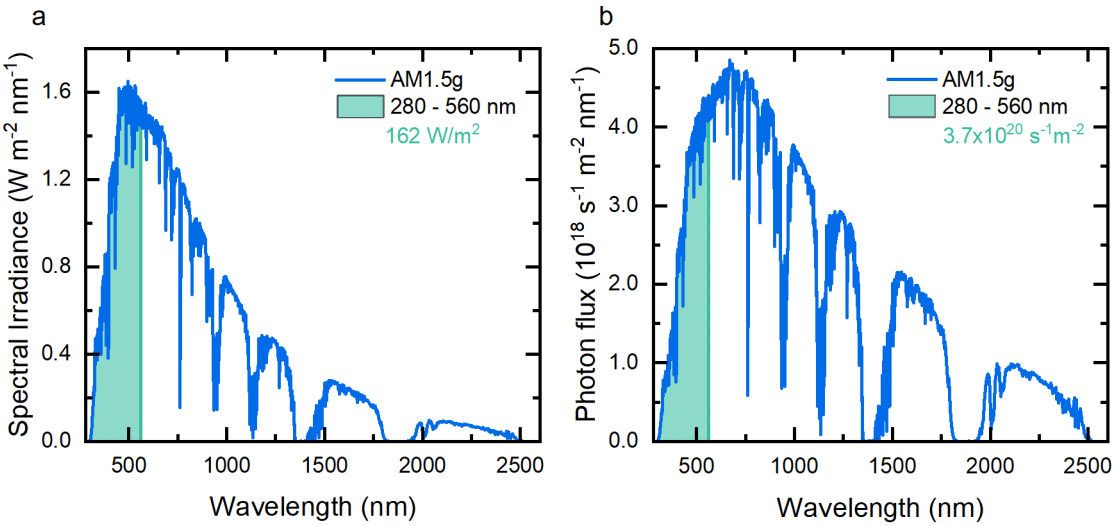

Figure 4.23: Calculation of the available spectral irradiance and photon flux for TIPS-Tc. The light available for absorption includes wavelengths from the far UV (280 nm) to the absorption tail of TIPS-Tc (560 nm). a) The spectral irradiance of the AM1.5g solar spectrum, with the available solar flux calculated by the integration from the range 280 – 560 nm. b) The solar photon flux, with the available photon flux calculated by the integration from the range 280 – 560 nm. Reproduced with permission from the ACS publications.[122]

4.5.1 Steady State Modelling

To understand the implications learnt about the effect triplet bi-molecular decay has on the transient behaviour of triplet harvesting, the kinetic model developed so far is extended to the steady-state. Starting from the differential equation for the triplet population

$$\frac{dT}{dt} = -(k_T + k_{TET})T - k_2T^2 + G \,,$$

(4.22)

where *G* is the rate of triplet generation from singlets undergoing singlet fission, we seek an expression for the triplet exciton transfer efficiency η_{TET}. After rearrangement under steady-state conditions, one arrives at the polynomial

$$k_2T^2 + (k_T + k_{TET})T - G = 0 \,.$$

(4.23)

Solving for positive values of the triplet exciton density, *T,* leads to

$$T = -\frac{k_T + k_{TET}}{2k_2} + \sqrt{\left(\frac{k_T + k_{TET}}{2k_2}\right)^2 + \frac{G}{k_2}}.$$

(4.24)

The triplet transfer efficiency is given by $\eta_{TET} = \frac{k_{TET}T}{G}$ and so substituting the above expression for T gives our desired triplet exciton transfer efficiency

$$\eta_{TET} = \frac{k_{TET}}{G}\left(\sqrt{\left(\frac{k_T + k_{TET}}{2k_2}\right)^2 + \frac{G}{k_2}} - \frac{k_T + k_{TET}}{2k_2}\right).$$

(4.25)

Under steady-state conditions, the rate of IR PL emission from the solution SF-PM can be expressed as $PL_{QD} = \phi G \eta_{TET} \eta_{QD}$. Where ϕ represents the PL collection factor and η_{QD} is the QD photoluminescence quantum efficiency.

4.5.2 Predicted Steady State Efficiency

With the expression (4.25) and the kinetic parameters found from the nsTA analysis, it is possible to predict the TET efficiency for any PbS-TET-CA QD concentration and incident fluence (Figure 4.24). This highlights three key relationships. First, that as the incident fluence increases the TET efficiency significantly drops, approaching zero at high enough fluences. The fluence at which the TET efficiency drops is heavily dependent on the QD concentration. Secondly, that the TET efficiency for the SF-PM solutions with 50 and 100 mg/mL of PbS-TET-CA QDs is effectively maintained up till excitation fluences equal to our benchmark, TIPS-Tc's solar-equivalent fluence. Lastly, we observe that the TET efficiency versus QD concentration relationship is very dependent on the fluence used during the measurements. High fluences effectively push the required QD

concentration for efficient triplet transfer to higher values. The effect of the bi-molecular triplet decay is particularly relevant for the steady-state determination of the SF-PM PLQE values as measured earlier in Section 4.3.3.

The kinetic parameters obtained by nsTA allows calculation of the triplet transfer efficiency, η_{TET}, at the laser fluence used in the IR PLQE measurements. Multiplication of this TET efficiency with a singlet fission yield of η_{SF} = (135 ± 5) % gives the exciton multiplication factor, $\eta_{EMF} = \eta_{SF}\eta_{TET}$, for the system in the case of purely triplet transfer to the QDs. These exciton multiplication factors are consistent with the values measured by the PLQE method.

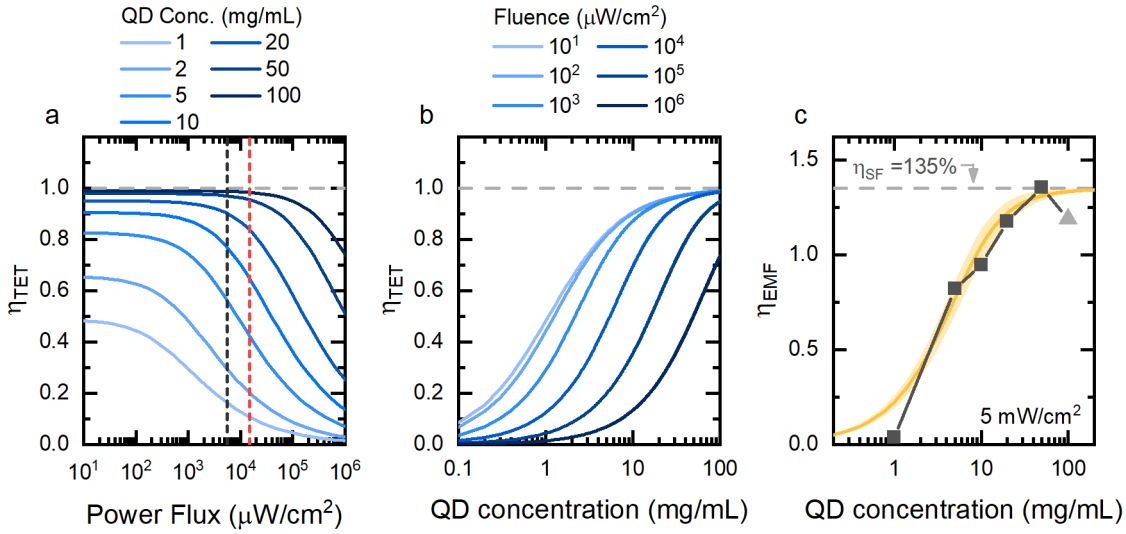

Figure 4.24: Steady-state dependence on fluence and QD concentration for TIPS-Tc solutions. Simulated triplet transfer efficiencies using the equations for the triplet transfer efficiency for various PbS-TET-CA QD concentrations (a) and incident fluences (b). The vertical dashed black line indicates the laser fluence used in the IR PLQE measurements (5 mW/cm²), while the red dashed line indicates the equivalent solar fluences (13.7 mW/cm²). c) Simulated exciton multiplication factor, based on a singlet fission efficiency of $\eta_{SF} = 1.35 \pm 0.05$, at the photon flux used for the IR PLQE measurements, using the extracted triplet transfer and decay rates (orange curve). The shaded region represents the uncertainty in the triplet transfer efficiency based on the propagation of uncertainties form the triplet decay rates. Exciton multiplication factors from the measured PLQE values (black squares), for solutions with varying QD concentrations together with TIPS-Tc (200 mg/mL), under 515 nm 500 μW/cm² excitation. The values for 100 mg/mL QD concentration have been highlighted as outliers due to self-absorption losses. The horizontal grey dashed line indicates the point at which 135% exciton multiplication factor occurs. Reproduced with permission from the ACS publications.[122]

At this point, we look to understand triplet harvesting in the extreme fluence regimes and investigate the appropriate metrics to quantify SF-PM performance. The expression

(4.25) for the triplet transfer efficiency, can be approximated in the regimes of low and high triplet generation rate as follows. In the low fluence regime, where $G \ll \frac{(k_T+k_{TET})^2}{k_2}$, the IR PL from triplet transfer tends to the function

$$PL_{QD} = \phi\eta_{QD}\frac{k_{TET}}{k_T + k_{TET}}G\,.$$

(4.26)

Here the QD PL rate is linear with the triplet generation rate. At high incident fluences, corresponding to triplet generation rates $G \gg \frac{(k_T+k_{TET})^2}{k_2}$, the IR PL trends to

$$PL_{QD} = \phi\eta_{QD}k_{TET}\sqrt{\frac{G}{k_2}}.$$

(4.27)

Thus, at sufficiently high triplet generation rates, we expect a transition to a square root dependence of the QD PL rate with the triplet generation rate. The intersection of these two regimes represents the threshold triplet generation rate and corresponds to the incident photon flux. Above this limit, triplet exciton transfer and triplet monomolecular decay are no longer competitive with triplet bi-molecular decay. This threshold triplet generation rate, is given by

$$G_{Th} = \frac{(k_T + k_{TET})^2}{k_2}.$$

(4.28)

The threshold photon absorption rate in the TIPS-Tc is given by $I_{Th} = G_{Th}/\eta_{sf}$. At the threshold generation rate G_{Th}, the triplet transfer efficiency is given by

$$\eta_{TET} = \left(\sqrt{\frac{5}{4}} - \frac{1}{2}\right) \times \frac{k_{TET}}{k_T + k_{TET}} = 0.618 \times \eta_{TET,0}\,,$$

(4.29)

where $\eta_{TET,0}$ is the triplet transfer efficiency in the low G regime. Although G_{Th} is useful for indicating when bi-molecular processes are competitive with mono-molecular triplet decay process, it is a less useful criterion for solution SF-PM design. For example, a more valuable criterion might be the generation rate at which the triplet transfer efficiency is $\eta_{TET} = \alpha \times \eta_{TET,0}$, where α is a percentage out of 100%. In this case, the generation

rate at which the triplet transfer efficiency drops to the fraction α of the low fluence limit, termed the α threshold generation rate, is given by

$$G_\alpha = \left(\frac{1-\alpha}{\alpha^2}\right) \times \frac{(k_T + k_{TET})^2}{k_2} = \left(\frac{1-\alpha}{\alpha^2}\right) \times G_{Th} \,. \tag{4.30}$$

However, this criterion does not guarantee the high performance of the SF-PM. Ideally what is required is a criterion at which the triplet exciton transfer efficiency is a given value β. In this case, the generation rate at which the triplet transfer efficiency drops to the fraction β, termed the β generation rate, is given by

$$G_\beta = \frac{k_{TET}^2}{k_2 \beta}\left(1 - \beta \frac{k_T + k_{TET}}{k_{TET}}\right). \tag{4.31}$$

One last key point that is necessary to consider when simulating the SF-PM efficiency for any concentration of QDs is to ensure that the triplet generation rate is calculated from the incident fluence while taking into account the photons absorbed directly to the QDs, as discussed in Section 4.3.1.

Finally, with all the necessary components in our theoretical toolbox, it is possible to simulate the SF-PM performance across the range of investigated PbS-TET-CA QD concentrations and a variety of incident fluences. Triplet transfer efficiencies under steady-state conditions are calculated via the parameters extracted from the transient measurements for the bi-molecular decay of the TIPS-Tc triplets, under 535 nm excitation (Figure 4.25 a and b). The product of triplet transfer efficiency and incident power flux (532 nm) is proportional to the QD PL rate. As described earlier, there is a transition from linear to a square root dependence on incident power flux and the asymptotes of the two regimes intercept at the threshold generation rate.

In Figure 4.25b we highlight the various SF-PM criteria developed here. The area below each curve depicts where the SF-PM performance is above the related limit. As expected, the G_β threshold is significantly more conservative than the other criteria. This is necessary to ensure sufficient performance of the SF-PM.

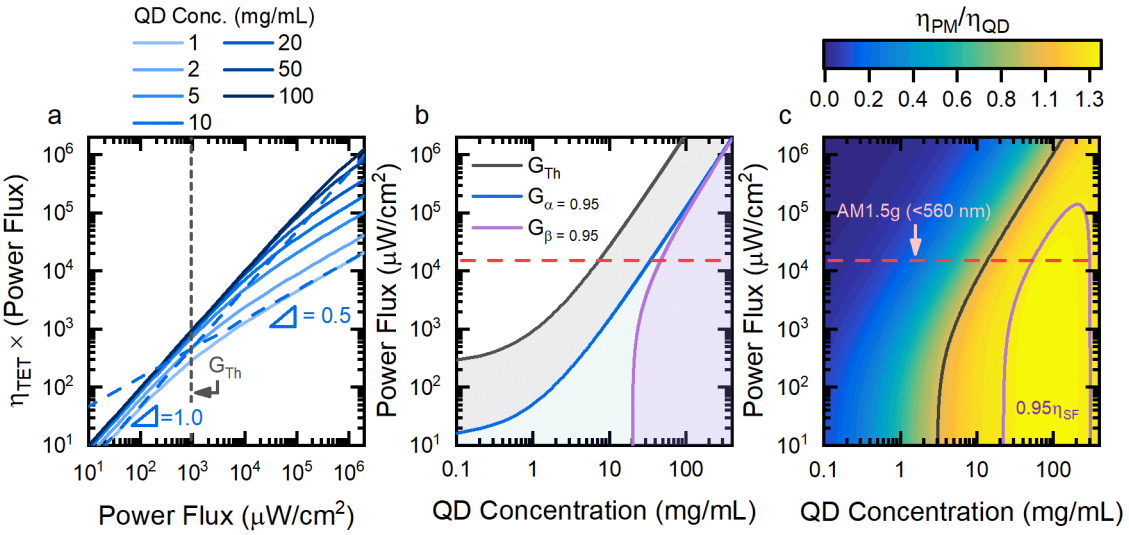

Figure 4.25: Simulated steady-state SF-PM response for TIPS-Tc:PbS-TET-CA solutions. a) Simulated steady IR PL (which is proportional to $\eta_{TET} \times (power\ flux)$) for solution of TIPS-Tc (200 mg/mL) and PbS-TET-CA (1-100 mg/mL). The low and high triplet generation density, asymptotic forms for the triplet transfer efficiency (with slope 1 and 0.5) were overlaid for the case of 1 mg/mL of PbS-TET-CA. b) Predicted threshold intensities, G_{Th}, G_{α} and G_{beta}, as function of the PbS-TET-CA concentration ($\alpha = \beta = 0.95$). The equivalent solar flux available for absorption by TIPS-Tc under the AM1.5g spectrum (red horizontal dashed line). c) Simulation of the solution phase SF-PM efficiency normalised by the PbS-TET-CA QD intrinsic PLQE, under 532 nm excitation. Including the drop in PLQE due to photons absorbed directly to the PbS-TET-CA QD. Two contours of interest are highlighted; the region in which the PM efficiency is larger than the QD PL efficiency η_{QD} (black) and when PM efficiency is 95% of the upper limit for PM efficiency given by the singlet fission yield (purple line). The equivalent solar flux available for absorption by TIPS-Tc under the AM1.5G spectrum (red horizontal dashed line). Reproduced with permission from the ACS publications.[122]

Figure 4.25c shows simulations of the normalised photon multiplication efficiency, η_{PM}/η_{QD}, across a range of power flux and PbS-TET-CA QD concentrations. Critically, the fraction of incident photons on the SF-PM that are absorbed directly by the PbS-TET-CA QDs has been included in this calculation. The result is that we can calculate the PLQE of the entire SF-PM, not just the triplet transfer efficiency. The results reveal that the intrinsic QD PLQE can be exceeded for a wide range of configurations, as illustrated by the area bound by the dark grey curve in Figure 4.25c. However, if we aim for a higher performance value of η_{PM}/η_{QD} equal to $0.95\eta_{SF}$ (corresponding to 95% of the initial singlet fission efficiency) this significantly reduces the useful parameter space, as shown by the purple highlighted contour. With inclusion of the required operating irradiance, the practical parameter space is further reduced, illustrated by the horizontal dotted red line corresponds to TIPS-Tc's solar-equivalent fluence. A minimum concentration of 30-

40 mg/mL of QDs is predicted to efficiently harvest the bulk of the triplets generated at solar fluence for this system. As we have shown, this is limited by the bimolecular triplet recombination of TIPS-Tc.

4.5.3 Steady State IR PL

To evaluate the effect of bi-molecular triplet decay on the photon multiplication efficiency of TIPS-Tc:PbS-TET-CA blends, steady-state PL spectra were measured and the spectrally integrated QD PL calculated at a range of laser fluences, as shown in Figure 4.26a. Under 532 nm excitation, we predominately measure the PL from the PbS-TET-CA QDs that arises after the fission and triplet transfer process.

By fitting of power-law functions of the form $y = Ax^n$, we observe at lower excitation densities the QD PL increases linearly with the flux. It then passes through a threshold triplet generation density, G_{Th}, after which the QD PL goes as the square root of the excitation density. This is consistent with the predictions of our kinetic modelling. The modelling predicted that the intercept of fits to these two regimes, termed the threshold triplet generation rate per unit volume, G_{Th}, is given by

$$G_{Th} = \frac{(k_T + k_{TET}X_0)^2}{k_2}. \qquad (4.32)$$

The expression predicts that the threshold will increase with QD concentration. Such concentration dependence is corroborated by the observation that the SF-PM solution with 2 mg/mL of PbS-TET-CA QDs has a threshold power flux within the power flux range investigated here. Conversely, the solution with higher QD concentration appears to not transition even at the highest power flux achieved. The measured PL counts for an SF-PM with TIPS-Tc and 2 mg/mL of PbS-TET-CA QDs shows a change from linear to square-root dependence at a threshold intensity of 2.9 ± 1.0 mW/cm^2, consistent with the value of 2.0 ± 1.2 mW/cm^2 expected from equation (4.32) and the nsTA kinetic parameters. In contrast, the solution with the higher concentration of QDs (100 mg/mL) shows little deviation from linearity over the range of intensities studied, indicating an insignificant effect from the bi-molecular decay of triplets over the power flux range used here.

We use PL counts divided by incident laser power as a measure of relative PLQE. For the solutions with TIPS-Tc (200 mg/mL) and 2 mg/mL of PbS-TET-CA QDs, PL/Power drops off at a rate, with respect to the power flux, close to the predicted (Figure 4.26b). We scale the observed PL counts by a factor of 1.7, to show the consistency between the

model and the observed relative PLQE trends. As the PL spectra measured are not absolute measurements, this use of a scaling factor can be justified by slight changes in the optical alignment of the apparatus during sample changes.

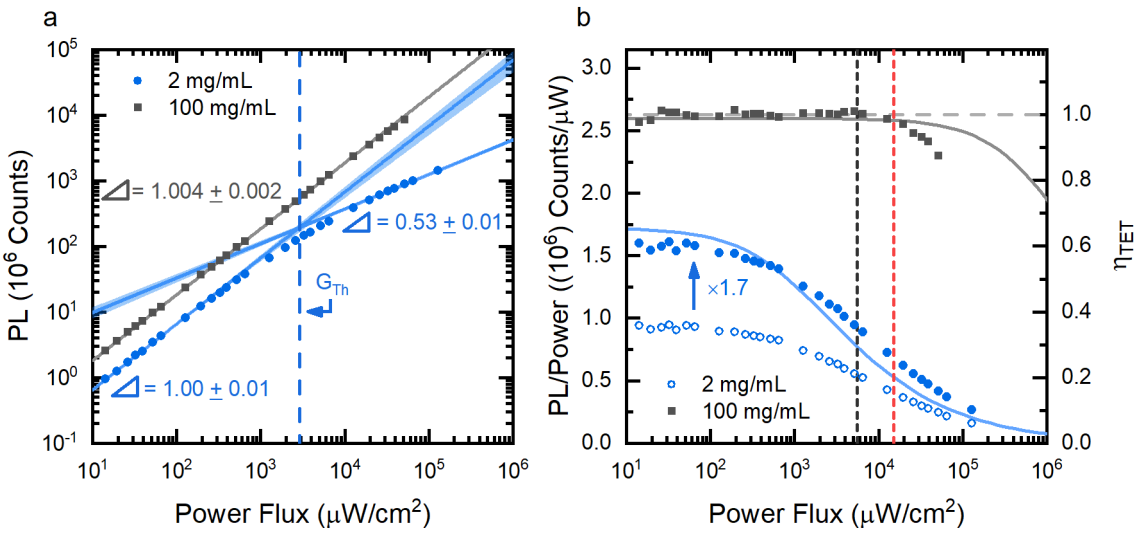

Figure 4.26: IR emission dependence on incident power flux for TIPS-Tc:PbS-TET-CA solutions. a) Total IR PL counts from PbS-TET-CA QDs for solutions of low (2 mg/mL, blue circles) and high (100 mg/mL, black squares) QD concentration with TIPS-Tc (200 mg/mL) for varying 532 nm excitation flux. The PL counts were fit with power-law relations to laser flux, either across the entire flux range (100 mg/mL) or separated into two fits (2 mg/mL), for low and high photon flux. The intercept of the fits to the low and high flux regimes gives as 2.9 ± 1.0 mW/cm² as the threshold power flux (blue vertical dashed line). b) IR PL normalised by the incident power flux, giving the relative PL yield, as a function of the incident power flux (solid black squares and hollow blue circles). Simulated triplet transfer efficiencies using the equations for the triplet transfer efficiency for 2 mg/mL (blue line) and 100 mg/mL (black line) PbS-TET-CA QD concentrations. The IR PL normalised by the incident power flux, for the TIPS-Tc:PbS-TET-CA solution with 2 mg/mL QDs, is scaled by 1.7 to illustrate the consistency with the simulated transfer efficiency. The vertical dashed black line indicates the laser fluence used in the IR PLQE measurements (5 mW/cm²), while the red dashed line indicates the equivalent solar fluences (13.7 mW/cm²). Reproduced with permission from the ACS publications.[122]

The relative PLQE for the solution with 100 mg/mL of PbS-TET-CA QDs is unchanged below the TIPS-Tc solar-equivalent fluence (the photon flux available for absorption by TIPS-Tc under the AM1.5G spectrum). As a result, we can indeed demonstrate efficient singlet fission photon multiplication under “real world” conditions. However, the relative PLQE does start to decrease at lower incident laser powers than expected. The drop in PL for 100 mg/mL of dots at high power flux is larger than expected from the bi-molecular decay rate of the TIPS-Tc triplets. This decrease in PLQE could be an indication

of photobleaching of the TIPS-Tc, non-radiative decay in the QD or increased triplet bi-molecular decay of TIPS-Tc triplet in the presents of the PbS-TET-CA QDs.

4.6 Diffusion vs Kinetically Limited Transfer

In Section 2.3.4 we introduced the theoretical framework to describe the dynamics of reactions that are purely diffusion-limited and those with a finite rate of reaction. Here we investigate the dynamics of the triplet transfer in solution phase from TIPS-Tc to the PbS-TET-CA QDs in relation to these two regimes. This leads to an investigation of how the properties of the TET-CA ligand shell influence the triplet transfer and what the implications are for improved triplet transfer.

4.6.1 Difference Between Purely Diffusion Limited and Observed Rates

The bi-molecular triplet transfer rate for a purely diffusion-limited reaction is given by $\gamma_{TET} = 4\pi R_{TET} D$, where R_{TET} is the effective distance of interaction between the TIPS-Tc triplet and the PbS-TET-CA QD ground state, and $D = D_{QD} + D_{SF}$ is the sum of the diffusion coefficient for the QD and the TIPS-Tc triplet state. This leads to

$$\frac{d[T]}{dt} \propto -\gamma_{TET}[X_0][T] = -4\pi R_{TET} D[X_0][T] \,. \tag{4.33}$$

We assume the interaction radius to be short-range and well approximated by the sum of the TIPS-Tc (~0.6 nm) and PbS-TET-CA QDs (~3 nm) radius. From Graham's law of diffusion, we estimate that the diffusion coefficient of TIPS-Tc molecules is at least 10 times larger than for PbS QDs, based on their relative molar masses.[147] Thus, for the purpose of estimating the rate of triplet transfer we use the approximation of no significant QD diffusion. Previously reported diffusion-ordered nuclear magnetic spectroscopy measurements suggest the molecular diffusion coefficient of TIPS-Tc in concentrated solution (200 mg/mL) is 5×10^{-10} $m^2 s^{-1}$ in toluene.[123] We take this value as a lower bound for the triplet diffusion coefficient, neglecting any increase in triplet diffusion that intermolecular triplet transfer may introduce. Under these conditions, we estimate a diffusion-limited triplet transfer rate of (11 ± 2)x10^9 $M^{-1} s^{-1}$.[123]

The nsTA measured triplet decay constant is very well described by a linear fit to the concentration of the PbS-TET-CA QDs, suggesting a bi-molecular triplet transfer rate of

$5.1 \times 10^8 \pm 0.1 \times 10^8$ $M^{-1} s^{-1}$ (Figure 4.18c). However, the predicted diffusion-limited rate is roughly 20 times higher than this value. That the observed rate is lower than the diffusion-limited rate suggests the process is kinetically limited. Possible reasons for this include the following: a rate-determining step limiting the reaction, such as Dexter transfer between the TIPS-Tc triplet and the TET-CA triplet; a low Gibbs free energy to drive the transfer; non-uniform coverage of the TET-CA ligand over the surface of the PbS-TET-CA QDs; and steric hindrance from residual OA ligands attached to the QD.[148]

4.6.2 Ligand Density Dependence

A series of QDs with varying amounts of TET-CA ligand were studied to gain an extended understanding of the effect the TET-CA ligand has on the transfer of triplet excitons from the TIPS-Tc. The series of PbS-TET-CA QDs were synthesised and the ligand density characterised by Dr Victor Gray and Dr Zhilong Zhang. PLQE measurements of the SF-PM solutions of TIPS-Tc with these PbS-TET-CA QDs were done by Dr Simon Dowland. Here we show the conversion of these PLQE measurements to calculations of the triplet exciton transfer rate, its dependence on the TET-CA ligand coverage, and outcomes for increasing the triplet transfer rate.

From PLQE measurements at 515 and 658 nm excitation, we calculate the exciton multiplication factor using the function

$$\eta_{EMF}(\lambda) = \frac{1}{\mu_{Tc}(\lambda)}\left(\frac{\eta_{PM}(\lambda)}{\eta_{QD}}\left(\mu_{QD}(\lambda) + \mu_{Tc}(\lambda)\right) - \mu_{QD}(\lambda)\right), \tag{4.34}$$

and the methods described in Section 4.3.3. The singlet fission yield for TIPS-Tc is taken to be 135 %, for calculation of the triplet transfer efficiency, $\eta_{TET} = \eta_{EMF}/\eta_{SF}$. Rearrangement of equation (4.25) leads to an expression for k_{TET} given by

$$k_{TET} = \frac{1}{2}\left(\frac{\eta_{TET}k_T}{1-\eta_{TET}} + \sqrt{\left(\frac{\eta_{TET}k_T}{1-\eta_{TET}}\right)^2 + \frac{4Gk_2\eta_{TET}^2}{1-\eta_{TET}}}\right). \tag{4.35}$$

We calculate k_{TET} based on a triplet generation rate corresponding to 1.25 mW/cm^2 excitation, 515 nm wavelength and the kinetic parameters determined previously by nsTA measurements, for each of the SF-PMs with PbS-TET-CA QDs with varying TET-CA ligand coverages and QD concentrations (Figure 4.27a). By individually fitting linear

functions with respect to the QD concentration for each TET-CA ligand density, we calculate the bi-molecular triplet transfer rate as a function of the TET-CA ligand coverage (Figure 4.27b). We observed a proportional relationship between the triplet transfer rate and TET-CA ligand coverage.

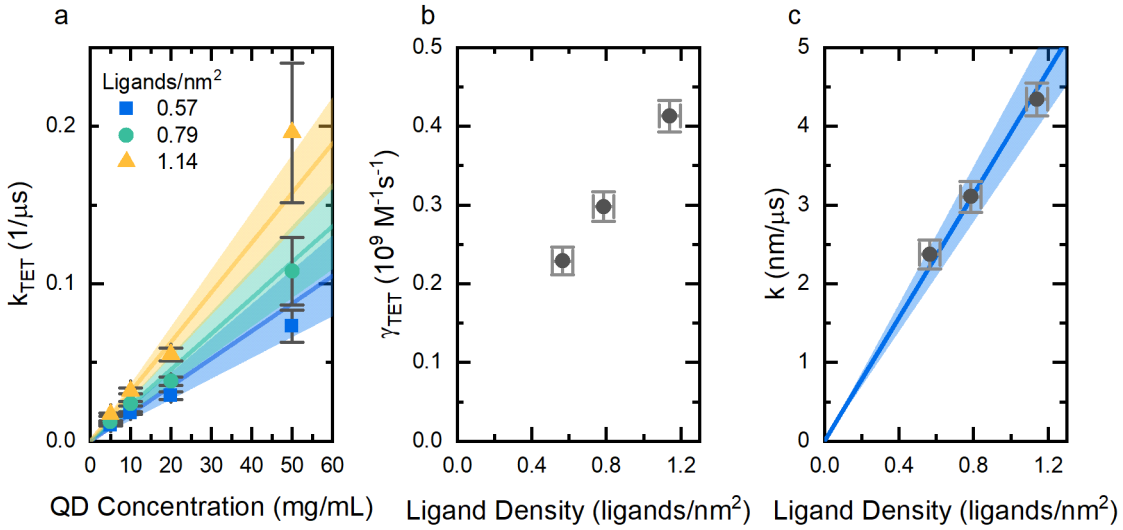

Figure 4.27: Ligand density dependence of the triplet transfer for TIPS-Tc:PbS-TET-CA solutions. a) Triplet transfer rate from TIPS-Tc (200 mg/mL) to PbS-TET-CA QDs with varying TET-CA ligand coverages (symbols). The triplet transfer rate is calculated using a triplet intrinsic decay rate of 4.4 ms^{-1} and bi-molecular decay rate 7.6x10^{-23} cm^3ns^{-1} and incident excitation of 1.25 mW/cm^2. Individual linear fits for each ligand density (solid lines and 95% confidence bounds shaded areas). b) Bi-molecular triplet transfer rate based on linear fitting of the triplet transfer rate as a function of the QD concentration. c) Triplet transfer velocity from TIP-Tc to PbS-TET-CA calculated using a triplet diffusion coefficient of 5 x 10^{-10} $m2\ s^{-1}$ and a triplet transfer radius of 3.6 nm. Linear fitting gives a slope of k_{lig} = 3.9 ± 0.1 $ligand^{-1}nm^3\mu s^{-1}$.

As discussed in Section 2.3.4 the bi-molecular triplet transfer rate for a diffusion mediated reaction with finite reaction rate is given by

$$\gamma_{TET} = 4\pi R_{TET} D \left(\frac{R_{TET}}{R_{TET} + \frac{D}{k}} \right), \tag{4.36}$$

where k is the finite triplet transfer "velocity". This k value represents the affinity of the triplet exciton to transfer from the TIPS-Tc to the PbS-TET-CA QD. Rearranging of equation (4.36) allows calculation of the triplet transfer velocity, k, as a function of the TET-CA ligand density (Figure 4.27c). The calculated triplet transfer velocities are consistent with a linear relationship to the TET-CA ligand density, σ_{lig}, given by

$$k = k_{lig}\sigma_{lig} \,,$$

(4.37)

with k_{lig} = 3.9 ± 0.1 ligand^{-1}nm^{3}µs^{-1} or equivalently k_{lig} = (2.4 ± 0.1)x10^8 M^{-1}s^{-1}. Using equations (4.25), (4.36) and (4.37), Figure 4.28 shows the consistency of this value for k_{lig} to predict the observed triplet transfer rates and efficiencies. In this way we highlight the consistency of the model and its power to predict the triplet transfer dynamics across a range of varying PbS-TET-CA QD parameters.

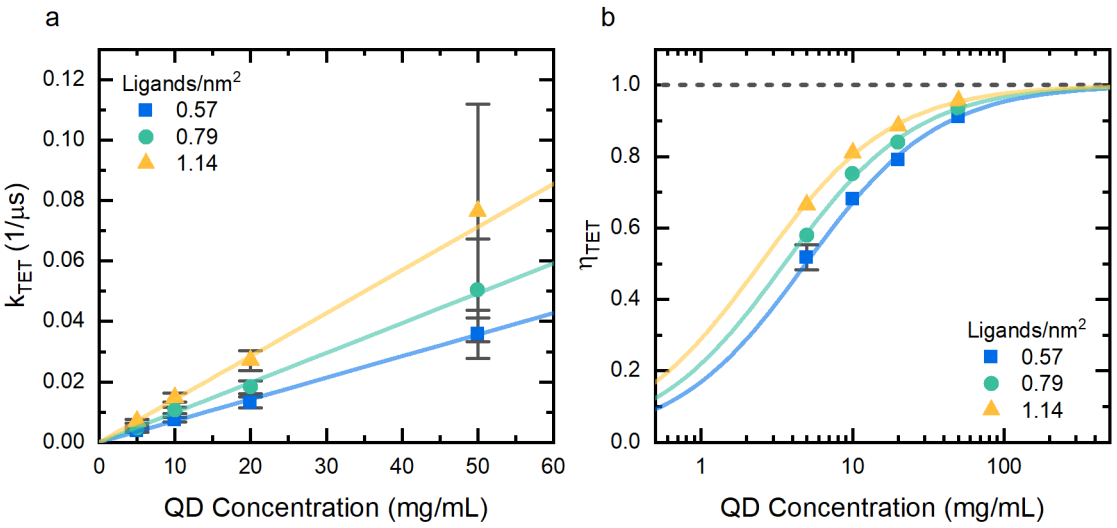

Figure 4.28: Parameterisation of the ligand-dependent triplet transfer rate.
a) Triplet transfer rate from TIPS-Tc (200 mg/mL) to PbS-TET-CA QDs with varying TET-CA ligand coverages (symbols). The triplet transfer rate is calculated using a triplet intrinsic decay rate of 4.4 ms^{-1} and bi-molecular decay rate 7.6x10^{-23} cm^{3}ns^{-1} and incident excitation of 1.25 mW/cm^2. b) Corresponding triplet transfer efficiencies (symbols). The error on each measurement is the same and highlighted on a lone data point for increased clarity. The solid lines show the calculated triplet transfer rate and efficiency using a single model with k_{lig} = 3.9 ± 0.1 ligand^{-1}nm^{3}µs^{-1}.

For a PbS-TET-CA QD concentration of $[X_0]$, the concentration of TET-CA ligands is

$$[lig] = 4\pi R_{core}^2 \sigma_{lig}[X_0] \,,$$

(4.38)

where R_{core} is the radius of the QDs PbS core. As we are in the significantly kinetic limited regime, (4.36) is well approximated by

$$\gamma_{TET} = 4\pi R_{TET}^2 k \,,$$

(4.39)

with triplet transfer rate, $k_{TET} = \gamma_{TET}[X_0]$. Substituting x and y leads to

$$k_{TET} = \gamma_{lig}[lig] = \left(\frac{R_{TET}}{R_{core}}\right)^2 k_{lig}[lig] \,.$$

(4.40)

With R_{TET} = 3.6 nm and R_{core} = 1.6 nm, we find a bi-molecular triplet transfer rate, per TET-CA ligand on the surface of the QD, of γ_{lig} = (1.2 ± 0.1)x10^7 M^{-1}s^{-1}. This value for the bi-molecular triplet transfer rate from TIPS-Tc triplet to TET-CA ligand triplet is not unreasonable. It is an order of magnitude slower than recent reports of triplet exciton transfer from an intramolecular singlet fission dimer, with TIPS-Tc based monomer units, to chloranil in solution phase.[149] However, the significant steric hindrance imposed by the ligand shell geometry could be the cause of the slower transfer rate. Equation (4.40) suggests the triplet transfer is limited by the bulk concentration of the TET-CA ligand. The anisotropic placement within the bulk, on the surface of the QDs, is irrelevant due to the diffusion of triplet significantly outcompeting the transfer step. This formulation of the triplet transfer rate includes a geometric factor, $(R_{TET}/R_{core})^2$, due to the spherical nature of the TET-CA ligands.

4.6.3 Optimised Triplet Transfer

Given the dependence on the TET-CA ligands, what is the upper limit of the possible triplet transfer rates? Based on a TET-CA ligand with dimensions perpendicular to the tetracene backbone of ~1.6x0.4 nm^2, we estimate a cross-sectional area per ligand of ~0.64 nm^2. Assuming maximal packing over the surface of the QD, this means a maximum surface density of ~1.56 ligands/nm^2. This ligand density is only slightly above what we have already synthesised, indicating we have nearly reached the maximum concentration of TET-CA ligands and corresponding triplet transfer rate. With a maximum ligand density of ~1.56 ligands/nm^2, we predict a maximum triplet transfer velocity of (6.2 ± 0.2)x10^{-3} m/s and correspond bi-molecular triplet transfer rate of (5.8 ± 0.2)x10^8 M^{-1}s^{-1}. Figure 4.29 shows the predicted triplet transfer rate from TIPS-Tc to PbS-TET-CA QDs as a function of the triplet transfer velocity to the QDs. As the triplet transfer velocity increases, γ_{TET} increases until it reaches the diffusion-limited regime where it saturates. For ideal SF-PM operation, it is necessary to have efficient triplet transfer to facilitate a high triplet transfer rate per QD. Therefore, the ideal triplet transfer velocity would be high enough such that diffusion-limited transfer is occurring. For example, values of k greater than 1 m/s would be needed. The observed triplet transfer velocities of the QDs with varying TET-CA ligand densities and the estimated

upper limit for a fully packed monolayer of TET-CA are significantly lower than this "ideal" regime.

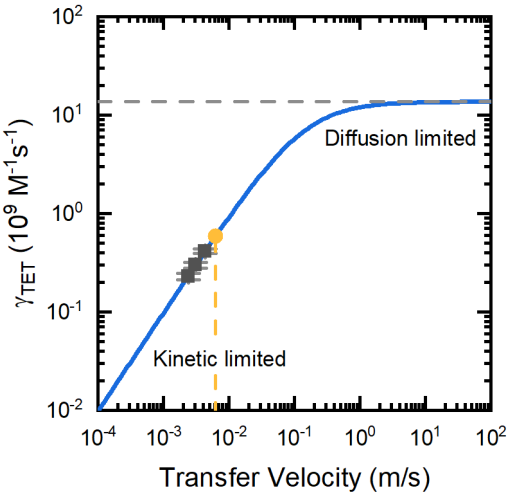

Figure 4.29: The transition from kinetically limited triplet exciton transfer to diffusion-limited. The bi-molecular triplet transfer rate from TIP-Tc to PbS-TET-CA as a function of the triplet transfer velocity (blue curve), calculated using a triplet diffusion coefficient of 5 x 10^{-10} m2 s^{-1} and a triplet transfer radius of 3.6 nm. Observed triplet transfer rates and velocities by measurement of SF-PM PLQE values (black squares). Vertical dashed yellow line shows the triplet transfer velocity predicted for QD with a fully packed monolayer of TET-CA ligands and its corresponding bi-molecular triplet transfer rate (yellow circle). Horizontal dashed grey line shows the diffusion-limited triplet transfer rate.

Our investigation suggests two routes to increase the triplet transfer rate. On inspection of equation (4.40), it appears that increasing the size of the PbS-TET-CA QD will yield increases in the triplet transfer proportional to the square of its radius. One possible future research route to achieve this effect could be to employ triplet ligands that are based on TIPS-Tc dimers, trimers or polymers. With similar electronic properties and significantly longer dimensions, these molecules could increase the rate of triplet transfer from the TIPS-Tc.[150] The second route would focus on increases to the intrinsic triplet transfer rate per ligand, k_{lig}, resulting in overall high triplet transfer rates and efficiencies. To achieve this, future work is needed to understand the nature of the TIPS-Tc to PbS-TET-CA transfer, such as investigation of the role Gibbs free energy plays in the process.[151]

4.7 Conclusion and Outlook

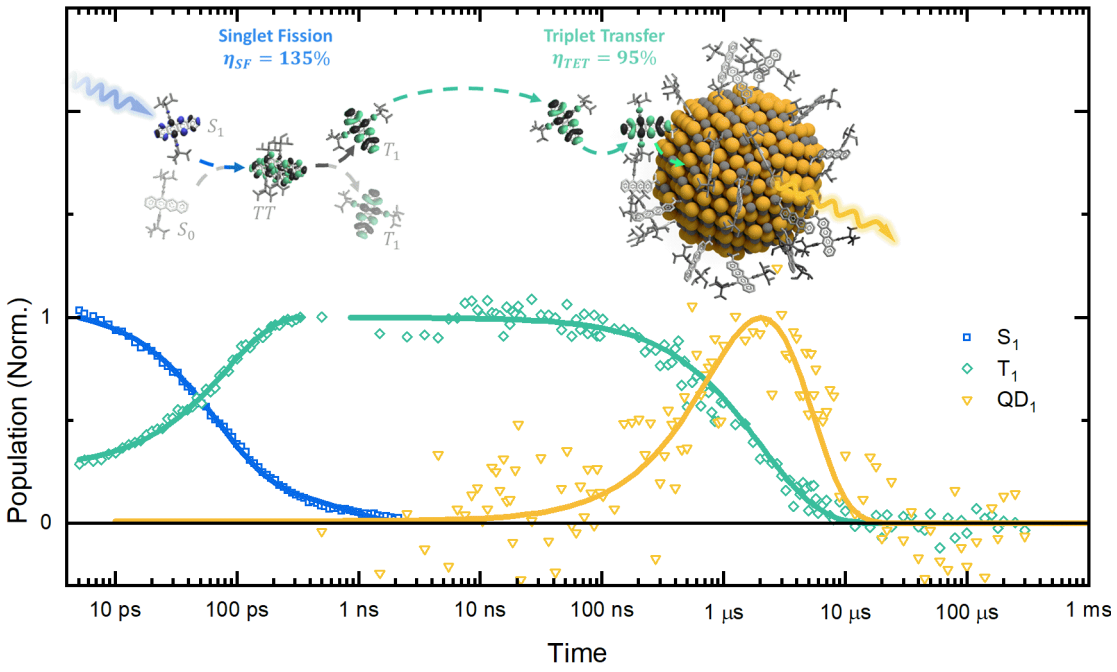

Figure 4.30: Overview of singlet fission, triplet transfer and QD excited state decay dynamics. The nsTA kinetics shown are for a TIPS-Tc:PbS-TET-CA solution (200 mg/mL:100 mg/mL). The kinetics in the first 2 ns show the singlet fission process for a TIPS-Tc solution (200 mg/mL).

We have demonstrated a solution-based bulk SF-PM system that meets many of the "realistic" requirements. In particular, the requirements pertaining to parasitic absorption, efficient triplet transfer and operation at solar irradiance, have been fulfilled. We calculate that it is possible to achieve an efficient SF-PM material, in which >95% of incident photons are absorbed by the singlet fission material, TIPS-Tc. At energies below the absorption of TIPS-Tc less than 5% of photons are absorbed by the PbS QDs. The development of such materials could involve advanced solution processing techniques adapted from LCD manufacturing. After absorption, efficient singlet fission occurs in the solution phase before quantitative harvesting of the triplet excitons via a low concentration of PbS QDs (≤ 50 mg/mL)), followed by the emission of IR photons. We have shown that in order to obtain efficient harvesting of the fission generated triplets it is necessary to engineer the surface ligands on the PbS QDs. TET-CA ligands are shown to be much more efficient than either OA or HA. Several surprising results are uncovered; for instance, while the transfer of the TIPS-Tc triplets to the PbS-TET-CA QD is the rate-limiting step, it occurs more slowly than would be expected for a purely

diffusion-limited process. On analysis of the triplet transfer dynamics, we find that the process is kinetically limited and that the rate of transfer is proportional to the number of TET-CA ligands per QD. The mixed nature of the QD ligand coverage (consisting of both of the TET-CA and OA) leads to the need for multiple collisions before the transfer is achieved to the TET-CA ligand. Triplet transfer to the PbS-TET-CA QDs is likely affected by the steric hindrance caused by the ligand shell and the intrinsic bi-molecular triplet transfer between TIPS-Tc and the TET-CA. We show that the improvements to triplet transfer offered by the TET-CA ligand are approaching the estimated maximum rate facilitated by a fully packed monolayer of TET-CA ligands. At this value the transfer is nevertheless kinetically limited and we discuss strategies to advance to a diffusion-limited rate. We also find that bi-molecular recombination of triplets is the major loss channel and limits the photon multiplication performance at high fluences. However, it is possible to arrange a sufficiently high concentration of QDs (30-50 mg/mL) such that 95% of the triplets present can be harvested at solar-equivalent fluence. These results thus establish that it is possible to have a photon multiplication scheme that can function at solar fluence and shows the potential of singlet fission photon multiplication as a means to break the Shockley–Queisser limit.

Currently, the limiting performance factors are the photoluminescence energy and quantum efficiency of the PbS-TET-CA quantum dots and the TIPS-Tc singlet fission yield. PbS QDs with high emission energy are needed for optical coupling to a Si PV. This, in turn, requires a higher triplet energy in the singlet fission material and triplet transmitter ligand. In a further project, we have shown that 200-300 meV is necessary to guarantee triplet transfer from the singlet fission material to the PbS QDs.[97] Consequently, a singlet fission material with triplet energy of at least 1.4-1.5 eV is required. As illustrated by Figure 4.31, material design with the aim of singlet fission yield approaching 200% will lead to significant improvements to the photon multiplication performance. An increased singlet fission yield will be necessary as with the current TIPS-Tc singlet fission yield of 135%, a QD with PLQE larger than 80% would be required in order to achieve an overall photon multiplication yield greater than 100%.

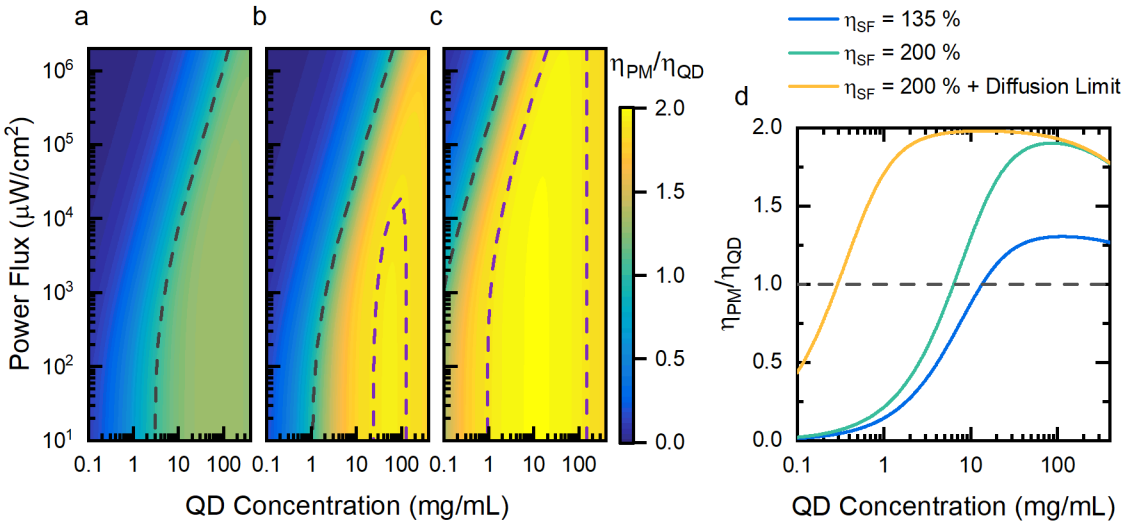

Figure 4.31: Simulations of the normalised efficiency for a TIPS-Tc:PbS-TET-CA solution. a) triplet kinetics and singlet fission yield (135%) as experientially observed, under 535 nm excitation. Prediction of the SF-PM efficiency for singlet fission yield of 200%, with the triplet kinetics as measured (b) and for triplet transfer at the expected diffusion-limited rate (c). Points at which the normalised photon multiplication efficiency are unity (black dashed line) and 190% (purple dashed line). d) Simulated photon multiplication normalised efficiency at effective solar fluence (13.7 mW/cm²).

Future improvements to the photon multiplication scheme should focus on increasing the transfer rate, resulting in a larger parameter space where triplets are effectively extracted with the need for a lower concentration of QDs (Figure 4.31). A reduction in the rate of bi-molecular recombination of triplets would also be highly desirable, for instance by tuning the electronic structure such that TTA events lead solely to the reformation of the singlet state, which could then be recycled. Lessons can be learnt from the photon upconversion field, where TTA yields for singlet generation can approach 100%.[145] The solution-based SF-PM system we have established here serves as a convenient and highly tuneable platform to understand the fundamental photophysics of the triplet transfer process from organic semiconductors to QDs, test materials combination, energetics, and surface chemistries, in order to guide the future development of solid-state SF-PM systems.

Ultimately, the SF-PM requires a solid-state implementation, which will involve careful control of nano-morphology, as well as energetics and surface chemistry of the QDs, as discussed in the following chapter.

Chapter 5

Solid State Singlet-Fission Photon-Multiplier

While the solution phase SF-PM system established in the previous chapter serves as a model system for understanding the triplet transfer process from organic semiconductors to inorganic QDs, the ultimate challenge for the singlet fission community is the development of a solid-state SF-PM system. That being said, the design rules elucidated by the solution-phase TIPS-Tc:PbS-TET-CA system does light the route to a solid-state implementation. Here we detail the development of a solid-state bulk organic semiconductor/quantum dot blend that efficiently harvests triplets generated by singlet fission.

To begin this chapter, we introduce the solid-state TIPS-Tc:PbS-TET-CA blend and its operation as an SF-PM. Morphological insights of the TET-CA ligands effect are highlighted. Under optimised morphologies the SF-PM's exciton multiplication factor is found to be ~190%, indicating highly efficient singlet fission followed by triplet transfer. After this overview we detail the optimisation of the SF process by morphological control, rule out any significant singlet exciton transfer and a singlet trapping process as a loss pathway in the singlet fission material. From here we dive into the characterisation of the triplet harvesting dynamics and mechanism of transfer to the PbS QDs. Of note we show that the triplet transfer rate is predominately controlled by the density of QDs, identify visible transient photoluminescence microscopy as a means to spatially map triplet transfer and observe sequential triplet transfer from the singlet fission host to the triplet transmitter ligand to the PbS QD. With the dynamics characterised, the final section investigates the consequences for the SF-PM's steady-state operation.

The results presented in this chapter demonstrate the many photophysical and morphological challenges towards achieving a solid-state singlet fission photon multiplier can be overcome by careful systems design.

Content in this chapter is adapted from the publication draft titled "Efficient Harvesting of Triplet Excitons Generated from Singlet Fission in a Bulk Organic-semiconductor/Quantum-Dot Blend". This draft is the result of collaboration between Jesse Allardice[a], Victor Gray[a,b*], Simon Dowland[a*], Daniel T. W. Toolan[c], Michael P. Weir[d], James Xiao[a], Zhilong Zhang[a], Jurjen F. Winkel[a], Géraud Delport[a], Samuel D. Stranks[a], Anthony J. Petty II[e], John Anthony[e], Richard Friend[a], Anthony J. Ryan[c], Richard A. L. Jones[d], Neil C. Greenham[a] and Akshay Rao[a]*

** These authors contributed equally*

[a]Cavendish Laboratory, University of Cambridge, J. J. Thomson Avenue, Cambridge, CB3 0HE, UK.
[b]Department of Chemistry, Ångström Laboratory, Uppsala University, Box 532, SE-751 20 Uppsala, Sweden.
[c]Department of Chemistry, The University of Sheffield, Sheffield S3 7HF, UK.
[d]Department of Physics and Astronomy, The University of Sheffield, Sheffield S3 7RH, UK.
[e]Center for Applied Energy Research, University of Kentucky, Research Park Dr., Lexington KY 40511, USA.

5.1 Introduction

Similar to the previous chapter, this chapter investigates the development of a singlet fission photon multiplier (SF-PM) as a means of harnessing the singlet fission process' potential in surprising the Shockley-Queisser limit. However, the key step forward developed here is the implementation of an SF-PM in a bulk solid-state blend, as illustrated in Figure 5.1. The SF-PM is designed to be an optically active layer lying on top of a conventional Si-PV, similar to that illustrated in Figure 5.1a. One key advantage of the SF-PM scheme over alternative means of utilising singlet fission is that no electrical contact between the PV cell and the singlet fission material is required. Thus, lowering the possibility of any unwanted altercations of the PV's electrical properties and corresponding efficiencies. Instead, the optical coupling of the singlet fission photon multiplier with the PV cell is utilised to offer power conversion efficiency gains.

A key design constrain for the SF-PM is that it must be an easily fabricated and durable structure, that can match the operational lifetime of the underlying PV cell. These requirements point towards a solid-state implementation, in thin-film form. Such a system can leverage the domain knowledge of thin-film fabrication from the organic field-effect transistor, organic light-emitting diode and organic photovoltaic research communities, which have similar structural requirements. With this in mind a solid-state SF-PM is sought, given that the following constraints can be meet;

- The SF-PM is made of a bulk composite material, with unconstrained thin-film thickness, such that sufficient high energy photon can be absorbed.
- The SF-PM morphology can be controlled such that the QD emitters are well dispersed within SF host, with minimal QD aggregation.
- The SF host is able to produce viable triplet excitons with yields approaching 200 %.
- Triplet transfer is possible such that the dispersion of QD emitters are able to efficiently harvest the triplet excitons, followed by IR photon emission.

The development of such a solid-state SF-PM presents many morphological and photophysical challenges. Creating a bulk composite of an organic semiconductor and inorganic QDs generally presents a significant morphological challenge. The mismatch in size, shape and surface energies of the two components, often results in aggregation or phase separation.[80,152–154] Subsequently, aggregation of the QDs is linked to a detrimental effect on the QD photophysical properties.[155–158] As synthesised PbS QDs,

with aliphatic ligands such as oleic acid (OA) are problematic, not only as the OA ligand has been shown to inhibit triplet transfer,[12,13,101] additionally they are suspected as the main cause of the QD aggregation due to an incompatibility with the SF host. It is therefore motivated to use a ligand with chemically matched properties to the SF host and that can facilitate triplet transfer. Taking inspiration from the solution phase SF-PM system, the use of PbS QDs functionalised with the triplet transmitter ligand 6,11-bis((triisopropylsilyl)ethynyl)tetracene-2-carboxylic acid (TET-CA) is of interest.

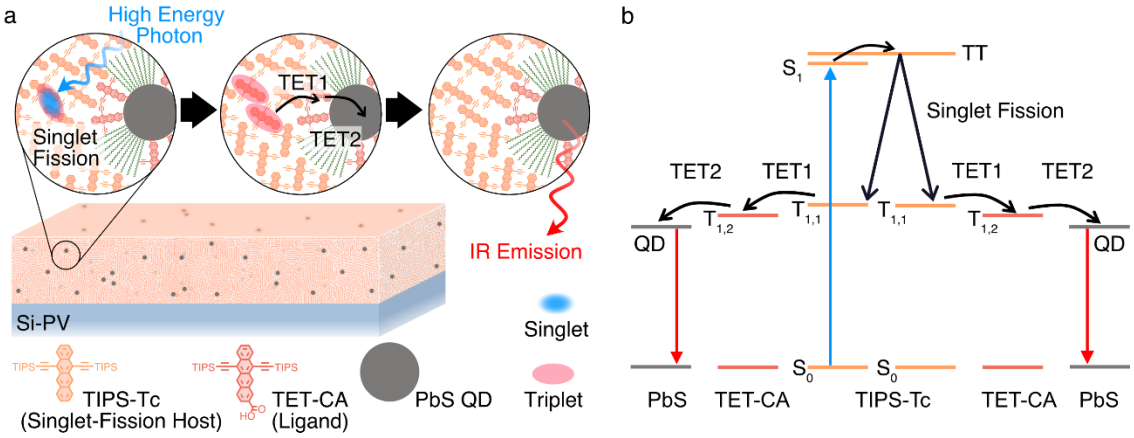

Figure 5.1: Schematic illustration of a bulk SF-PM material integrated with a Si PV device. a) The triplet acceptor PbS quantum dots are evenly dispersed within an optically dense, TIPS-Tc, singlet fission host. b) Energy diagram describing the processes involved in photon multiplication based on singlet fission. First, a high-energy photon is absorbed, followed by rapid singlet-fission in TIPS-Tc generating two triplet excitons ($T_{1,1}$). The triplet excitons are transferred via a TIPS-Tc carboxylic acid (TET-CA) ligand to PbS quantum dots which emit a photon when returning to the ground state. Illustration reproduced with permission from Dr Victor Gray.

Here we demonstrate a quantum dot surface engineering approach allowing morphological control of the QD dispersion within an SF host. This approach overcomes a long-standing materials challenge in the mixing of organic semiconductors with inorganic quantum dots.[79,86,159–163] Similar to the previous chapter, as singlet fission material we take 5,12-bis((triisopropylsilyl)ethynyl)tetracene (TIPS-Tc) for its high solubility, and solution-processability, with known singlet fission yield of 130-180% in polycrystalline films.[164] QDs with exciton peak absorption at 1.08 eV, were used as the IR-emitting acceptor. Ligand exchanged of as synthesised PbS QDs with OA ligands (PbS-OA), with the TET-CA ligand, is used to create triplet transmitter functionalised QDs (PbS-TET-CA). Bulk photon multiplier films were fabricated by blade coating solutions of TIPS-Tc with either PbS-OA or PbS-TET-CA QDs from toluene, at varying mass ratios of the components. With the TIPS-Tc:PbS-TET-CA scheme, similar to the solution phase system

in the previous chapter, a downhill energy cascade from SF-host triplet to QD excited state is arranged (Figure 5.1b).

5.2 Morphology Characterisation

Collaborators from Sheffield have investigated the ligand exchange from PbS-OA to PbS-TET-CA using small-angle X-ray and neutron scattering measurements (SAXS and SANS); along with grazing incident small-angle X-ray scattering to characterise the QD dispersion within TIPS-Tc:QD films and studied the TIPS-Tc crystalline domains by polarised optical microscopy (Figure 5.2).

Of particular note small X-ray and neutron scattering measurements on solutions of PbS-OA and PbS-TET-CA QDs allowed determination of a ~1.6 nm core radius, while fitting of the neutron scattering data allowed determination of the TET-CA ligand density on the surface of the PbS QDs (Figure 5.2a). They concluded that ligand exchange is successful and results in a TET-CA ligand density of 1.3± 0.1 ligands/nm^2. However, the fitting is consistent with the presence of residual OA ligands attached to the PbS QDs, indicating a mixed ligand envelope is achieved.

Subsequent characterisation of the QD dispersion, in TIPS-Tc:QD films, was achieved by them with grazing incident small-angle X-ray scattering (Figure 5.2b-d). X-ray scattering from the TIPS-Tc:QD films show clear structure factors between 0.05 and 0.35 Å^{-1}, representing colloidal crystallisation of aggregated quantum dots. The significant size of this peak in the TIPS-Tc and unmodified PbS-OA QDs blends indicated the presence of highly aggregate QD structures. The higher scattering density due to structures larger the QD (q < 0.05 Å^{-1}) for the TIPS-Tc:PbS-TET-CA blends indicates a highly disordered dispersion of the PbS-TET-CA QDs within the SF host. The collaborators performed fitting using a colloidal crystal model, of key features in the 1D radially integrated scattering. These fits indicated that the PbS-OA QDs form highly ordered aggregate structures within the SF host material. In contrast, the blends with the TIPS-Tc based ligand showed much weaker colloidal ordering and significantly enhanced contact between the QDs and the SF host. These results are consistent with TEM images obtained for both films and schematic structures are illustrated in Figure 5.2 g and h.

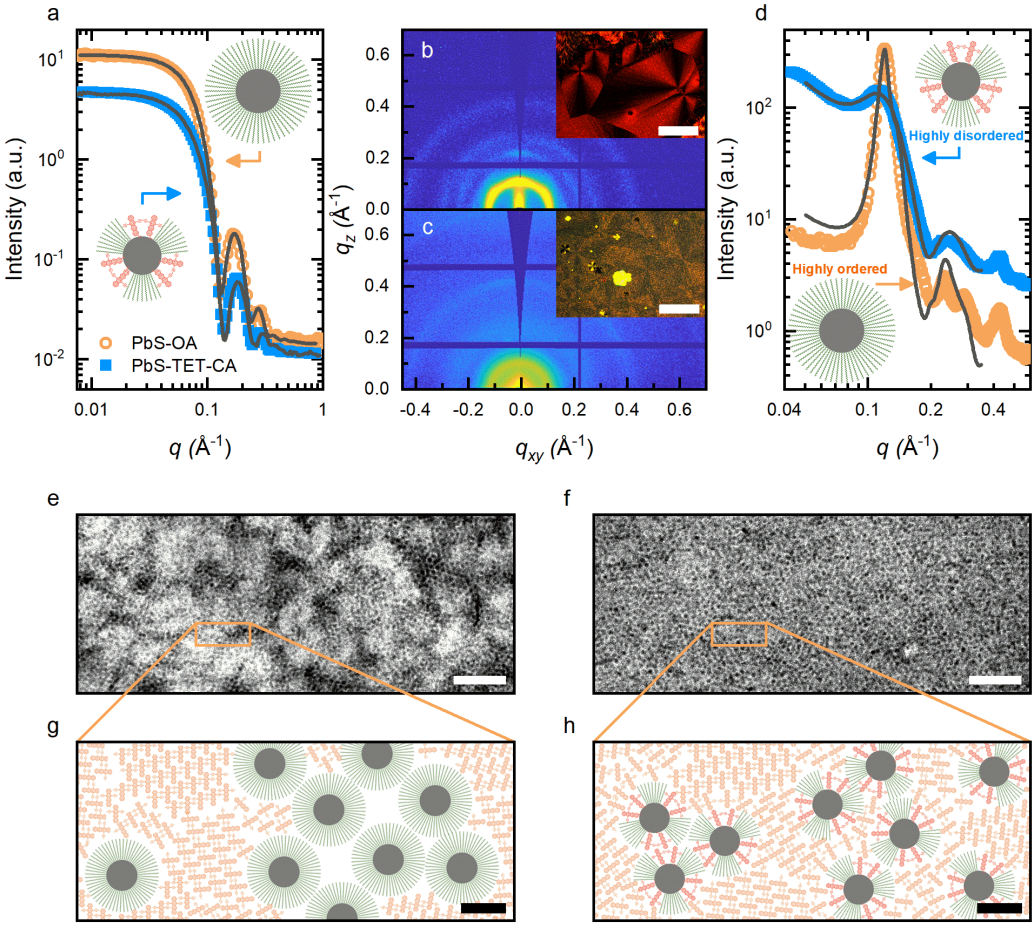

Figure 5.2: Ligand dependence of the PbS QD dispersion within the singlet fission host. a) SANS data from before and after ligand exchange, PbS-OA (orange open circles) and PbS-TET-CA (blue closed squares), following subtraction of appropriate backgrounds, with associated fits (black curves). Insets: schematic illustration of the population of ligands shifting from all OA (PbS-OA) to a mixture of OA and TET-CA (PbS-TET-CA). Two-dimensional grazing incidence X-ray scattering data for TIPS-Tc:PbS-OA (b) and TIPS-Tc:PbS-TET-CA films (c), inserts showing POM images (500 μm scale bar), with one dimensional radially integrated data shown (d), with TIPS-Tc:PbS-OA (orange open circles), TIPS-Tc:PbS-TET-CA (blue closed squares) and associated fits to an FCC colloidal crystal model (black curves). TEM (50 nm scale bar) for TIPS-Tc:PbS-OA (e) showing large aggregates (dark regions) within the SF host (lighter regions) and PbS-TET-CA (f) showing a significantly more homogenous QD dispersion within the TIPS-Tc host. Illustration (5 nm scale bar) of the bulk SF-PM structures for the highly ordered parking of the PbS-OA quantum dots (g) and the highly disordered dispersion of PbS-TET-CA QD (h) within the TIPS-Tc. Scattering and POM measurements, and TEM imagery were performed by collaborators from the University of Sheffield and Dr James Xiao respectively and reproduced with permission.

Finally, Polarisation optical microscopy images obtained by the University of Sheffield collaborators, showed reduced TIPS-Tc crystalline domain sized and increased nucleation density for the TIPS-Tc:PbS-TET-CA blends relative to the OA covered QDs (inserts in Figure 5.2 b and c). Suggesting that the PbS-TET-CA QDs are involved in the TIPS-Tc crystallisation process.

In summary, PbS QDs functionalised with the TET-CA ligand were observed to achieve highly disordered structures within the singlet fission host material. Favourable interaction by π-π stacking between the TET-CA ligand and the bulk TIPS-Tc host material is likely the mechanism for the improved dispersibility of the PbS-TET-CA QDs. In comparison, the aliphatic OA ligand, which is more unfavourable than the highly conjugated TIPS-Tc, results in phase separation. The dispersibility of the PbS-TET-CA QDs makes it possible to move beyond bilayer architectures and open up the possibility of harvesting triplet excitons in a bulk system.

5.3 Initial Optical Characterisation

We begin the photophysical investigation of the TIPS-Tc:PbS-TET-CA films, made under optimised fabrication methods, with the characterisation of their steady-state optical properties. The films presented in this section were fabricated using a vacuum solvent removal method and aged for 1 week prior to their optical characterisation (details in the following section). The absorption and photoluminescence of TIPS-Tc:PbS-OA and TIPS-Tc:PbS-TET-CA films are shown in *Figure* 5.3. All films studied here have an absorbance greater than 1.5 (>95 % absorption) at the TIPS-Tc absorption peak (545 nm), with low PbS quantum dot absorption across the visible region (*Figure* 5.3a). Thus, meeting the optical thickness requirements for the solid-state SF-PM system.

The TET-CA ligand not only produces good quantum dot dispersibility within the crystalline TIPS-Tc host material but is expected to lead to efficient triplet transfer. To evaluate the photon multiplication performance in the films, we measure the PLQE when exciting the SF host material TIPS-Tc (at 515 nm) and compare to direct excitation of the PbS-TET-CA quantum dots (at 658 nm). PLQE measurements were performed at low fluence to minimise any bimolecular decay losses. As seen in **Figure 5.3**b, the PLQE of the TIPS-Tc:PbS-TET-CA film increases from (15.4 ± 1.0) % (658 nm, quantum dot only) to (24.5 ± 1.0) % under photoexcitation of the SF host (515 nm, quantum dot + SF host).

This enhancement of (59 ± 12) % suggests efficient SF followed by triplet transfer to the emissive quantum dots.

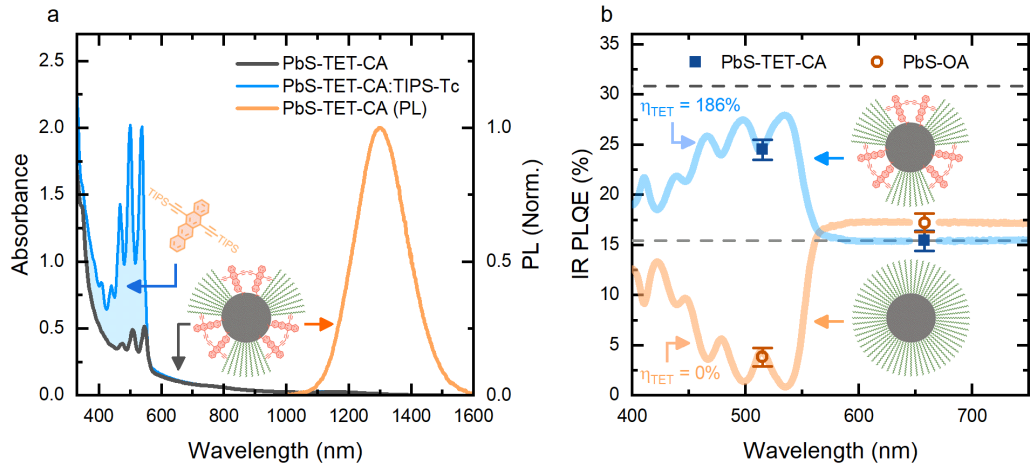

Figure 5.3: Absorbance and IR PL due to triplet harvesting in a TIPS-Tc:PbS-TET-CA film. a) Absorbance (blue curve) and normalised IR PL (orange curve) of a TIPS-Tc:PbS-TET-CA thin film. For comparison the absorbance of PbS-TET-CA quantum dots in toluene (black curve), the difference highlighting the TIPS-Tc absorption (blue area). b) The measured absolute IR PLQE under 515 nm and 658 nm excitation for TIPS-Tc:PbS-TET-CA (blue closed squares) and TIPS-Tc:PbS-OA (orange open circles) thin films. Based on these PLQE measurements, the light blue curve shows the expected IR PLQE wavelength dependence for the TIPS-Tc:PbS-TET-CA thin film, in the low-fluence regime. The light orange curve shows the expected IR PLQE wavelength dependence for the TIPS-Tc:PbS-OA thin film, with absolutely no triplet transfer to the PbS-OA quantum dots. Horizontal dashed lines show the SF-PM performance relative to 100% (grey) and 200% (black) of the intrinsic quantum dot PLQE in the TIPS-Tc:PbS-TET-CA thin film. Films are at TIPS-Tc:QD mass ratio of 2:1 and were vacuum treated and aged for 1 week. Absorption spectra were measured by Dr Simon Dowland.

We quantify the efficiency of the SF-PM system, by calculation of the exciton multiplication factor η_{EMF} in the low fluence regime, where the SF-PM normalised efficiency is given by

$$\frac{\eta_{PM}(\lambda)}{\eta_{QD}} = \alpha_{QD}(\lambda) + \alpha_T(\lambda)\eta_{EMF} \,. \qquad (5.1)$$

We take the measured values of η_{QD} = (15.4 ± 1.0) % (excitation at 658 nm, QD only) and $\eta_{PM}(\lambda = 515\,nm)$ = (24.5 ± 1.0) % (excitation at 515 nm, QD + SF host) and combining with the relative absorption in the PbS-TET-CA quantum dots and the SF host (approximated by values measured in the solution phase), an exciton multiplication factor of η_{EMF} = (186 ± 18) % is extracted. In the case of triplet transfer, η_{EMF} is given

by the product of the triplet transfer efficiency η_{TET} and the singlet fission yield η_{SF}. From the η_{EMF} value, we calculate $\eta_{PM}(\lambda)$, the expected IR PLQE wavelength dependence across the full excitation window, in the low-fluence limit (Figure 5.3b).

In contrast to the PbS-TET-CA:TIPS-Tc films, films of PbS-OA:TIPS-Tc show a drop in PLQE when the SF host is excited, from (17.2 ± 1) % (658 nm, quantum dot only) to (3.8 ± 1) % (515 nm, quantum dot + SF host) (*Figure* 5.3b). The measured PLQE value at 515 nm is consistent with the expected IR PLQE wavelength dependence for a film with no triplet transfer from the TIPS-Tc to the PbS-OA quantum dots.

5.3.1 Magnetic Field Dependent PL

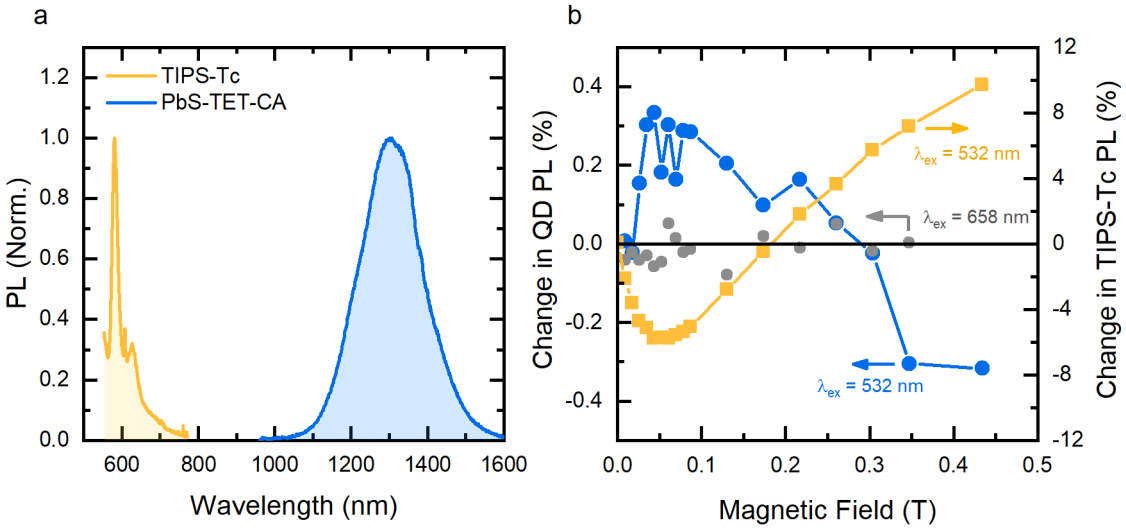

Figure 5.4: Magnetic dependent PL Identification of triplet transfer in a TIPS-Tc:PbS-TET-CA film. a) TIPS-Tc singlet (orange curve) and PbS-TET-CA QD (blue curve), normalised PL emission spectra of a TIPS-Tc:PbS-TET-CA film (100:50 mg/mL), under 532 nm excitation, at zero applied field. b) Percentage change in the QD (blue and grey circles) and TIPS-Tc (orange squares) PL, for a TIPS-Tc:PbS-TET-CA film. The QD emission resulting from triplet transfer from TIPS-Tc after excitation with 532 nm laser light (blue circles) drops on the application of a high magnetic field (>0.3 T). Whereas, PL from the TIPS-Tc increases with large applied magnetic fields (orange squares). Direct excitation of the QD, with 658 nm laser light, results in no effect with an applied magnetic field (grey squares). Films were vacuum treated and aged for 1 week.

To further verify that the PLQE enhancement originates from SF and triplet transfer we perform magnetic-field-dependent PL measurements (Figure 5.4). Direct excitation of the PbS-TET-CA QD with 658 nm laser light results in no observed magnetic dependence (for fields less than 0.5 T), similar to previous observations. [11, 12, 14] We observe an initial decrease in TIPS-Tc PL at low magnetic fields (<150mT) followed by an increase at higher

magnetic fields. Such behaviour is typical for SF materials.[9,122] In contrast, the PbS-TET-CA QD IR PL shows the opposite trend, indicating that the excited QD states are the result of triplets generated by singlet fission, transferred from the TIPS-Tc.[81,118,122]

In summary, we have demonstrated TIPS-Tc:PbS-TET-CA blends with significant absorption contrast between the SF host and the PbS QDs, which show a considerable exciton multiplication factor approaching 200 %. Additionally, we provide sufficient evidence that this exciton multiplication factor is likely the result of singlet fission and triplet transfer. Thus, we have shown that it is possible to construct an efficient singlet fission photon multiplication in a bulk solid-state system. For the remainder of this chapter, we develop an understanding of intricacies of this system.

5.4 Optimisation of the SF Host Morphology

With the knowledge that a solid-state SF-PM can be demonstrated we next take a step backwards and detail the necessary optimisation of the singlet fission process that was undertaken. We show that optimisation of the SF host morphology is critical to achieving adequate singlet fission yields. The process of finding a singlet fission viable material can be as easy as taking a highly soluble small organic semiconductor molecule with appropriate excited singlet and triplet state energies, for exergonic singlet fission to be possible, and mixing it in solution at a sufficient concentration. Within these conditions the diffusion assisted collision of an excited singlet state molecule and a ground state molecule, allow for sampling of a large parameter space of chromophore coupling geometries.[55,123] A singlet fission favouring geometry is commonly found and singlet fission can occur. Taking the same molecule in polycrystalline or single crystal form does not guarantee that singlet fission will occur. In a solid-state systems singlet fission can be hampered as crystallisation can limit accessible chromophore coupling geometries, cause aggregation assisted energy level shifting.[165–168] Polycrystalline morphology can affect singlet fission yields and rates, or introduce excited state traps.[123,169–171]

In TIPS-Tc alone there is an ongoing debate as to the exact nature and utility of some of the observed photoexcited states in the singlet fission process. In particular, the observed excimer like state, that appear ~100 ps after photoexcitation of TIPS-Tc in solution and thin-film phase, with associated broad red-shifted emission (relative to the singlet emission). The excimer like state has been pointed to as either a necessary intermediate state in the singlet fission process or a loss channel from the singlet state.

[58,66,123] Another key observation was the identification of vibronically coherent ultrafast triplet pair state formation in TIPS-Tc films.[58] The coupling of electronic and vibration degrees of freedom result in triplet pair formation on a < 500 fs timescale, with corresponding partial loss of singlet population. The remainder of the singlet population decays on a slower 10s of picoseconds timescale with the corresponding rise of the triplet pair signatures.

5.4.1 Singlet Fission Dynamics

We start our investigation of the TIPS-Tc:QD films with measurement of picosecond and nanosecond transient absorption (psTA and nsTA) spectra. From these measurements, we identify any effects the PbS-TET-CA QDs have on the singlet fission process in the TIPS-Tc SF host. Figure 5.5a shows the measured psTA spectra of pristine TIPS-Tc after photoexcitation at 535 nm. Similar to previous reports we observed the loss of the singlet exciton over the first ~20 ps, as identified by the loss of the TIPS-Tc stimulated emission (SE) peak at ~580 nm.[58] A corresponding growth of the photoinduced absorption (PIA) peak at ~860 nm is assigned to the generation of triplet excitons. Decomposition of the dynamics into two components, for the pristine TIPS-Tc and TIPS-Tc:PbS-TET-CA psTA spectra, is achieved with the genetic algorithm. The decomposed kinetics are consistent with a sequential reaction from an initially photoexcited singlet state to a subsequent state over a ~20 ps timescale (Figure 5.5c).

Comparison of the initial dominate spectral component, assigned to the singlet exciton, shows little difference with the addition of the PbS-TET-CA QDs. To make clear differences in the subsequent dominate spectral component, normalisation to the maximum signal strength of the decomposed singlet component is calculated (Figure 5.5b). With this normalisation we witness that, on the addition of the PbS-TET-CA QDs to the SF host, the second spectral component has an increased triplet PIA strength at 860 nm and a reduction in the broad PIA background across the probe range. These spectral differences indicate that there exist a third species with associated spectral features and the decomposed second spectral component is the sum of two distinct excited states with varying populations. The pristine TIPS-Tc film appears to have a higher proportion of the state associated with a broad PIA, which we will refer to as a singlet trap state. An assignment we will justify in the following discussion. The presence of the PbS-TET-CA QDs increased the proportion of the second decomposed spectra with a signal from the sharp triplet PIA at 860 nm. The increased triplet proportion is additionally correlated with an increased initial population of the triplet and trap mixed

spectra spectral component at early times (200 fs). A possible indication of an increased proportion of the singlet fission process occurring via the vibronically coherent ultrafast channel mentioned earlier.

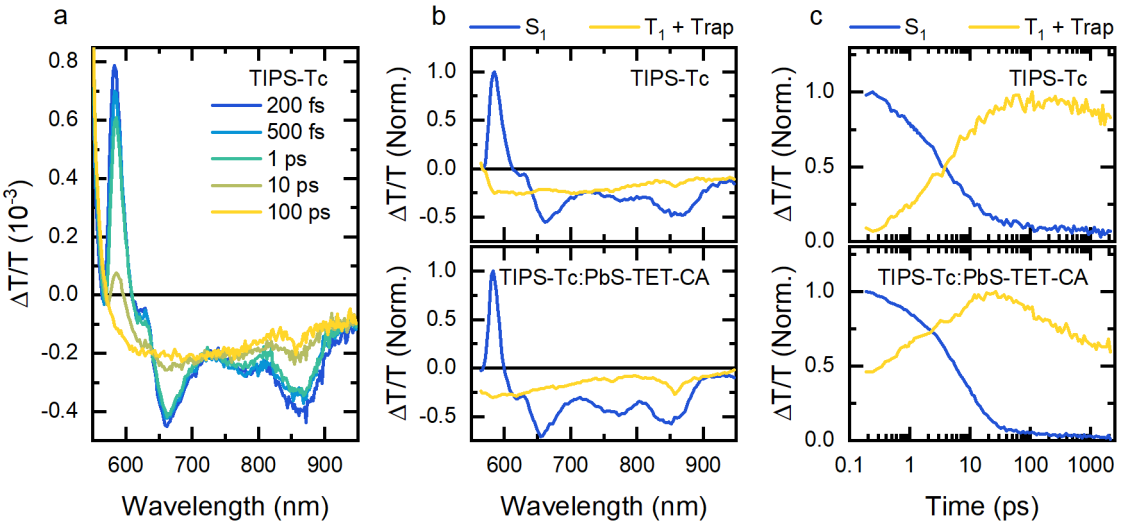

Figure 5.5: Influence of PbS-TET-CA QDs on the TIPS-Tc SF host singlet fission dynamics. Non-aged films, without vacuum solvent removal. a) psTA spectra of a TIPS-Tc film after 535 nm excitation. Decomposition into two components is achieved by the genetic algorithm, into spectra (b) and kinetics (c) of psTA maps. Films of TIPS-Tc and TIPS-Tc:PbS-TET-CA (200:100) were excited at 535 nm with 15 uJ/cm^{-2}. The components are assigned to the spin-singlet character of the multiexciton state (blue curves) and the combination of spectra due to the triplet excitons and a trap state (yellow curves).

The singlet trap features being larger in the pristine TIPS-Tc film, is significant evidence that the singlet trap state is not induced by the PbS QDs. The trap state is likely part of the polycrystalline TIPS-Tc system. We have observed no reduction of the TIPS-Tc singlet fission yield due to the presence of the PbS-TET-CA QDs. To the contrary, the QDs appear to be increasing the triplet yield.

5.4.2 Separation of Triplet and Trap Dynamics

Now we shift our focus to the nsTA spectra to distinguish the kinetics and spectra of the triplet excitons and the singlet trap state. Figure 5.6 shows the nsTA spectra for films of pristine TIPS-Tc and TIPS-Tc:PbS-TET-CA blends. For both films under photoexcitation of the SF host (535 nm), there were strong triplet exciton PIAs observed at ~860 and ~970 nm.[58] The blend film additionally shows a positive signal at 1000-1250 nm assigned to the PbS QD ground state bleach (GSB) and a negative PIA signal from 750 to 1000 nm, due to a QD excited state population. The initial strength of this excited QD state is

assigned to direct excitation by the pump beam. These spectral features are consistent with the observed spectra of the TIPS-Tc:PbS-TET-CA films, under selective photoexcitation of the PbS QDs at 600 nm.

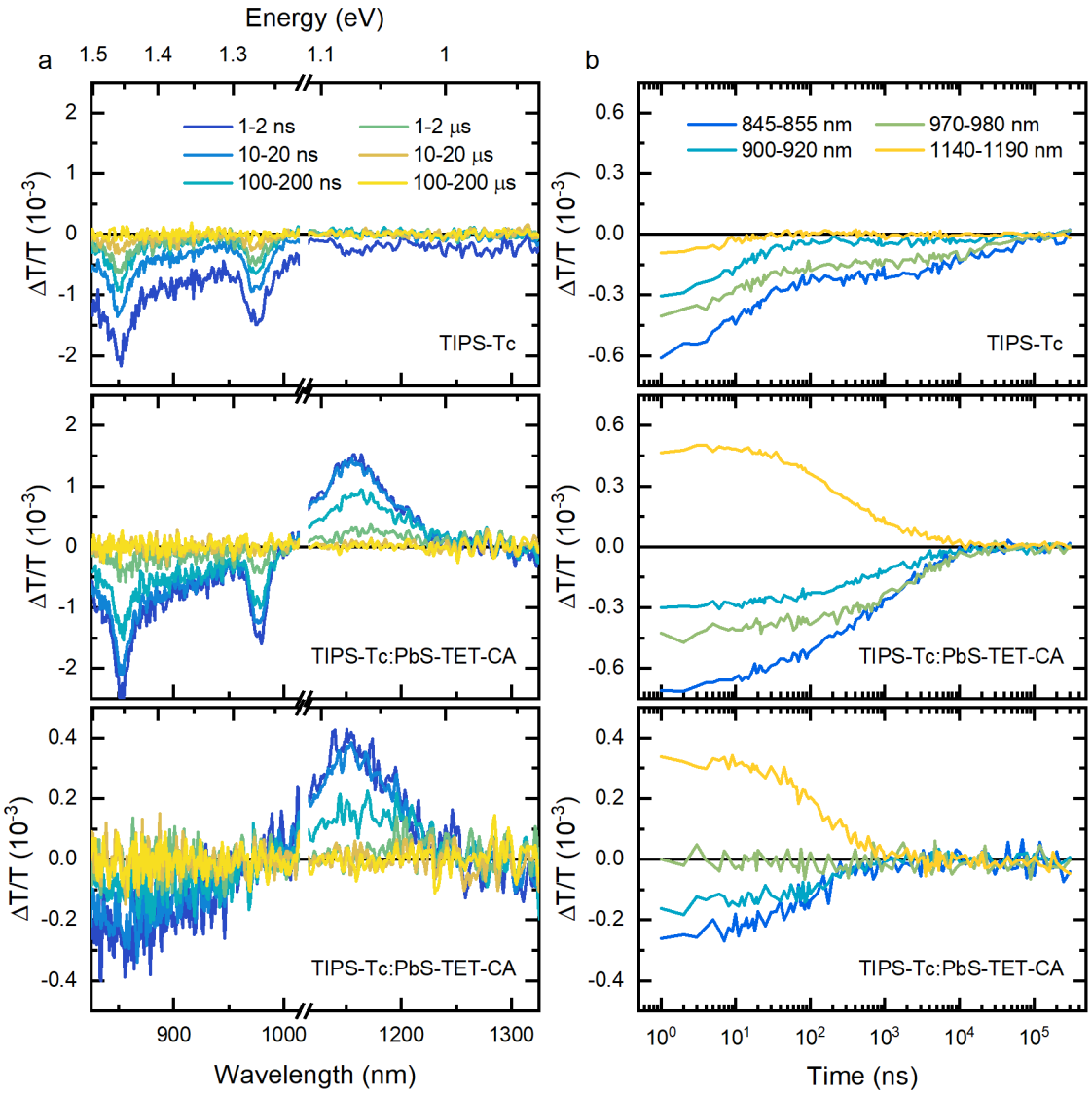

Figure 5.6: Identification of excited states by nsTA spectra of TIPS-Tc:PbS-TET-CA films. Non-aged films, without vacuum solvent removal. nsTA spectra (a) and kinetics (b), averaged over the indicated ranges, for TIPS-Tc:PbS-TET-CA films with 0 and 200 mg/mL of PbS-TET-CA QDs, top and middle respectively, excited at 535 nm with (a) 200 µJ/cm² and (b) 20 µJ/cm². The bottom panel shows the nsTA data for the TIPS-Tc:PbS-TET-CA film with 200 mg/mL of PbS-TET-CA QDs, excited at 600 nm with 12 µJ/cm².

Most obvious in the pristine TIPS-Tc films, there is a broad PIA across the probe range, present at early times. This PIA, consistent with the psTA features of the singlet trap

state, decay within 100 ns. The resultant spectrum consists of predominantly the sharp triplet exciton PIA peaks. To distinguish the dynamics of the various species we utilise the genetic algorithm to decompose the spectra into three components (Figure 5.7). To aid the algorithm with the decomposition we use the following fixed reference spectra; the triplet exciton spectrum is extracted from the nsTA spectra of the TIPS-Tc film under 535 nm excitation, averaged over the 100-200 ns range and the QD excited state spectra taken as the average spectrum between 2-100 ns time range after 600 nm exciton of the TIPS-Tc:PbS-TET-CA film. The final spectrum, assigned to the singlet trap state is determined via the genetic algorithms decomposition of the pristine TIPS-Tc nsTA spectrum with the use of the triplet reference spectrum. The decomposed trap spectrum matches the description earlier of a broad PIA across the probe range.

For the pristine TIPS-Tc films (0 mg/mL of PbS-TET-CA QDs in the precursor solution) the decomposed kinetics show the decay of the initial triplet population, present at 1 ns after photoexcitation, decaying over a 10s of microseconds time period. The trap kinetics decay within 100 ns, over which time there is no corresponding rise in the triplet kinetics. Whereas, the decomposed kinetics of the TIPS-Tc:PbS-TET-CA film (200:200 mg/mL precursor solution) show no population of the trap state for all probe times, while still having a significant triplet population. These observations are consistent with the trap state not being an intermediate to the triplet state. Of note for discussion in the subsequent section on triplet harvesting, the decomposed triplet kinetics show a reduced lifetime in the TIPS-Tc:PbS-TET-CA films, as a result of triplet transfer to the PbS-TET-CA QDs. As the trap and triplet populations appear to decay independently of each other, it is reasonable to compare the initial magnitude of these populations to understand the predetermining processes, as illustrated by Figure 5.7c. As the QD mass fraction in the SF host is increased we observe a significant increase in the nsTA spectra assigned to the initial triplet population. The triplet population is inversely proportional to the initial trap population. An inverse correlation such as this, along with the observation that the trap decay does not result in an increase of the triplet exciton state, is strong evidence that the trap state is a loss channel competing with the generation of triplets. As discussed earlier, there have been many reports of film morphology affecting the singlet fission process. The polarisation optical microscopy observations of increased TIPS-Tc nucleation with the addition of PbS-TET-CA QDs illustrates the significant effect the PbS-TET-CA QDs can have on the SF host morphology (inserts Figure 5.2 b and c). Therefore, the SF host's triplet yield dependence on the QD mass fraction in the blend films is likely the result of a morphological change in the SF host caused by the PbS-TET-CA QDs.

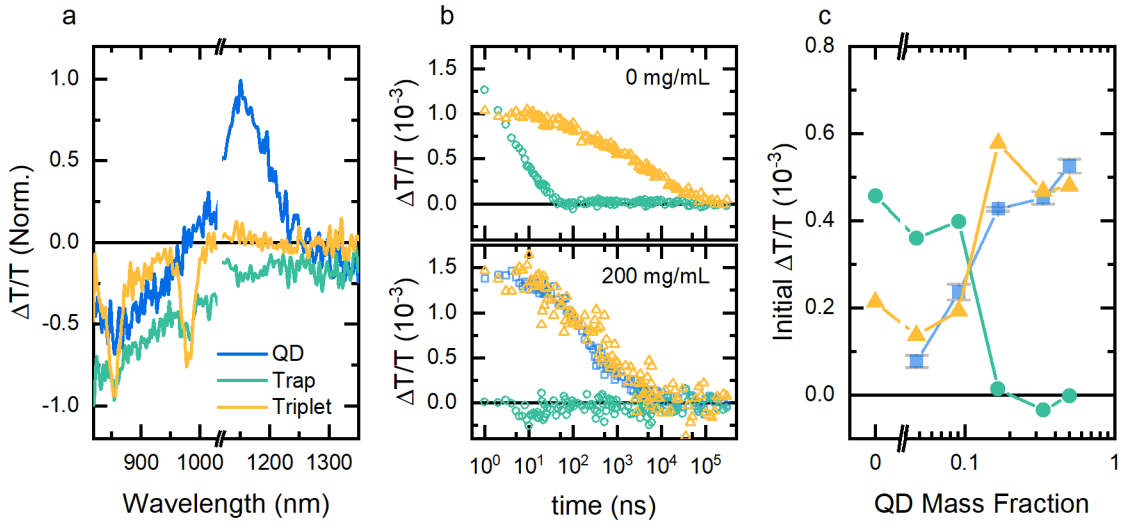

Figure 5.7: Decomposition of nsTA maps for TIPS-Tc:PbS-TET-CA films. Non-aged films, without vacuum solvent removal. a) Decomposition into three components, PbS-TET-CA QD excited state (blue), TIPS-Tc triplet (orange) and TIPS-Tc trap states (green), is achieved by the genetic algorithm. b) Decomposed kinetics for the QD excited state, triplet and trap states for films made from 200 mg/mL of TIPS-Tc with 0 and 200 mg/mL of PbS-TET-CA QDs, top and bottom respectively. c) Initial nsTA signal strength, 1 ns after photoexcitation, of the QD excited state, triplet and trap states as a function of the PbS-TET-CA QD mass fraction. Films were excited at 535 nm with 20 μJ/cm².

To gain further insight, transient photoluminescent (trPL) spectroscopy was employed to investigate the emissive properties of the photoexcited species and triplet dynamics. Figure 5.8a shows the obtained visible PL spectra after selective photoexcitation at 400 nm of TIPS-Tc in films of TIPS-Tc and TIPS-Tc:PbS-TET-CA. We observe considerable differences in spectral features between the two films. the blend film has a PL emission spectrum with peaks at ~550, 580 and 630 nm that are consistent with the vibrionic structure of the TIPS-Tc singlet emission.[58] Whereas, the pristine TIPS-Tc emission is significantly red-shifted in comparison, with a peak at ~650 nm. This red-shifted emission is consistent with emission from an excimer like state, as has previously been noted [55,58,66,123] In the following we will show evidence that this excimer like state and the singlet trap are the same and from now we use the two names interchangeably.

Again, we use the genetic algorithm to decompose the spectra into their respective components. Decomposition of the trPL spectra into two components, yield spectra that are assigned to the singlet and excimer emission, respectively (Figure 5.8b). To highlight the relative strength of the emission from the two components and allow easy comparison between the films, we normalise the components relative to the maximum signal from the decomposed singlet kinetics (Figure 5.8c). From the decomposition of

the pristine TIPS-Tc film's PL spectra, we observe kinetics in which there is a rapid loss of the singlet emission within the first 2 ns after photoexcitation. Given the ~2 ns time resolution of the trPL measurement, this singlet decay is consistent with the <100 ps decay observed via psTA for the same film. Subsequently, the excimer like emission decay with a ~10 ns decay constant. After 100 ns there is a resurgence of both the singlet excimer emission with much longer ~100 µs lifetimes. Decomposed trPL kinetics for the TIPS-Tc:PbS-TET-CA films show similar initial decays for the singlet and excimer emission. However, the relative levels of the excimer emission were significantly lower in this film. Additionally, the delayed trPL components were significantly weaker.

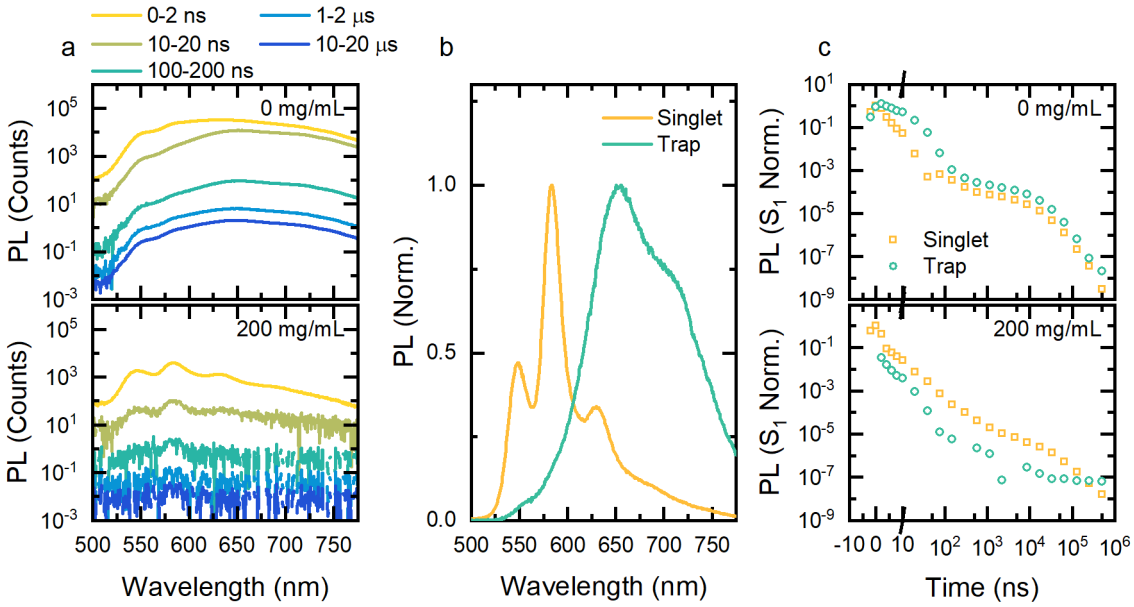

Figure 5.8: Identification of excimer state by visible transient PL from TIPS-Tc:PbS-TET-CA films. Non-aged films, without vacuum solvent removal. a) Transient PL spectra for films with 0 and 200 mg/mL of PbS-TET-CA QDs, top and bottom respectively. Samples were excited at 400 nm with 1000 uW (1.6 mJ/cm^2). b) Decomposition into two components, TIPS-Tc singlet and TIPS-Tc trap emission, is achieved by the genetic algorithm. c) Decomposed kinetics for the singlet and trap emission for films with 0 and 200 mg/mL of PbS-TET-CA QDs, top and bottom respectively.

To identify the cause of the delayed, long-lived singlet and excimer PL, fluence dependent trPL measurements were obtained and decomposed in the same way (Figure 5.9a). Here we observe that the strength of both the delayed singlet and excimer emission increase in strength, relative to the initial decay components, with increased excitation fluence. Previous studies of singlet fission materials have identified similar behaving long-lived PL signals and assigned the cause to non-geminate triplet-triplet annihilation (TTA) regenerating the singlet exciton.[47,48,172] From our nsTA studies, the dominate excited state species in the SF host at times > 100 ns after photoexcitation is

the triplet exciton. Any increase in the pump fluence should result in an increased triplet density after the singlet fission process has occurred. Consequently, the increase in triplet density will lead to an increased proportion of TTA occurring across the lifetime of the triplet, leading to an increased delayed excited singlet density and resultant singlet emission. These predictions are consistent with our observed singlet fluence dependence.

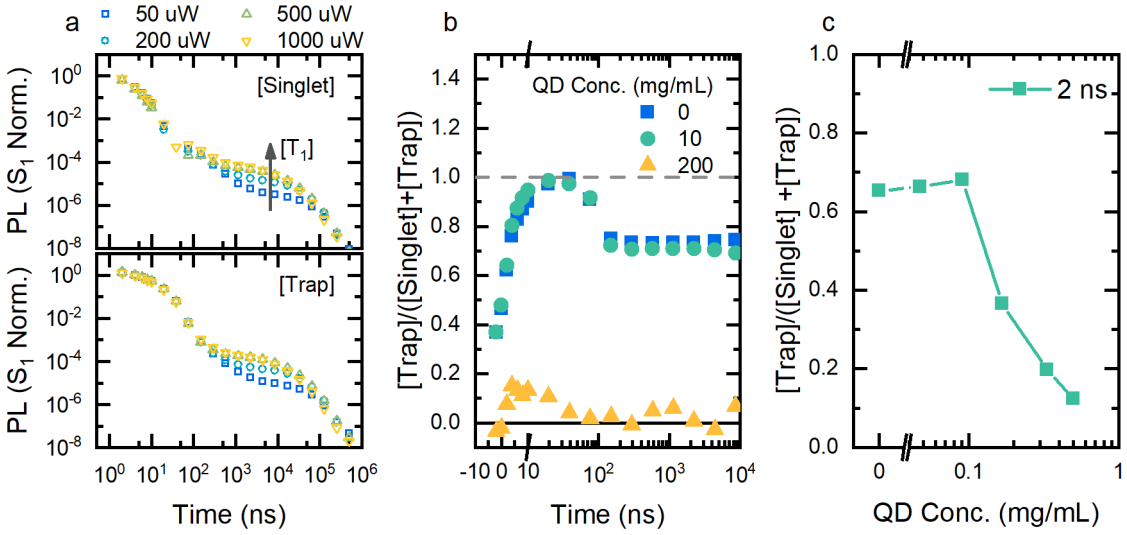

Figure 5.9: Triplet-triplet annihilation and evidence of non-sequential singlet fission. Non-aged films, without vacuum solvent removal. a) Singlet and trap population from the decomposition of the transient PL from a TIPS-Tc film under varying fluences from 50-1000 uW (80-1600 μJ/cm^2) at 400 nm excitation. b) The ratio of the PL signal strength from the trap state to total PL strength as a function of time after photoexcitation with 1000 uW (1.6 mJ/cm^2) at 400 nm. films used were made from solutions at 200 mg/mL TIPS-Tc and PbS-TET-CA QD concentrations as shown. c) The ratio of the PL signal strength from the trap state to total PL strength as a function of PbS-TET-CA QD mass fraction at 2 ns after photoexcitation with 50 uW (80 μJ/cm^2) at 400 nm.

Interestingly the increased fluence also increases the strength of the delayed excimer emission, suggesting that TTA can result in the generation of the excimer state. Figure 5.9b highlights the relative ratio of the excimer emission to the total emission, for TIP-Tc:PbS-TET-CA films with a variety of QD mass fractions. We observe PL that is singlet dominated at early times (< 5 ns), excimer dominated at intermediate times (10-50 ns) and shifting to higher levels of singlet emission at later times (>100 nm). Behaviour such as this, in concentrated TIPS-Tc solutions, has been analysed previously with the conclusion that it is the result of TTA directly to the singlet followed by singlet decay to the excimer state.[66] In that report, the authors were able to rule out TTA directly to the excimer state as a dominate kinetic pathway. Based on the similar trend in excimer to

total PL ratio observed here, we suggest that the same is true for the solid-state TIPS-Tc system.

At increased QD mass fractions, we see similar singlet and excimer dynamics, however, the fraction of the PL due to excimer emission is significantly lower (Figure 5.9b). Based on the above arguments for TTA directly to the singlet state as the dominant channel, the decreased excimer ratios in the delayed component is consistent with a lower fraction of the singlet exciton decaying to the excimer state. The initial proportion of excimer traps as a function of QD mass fraction is highlighted in figure Figure 5.9c, strongly suggesting that the inclusion of QDs reduces the excimer formation in the films. Furthermore, the similar kinetics of the initial excimer trPL decay, regeneration of excimer states via TTA to the singlet and the dependence of the excimer population on the QD mass fraction are all consistent with the singlet trap and the excimer state being one and the same.

5.4.3 Fabrication Control of SF Host Morphology

We have shown that the addition of PbS-TET-CA QDs to the TIPS-Tc SF host cause increased triplet yields, likely due to the formation of a TIPS-Tc morphology that favours singlet fission over the production of the singlet trap state. We now seek a method to force a similar morphological change, and associated high triplet yields, independent to the PbS-TET-CA QDs. We measure psTA spectra of TIPS-Tc:PbS-TET-CA films prepared under a variety of fabrication conditions, to identify the optimal method. Taking inspiration from the increased TIPS-Tc nucleation density at high QD mass fractions, we investigate the use of post blade-coating solvent removal. The removal of residual solvent from the SF host soon after blade-coating is expected to halt crystal growth and result in smaller crystal domains, similar to the effect of increased nucleation density. The solvent removal is achieved by placing the freshly blade coated films in a vacuum chamber for an extended period of time, at ~10 mbar of pressure. Alternatively ageing the films for a period of 1 week is investigated as a means to control the SF-PM morphology.

Figure 5.10a shows the psTA spectra for a TIPS-Tc:PbS-TET-CA (100:20) film that was subjected to vacuum solvent removal and 1 week of ageing. Similar to our early psTA measurements of TIPS-Tc:PbS-TET-CA films we observe a <100 ps loss of the singlet exciton, as identified by the SE at ~580 nm. However, the subsequent triplet PIA at 860 nm appears significantly larger than the previous measurements.

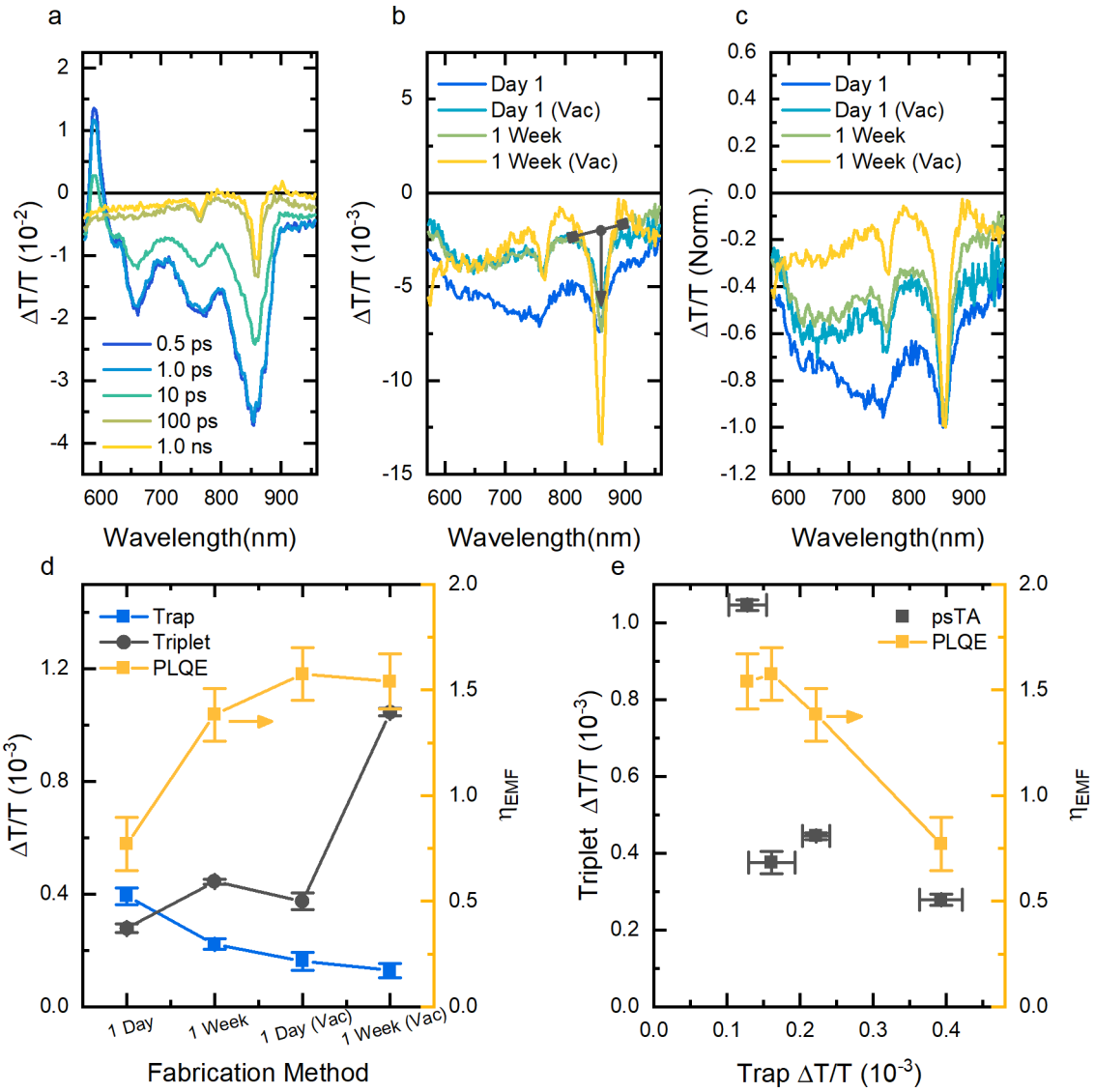

Figure 5.10: Morphological effects on triplet yield resulting from singlet fission.
a) psTA spectra of a TIPS-Tc:PbS-TET-CA (100:20 mg/mL) film subjected to vacuum solvent removal and 1 week of ageing. b,c) psTA spectra after the singlet fission process has occurred (100 ps) for TIPS-Tc:PbS-TET-CA (100:20 mg/mL) films produced under a variety of conditions. The black line from 800-900 nm shows the interpolated background PIA signal assigned to the singlet trap state and the downwards pointing arrow illustrates the magnitude taken for the triplet PIA peak. figure b shows the raw psTA spectra, while spectra in c have been normalised to the triplet PIA peak. All samples we excited at 535 nm with 15 uJ/cm^{-2}. d,e) psTA signal strengths at 100 ps after photoexcitation, determined by owe peak fitting method, for the TIPS-Tc singlet trap state and the TIPS-Tc triplet state as a function of the processing methods. Corresponding SF-PM performance as quantified by calculation of the exciton multiplication factors measured by the PLQE values.

Comparison of the psTA spectra obtained for films prepared under the various methods results in significantly adjusted strengths of the triplet peak and the broad singlet trap PIA from ~600 – 950 nm (Figure 5.10b). To clarify this effect the psTA spectra, after singlet decay, have been normalised to the triplet PIA peak value and shown in Figure 5.10c. Here it is clear that there are vastly differing ratios of the triplet PIA and trap PIA across the investigate film fabrication methods. The vacuum treated and aged film shows the highest ratio of triplet PIA to trap PIA, indicating it as the optimal fabrication method.

Without significant decay of the trap or triplet state over the 2ns time window available in the psTA measurement, there is too little time evolution between the two species to perform a reasonable decomposition. In place, we turn to a simple peak fitting method to quantify the strength of the two PIAs. We quantify the trap PIA signal strength by taking the mean values of the psTA spectra at two wavelength ranges on either side of the triplet PIA peak (790-800 and 910-920 nm). By interpolation at 860nm, via a straight line fit between these two values, we define the strength of the trap PIA as a background to the triplet PIA peak at 860 nm. The strength of the triplet PIA signal is then taken as the value at the triplet PIA peak at 860 nm minus this trap background signal. Figure 5.5d illustrates the relevant points for the day-old film prepared without vacuum solvent removal.

The extracted triplet and trap PIA strengths are shown in Figure 5.10d, for the various film fabrication methods. The triplet PIA strength shows a strong inverse proportionality with the trap strength (Figure 5.10e). Rather than inferring triplet yields from an assigned PIA peak, IR PLQE measurements of the same films were performed as it allows for a comparison of triplet yields as measured by the exciton multiplication factors. We find that the trends observed for the triplet and trap populations by psTA are consistent with those for the η_{EMF} values. In particular the η_{EMF} values are inverse proportional with observed trap PIA signal strength. We do expect some variation between the PLQE and psTA values, as the sample ageing is observed to influence triplet yield and the two measurements were done as close as possible to each other but not simultaneously.

5.4.4 Dynamics of Singlet Trapping

In the following, we will show that the trap state does indeed behave the same as a singlet exciton trap, acting as a loss channel competing with the singlet fission process. Figure 5.11a shows the mean psTA kinetics between 580-590 nm (normalised between

the minimum and maximum values) for TIPS-Tc:PbS-TET-CA films with differing fabrication methods. We see a clear trend between the fabrication method and the decay of the singlet states SE. The SE decay for the film with the highest triplet PIA strength (subjected to vacuum solvent removal and 1 week of ageing), shows an ultrafast (<1 ps) decay of a portion of the SE, in agreement with the ultrafast component of the singlet fission process identify in previous works. To quantify the decay of the singlet SE peak we fit the psTA kinetics with a multi-exponential of the form

$$y = \sum_{i=1}^{3} a_i e^{-k_i \times t} \, .$$

(5.2)

Here the first component captures a proportion of the singlet population that undergoes vibronically coherent ultrafast triplet formation. The second decay rate captures the decay of the remaining excitations with spin-singlet character. The third component captures the subsequent trap and triplet population that occurs.

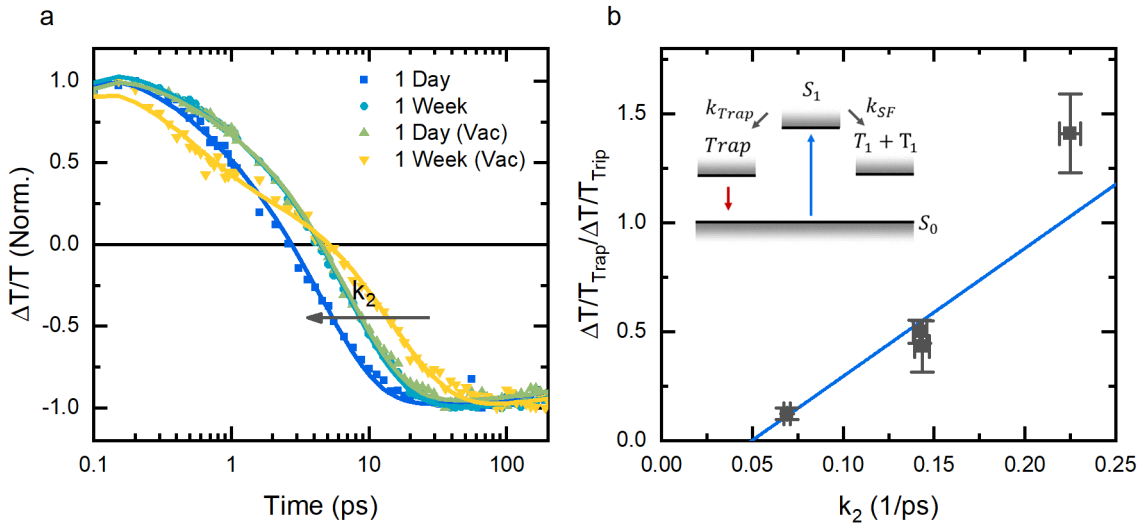

Figure 5.11: TIPS-Tc singlet trapping dynamics in TIPS-Tc:PbS-TET-CA films.
a) Normalised psTA kinetics of the TIPS-Tc SE peak (~580 nm) in films of TIPS-Tc:PbS-TET-CA (100:20 mg/mL) (solid data points), excited at 535 nm with 15 uJ/cm^{-2}. Kinetics fit with a multiexponential function (solid lines). b) The ratio of the trap to triplet psTA signal strengths, at 100 ps after photoexcitation, as a function of the spin-singlet character decay rate k_2 (black squares). Linear fit to the trap to triplet ratio as a function of k_2 (blue line), giving a singlet fission rate of k_{SF} = 0.05 ± 0.02 ps^{-1}, from the x-axis intercept.

Figure 5.11b shows the ratio of the psTA trap PIA strength to the triplet PIA strength as a function of the fitted rate for the slow component of the singlet decay. We observe that a high singlet decay rate is associated with a higher trap to triplet ratio. To gain an understanding of this trend we build a kinetic model of the singlet fission process. The model is of a simple kinetic dynamics nature and does not include any of the quantum mechanics that are needed to fully understand the vibrionic coupling that results in the ultrafast component of singlet loss. We start with the assumption that the vibronically coherent ultrafast component of singlet loss exists and that the fraction, η_{Vib}, of the photoexcited singlet states that form triplets through this vibronically coherent process do so within the first picosecond. The remaining $(1-\eta_{Vib})$ proportion of the photoexcited TIPS-Tc singlet states, S_1, decay dynamics are described by

$$\frac{dS_1}{dt} = -\left(k_S + k_{SF} + k_{Trap}\right)S_1 \,,$$

(5.3)

where k_S, k_{SF} and k_{Trap} are the intrinsic singlet decay rate, the rate for the slow component of the singlet fission process and the singlet trapping rate, respectively. The reported singlet decay rate for TIPS-Tc in dilute solutions is on the order of 10 ns.[56] Thus, in comparison to the ~10 ps lifetime of the singlet SE observed here, the intrinsic singlet decay rate is insignificant and so is ignored for the remaining of the calculation. The total decay rate of S_1 is simplified to $k_2 = k_{SF} + k_{Trap}$. The fraction of S_1 that undergoes singlet fission is given by

$$\eta_{SF} = \frac{k_{SF}}{k_{SF} + k_{Trap}} = \frac{k_{SF}}{k_2}.$$

(5.4)

The fraction that is trapped is given by $\eta_{Trap} = 1 - \eta_{SF}$. The observed signal strengths of the triplet PIA and trap PIA at 100 ps, after the decay of the singlet, are proportional to these fractions, respectively. Finally, within this kinetic model of morphology dependent singlet trapping, the ratio of the trap to triplet psTA PIA signal strengths is given by

$$\frac{\left(\frac{\Delta T}{T}\right)_{Trap}}{\left(\frac{\Delta T}{T}\right)_{Trip}} \propto \frac{1-\eta_{SF}}{\eta_{SF}} = \frac{k_2}{k_{SF}} - 1$$

(5.5)

Finally fitting of a linear function of this form, to the extracted trap to triplet ratio as a function of k_2, yields a rate for the slow component of the singlet fission process of k_{SF} = 0.05 ± 0.02 ps^{-1}. This singlet fission rate is consistent with previous reports of ~10 ps time-constant for the slow component of singlet fission in TIPS-Tc films. Based on this singlet fission rate and the measured rates for k_2, the predicted singlet trapping efficiency varies from (30 ± 30) % to (80 ± 10) %, across the investigate film fabrication methods. A singlet trapping efficiency of (80 ± 10) % represents a significant loss channel in competition with the singlet fission process and should be considered a key performance metric for the optimisation of the solid-state SF-PM system. For the film with the lowest singlet trapping rate, we predict a singlet fission efficiency of (70 ± 30) %, resulting in a triplet yield of (140 ± 60) %. Which is consistent with the exciton multiplication factor of (154 ± 13) %, assuming efficient triplet transfer. These trapping efficiencies represent quantum efficiencies for the slow component of singlet fission, i.e. the probability of singlet trapping given it didn't undergo ultrafast singlet fission. Based on a fractional amplitude of the singlet decay that undergoes ultrafast singlet fission, for the film with the lowest singlet trapping rate, we calculate that this ultrafast route to singlet fission is observed to convert up to ~34% of the initial photoexcited singlet population (η_{Vib} = 0.34). Meaning that the fraction of photoexcited singlet states that undergo singlet trapping for this particular film would be reduced to $(1-\eta_{Vib})\eta_{Trap}$ = (20 ± 20) %. As such, the ultrafast component of singlet fission could offer a means to overcome the singlet trapping loss channel. If a higher fraction of the photoexcited singlet can be engineered to decay via the ultrafast channel, triplet generation could be engineered to out-compete the singlet trapping.

The findings presented above is of interest to the field of singlet fission. Generally, faster spin-singlet character decay rates have been interpreted as more efficient singlet fission.[167] Here we present one situation in opposition to the generalized interpretation as we observe that a longer-lived spin-singlet character is associated with lower trapping and a higher singlet fission yield.

To summarise, singlet fission is not reduced by the presence of the PbS-TET-CA QDs. To the contrary, the TET-CA functionalised QDs leads to an observable increase of the triplet signals relative to the spectral signatures of a competing species. The additional

specie is shown to behave in a manner compatible with that of a singlet trap state. The decay of the singlet trap state does not result in appreciable increases in the triplet population and the dynamics match that of the excimer like emissive state. The regeneration of this trap state at time periods long after photoexcitation (>100 ns) indicates that triplet-triplet annihilation to the singlet exciton followed by decay to the singlet trap is the dominant kinetic pathway, further evidencing that it is not an intermediate state between singlet and triplet states. We find an inverse correlation between the singlet fission triplet yield, as measure by both nsTA and PLQE experiments, and the observed trap population. Finally, we show direct evidence that the increased singlet decay rate due to trapping to this excimer like state occurs in competition to the singlet fission process. Alternative to having the PbS-TET-CA QD mass fraction control the abundance of the trap state within the films, we identify post blade-coating solvent removal and sample ageing as fabrication methods which result in the reduction of trap states and concomitant enhancement of the singlet fission yields.

We identify enhancement of the vibronically coherent, ultrafast, component of the singlet fission process as a possible means to reduce the singlet trapping efficiency. In agreement with our steady-state magnetic dependent PL results, which identify triplet exciton transfer as the dominant pathway resulting in QD excited state emission, we observe no significant singlet quenching that could be assigned to singlet exciton transfer to the QDs.

5.5 Triplet Harvesting Dynamics

Armed with the insights gained so far into the singlet fission process occurring in our solid-state SF-PM films we descend further down the rabbit hole, to investigate the dynamics of the triplet harvesting process. We perform a nsTA fluence series to confirm bimolecular decay of the TIPS-Tc triplet (Figure 5.12). Excitation of a film of TIPS-Tc with 535 nm incident pump shows a faster decay of the TIPS-Tc triplet signal (PIA at 970 nm) at higher fluences. This nonlinear effect with respect to the triplet population is consistent with the presence of a bi-molecular triplet decay channel. Due to the limited wavelength resolution of the nsTA experiment, we were unable to discern the subtle shifts in the triplet PIA peak position that have previously been associated with the thermally activated separation of the correlated triplet pair state and the individual free triplets.[58,123,173] Thus, when addressing the triplet population, at any time after loss of

the singlet exciton due to singlet fission, we are referring to both correlated and free triplet together. However, the observed excitation dependence of the triplet PIA decay indicates that the triplet excitons we observe on >100 ns timescale are free triplets, not in the correlated triplet-triplet pair state.[164] With this fluence dependence in mind, the subsequent nsTA measurements to investigate the harvesting of the triplet population are conducted at sufficiently low fluences.

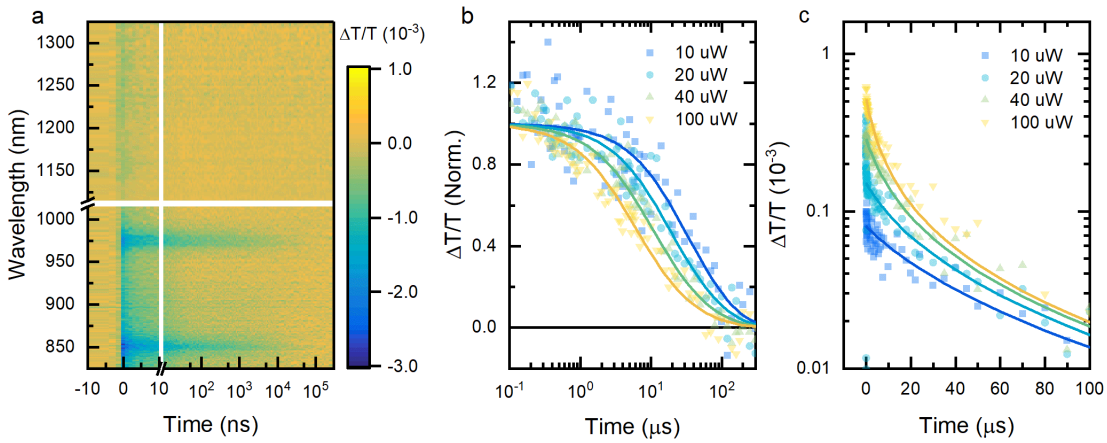

Figure 5.12: Triplet bi-molecular decay in nsTA of a TIPS-Tc film under 535 nm excitation. a) nsTA map under 100 μW excitation. Normalised (b) and raw (c) nsTA kinetics at probed at 970 nm under fluences 20, 40, 80 and 200 μJ/cm^2. The solid lines are a guide to the eye to illustrate the non-linear behaviour of the triplet population dynamics.

5.5.1 Microsecond Triplet Transfer

Figure 5.13a shows the measured nsTA maps of TIPS-Tc, TIPS-Tc:PbS-TET-CA and TIPS-Tc:PbS-OA films, under excitation predominately of the SF host (515nm). We observe the TIPS-Tc triplet PIAs at ~860 and ~970 nm. The use of 515 nm excitation, a wavelength between two of the vibrionic absorption peaks of TIPS-Tc, may at first seem illogical. However, this choice was in fact extensively considered. Due to the already noted triplet bi-molecular decay, extraction of monomeric triplet decays with 535nm excitation proved experimentally challenging, within the achievable signal-to-noise constraints. Excitation at a wavelength still within the TIPS-Tc absorption spectrum, but off the absorption peak with its corresponding short pump penetration depth, allows excitation of similar total triplet populations with significantly lower excitation densities. Leading to lower proportions of bi-molecular decay and sufficiently monomeric triplet decays for extraction of the intrinsic triplet lifetime. These triplet PIA features are significantly quenched in the PbS-TET-CA:TIPS-Tc films (Figure 5.13b). The quenching can be caused

by processes such as the introduction of triplet trap states or the presence of triplet exciton transfer to the QDs. To confirm the later, we shift to an interrogation of the QD excited state population.

Due to the overlap of the TIPS-Tc and PbS QD absorption, excitation with 515 nm pump leads to substantial excitation of the QDs directly. The nsTA spectra reflect the effect of the direct excitation as observed by the positive nsTA feature assigned to QD GSB at ~1150 nm, for times greater than 1 ns after photoexcitation (Figure 5.14). In this same wavelength region there is spectral overlap with the singlet trap PIA, as observed by the negative nsTA signal in a pristine TIPS-Tc film. The negative singlet PIA signal is sufficiently decayed after 50 ns, such that it does not interfere with normalisation of the QD GSB strength at this time point. Upon normalisation an extension of the QD GSB under excitation of the SF host, relative to selective excitation of the QD (600 nm). Taking the difference, between the nsTA kinetic under 515 nm excitation and a bi-exponential fit to the same kinetic under 600 nm excitation, highlights the population of additional QD excited states, $[QD_1]$. Here we see an additional QD excited state population that rises over the cause of ~1 µs, followed by a ~10 µs decay. These timescales are consistent with the additional QD excited state population being the result of triplet exciton transfer from the TIPS-Tc triplet state, $[T_{1,1}]$. In the low triplet excitation density regime, appropriate for the current experimental conditions, the TIPS-Tc triplet population, $[T_{1,1}]$, can be described by

$$\frac{d[T_{1,1}]}{dt} = -(k_1 + k_{TET})[T_{1,1}]\,. \tag{5.6}$$

Here k_1 is the intrinsic triplet decay rate and k_{TET} is the triplet transfer rate to the PbS-TET-CA QDs. We have imposed the assumption that there is negligible triplet trapping introduced by the QD disturbing the SF host. With the evidence of significant triplet transfer by inspection of the exciton multiplication factors found in Section 5.3, this assumption is reasonably substantiated.

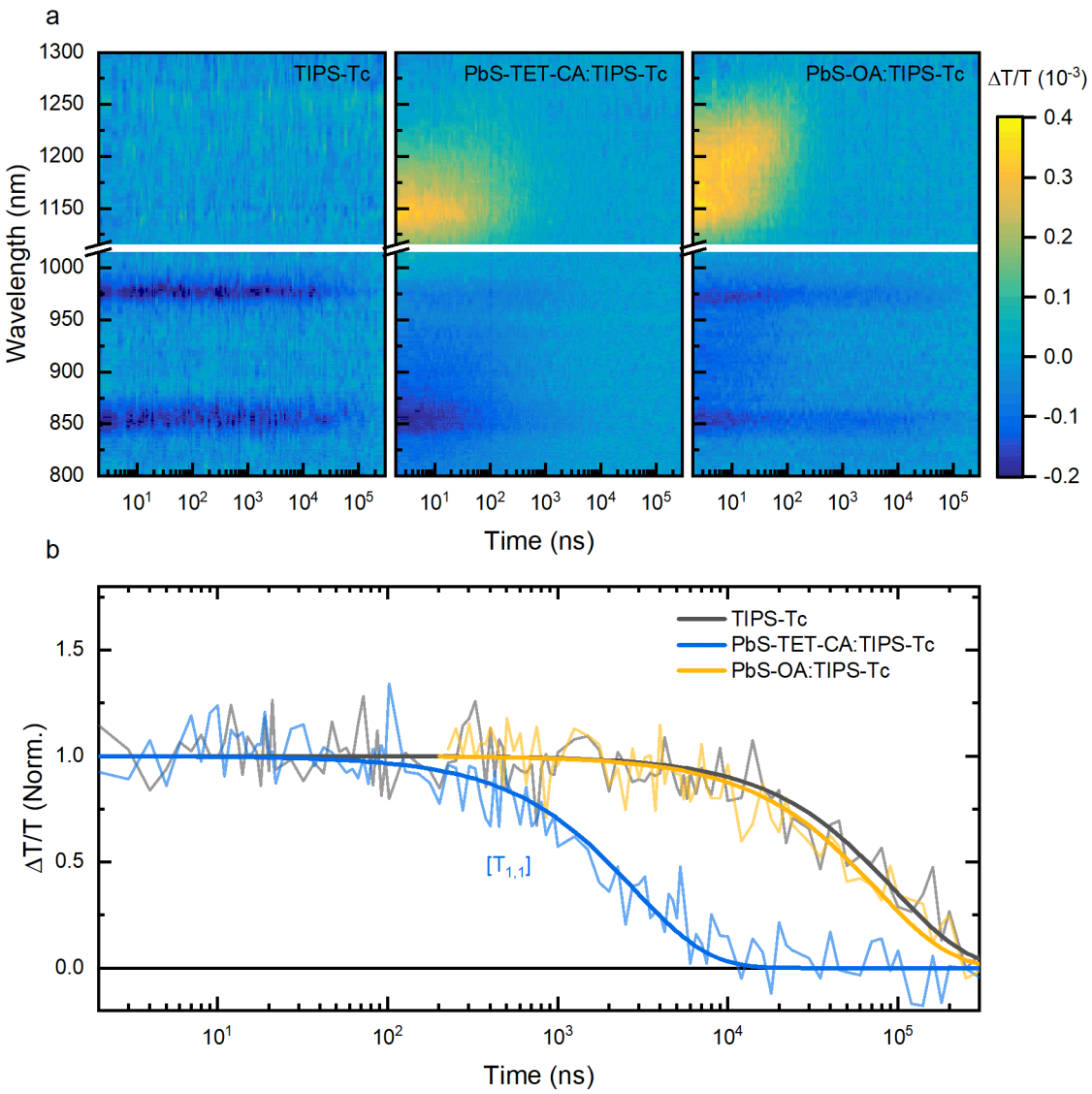

Figure 5.13: Time-resolved triplet harvesting in TIPS-Tc:PbS-TET-CA films.
a) Nanosecond transient absorption maps for films of TIPS-Tc, either pristine, with PbS-TET-CA or PbS-OA QDs, excited at 515 nm with ~15 μJ/cm^2. The TIPS-Tc triplet PIA peaks at 850 and 970 nm are clear in all cases. However, the triplet lifetime varies between the films, the TIPS-Tc:PbS-TET-CA film having the shortest lifetime. Predominately due to direct photoexcitation, in the SF-PM systems the QD GSB is observed at 1100-1250 nm from early times (<2 ns). In the TIPS-Tc:PbS-OA there is clear red-shifting of the QD GSB within the first 10 ns after photoexcitation. b) Normalised nsTA kinetics at the TIPS-Tc triplet PIA (965-980 nm) for films of TIPS-Tc, either pristine (light grey curve), with PbS-OA (light orange curve) or with PbS-TET-CA quantum dots (light blue curve), excited at 515 nm with ~15 μJ/cm^2, with mono-exponential fits (darker curves).

Fitting of the triplet PIA kinetics at ~970 nm with mono-exponential decays allows the extraction of the triplet intrinsic decay rate and the triplet transfer rate (Table 5.1). For the PbS-TET-CA:TIPS-Tc films we extraction a triplet transfer rate of 0.34 ± 0.03 μs^{-1}. Comparison with the intrinsic triplet decay rate of (1.05 ± 0.10) x 10^{-2} μs^{-1}, we estimate a triplet transfer efficiency of η_{TET} = (97 ± 11) %, suggesting that the PbS-TET-CA QDs are able to efficiently harvest the majority of the singlet fission generated triplet excitons. The first such demonstration in an organic semiconductor and inorganic QD, bulk solid-state system. Based on an exciton multiplication factor of η_{EMF} = (186 ± 18) %, for the same TIPS-Tc:PbS-TET-CA film, obtained by IR PLQE measurements, we can predict the singlet fission efficiency occurring within the SF host. Using the expression $\eta_{EMF} = \eta_{SF}\eta_{TET}$ and the triplet transfer efficiency found here, we calculate a singlet fission yield of η_{SF} = (192 ± 28) %. The estimated singlet fission yield is in agreement with the upper bound of previously reported values. The predicted yield, in agreement with a value approaching 200 % yield in the solid state, is testament to the morphological control of the singlet fission process that we developed in Section 5.4. Along with the ability of a significantly more direct method of triplet yield estimation, based on triplet extraction efficiencies rather than the usual spectroscopic determination by triplet attenuation estimates. Being able to determine the singlet fission yield in a more direct manner also respects a significant step forward for the singlet fission community.[55,58,173]

In comparison, significantly less quenching of the TIPS-Tc triplet is observed with films containing the PbS-OA QDs. The extracted triplet transfer rate of (2.8 ± 1.6) x 10^{-3} μs^{-1}, is significantly slower than for the PbS-TET-CA QDs. Due to propagation of the large percentage uncertainty in this rate, the calculate triplet transfer efficiency of (20 ± 15) % has a large uncertainty range. Though, it is most definitely a low efficiency, in agreement with the observation of negligible triplet transfer as measured by IR PLQE results of the same film (Section 5.3). These observations are compatible with previous results for triplet exciton transfer in bilayers of organic semiconductors and PbS-OA QDs.[81,101,118]

Later in Section 5.6 we use transient IR photoluminescence measurements, which have significantly improved signal to noise for the QD transient population, to gain further insight into the transfer of triplet exciton to the PbS QDs and the possibility of intermediate states.

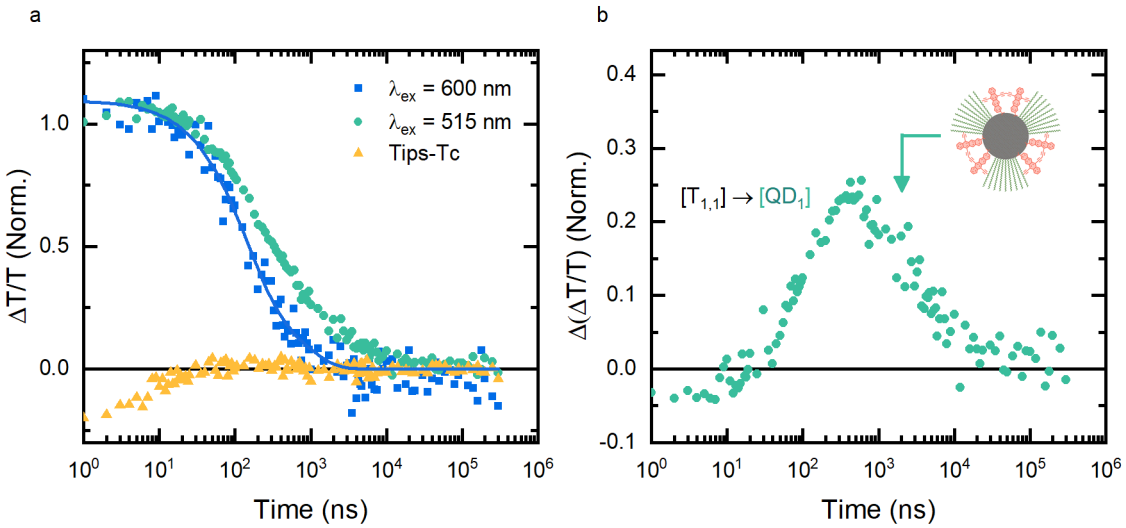

Figure 5.14: Identification of triplet transfer to QD excited states in TIPS-Tc:PbS-TET-CA films. a) nsTA kinetics at the QD GSB, averaged across the range 1140-1190 nm, for a TIPS-Tc:PbS-TET-CA film (200:200 mg/mL precursor solution), under 515 nm, 20 μJ/cm^2 (green circles) and 600 nm, 12 μJ/cm^2 (blue squares) excitation. Kinetics have been normalised to the value at 50 ns after photoexcitation. The QD GSB under 515 nm excitation has been fit with a bi-exponential fit as a guide to the eye (blue curve). Corresponding kinetic for pristine TIPS-Tc excited at 515 nm, normalised by the same value as the blend film (orange triangles). b) nsTA difference kinetic, for TIPS-Tc:PbS-TET-CA film, between nsTA data at 515 nm excitation and nsTA fit at 600 nm excitation (green circles).

5.5.2 Reduced QD Excited State Trapping

We temporally digress to examine the interaction between PbS QDs when embedded in the SF host. We monitor the QD GSB to track the relaxation of the QD excited state population to low energy sites. As the excited states transfer between QDs, to lower energy QD sites, the GSB should shift to longer wavelengths.[174] Inspection of the PbS-OA QD GSB, under selective excitation of the QDs in the blend films, shows a significant redshift over the course of its decay (Figure 5.15a). Suggesting significant interdot transfer, a hallmark of QD aggregation.[158] Whereas, the PbS-TET-CA QD GSB shows little redshift in wavelength. Indicating weaker interdot transfer, compatible with a greater isolation of the QDs within the singlet fission host. Figure 5.15b shows the decay in QD excited state population over the same time period. The PbS-OA QDs excited state population shows a significantly reduced lifetime in comparison to the PbS-TET-CA QDs. Fitting of the QD GSB with mono-exponential decays suggests 72 ± 2 ns and 306 ± 14 ns lifetimes respectively of the PbS-OA and PbS-TET-CA QDs in the TIPS-Tc:QD films.

Fitting of the QD GSB with a Gaussian peak shape, allows extraction of the peak position and tracking of the excited state relaxation. We convert the wavelength shift to an energy change and fit the shift in energy to a mono-exponential decay (Figure 5.15c). The PbS-OA QDs show a dramatically faster and larger drop in the energy of the QD excited state population.

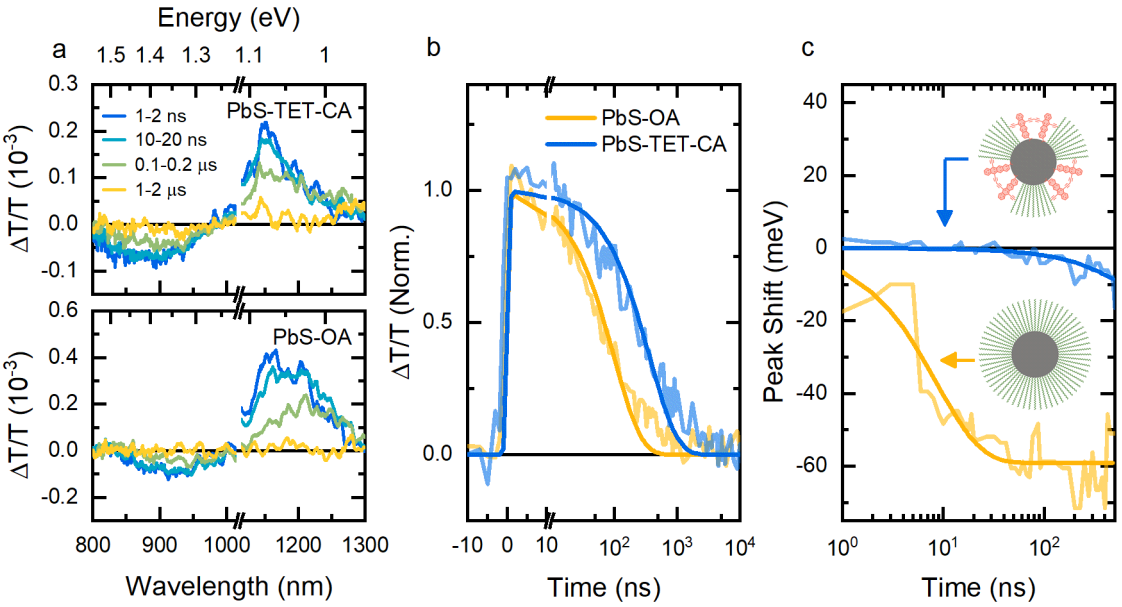

Figure 5.15: Interdot excited state transfer and trapping in TIPS-Tc:QD films.
a) Nanosecond transient absorption spectra for films of TIPS-Tc with PbS-TET-CA or PbS-OA QDs, excited at 658 nm with ~15 µJ/cm^2. Films were prepared at 2:1, TIPS-Tc:QD mass ratio. Transient absorption spectra are averaged over the time ranges indicated. b) Nanosecond transient absorption kinetics of the PbS QD GSB (1120-1180 nm). The kinetics have been fit with mono-exponential decays. The PbS-OA GSB decays with a 72 ± 2 ns lifetimes. The PbS-TET-CA GSB decays with a 306 ± 14 ns lifetimes. c) Shift in peak position of the maximum signal of the GSB of the PbS quantum dot, in films of TIPS-Tc:PbS-OA (light orange curve) and TIPS-Tc:PbS-TET-CA (light blue curve), with mono-exponential fits (darker curves). The shifts in peak wavelength have been parameterised with an exponential decay with constant offset. The peaks of the PbS-OA QD GSB drops by 60 ± 10 meV, with a time constant of 9 ± 1 ns. The peaks of the PbS-TET-CA QD GSB drops by 10 ± 5 meV, with a time constant of 1500 ± 200 ns.

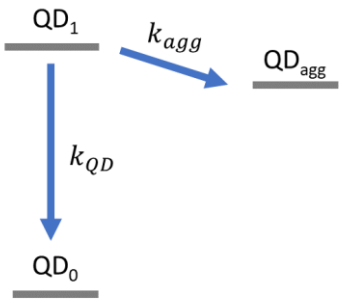

Figure 5.16: Competition between exciton decay and transfer to low energy QD sites. Illustration off the simple kinetic model used to capture the branching between aggregation assisted hoping to lower QD sites QD_{agg}, and isolated QD decay rate.

We construct a kinetic model, as illustrated by Figure 5.16, that simplistically assumes a branching between QD excited state decay and transfer to a low energy QD site. Within this model, we estimate the QD aggregation assisted trapping efficiency as

$$\eta_{agg} = \frac{k_{agg}}{k_{agg} + k_{QD}} \ . \tag{5.7}$$

Taking the rates from the fitting to the position of the QD GSB peak and the decay of the total area under the GSB we calculate interdot transfer assisted trapping efficiencies of (90 ± 20) % and (17 ± 2)% for the OA and TET-CA capped QDs respectively.

Even without the considerations of triplet transfer, these observations show the powerful effects the TET-CA ligand has on the intrinsic excited state dynamics of the PbS QDs alone, when dispersed within the SF host. Without functionalisation, we observe substantial interdot energy transfer associated with QD aggregation. Functionalisation with the TET-CA ligand results significant improvement of the excited state lifetime and reduction of the efficiency of excited state trapping. These insights are in accordance with the morphological insight, from X-ray scattering and TEM characterisation of the films, that the PbS-TET-CA QDs are significantly more well-dispersed within the SF host and QD aggregation is reduced (Section 5.2).

	k_1 (1/us)	k_{TET} (1/us)	η_{TET} (%)	k_{QD} (1/us)	k_{agg} (1/us)	η_{agg} (%)
TIPS-Tc	0.0105 ± 0.0010	-	-	-	-	-
PbS-TET-CA:TIPS-Tc	0.0105 ± 0.0010	0.34 ± 0.03	0.97 ± 0.11	3.27 ± 0.15	0.68 ± 0.08	17 ± 2
PbS-OA:TIPS-Tc	0.0105 ± 0.0010	0.0028 ±0.0016	0.20 ± 0.15	13.8 ± 0.4	110 ± 20	90 ± 20

Table 5.1: Kinetic parameters obtained from fitting nanosecond transient absorption kinetics. Triplet intrinsic k_1 and transfer k_{TET} rates were calculated from fitting of mono-exponential functions to the TIPS-Tc triplet PIA at 865-980 nm, under 515 nm excitation at ~15 μJ/cm^2. The QD intrinsic decay rate is established from a mono-exponential fit to the GSB at 1120-1180 nm, under 658 nm excitation at ~15 μJ/cm^2. The triplet exciton transfer efficiency, η_{TET}, is calculated from the ratio between the triplet transfer rate and the sum of all relevant triplet decay channels. QD excited state aggregation induced trapping rate and efficiency calculated by peak fitting the QD GSB decay after 658 nm excitation.

5.5.3 Quenching of Triplet-Triplet Annihilation PL

Having gained valuable insight into the dynamics of triplet harvesting in TIPS-Tc:PbS-TET-CA films by transient absorption, we now investigate the related effects on the emissive properties of the films. As introduced in Section 5.4.2, the delayed singlet photoluminescence is the result of triplet-triplet annihilation regenerating the singlet state. The delayed singlet emission occurs on microsecond timescales, long after the generation of the triplet excitons by singlet fission. Thus, the delayed singlet fluorescence, PL_{TTA}, is proportional to the square of the density of TIPS-Tc triplet density $\left[T_{1,1}\right]^2$.[145] Taking the time dependence of the triplet density in the low fluence as described by equation (5.6), the time dependence of the delayed singlet emission can be written as

$$\frac{d\sqrt{PL_{TTA}}}{dt} \propto \frac{d\left[T_{1,1}\right]}{dt} = -(k_1 + k_{TET})\left[T_{1,1}\right]. \tag{5.8}$$

With this in mind, Figure 5.17a shows the square root of the delayed singlet kinetics, as decomposed by the spectra determined in Section 5.4.2 by the genetic algorithm, and fit with bi-exponential decay functions. As the PbS-TET-CA QD mass fraction in the SF

host increases we witness a substantial reduction of the delayed singlet emission. With the interpretation that the delayed singlet emission is due to TTA, these observations are consistent with the observation of triplet harvesting from the nsTA experiments. We find that fitting the square root of the singlet PL with a bi-exponential decay is required to reproduce the triplet dynamics. The faster decay rate is in agreement with the triplet transfer rates seen by nsTA measurements and this value is interpreted as the sum of intrinsic triplet decay and transfer rate (Figure 5.17b). The extracted triplet transfer rate shows a gradual increased with increasing QD mass fraction. From a SF-PM performance point of view there is an advantage in keeping the parasitic QD absorption to a minimum. Therefore, the minimum QD mass fraction, at which efficient triplet transfer is achieved, is an incredibly useful parameter. Figure 5.17c displays the triplet transfer efficiency based on the ratio of extracted triplet transfer rate and the decay rate for pristine TIPS-Tc. In this way we illustrate that at TIPS-Tc:PbS-TET-CA mass ratios of 5:1, triplet transfer greater than 90% can be achieved, establishing an approximate lower bound on the desired QD mass fraction of ~10 %.

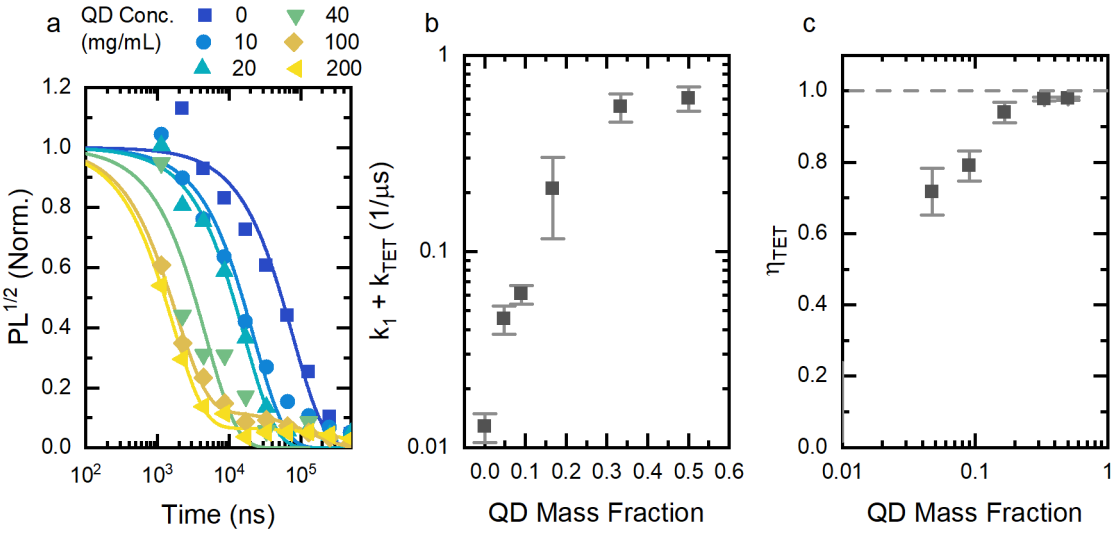

Figure 5.17: Identification of triplet transfer by monitoring the TIPS-Tc visible PL.
a) Square root of the Singlet component of transient PL from films of TIPS-Tc (200 mg/mL) and varying amounts of PbS-TET-CA under excitation 80 µJ/cm² of 400 nm. The kinetics have been fit with bi-exponential decays and normalised to the initial value of the decay for clarity. b) Fitted fast decay rate (k_1) as a function of the QD mass fraction. c) Resulting triplet transfer efficiency based on k_1 and an intrinsic triplet decay rate of k_T = 13 ± 2 ms^{-1}.

The slow exponential decay component indicates the presence of unharvested triplet excitons. This population of long lived TIPS-Tc triplets might be the result of back transfer of triplet excitons from the PbS-TET-CA QDs to the TIPS-Tc.[97] Alternatively, the remaining

triplet population might be from spatial variation of the triplet harvesting leading to pockets of unharvested triplets. This later possibility is explored in the following section.

5.5.4 Spatial Variation of Triplet Harvesting

We perform spatial-temporal mapping of the TIPS-Tc visible PL (550 ± 40 nm emission), using confocal microscopy time-correlated single photon counting (TCSPC) measurements to investigate the spatial variation of the triplet harvesting by PbS-TET-CA QDs. Figure 5.18a shows the summation of the PL kinetics over the ~1000 μm^2 area of investigation.

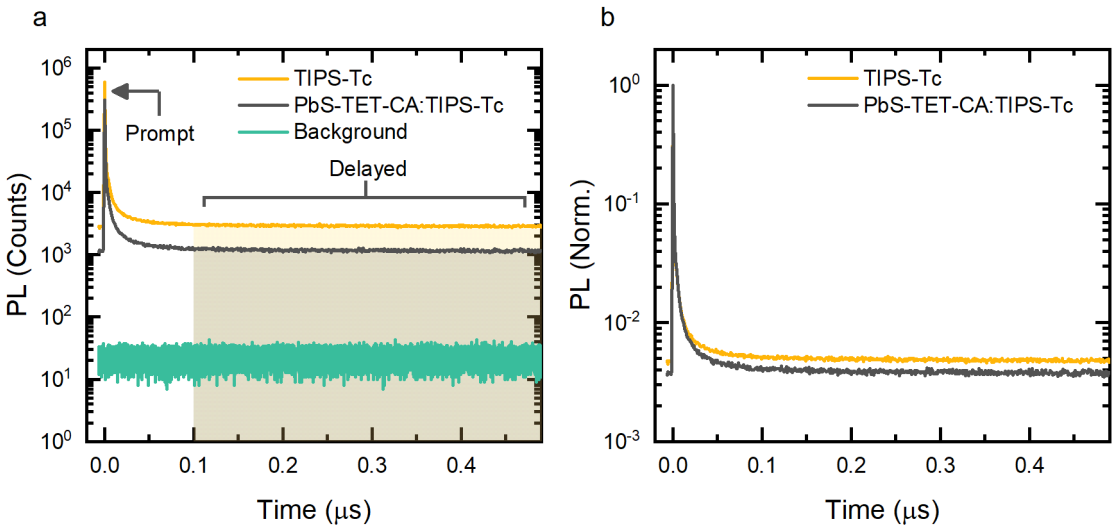

Figure 5.18: TIPS-Tc transient visible PL in TIPS-Tc and PbS-TET-CA:TIPS-Tc films. The TIPS-Tc PL decay is detected at 550 ± 40 nm after 405 nm excitation at a fluence of 50 μJcm^{-2} and 2 MHz pump rep rate. a) Kinetics found by summation of PL decays over entire ~1000 μm^2 area of investigation. With no sample in the microscope, the background counts over the same integration time was measured (green curve). b) Background corrected and normalised PL kinetics. The TIPS-Tc:PbS-TET-CA film was prepared at a 2:1 mass ratio.

We assign the fast decaying, prompt component (<2 ns lifetime) to the quenching of the singlet emission by singlet fission and the longer delayed component (more than 100 ns after the pump) to long-lived singlet emission resulting from triplet-triplet annihilation back to the singlet state. We distinguish this delayed component from the background detector counts by explicitly measuring the corresponding counts, with no sample under excitation, over the same detector acquisition period. Removal of this background signal allows correction of the PL kinetics followed by normalisation to the value at t=0 (Figure 5.18b). With this normalisation it is clear that the addition of PbS-TE-CA QDs to the TIPS-

Tc film, results in a decreased delayed PL component. In accordance with results from the trPL measurements.

The average counts per nanosecond, for the prompt (0-3 ns) and delayed component (100-500 ns) were calculated spatially. The normalisation of the delayed component by this prompt count rate gives a quantity that is approximately independent of the local density and mount of TIPS-Tc material. Instead, it is only predominately dependent on the local triplet density. This approach is similar to a normalisation of kinetics to the initial PL counts and gives an effective "TTA map" of the films (Figure 5.19 a and b). The film of pristine TIPS-Tc shows little spatial dependence of the "normalised" delayed component. Indicating a uniform triplet density across the film. However, the PbS-TET-CA:TIPS-Tc film shows variations in the intensity of the TTA intensity on the micron scale. This spatial variation could be the result of spatial variation of the triplet yield from singlet fission, variations in the density of PbS-TET-CA as associated harvesting or differences in the triplet diffusion coefficient, among other possibilities.

The spatial dependence of the TTA intensity can be represented as a distribution of delayed PL intensity (Figure 5.19c). The distribution of delayed PL counts is clearly lower for the PbS-TET-CA:TIPS-Tc films in agreement with the nsTA measurement of triplet quenching. Under the assumption that this spatial variation is due to triplet density variations, the quasi-steady-state nature of the TTA PL suggests that the treatment of magnitude of the singlet emission, due to TTA, as proportional to the square of the triplet density, $PL_{TTA} \propto \left[T_{1,1}\right]^2$ is appropriate. Thus, by taking the square root of PL_{TTA}, we can make the conversion from the delayed component counts to relative triplet population. Here we see the PbS-TET-CA:TIPS-Tc films have lower triplet densities, which we assign to the harvesting of TIPS-Tc triplets by the PbS QDs (Figure 5.19d).

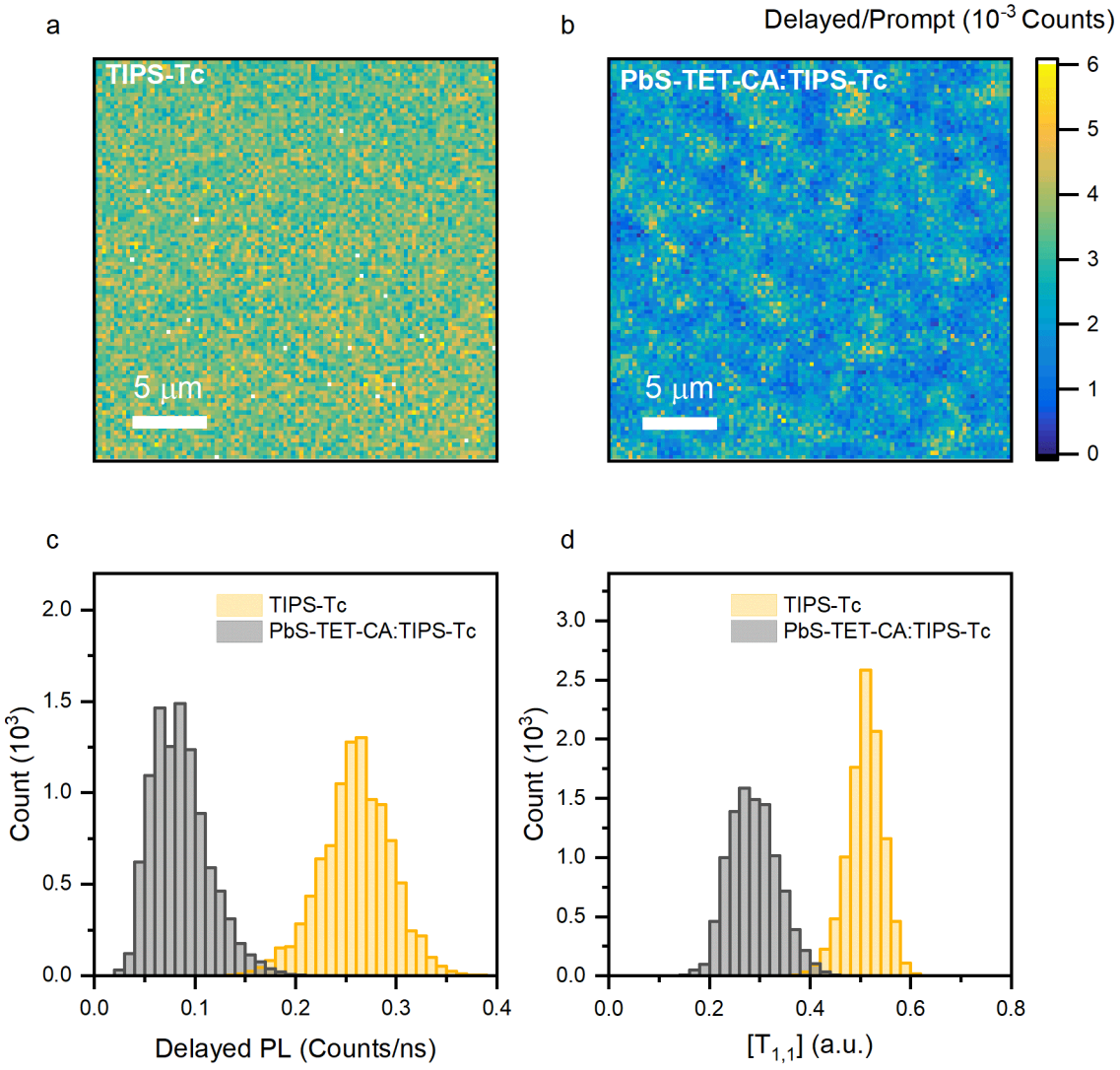

Figure 5.19: Spatially variations in the triplet exciton density.
Triplet-triple annihilation PL maps of TIPS-Tc (a) and PbS-TET-CA:TIPS-Tc (b) films. The TIPS-Tc PL decay is detected at 550 ± 40 nm after 405 nm excitation at a fluence of 50 µJcm^{-2} and 2 MHz pump rep rate. The delayed TIPS-Tc PL was normalised by the prompt TIPS-Tc PL counts. Distributions for spatially resolved delayed TIPS-Tc visible PL (c) and corresponding TIPS-Tc triplet density (d). In films of TIPS-Tc and PbS-TET-CA:TIPS-Tc, the TIPS-Tc PL decay is detected at 550 ± 40 nm after 405 nm excitation at a fluence of 50 µJcm^{-2} and 2 MHz pump rep rate.

These initial measurements present a spatial mapping of the triplet-triplet annihilation generated fluorescence as useful microscopy techniques to probe triplet transfer in SF-PM films. To relate the spatial variation of the triplet harvesting to the overall SF-PM performance further investigations are suggested.

5.5.5 QD Concentration Dependence of Triplet Harvesting

Here we develop a theoretical framework to describe the triplet harvesting in SF-PM films. In particular the variation of triplet transfer with the density of QD emitters within the SF host. We start with the rate equation for the triplet exciton density $[T_1]$ in the SF-host material

$$\frac{d[T_1]}{dt} = G_T - k_T[T_1] - \gamma_{TET}(t)[QD_0][T_1]\,. \tag{5.9}$$

Where G_T is the triplet generation rate, k_T is the intrinsic triplet decay rate, $[QD_0]$ is the density of ground state QDs (we assume that the excitation rate is in the low excitation regime where the fraction of excited QDs is low compared to the total number of QDs and so $[QD_0]$ is the same as the density of QDs in the film) and $\gamma_{TET}(t)$ is the bimolecular triplet transfer rate.[175] For diffusion-limited transfer in an isotropic system the bimolecular transfer rate can be expressed as

$$\gamma_{TET}(t) = 4\pi RD\left(1 + \frac{R}{\sqrt{2\pi Dt}}\right), \tag{5.10}$$

where D is the triplet exciton diffusion coefficient and R is the exciton capture radius. For typical triplet diffusion coefficients (~1x10^{-3} cm^{2}s^{-1}) and R ~1 nm, the time-dependent component becomes negligible after $t > 20$ ps. [176,177] From our nsTA and trPL investigations triplet harvesting is dominated by transfer on microsecond timescales and so the bimolecular triplet transfer rate can be reduced to $\gamma_{TET} = 4\pi RD$. In this case the triplet transfer rate can be expressed as[178]

$$k_{TET} = \gamma_{TET}[QD_0] = 4\pi RD[QD_0]\,. \tag{5.11}$$

With the introduction of a finite triplet transfer velocity k, the triplet transfer rate is given by[102,106]

$$k_{TET} = 4\pi DR[QD_0]\left(\frac{R}{R + D/k}\right). \tag{5.12}$$

We now consider a film of total volume V_{Tot}, mass m_{Tot} and QD mass fraction f. The QDs aggregate into N_q quenching domains with number density n_q and domain size V_q. The QD mass fraction is given by $f = m_q/m_{Tot} = m_q/(m_q + m_{sf})$, where m_q is the

total mass of quencher (QDs) and m_{sf} is the total mass of SF-host in the system. For quencher mass density ρ_q and SF-host density ρ_{sf} the density of quenching domains with a size V_q is given by

$$n_q = \frac{1}{V_q}\left(\frac{f\rho_{sf}}{\rho_q + f(\rho_{sf} - \rho_q)}\right) = \frac{f_V}{V_q}. \quad (5.13)$$

Where f_V is the QD volume fraction of the film. Under the assumption that the density of SF-host and QD quencher are relatively equal, the expression simplifies to $n_q \approx f/V_q$. However, we avoid this simplification and maintain the explicit dependence on the density of the components. The resulting triplet transfer rate is given by,

$$k_{TET} = 4\pi R_q D n_q \left(\frac{R_q}{R_q + D/k}\right) = \frac{4\pi R_q D}{V_q}\left(\frac{R_q}{R_q + D/k}\right) f_V\,, \quad (5.14)$$

where R_q is the radius of the harvesting sphere, in this case a single QD. The expression for k_{TET} is of the form $k_{TET} = \gamma_V f_V$, where γ_V is the QD volume fraction dependent triplet transfer rate. Based on previous crystallographic measurements describing the unit cell of TIPS-Tc (3625 Å^3) and its molar mass (589 g/mol), we calculate a density of ~1.08 x 10^{-24} g/Å^3 for the TIPS-Tc phase.[58] The mass density for the PbS QDs phase was calculated for a spherical PbS core (7.6 x 10^{-24} g/Å^3) of radius 22 Å with a OA ligand shell consisting of 130 ligands in a thickness of 13 Å. Resulting in an overall QD mass density of ~2.23 x 10^{-24} g/Å^3. Taking the packing factor of a face-centred cubic crystal (0.74) and applying it to the QDs density yields a QDs aggregate density ~1.64 x 10^{-24} g/Å^3.

So far we have demonstrated calculation of the triplet exciton transfer rate by transient measurement including nsTA and trPL. Steady-state techniques such as the IR PLQE measurement lead us to calculate the triplet exciton transfer efficiency. Here we combine all the obtained measurements to determine the most general description of the SF-PM performance as a function of the density PbS-TET-CA QDs in the films. We use the triplet transfer efficiency, in the low fluence limit, as described by

$$\eta_{TET} = \frac{k_{TET}}{k_{TET} + k_T}, \quad (5.15)$$

to calculate the rates and efficiencies displayed in Figure 5.20, from multiple measurements across a range of experimental techniques. Equation (5.15) allows conversion between values determined in the transient and steady-state domains. We

take the intrinsic triplet decay rate, k_T, for TIPS-Tc to be ~0.01 ± 0.005 μs^{-1}, as determined by nsTA of pristine TIPS-Tc. On linear fitting of the form $k_{TET} = \gamma_V f_V$, we extract a slope of γ_V = 1.16 ± 0.09 μs^{-1}. From this generalisation we can confidently say that a TIPS-Tc:PbS-TET-CA with a QD volume fraction above 10% (~8% QD mass fraction), will be able to harvest 90 % of the singlet fission generated triplet. What is more, we can predict the triplet transfer efficiency as a function of QD volume fraction.

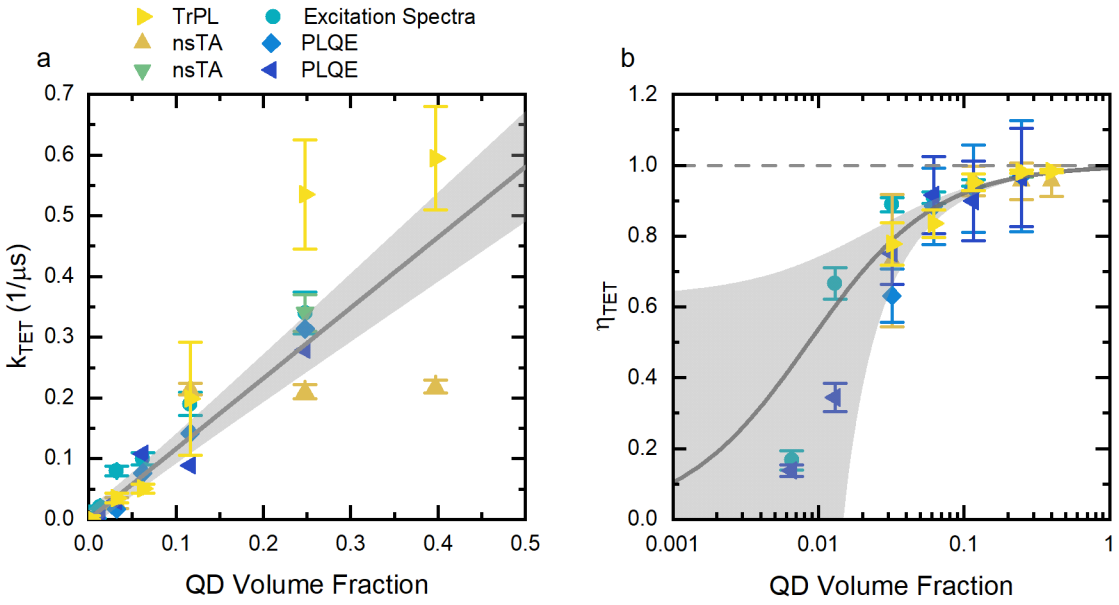

Figure 5.20: Triplet harvesting dependence with QD density in TIPS-Tc:PbS-TET-CA films. Triplet transfer rates (a) and efficiencies (b), determined by a range of steady-state and transient techniques with multiple sample redundancies, as functions of the QD volume fraction in the films.

In the absence of a measured value for the triplet diffusion coefficient for TIPS-Tc we use a previously reported value for the closely related TIPS-Pentacene.[151] Using values, D = 10^{-5} cm^{2}s^{-1}, r_{QD} = 3.5 nm giving V_{QD} of 1.80 nm^3 for a spherical QD, we calculate a triplet transfer velocity of k = 1.37 ± 0.14 nm/μs using,

$$k = \frac{1}{\frac{4\pi r_{QD}^2}{\gamma_V V_{QD}} - \frac{r_{QD}}{D}}. \qquad (5.16)$$

This value for the triplet transfer velocity is slower than those found for transfer in the solution phase, of 2.5-4.5 nm/μs, by equivalent methods (Section 4.6.2). In this case the ratio kr/D is ~ 0.005 << 1, and so the triplet exciton transfer in these TIPS-Tc:PbS-TET-CA films is in the kinetically limited transfer regime. Rather than being purely limited by

diffusion of triplets to the QDs. A recent study on a related system showed kinetically limited charge-transfer formation in TIPS-Pentacene:hole-acceptor films, the similar to our findings here.[151]

The diffusion-limited transfer rate based on the values used here would result in a QD volume fraction dependent transfer rate of γ_V = 240 μs^{-1}, two orders of magnitude faster than observed. Similar to the solution phase, if the triplet transfer velocity could be increased then triplet transfer rates approaching the significantly higher diffusion-limited rate, could be achieved. Meaning improved triplet harvesting at lower QD densities might be achievable.

The modelling here is likely pushing the limits of the method's applicability. In particular the assumption of non-interaction, spherical quenching domains is particularly weak given the TEM observation of web-like aggregation of PbS-OA QDs in the SF-host. Future studies, possibly involving Monte-Carlo methods, could yield more representative results.[151]

5.6 Sequential Triplet Transfer

With a solid understanding of the triplet transfer from the TIPS-Tc, we seek to further understand the photophysics for the resulting excited QD states. We employ IR time-correlated single photon counting to investigate the transient QD population dynamics, resulting from triplet transfer, at improved temporal-signal quality relative to the transient absorption methods. Initial measurements determine an instrument response function (IRF) with a full width half maximum of 5.5 ± 0.5 ns for the IR transient PL setup (Figure 7.9). The IRF is shorter by 2 orders of magnitude than any of the time constants we observe in the triplet transfer processes. As such we treat the IRF as instantaneous relative to the dominate triplet transfer processes.

With the laser excitation blocked before entering the sample area, the detector counts due to ambient conditions were measured for the same exposure time as the transient PL measurements. The mean detector counts per time bin, across the time window, represents the background PL counts. The PL kinetics were corrected by subtraction of this value. After subtraction of the background value, positive values for the PL kinetics at times before the laser pulse are observed. These PL levels ($t < 0$) arise due to the periodic nature of the experiment. Periodicity in the PL kinetics is explicitly included in

the following time-series deconvolution analysis, due to the periodicity of the fast Fourier transform.

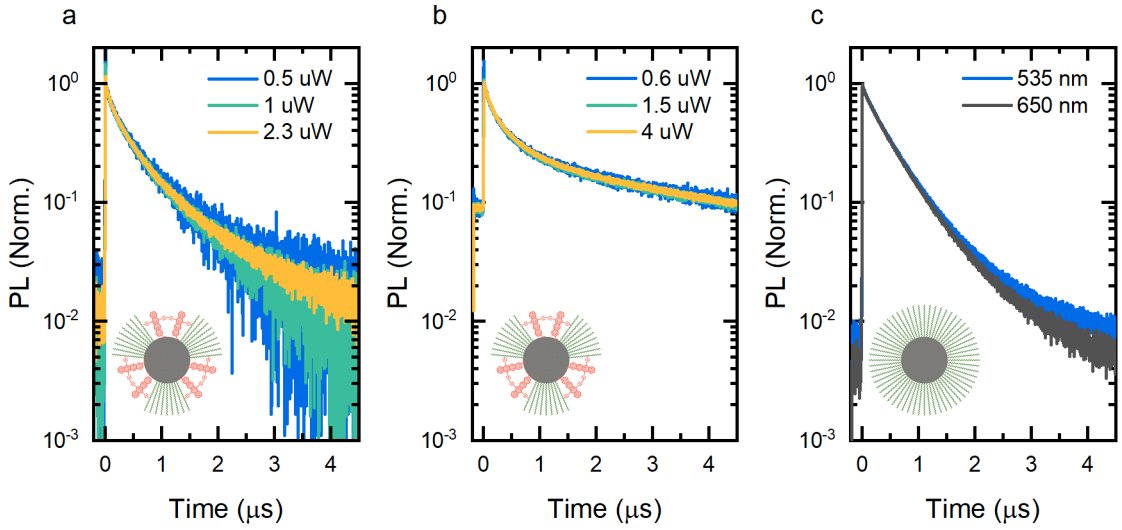

Figure 5.21: Normalised IR transient PL kinetics for a PbS-TET-CA:TIPS-Tc film. The PbS-TET-CA:TIPS-Tc film was excited at 650 nm (a) and 535 nm (b) with varying fluences. 650 nm excitation at ~2.5, 5, and 10 nJ/cm^2, and 535 nm excitation at ~2, 7, and 15 nJ/cm^2, with 0.2 MHz repetition rate was used. Contribution to the detected counts by background counts was removed before normalisation to the initial value of the PL decay. c) Normalised IR Transient PL Kinetics. The PbS-OA:TIPS-Tc film was excited at 650 nm (2.3 μW, 10 nJ/cm^2) and 535 nm (4.0 μW, 15 nJ/cm^2), at 0.2 MHz repetition rate. Contribution to the detected counts by background counts was removed before normalisation to the initial value of the PL decay.

We perform fluence-dependent measurements to investigate the effect of any non-linear behaviour of the QD excited state (650 nm excitation) or TIPS-Tc triplet decay (535 nm excitation) (Figure 5.21). Over the range of incident fluences investigated, we observed no dependence of the transient IR PL decay, indicating even at the highest fluence used 15 nJ/cm^2, the system is in the low excitation density regime where bimolecular decay in the QD or the TIPS-Tc triplet can be ignored. The IR PL shows an extended lifetime under excitation of the TIPS-Tc (535 nm) relative to excitation of the QD alone (650 nm) in the TIPS-Tc:PbS-TET-CA film. The TIPS-Tc:PbS-OA film does not show any significant extension, in agreement with the steady-state observation that effectively no triplet transfer is occurring in the TIPS-Tc:PbS-OA films. We extract QD excited state decay rates of 2.3 ± 0.2 μs^{-1} and 2.5 ± 0.2 μs^{-1} by fitting the transient IR PL decay of TIPS-Tc:PbS-OA and TIPS-Tc:PbS-TET-CA, respectively, under 650 nm excitation (Figure 5.22).

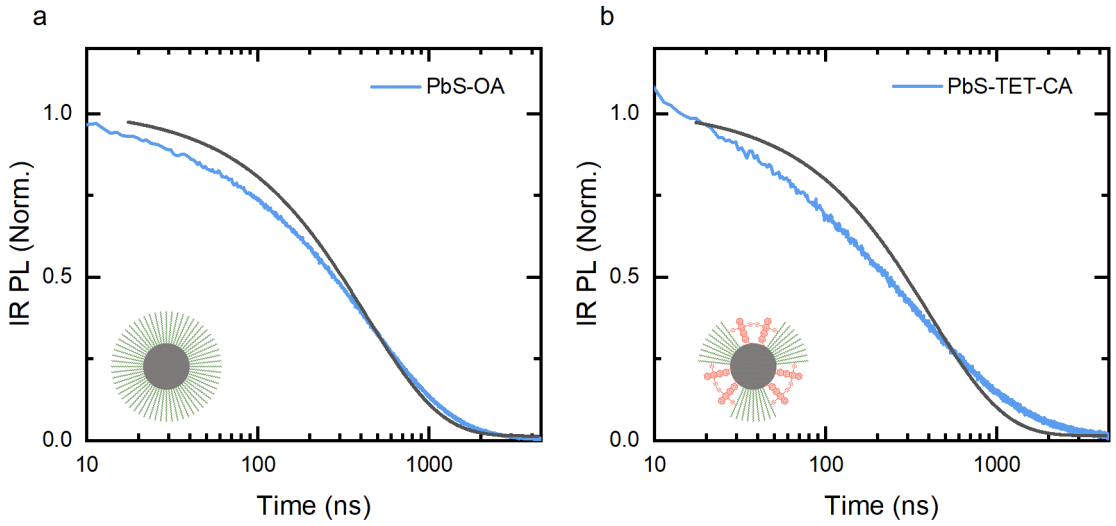

Figure 5.22: Intrinsic PbS QD IR transient PL kinetics for TIPS-Tc:QD films.
a) PbS-OA:TIPS-Tc and b) PbS-TET-CA:TIPS-Tc excited at 650 nm with fluence 10 nJ/cm^2, 0.2 MHz repetition rate (QD preferentially excited). The PL decay was fitted with a single exponential decay with decay rates 2.3 ± 0.2 µs^{-1} and 2.5 ± 0.2 µs^{-1} respectively.

5.6.1 Triplet Flux Deconvolution

The excited state flux, assigned to triplet transfer, into the PbS QD, $\phi_T(t)$, is found by deconvolving the intrinsic QD response $h(t)$ (658 nm excitation, the QDs impulse response) from the observed QD response with triplet exciton transfer $y(t)$ (535 nm excitation). Here the ansatz is that the QD dynamics can be related to the intrinsic response as follows[81]

$$y(t) = h(t) * \big(\delta(t) + \phi_T(t)\big)\,. \tag{5.17}$$

Where $\delta(t)$ is a delta function representing the fraction of photons in the 535 nm pump pulse that excites the QDs directly. To achieve appropriate levels of signal to noise, we perform a post-processing step where the $y(t)$ and $h(t)$ time series are binned, taking the average of 40 data points and reducing it to 1 data point respectively (at the mean time of the 40 data points). The deconvolution is calculated using a fast Fourier transform (FFT) as described by

$$\delta(t) + \phi_T(t) = FFT^{-1}\left[\frac{FFT[y(t)](\omega)}{FFT[h(t)](\omega)}\right](t)\,. \tag{5.18}$$

The first 2 two data points of the deconvolved kinetics are removed, effectively removing the $\delta(t)$ component of the QD excited state generation term. The remaining data points correspond to the triplet flux into the PbS QDs (Figure 5.23b). The triplet flux is then convolved with the intrinsic QD decay $h(t)$ to give the PbS QD IR PL that is due to triplet transfer alone (Figure 5.23c). This delayed PL is directly proportional to the QD population. The triplet flux shows an unexpected behaviour, where it rises over the first ~500 ns after the pump pulse. In previous reports on bilayers of tetracene and PbS QDs, the deconvolution of the QD PL showed a triplet flux that did not rise at all after the pump excitation and only decayed over a µs timescale.[81]

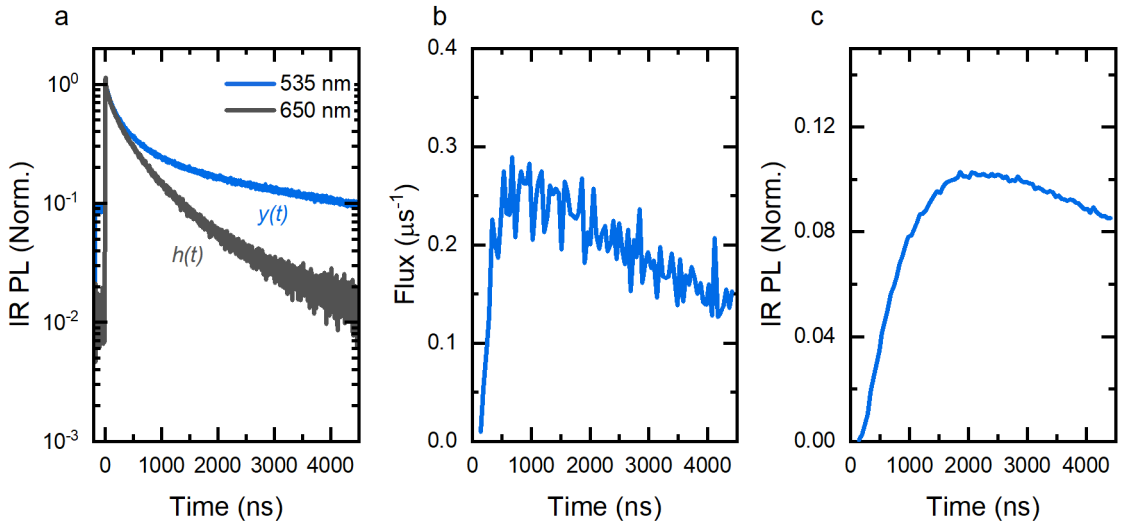

Figure 5.23: Determination of triplet exciton flux into PbS QDs in a TIPS-Tc:PbS-TET-CA film. a) PbS-TET-CA:TIPS-Tc transient IR PL for the PMF under intrinsic decay (658 nm excitation) and triplet transfer (535 nm excitation), at 0.2 MHz repetition rate. b) Deconvoluted excitation flux into the PbS QD along with the expected triplet flux from the TIPS-Tc triplet population decay (green dashed line). c) Triplet flux convolved with the intrinsic QD decay (h(t)) to give the PbS PL resulting from purely triplet transfer.

5.6.2 Triplet Transfer Models

Here we discuss possible kinetics schemes for the triplet transfer between TIPS-Tc and PbS QDs and compare the dynamics to the IR transient PL measurements. We propose two kinetic models, the first requires only two species, the TIPS-Tc triplet $[T_{1,1}]$ and the excited QD state $[QD_1]$; the second introduces a third intermediate species $[I]$.

5.6.2.1 Two-Species Model

In this kinetic scheme we assume there are only two states participating in the triplet transfer, the TIPS-Tc triplet state $[T_{1,1}]$ and the excited PbS QD state $[QD_1]$. The dynamics of this system are described as follows

$$\frac{d[T_{1,1}]}{dt} = -(k_1 + k_{TET})[T_{1,1}] - k_2\left[T_{1,1}\right]^2 + \eta_{SF} \cdot G_T(z)\,, \tag{5.19}$$

$$\frac{d[QD_1]}{dt} = -k_{QD}[QD_1] + k_{TET}\left[T_{1,1}\right], \tag{5.20}$$

with rates as described earlier. To simplify this system of differential equations we assume the case of the low $[T]$ limit where contribution by the $k_2[T]^2$ can be ignored and that triplet transfer out-competes triplet intrinsic decay ($k_1 + k_{TET} \sim k_{TET}$). Solving this system leads to a triplet population given by

$$[T_{1,1}]\,(t) = [T_{1,1}]_0 e^{-k_{TET}t}, \tag{5.21}$$

where $\left[T_{1,1}\right]_0$ is the initial triplet density after singlet fission. The triplet flux into the QD is then given by

$$\phi_T(t) = k_{TET}\left[T_{1,1}\right](t) = k_{TET}\left[T_{1,1}\right]_0 e^{-k_{TET}t}. \tag{5.22}$$

The QD population due to triplet transfer is given by

$$[QD_1]_\phi(t) = -\frac{k_{TET}\left[T_{1,1}\right]_0}{k_{TET} - k_{QD}}\left(e^{-k_{TET}t} - e^{-k_{QD}t}\right). \tag{5.23}$$

The QD population due to direct excitation (650 nm excitation) is

$$[QD_1]_{PL}(t) = [QD_1]_0 e^{-k_{QD}t}\,, \tag{5.24}$$

where $[QD_1]_0$ is the initial excited QD population. This set of equations allows for simultaneous calculation of the QD intrinsic PL decay, $[QD_1]_{PL}(t)$, the triplet flux into the QD, $\phi_T(t)$, and QD population due to transfer, $[QD_1]_\phi(t)$. Figure 5.24 shows the best achieved global fitting of these functions to the measured values. The quality of this fit is very poor, showing large systematic discrepancies of the observed trends. Notably,

the triplet flux does not rise over the first ~500 ns as observed in the measured data and the QD population from transfer peaks and falls faster than measured. We constrain the system such that the triplet transfer rate is the same as given by the ns-TA measurements. The value for the QD intrinsic decay rate k_{QD} is slightly smaller than the values measured by the fitting of the QD GSB in ns-TA and the observed transient PL decay (Table 5.2).

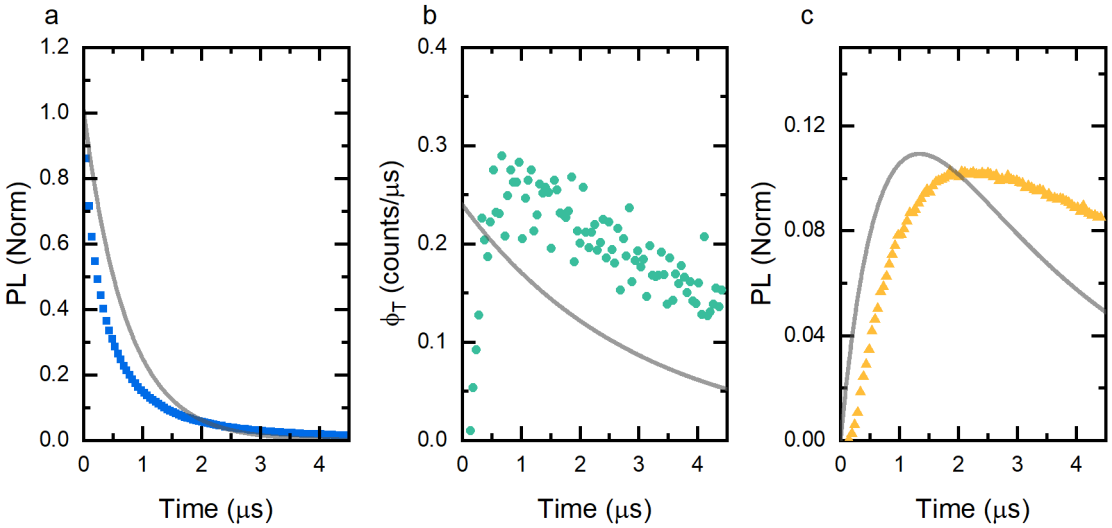

Figure 5.24: Two species model fitting of the IR transient PL for a PbS-TET-CA:TIPS-Tc film. The intrinsic QD PL decay, triplet flux into the QD and QD PL counts from triplet transfer, was fitted globally. a) PbS-TET-CA:TIPS-Tc intrinsic QD PL decay (650 nm excitation). b) Triplet flux into the PbS QD in a film of PbS-TET-CA:TIPS-Tc after 535 nm excitation of the SF-host. ***c)*** *PbS-TET-CA:TIPS-Tc QD PL resulting from triplet transfer (after excitation with 535 nm), calculated by convolution of the triplet flux and the PbS-TET-CA intrinsic decay dynamics.*

k_{TET} (1/µs)	k_{QD} (1/µs)	k_{QD} (1/µs)	k_{QD} (1/µs)
TA fit	TA fit	TrPL fit	Transfer TrPL fit
0.34 ± 0.03	3.3 ± 0.2	2.5 ± 0.2	1.4 ± 0.1

Table 5.2: Transient IR PL two-species fitting parameters. Comparison of the triplet transfer kinetic parameters for a two-species model with global fitting to the intrinsic QD decay, triplet flux and QD PL from triplet transfer.

Figure 5.25 shows the best achieved two species fitting against the measured QD PL from transfer alone (not globally fitted). The fitted kinetic for the transient PL from triplet transfer is reasonable, showing a lower discrepancy with the measured response. However, the corresponding kinetics for the QD intrinsic decay and triplet flux show considerable deviation from the data. This fitting method requires a significantly slower QD decay relative to the values measured by nsTA and transient PL alone (Table 5.3). This discrepancy between QD decay rate extracted by the QD population from triplet transfer (535 nm excitation) and the rate obtained by optical excitation of the QDs directly (650 nm excitation) is consistent with the hypothesis that there exist two subsets of QDs within the film. One set that is affected by QD aggregation to a greater extent, resulting in short QD lifetimes due to trapping and lower triplet transfer due to the separation of triplet donor and acceptor. The other subset of QDs are isolated within the SF-host having slower decay (similar to the rate measured for an isolated dot in solution ~0.5 μs^{-1}) and high triplet transfer due to the maximal interaction between donor and acceptor. The rise in triplet flux could be an artefact in this case as the ansatz in equation 11.1 would not be valid. We leave the investigation of this hypothesis to future work.

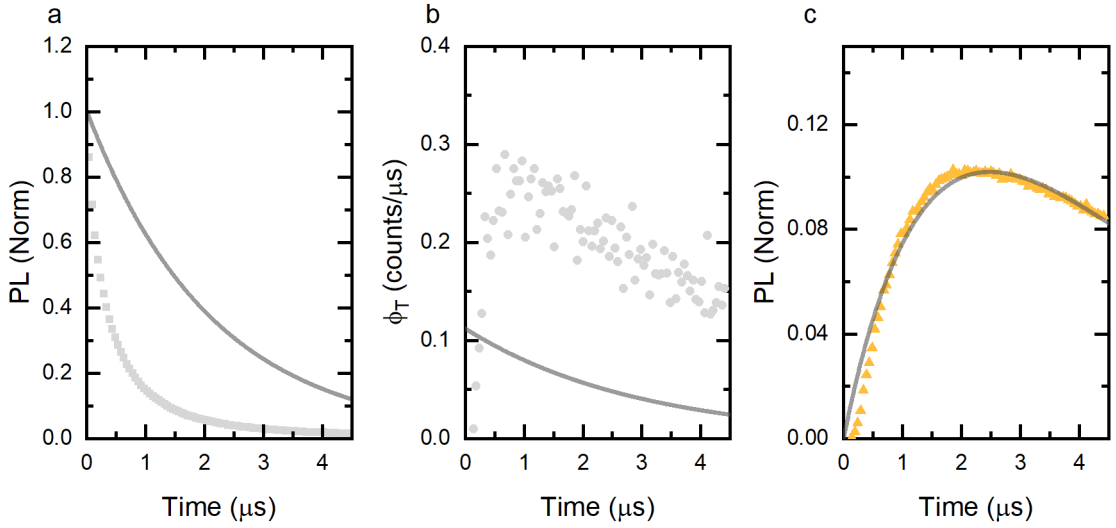

Figure 5.25: Restricted two species model fitting of the IR transient PL.
Only data for QD PL from transfer was fitted and the required intrinsic QD PL decay, triplet flux into the QD plotted beside the measured counts. a) PbS-TET-CA:TIPS-Tc intrinsic QD PL decay (650 nm excitation). b) Triplet flux into the PbS QD in a film of PbS-TET-CA:TIPS-Tc after 535 nm excitation of the SF-host. c) PbS-TET-CA:TIPS-Tc QD PL resulting from triplet transfer (after excitation with 535 nm), calculated by convolution of the triplet flux and the PbS-TET-CA intrinsic decay dynamics.

k_{TET} (1/μs)	k_{QD} (1/μs)	k_{QD} (1/μs)	k_{QD} (1/μs)
TA fit	TA fit	TrPL fit	Transfer TrPL fit
0.34 ± 0.03	3.27 ± 0.15	2.5 ± 0.2	0.50 ± 0.05

Table 5.3: Transient IR PL two-species fitting parameters, with constraints.
Comparison of the triplet transfer kinetic parameters for a two-species model with the fitting of the QD PL from transfer alone.

5.6.2.2 Three-Species Model

In this kinetic scheme, we assume the existence of an intermediate state $[I]$ participating in the triplet transfer. The dynamics of this system are described as follows,

$$\frac{d[T_{1,1}]}{dt} = -\left(k_1 + k_{TET_1}\right)[T_{1,1}] - k_2[T_{1,1}]^2 + \eta_{SF} \cdot G_T(z)\,, \tag{5.25}$$

$$\frac{d[I]}{dt} = -k_{TET_2}[I] + k_{TET_1}[T_{1,1}]\,, \tag{5.26}$$

$$\frac{d[QD_1]}{dt} = -k_{QD}[QD_1] + k_{TET_2}[I]\,, \tag{5.27}$$

where k_{TET1} is the triplet transfer rate from the TIPS-Tc to the intermediate (this rate is the same as the previous discuss k_{TET} as it quantifies triplet loss from the TIPS-Tc) and k_{TET2} is the rate of triplet transfer from the intermediate to the QD excited state. To simplify this system of differential equations we assume the case of the low $[T]$ limit where contribution by the $k_2[T]^2$ can be ignored and that triplet transfer out-competes triplet intrinsic decay ($k_1 + k_{TET_1} \sim k_{TET_1}$) and there is 100% transfer from the intermediate to the QD. Solving this system leads to a triplet population given by,

$$[T_{1,1}](t) = [T_{1,1}]_0 e^{-k_{TET_1} t}, \tag{5.28}$$

where $\left[T_{1,1}\right]_0$ is the initial triplet density after singlet fission. The intermediate state population is given by,

$$[I](t) = -\frac{k_{TET_1}[T_{1,1}]_0}{k_{TET_1} - k_{TET_2}}\left(e^{-k_{TET_1}t} - e^{-k_{TET_2}t}\right), \tag{5.29}$$

where we assume the initial population of the intermediate state is $[I](0) = 0$. The triplet flux into the QD is,

$$\phi_T(t) = k_{TET_2} I(t) = -\frac{k_{TET_1} k_{TET_2}[T_{1,1}]_0}{k_{TET_1} - k_{TET_2}}\left(e^{-k_{TET_1}t} - e^{-k_{TET_2}t}\right), \tag{5.30}$$

The QD population due to this transfer is given by,

$$[QD_1]_\phi(t) = \frac{k_{TET_1} k_{TET_2}[T_{1,1}]_0\left(k_{QD}(e^{-k_{TET_2}t} - e^{-k_{TET_1}t}) + k_{TET_2}(e^{-k_{TET_1}t} - e^{-k_{QD}t}) + k_{TET_1}(e^{-k_{QD}t} - e^{-k_{TET_2}t})\right)}{(k_{TET_1} - k_{TET_2})(k_{TET_1} - k_{QD})(k_{TET_2} - k_{QD})}, \tag{5.31}$$

while the QD population due to direct excitation (650 nm excitation) is,

$$[QD_1]_{PL}(t) = [QD_1]_0 e^{-k_{QD}t}, \tag{5.32}$$

where $[QD_1]_0$ is the initial excited QD population. This set of equations allows for simultaneous calculation of the QD intrinsic PL decay, $[QD_1]_{PL}(t)$, the triplet flux into the QD, $\phi_T(t)$, and QD population due to transfer, $[QD_1]_\phi(t)$. Figure 5.26 shows the best achieved global fitting of these functions to the measured values. We constrain the system such that the triplet transfer rate k_{TET1} is the same as given by the ns-TA measurements. The agreement between measured values and fit is the strongest out of the three investigated fitting procedures, reproducing the observed rises and falls in the various time-dependent quantities. To accurately fit the rise in the triplet flux requires the k_{TET2} fitting parameter. The introduction of an intermediate state is not arbitrary as it has been shown that the TET-CA ligand is crucial to the triplet transfer process in solution and its rate of transfer into the PbS QD has been calculated.[179] Thus we assign the intermediate state as the TET-CA triplet $[I] = [T_{1,2}]$.

Table 5.4 compares the various kinetic parameters. The value for the QD intrinsic decay rate k_{QD} is again slightly smaller than the values measured by the fitting of the QD GSB in ns-TA and the observed transient PL decay. This discrepancy might be due to the two QD subset hypothesis mentioned previously.

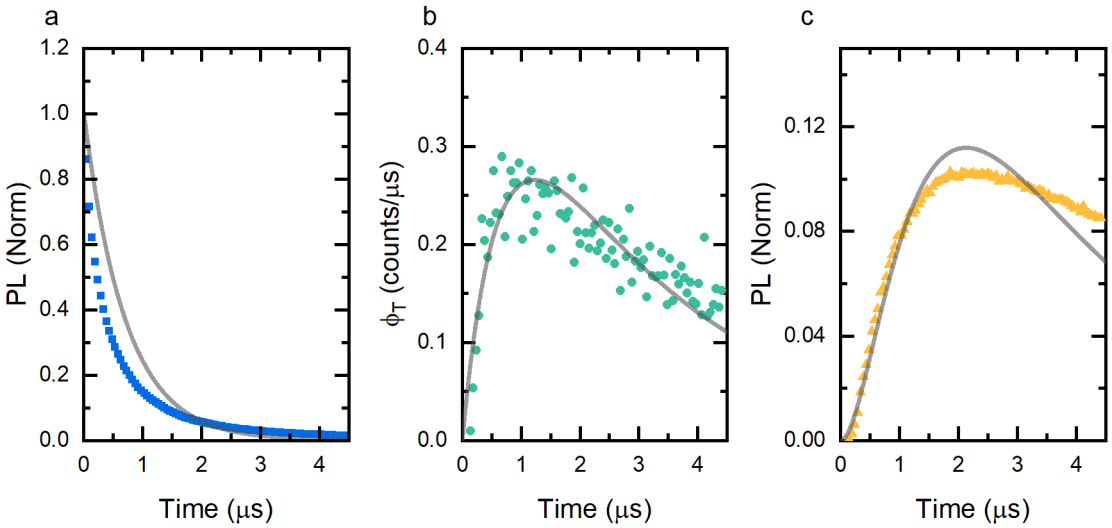

Figure 5.26: Three species model fitting of the IR transient PL for a PbS-TET-CA:TIPS-Tc film. The intrinsic QD PL decay, triplet flux into the QD and QD PL counts from triplet transfer, was fitted globally. a) PbS-TET-CA:TIPS-Tc intrinsic QD PL decay (650 nm excitation). b) Triplet flux into the PbS QD in a film of PbS-TET-CA:TIPS-Tc after 535 nm excitation of the SF-host. c) PbS-TET-CA:TIPS-Tc QD PL resulting from triplet transfer (after excitation with 535 nm), calculated by convolution of the triplet flux and the PbS-TET-CA intrinsic decay dynamics.

k_{TET1} (1/µs)	k_{TET2} (1/µs)	k_{QD} (1/µs)	k_{QD} (1/µs)	k_{QD} (1/µs)
TA fit	$\phi_T(t)$ fit	TA fit	TrPL fit	Transfer TrPL fit
0.34 ± 0.03	1.6 ± 0.1	3.27 ± 0.15	2.5 ± 0.2	1.40 ± 0.2

Table 5.4: Transient IR PL three-species fitting parameters. Comparison of the triplet transfer kinetic parameters for a three-species model with global fitting to the intrinsic QD decay, triplet flux and QD PL from triplet transfer.

In summary, the transient PL dynamics of the TIPS-Tc:PbS-TET-CA films under photoexcitation of the SF host display an extension of the PL decay in agreement with the presence of triplet exciton transfer. Deconvolution of the QD photoluminescence indicates a triplet exciton flux into the PbS QDs that rises over the first microsecond after photoexcitation. Analytical modelling of multiple triplet transfer mechanisms is presented. A three-species sequential transfer model is the most consistent with the measured kinetics. Indicating the identification of an intermediate state in the triplet transfer process from the TIPS-Tc triplet to the PbS QD. We present the TET-CA triplet as a likely candidate for the intermediate state.

5.7 Modelling of Steady-State Operation

With an in-depth understanding of the dynamics present in the TIPS-Tc:PbS-TET-CA films, we return to an extended investigation of its steady-state operation. Of particular importance for a realistic SF-PM is the performance under incident light across the visible spectrum, not just at a single wavelength. Such an understanding must include accurate quantification of the triplet excitation density that results from excitation at a particular wavelength. With this in aim, we begin with an expansion of the model developed for the solution-phase SF-PM to explicitly include the spatial variation of the triplet excitation density through the film's thickness. When investigating the extraction of triplet excitons from the SF-host material the dynamics, the TIPS-Tc triplet $[T_{1,1}]$ and QD excited state $[QD_1]$ populations can be described as follows

$$\frac{d[T_{1,1}]}{dt} = -(k_1 + k_{TET})[T_{1,1}] - k_2[T_{1,1}]^2 + \eta_{SF} \cdot G_T(z)\,, \tag{5.33}$$

$$\frac{d[QD_1]}{dt} = -k_{QD}[QD_1] + k_{TET}[T_{1,1}] + G_{QD}(z)\,, \tag{5.34}$$

at a distance *z* into the film. Where k_1 and k_{TET} are the TIPS-Tc triplet intrinsic decay rate and triplet transfer rate; k_{QD} is the QD excited state decay rate; η_{SF} is the TIPS-Tc singlet fission efficiency; and G_T and G_{QD} are the TIPS-Tc and QD excited state generation rate due to photon absorption, respectively. For an SF-PM material with optical attenuation coefficient μ the incident light intensity decays via $I(z) = I_0 e^{-\mu z}$, resulting in a total generation rate $G(z) = G_T(z) + G_{QD}(z)$, given by $-\frac{dI}{dz} = \mu I_0 e^{-\mu z}$. The individual component generations rates are given by, $G_i(z) = \alpha_i G(z)$, where α_i is related to the individual components attenuation coefficients μ_i by

$$\alpha_i = \frac{\mu_i}{\sum_j \mu_j} \tag{5.35}$$

Here, the focus is on the TIPS-Tc triplet exciton photophysics in the TIPS-Tc, thus this description neglects the effects of a possible intermediate state facilitating the transfer between the SF-host and QD. Additionally, we assume diffusion is relatively slow compared to the spatial variation of the population densities across the thickness of the film, such that we exclude any explicit interaction between spatially adjacent population densities. Due to the disordered and polycrystalline nature of the TIPS-Tc films, we

assume the fractional absorption of each component, α_i, are well approximated by the previously measured values in the solution phase.[122] Solving of this set of equations for a thin film SF-PM of thickness *L* allows the calculation of the spatial dependence of the photon flux *I(z)*, TIPS-Tc triplet density $[T_{1,1}](z)$ and the triplet transfer efficiency $\eta_{TET}(z)$. Figure 5.27 illustrates one such example calculation. The inclusion of a bimolecular decay rate reduces the expected triplet population in volumes where the density is high, resulting in a corresponding reduction in the local triplet transfer efficiency.

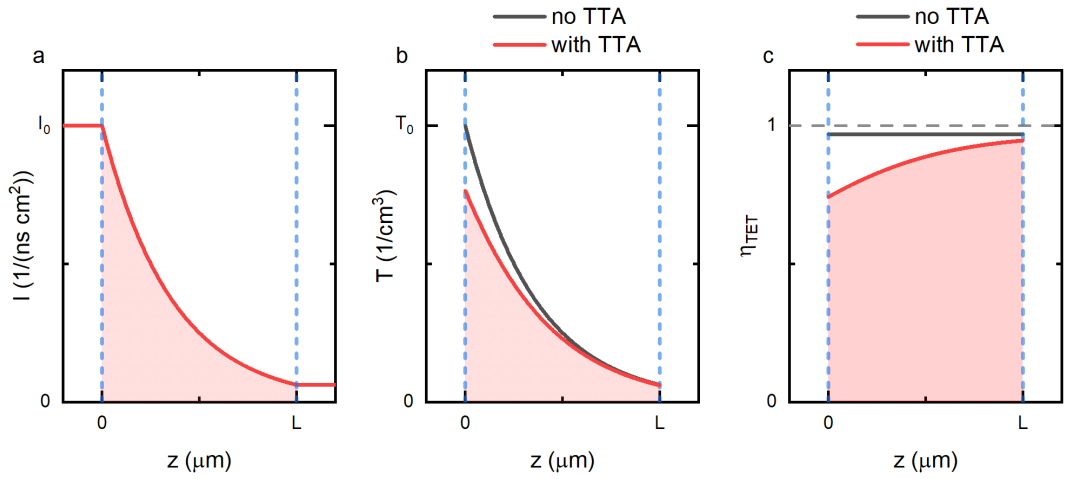

Figure 5.27: Illustration of the spatial variation in triplet harvesting.
Example calculation of the light intensity (a), triplet exciton density (b) and triplet exciton transfer efficiency (c) in a SF-PM thin film as a function of depth into the film.

To calculate the SF-PM efficiency under continuous illumination we solve the rate equations (5.33)and (5.34) for steady-state conditions, where the system of differential equations reduces to

$$(k_1 + k_{TET})[T_{1,1}] + k_2[T_{1,1}]^2 = \eta_{SF} \cdot G_T(z)\,, \tag{5.36}$$

$$k_{QD}[QD_1] = k_{TET}[T_{1,1}] + G_{QD}(z)\,. \tag{5.37}$$

Solving for positive $[T_{1,1}]$ leads to

$$[T_{1,1}] = -\frac{k_1 + k_{TET}}{2k_2} + \sqrt{\left(\frac{k_1 + k_{TET}}{2k_2}\right)^2 + \frac{\eta_{SF} \cdot G_T(z)}{k_2}}.$$

(5.38)

The triplet transfer efficiency is given by $\eta_{TET}(z) = \frac{k_{TET}T}{\eta_{SF} \cdot G_T(z)}$. Substituting the above expression for $[T_{1,1}]$ gives

$$\eta_{TET}(\mathrm{z}) = \frac{k_{TET}}{\eta_{SF} \cdot G_T(z)}\left(\sqrt{\left(\frac{k_1 + k_{TET}}{2k_2}\right)^2 + \frac{\eta_{SF} \cdot G_T(z)}{k_2}} - \frac{k_1 + k_{TET}}{2k_2}\right),$$

(5.39)

Then substituting the value for $G_T(z)$ gives

$$\eta_{TET}(\mathrm{z}) = \frac{k_{TET}}{\eta_{SF} \cdot \alpha_T G(z)}\left(\sqrt{\left(\frac{k_1 + k_{TET}}{2k_2}\right)^2 + \frac{\eta_{SF} \cdot \alpha_T G(z)}{k_2}} - \frac{k_1 + k_{TET}}{2k_2}\right).$$

(5.40)

The overall SF-PM efficiency is given by

$$\eta_{PM}(z) = \eta_{QD}\left(\alpha_{QD} + \alpha_T \eta_{SF} \eta_{TET}(z)\right).$$

(5.41)

The rate of IR PL emission from the SF-PM can be expressed as $PL_{QD}(z) = \eta_\Omega G(z) \eta_{PM}(z)$. Where η_Ω represents the PL collection and detector efficiency. The total IR PL is found by integration over the thickness of the film L to give

$$PL_{QD} = \int_0^L PL_{QD}(z)\, dz\,.$$

(5.42)

Substituting the relevant expression leads to

$$PL_{QD} = \int_0^L \eta_\Omega \eta_{QD} \left(\alpha_{QD} G(z) + k_{TET} \left(\sqrt{\left(\frac{k_1 + k_{TET}}{2k_2} \right)^2 + \frac{\eta_{SF} \cdot \alpha_T G(z)}{k_2}} - \frac{k_1 + k_{TET}}{2k_2} \right) \right) dz \,. \tag{5.43}$$

Substituting $G(z) = \mu I_0 e^{-\mu z}$ leads to

$$PL_{QD} = \int_0^L \eta_\Omega \eta_{QD} \left(\alpha_{QD} \mu I_0 e^{-\mu z} + k_{TET} \left(\sqrt{\left(\frac{k_1 + k_{TET}}{2k_2} \right)^2 + \frac{\eta_{SF} \cdot \alpha_T \mu I_0 e^{-\mu z}}{k_2}} - \frac{k_1 + k_{TET}}{2k_2} \right) \right) dz \,. \tag{5.44}$$

The integral $\int_0^U \sqrt{Y^2 + X e^{-Jz}} - Y \, dz$ has an analytical solution given by

$$\frac{\sqrt{X\, e^{-J\,U} + Y^2} \left(-2\sqrt{Y^2\, e^{J\,U} + X} + 2\,Y\, e^{\frac{J\,U}{2}}\, log\left(Y \left(e^{-\frac{J\,U}{2}} \sqrt{Y^2\, e^{J\,U} + X} + Y \right) \right) + J\,U\,Y\, e^{\frac{J\,U}{2}} \right)}{J\sqrt{Y^2\, e^{J\,U} + X}} + 2\,\frac{\left(\sqrt{X + Y^2} - Y\, log\left(Y \left(\sqrt{X + Y^2} + Y \right) \right) \right)}{J} - U\,Y \,. \tag{5.45}$$

We use the expression (5.45) to solve PL_{QD} for a given value of the system parameters. To apply this model for the triplet harvesting we have explicitly measured, the TIPS-Tc thin-film attenuation coefficient μ_T (Figure 7.8), while the fractional absorption of the components is taken from previous solution-based measurements (Section 4.3.1), the IR PLQE values at 515 nm and 650 nm excitation (in a low fluence measurement), the spectra and incident fluence for the excitation spectra (Section 5.7.1), the IR PL fluence dependence under 515 nm excitation (Figure 5.28) and the kinetic rates k_1 and k_{TET} by fitting to ns-TA dynamics (Section 5.5.1). By fitting the experimental data to (5.45) allows us to extract the singlet fission yield η_{SF}, the effective film thickness L, the product $\eta_\Omega \eta_{QD}$ and the bimolecular decay rate k_2. With these parameters known we can then simulate the SF-PM IR PL for arbitrary excitation wavelength and incident fluence.

The exciton multiplication factor and singlet fission yield for the particular TIPS-Tc:PbS-TET-CA film of the current investigation were found to be, η_{EMF} = (186 ± 18) % and η_{SF} = (192 ± 28) %, respectively, as discussed earlier in this work (Section 5.3). With the solid-state TIPS-Tc attenuation coefficient, $\mu_{Tc}(\lambda)$, and the fractional absorption ($\alpha_{Tc}(\lambda)$) from solution phase measurements we calculate the QD attenuation coefficient of the films by,

$$\mu_{QD}(\lambda) = \mu_{Tc}(\lambda)\left(\frac{1}{\alpha_{Tc}(\lambda)} - 1\right) = \frac{\mu_{Tc}(\lambda)}{\epsilon_{Tc}} \cdot \frac{c_{QD}}{c_{Tc}}\ \epsilon_{QD}\ , \tag{5.46}$$

in terms of the molar attenuation coefficients, ϵ_{Tc} and ϵ_{QD} with the molar ratio c_{QD}/c_{Tc}. With the calculated attenuation coefficients we can calculate the total attenuation spectrum for the film and calculate values for PL_{QD} in the range 600-750 nm (matching with the QD only excitation spectrum). Comparison with measured excitation spectra in this spectral region gives a reasonable fit for values of L = 21.5 µm and $\eta_\Omega\eta_{QD}$ = 9300 counts. The value for $\eta_\Omega\eta_{QD}$ effectively acts as a conversion factor between percentage absorption and detector counts. The absolute PL excitation spectra (data and simulated values) can be normalised by the absorption spectrum $A(\lambda) = I_0\left(1 - e^{-\mu(\lambda)L}\right)$, to give the relative PLQE excitation spectra. Finally, we have all parameters needed to calculate for arbitrary excitation wavelength and incident fluence, the IR PL excitation spectrum (Figure 5.29), relative IR PLQE spectra (Figure 5.31) and triplet transfer efficiency as a spectrum and function of the light penetration depth (Figure 5.32).

5.7.1 Fluence Dependence

We begin the application of this theoretical framework with a characterisation of the IR photoluminescence dependence on incident power flux. We use PL counts divided by incident power as a measure of relative PLQE. For the PbS-TET-CA:TIPS-Tc film the relative PLQE drops with increased incident power flux (Figure 5.28). We have the parameters needed to calculate the SF-PM response for any incident fluence and wavelength of excitation (400-1400 nm), for a given value of k_2, which we extract via fitting to the fluence-dependent IR relative PL in (Figure 5.28). The decrease in relative IR PLQE is qualitatively reproduced with a bimolecular decay constant of k_2 = (8 ± 2) x 10^{-19} cm^3ns^{-1}.

Using the solar equivalent fluence calculated previously for TIPS-Tc we calculate a solar equivalent fluence under 532 nm laser excitation of 13700 µW/cm^2.[122] At this fluence we observe a ~30% reduction in the IR PLQE of the SF-PM system relative to its low fluence value.

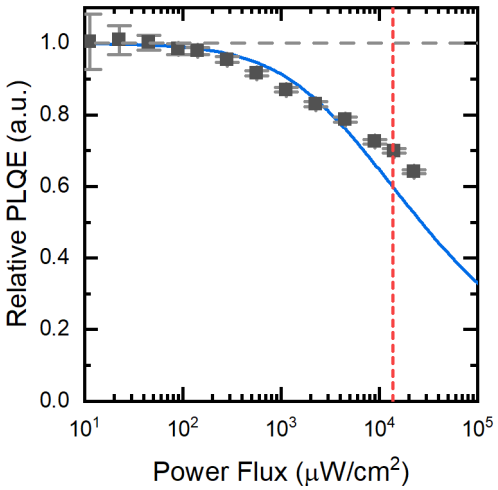

Figure 5.28: Steady-State IR PL from triplet harvesting in a film of PbS-TET-CA:TIPS-Tc. The relative IR PLQE as a function of incident 532 nm excitation fluence is calculated by division of the detected counts by the incident fluence and normalised to the low fluence region. The simulated response agrees with the measured values for a bi-molecular decay rate of $k_2 = (8 \pm 2) \times 10^{-19}$ cm^{3}ns^{-1} (blue curve). The vertical red line shows the solar equivalent fluence (13700 µW/cm^2 at 532 nm excitation)for the PbS-TET-CA:TIPS-Tc film.

We anticipate that the bimolecular decay constant will be significantly dependant on film morphology. The degree of polycrystallinity has been shown to affect the triplet exciton diffusion and associated triplet bimolecular decay.[180] Hence it opens the possibility of morphology optimisation with the goal of reducing the effect of triplet bimolecular decay on the efficiency of triplet extraction. Triplet bimolecular decay in organic thin films is known to occur via a multitude of pathways including trap assisted, singlet-triplet annihilation and triplet-triplet annihilation.[16,42] These pathways are both sample preparation dependent and intrinsic to the organic molecule. The relationship between triplet-triplet annihilation and the other decay channels has been extensively studied in the field of upconversion. Recent studies have shown that competing pathways can be overcome so that triplet-triplet annihilation to the singlet exciton can approach 100%.[145,181,182] Application of these approaches to the current system could produce a more optimal SF-PM where the recycling of triplets that undergo triplet-triplet annihilation to the singlet followed by efficient singlet fission back to two triplets

out competes other bimolecular decay pathways. In such a case the reduction of the SF-PM IR PLQE at high excitation densities could be mitigated resulting in a more versatile system for application in real-world conditions.

5.7.2 Wavelength Dependence

At this point, we step forward to investigate the SF-PM excitation wavelength dependence. We find that the excitation spectrum of the TIPS-Tc PL (emission at 600 ± 2 nm) matches the absorption spectrum of TIPS-Tc. The TIPS-Tc absorption spectrum is calculated using the same path length mentioned earlier ($L = 21.5\,\mu\mathrm{m}$) and its own linear scaling constant to overlay with the excitation spectrum. The agreement between excitation and absorption spectra indicates that at the photon flux investigated, there is no significant non-linear population dependence on the TIPS-Tc singlet emission.

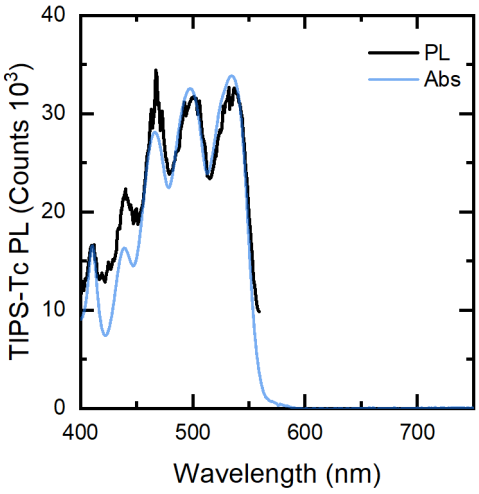

Figure 5.29: Comparison of TIPS-Tc absorption and excitation spectra.
TIPS-Tc thin-film Vis PL excitation spectra (black) along with overlaid absorption spectrum (light blue). Here the TIPS-Tc emission is detected (600 ± 2 nm emission) under an excitation photon flux of (3.5 ± 0.4) x 10^7 $cm^{-2}ns^{-1}$.

Excitation spectra of PbS-OA:TIPS-Tc films shows that there is effectively no triplet transfer from the TIPS-Tc to the PbS QDs (Figure 5.30a). The reduction in IR PL (1300 ± 20 nm) at wavelengths where the TIPS-Tc is absorbing indicates that the TIPS-Tc is “shadowing” the QDs, resulting in lower QD emission. Using the model of the SF-PM

built up over the last section, we simulate the excitation spectrum for the system in the case of zero triplet transfer. Figure 5.30b shows that the calculated excitation spectrum in this zero triplet transfer case exhibits similar trends with the measured values, indicating that there is little triplet transfer occurring in the PbS-OA:TIPS-Tc Films.

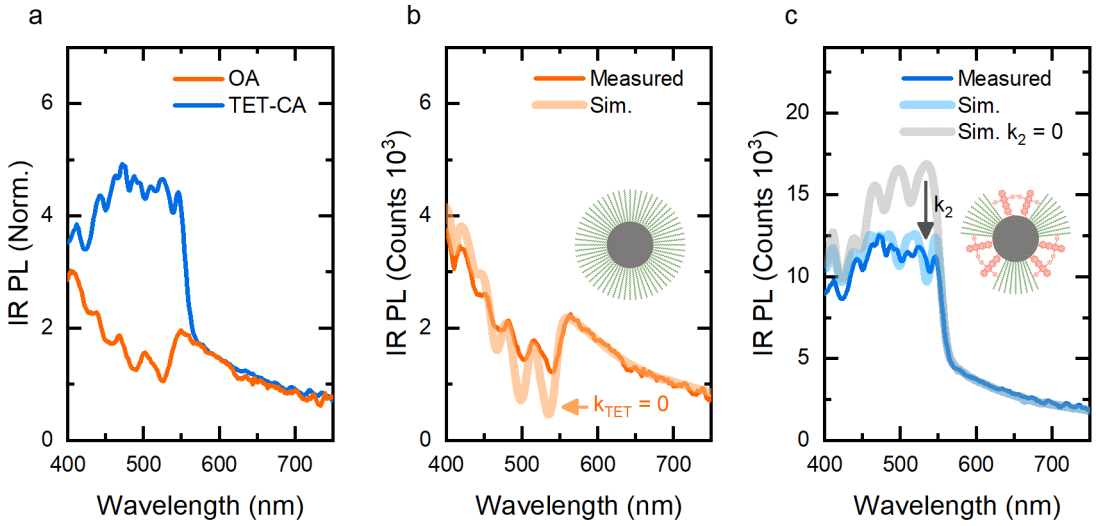

Figure 5.30: PbS QD IR PL excitation spectra of PbS-OA:TIPS-Tc and PbS-TET-CA:TIPS-Tc films. PbS QD emission detected at 1300 ± 20 nm, under an excitation photon flux of (3.5 ± 0.4) x 10^7 $cm^{-2}ns^{-1}$. a) Comparison of the IR PL excitation spectra for PbS-OA:TIPS-Tc (orange) and PbS-TET-CA:TIPS-Tc (blue), normalised to the average value between 650-700 nm. Excitation spectra of PbS-OA:TIPS-Tc (b) and PbS-TET-CA:TIPS-Tc (c) with simulated excitation spectrum, under TIPS-Tc solar-equivalent fluence. We find the PbS-OA:TIPS-Tc spectrum is consistent with simulation where there is no triplet transfer (light orange curve). In comparison the PbS-TET-CA:TIPS-Tc film's excitation spectrum matches with the simulated spectrum for kinetic parameters detailed in Table 5.1 and a triplet bimolecular decay rate of k_2 = (8 ± 2) x 10^{-19} cm^3ns^{-1} (light blue curve). The expected IR PL wavelength dependence (light grey curve) for the PbS-TET-CA:TIPS-Tc thin film in the low fluence regime.

In contrast, excitation spectra of PbS-TET-CA:TIPS-Tc films show high levels of triplet transfer from TIPS-Tc to the PbS QDs (Figure 5.30c). The drastically increased IR PL at wavelengths where the TIPS-Tc is absorbing indicates efficient triplet exciton transfer from the TIPS-Tc to the PbS-TET-CA QDs. Calculation of the excitation spectrum using equation (5.44), the kinetic parameters in Table 5.1 and those described earlier gives qualitative agreement with the measured spectrum. In Figure 5.30c we also show the simulated excitation spectrum is significantly higher in the case where the triplet bimolecular decay constant has been set to zero ($k_2 = 0$).

Using the absorption spectrum of the PbS-TET-CA:TIPS-Tc film we calculate a relative PLQE spectrum from the excitation spectra. As illustrated by Figure 5.31 the relative

PLQE is greater than the intrinsic value, for wavelengths where the TIPS-Tc is significantly absorbing (450-560 nm). The IR PLQE values under low fluence, 515 and 658 nm excitation, are used to construct the relative PLQE spectrum in the case of negligible bimolecular triplet decay ($k_2 = 0$). Subsequent inclusion of the triplet bimolecular decay rate (k_2 = (8 ± 2) x 10^{-19} cm^3ns^{-1}) as measured by IR PL fluence dependence and the TIPS-Tc solar equivalent fluence ($(3.5 \pm 0.4) \times 10^{16}$ photons $s^{-1}cm^{-2}$) used at each excitation wavelength allows a comparison of the simulated and measured relative PLQE spectrum.

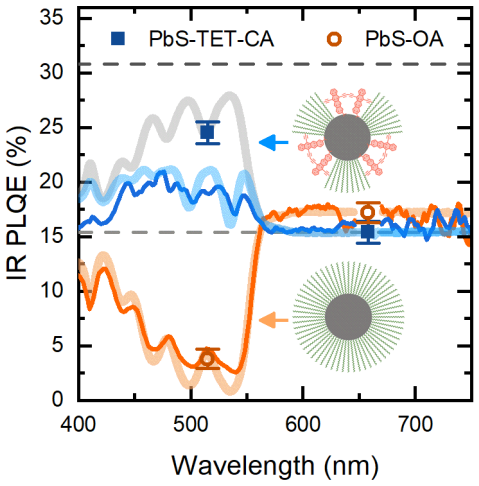

Figure 5.31: Excitation wavelength dependent IR PLQE in TIPS-TC:QD films.
The measured absolute IR PLQE under 515 nm and 658 nm excitation for PbS-TET-CA:TIPS-Tc (blue closed squares) and PbS-OA:TIPS-Tc (orange open circles) thin films. Based on these PLQE measurements, the light grey curve shows the expected IR PLQE wavelength dependence for the PbS-TET-CA:TIPS-Tc thin film, in the low-fluence regime. The light orange curve shows the expected IR PLQE wavelength dependence for the PbS-OA:TIPS-Tc thin film, with absolutely no triplet transfer to the PbS-OA quantum dots. The dark blue (PbS-TET-CA:TIPS-Tc) and dark orange (PbS-OA:TIPS-Tc) curves show the measured IR PLQE wavelength dependence, at the solar-equivalent fluence for TIPS-Tc. Horizontal dashed lines show the SF-PM performance relative to 100% (grey) and 200% (black) of the intrinsic quantum dot PLQE in the PbS-TET-CA:TIPS-Tc thin film. Films were vacuum treated and aged for 1 week.

A related effect has been observed for the fluence dependence of singlet exciton emission in tetracene crystals, where triplet bimolecular decay to the singlet was found to increase the efficiency of singlet PL at high fluences (> 10^{15} photons $s^{-1}cm^{-2}$).[183] However in the current case, it is the transfer of triplet excitons to the PbS QDs that is resulting in luminescence and so triplet bimolecular decay in the TIPS-Tc SF-host is

reducing the triplet exciton transfer efficiency where the corresponding excitation density is too high.

As discussed earlier, using the absorption of the films and the measured PLQE (under 658 nm exciton), we normalise the IR excitation spectra of the PbS-TET-CA:TIPS-Tc films to calculate the triplet excitation transfer efficiency spectrum $\eta_{TET}(\lambda)$ (Figure 5.32a) at an incident photon flux of (3.5 ± 0.4) x 10^7 $cm^{-2}ns^{-1}$.

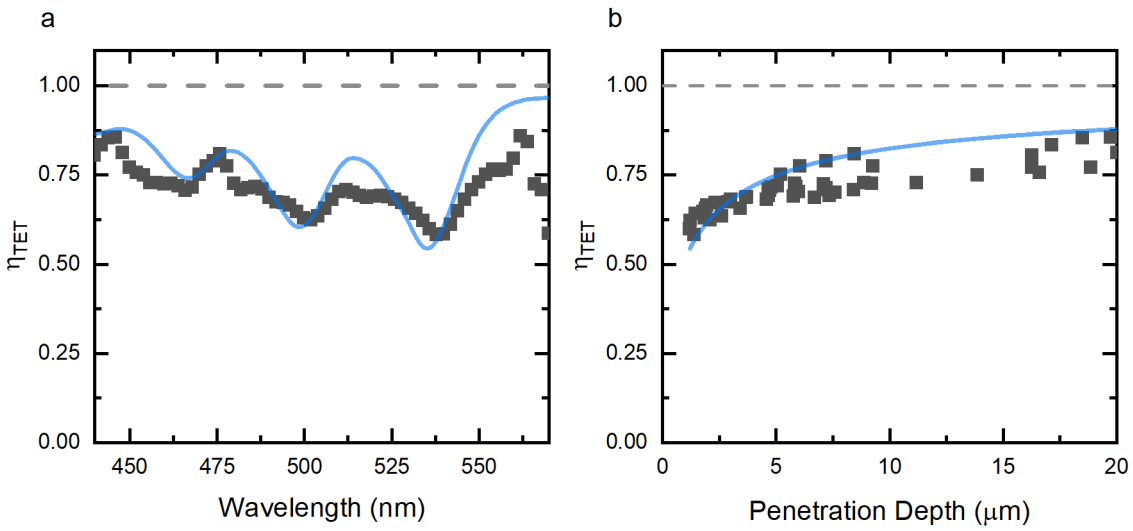

Figure 5.32: Excitation wavelength dependence of the triplet transfer efficiency.
a) PbS-TET-CA: TIPS-Tc measured (black squares) and simulated (blue curve) triplet exciton transfer efficiency as a function of excitation wavelength at a photon flux of (3.5 ± 0.4) x 10^7 $cm^{-2}ns^{-1}$ at each wavelength. The triplet exciton transfer efficiency is calculated by normalisation with the absorption spectra of the SF-PM components. Kinetic parameters for the simulated spectrum are detailed in Table 5.1 along with a triplet bi-molecular decay rate of k_2 = (8 ± 2) x 10^{-19} cm^3ns^{-1}. b) Triplet exciton transfer efficiency η_{TET} as a function of the TIPS-Tc penetration depth. The penetration depth is calculated as $1/\mu$, where μ is the attenuation coefficient. The lowest triplet transfer efficiency is observed at wavelengths where the TIPS-Tc attenuation coefficient is the largest.

The relative PLQE excitation and $\eta_{TET}(\lambda)$ spectra show reduced efficiency at the peak TIPS-Tc absorption (~470, ~500 and ~535 nm). The observed reduction is caused by the high excitation density produced in the film resulting in increased triplet bimolecular decay and lower triplet harvesting. The calculated spectra based on a parameterisation of this triplet bimolecular decay gives qualitative agreement with the measured values. Figure 5.32b illustrates the dependence of the triplet exciton transfer efficiency on the penetration depth of the incident light into the SF-PM. The shorter the penetration depth the lower the triplet exciton transfer efficiency.

The observation of wavelength dependent SF-PM performance, associated with variation of the triplet exciton density within the films, draws to attention previously unforeseen constraints. The potential of reductions in triplet transfer efficiency due to triplet bi-molecular decay will have critical implications for the deployment of a realistic SF-PM under solar irradiance. We have shown that the current TIPS-Tc:PbS-TET-CA system shows significant (~30 %) reductions in performance under solar-equivalent fluences. The model developed here illustrates a means to understand the consequences of triplet bi-molecular decay. Future work should focus on extending the framework to predict performance not just as a function of incident wavelength but for a prescribed solar spectrum. Thus, fully modelling the SF-PM performance under real-world conditions. Such calculations could be experimentally verified by the development of a solar simulator equivalent version of a PLQE measurement.

5.8 Conclusion and Outlook

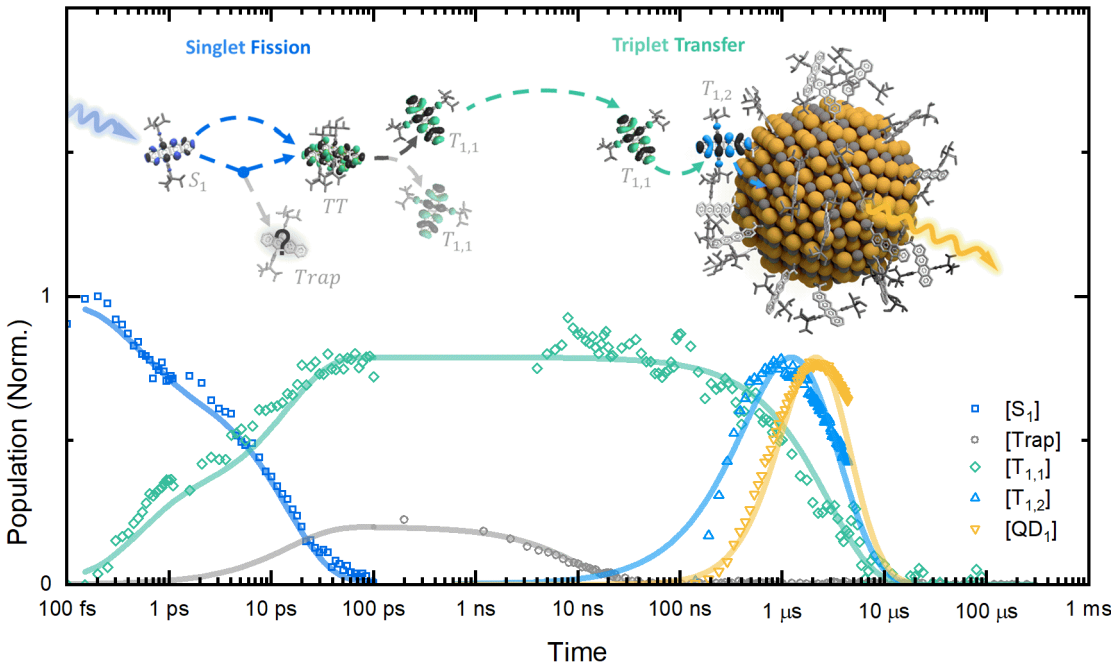

Figure 5.33: Overview of singlet fission, singlet trapping and triplet harvesting dynamics. Singlet population is extracted from the decay of the TIPS-Tc stimulated emission, while the rise of the TIPS-Tc triplet population [$T_{1,1}$] is determined by decomposition via the genetic algorithm. The rise of the trap state population is inferred from the trapping rate of the singlet state. The ratio of the trap state population to triplet state (and all following state due to triplet harvesting) is taken from the kinetic analysis that in the best-observed film resulted in (20 ± 20) % singlet trapping. On the nanosecond and greater timescales, the decay of the singlet trap independently to the TIPS-Tc triplets [$T_{1,1}$] transferring to TET-CA triplets [$T_{1,2}$] and then finally leading to emission from the excited PbS quantum dot state [QD_1]. [Trap] and [$T_{1,1}$] populations determined from nsTA, while the [$T_{1,2}$] and [QD_1] populations were determined from transient IR PL.

In summary, we have demonstrated a bulk organic-inorganic film for photon multiplication based on singlet fission. PbS quantum dots were used as an efficient triplet-harvesting and IR-emitting material in a TIPS-Tc singlet fission host. Functionalisation of the quantum dot surface with a highly soluble TIPS-Tc-carboxylic acid ligand allows fabrication of films with an improved quantum dot dispersion within the SF host. Use of the aliphatic OA ligand with its unfavourable interaction with the highly conjugated TIPS-Tc results in phase separation and results in negligible triplet transfer from SF host to PbS quantum dots. In contrast, the TET-CA ligand enables efficient triplet transfer from the TIPS-Tc host to the quantum dots. This TET-CA ligand

also results in minimized aggregation-induced, interdot excited state transfer and trapping. An enhanced IR PLQE consistent with a ~190% exciton multiplication factor has been demonstrated. In this way, we are able to demonstrate SF-PM performance exceeding the solution-phase system as the singlet fission yield is improved in the solid-state (η_{SF}: 135 % (solution) → 192 % (solid-state)).

We find the PbS-TET-CA QDs reduce singlet decay in TIPS-Tc to a trap state with excimer like properties. The singlet trap state is found to be a significant loss pathway in competition with the singlet fission process, and does not lead to the generation of any significant triplet generation itself. We show direct evidence of the increased singlet decay rate due to trapping to this state, in competition with the singlet fission process (Figure 5.33). As an alternative to having the PbS-TET-CA QD mass fraction control the abundance of this trap state within the films, we identify fabrication methods with similar morphological effects that result in the reduction of trap states and enhanced singlet fission yields.

The dynamics of triplet harvesting in TIPS-Tc films are extensively studied. Key findings were; kinetically limited triplet harvesting was found to occur on a microsecond timescale, triplet harvesting was discernible with transient absorption, transient IR photoluminescence, and transient visible photoluminescence. The latter opens up readily accessible microscopy visualisation of the spatial variation in triplet harvesting. Modelling of IR photoluminescence is used in the identification of an intermediate state in the triplet transfer process from the TIPS-Tc triplet to the PbS QD. We present the TET-CA triplet as a likely candidate for this intermediate state (Figure 5.33). We draw particular attention to the role of triplet bi-molecular decay in the dependence of the SF-PM efficiency with the wavelength and intensity of excitation.

Future work is necessary to increase the intrinsic PLQE of the quantum dots and increase the IR emission energy to match the Si-PV absorption. Additional studies should focus on extending the SF-PM modelling to predict performance, not just as a function of incident wavelength, but for a prescribed solar spectrum. This would allow full modelling the SF-PM performance under real-world conditions. Such calculations could be experimentally verified by the development of a solar simulator equivalent version of a PLQE measurement or direct coupling with a Si-PV device in a power conversion efficiency measurement. An improved theoretical model, possibly involving Monte-Carlo methods, could yield more representative results of triplet transfer in the organic-QD composite.

The QD parasitic absorption will likely be an ongoing constraint for the deployment of a realistic SF-PM. One possible means to mitigate its effect would be to add a singlet sensitizer to the SF host. This singlet sensitizer would be designed to increase the SF-PMs absorption relative to the QD parasitic absorption, such that after photoexcitation of a singlet exciton in this singlet sensitizer, singlet energy transfer to the SF host would occur. The resulting singlet exciton would then undergo singlet fission and triplet transfer as usual. The applicability and advantages of utilisation of singlet sensitisation should be investigated for possible improvement of the SF-PM system.

Finally, the approach taken here to overcome the long-standing challenge to achieve well-dispersed quantum dots in an organic host will be applicable to other optoelectronic applications where organic-inorganic binary mixtures are desired.

Chapter 6

Triplet-Triplet Annihilation Upconversion

In this final results chapter, we shift our focus to triplet-triplet annihilation upconversion. We employ a system closely related to the SF-PM schemes developed in the previous chapters, leveraging the knowledge we have gained. Here, we detail the investigation of a solution-phase system where triplet excitons generated by inorganic quantum dots are harvested for triplet-triplet annihilation.

We begin this chapter by introducing the solution-phase PbS-TET-CA:Rub system and demonstrate its operation as a triplet-triplet annihilation upconverter. Upon the quantification of upconversion efficiency for this system, we find that the combination of triplet generation in the PbS-TET-CA QDs and subsequent triplet exciton transfer to the rubrene triplet annihilator are limiting factors. In the third section, we identify the rapid formation of a trap state in the PbS-TET-CA QD system, followed by a quasi-equilibrium with the initial QD excitonic state. This quasi-equilibrium of trap and QD exciton undergoes significant decay from the trap state, leading to reduced triplet generation on the TET-CA ligand on delayed timescales. In the final section, we show that triplet transfer from the PbS-TET-CA QD to the triplet annihilator occurs on dual timescales. Rubrene adsorption to the surface of the PbS-TET-CA QDs is identified as the source of a fast component of triplet transfer, occurring significantly faster than the second triplet transfer component, which is diffusion mediated. We highlight the effect of these triplet transfer mechanisms on both the dynamics and efficiency of the triplet-triplet annihilation upconversion.

The results presented in this chapter identify and characterise key loss pathways in the triplet-triplet annihilation upconversion process for PbS QDs with triplet transmitter ligands and adsorption capable triplet annihilators. The understanding gathered here enables future work to reduce these loss pathways, which will benefit system design for both TTA-UC and SF-PM devices.

Content in this chapter is adapted from the publication draft titled "Excited State Trapping and Ligand Shells with Annihilator Adsorption in a PbS QD Upconversion System".
This draft is the result of collaboration with Nathaniel J. L. K. Davis[a,b], Victor Gray[a,c], Naoyuki Nishimura[a], Simon Dowland[a], Leah Weiss[a], James Xiao[a], Zhilong Zhang[a], Peter Budden[a], Anthony J. Petty II[d], John Anthony[d], Neil C. Greenham[a] and Akshay Rao[a].

[a]Cavendish Laboratory, University of Cambridge, J. J. Thomson Avenue, Cambridge, CB3 0HE, UK.
[b]The MacDiarmid Institute for Advanced Materials and Nanotechnology, The Dodd-Walls Centre for Photonic and Quantum Technologies, School of Chemical and Physical Sciences, Victoria University of Wellington, Wellington 6140, New Zealand.
[c]Department of Chemistry, Ångström Laboratory, Uppsala University, Box 532, SE-751 20 Uppsala, Sweden.
[d]Center for Applied Energy Research, University of Kentucky, Research Park Dr., Lexington KY 40511, USA.

6.1 Introduction

So far, we have focused on utilising singlet fission photon multiplication for spectral management. Now we shift attention to triplet-triplet annihilation upconversion (TTA-UC) as a means of breaking the Shockley-Queisser limit by absorbing low energy photons and emitting high energy photons. TTA-UC devices commonly operate as follows: low energy photons are absorbed in a triplet sensitizer material, typically an inorganic QD such as nanocrystals of PbS, PbSe or CdSe. The photoexcited QD then transfers a triplet exciton to an organic molecule in close proximity, such as a ligand attached to the surface of the QD, a 'triplet transmitter'. The triplet exciton on the transmitter molecule is subsequently transferred a second time to an organic molecule, the 'triplet annihilator'. It is in this annihilator material that triplet excitons come together to undergo triplet-triplet annihilation (TTA) and subsequently emit fluorescence from the spin-singlet state of the annihilator. Previous reports have indicated that utilisation of TTA-UC could improve the maximum possible power conversion efficiency of silicon-based photovoltaics from ~31 % to ~39 %.[115] Reaching such impressive efficiency gains requires optimisation of each of the constituent steps in the TTA-UC process. Recent advances have led to TTA-UC devices with upconversion quantum efficiencies approaching ~8 %.[184] A complete understanding of the loss pathways and methods to improve the efficiency of TTA-UC devices is beneficial to ongoing progress in this field of research.

Here, we investigate the loss channels present and the mechanism of triplet exciton transfer in a QD-transmitter-annihilator system (Figure 6.1a). As our triplet sensitizer and triplet transmitter complex we selected PbS QDs covered in 6,11-bis-((triisopropylsilyl)ethynyl)tetracene-2-carboxylic acid)) ligands, referred to as TET-CA. The QDs are of bandgap greater than 1.3 eV, such that triplet exciton transfer (~1.2 eV) to the TET-CA triplet exciton state is energetically favourable.[97] As triplet annihilator, we chose the well-studied organic molecule 5,6,11,12-Tetraphenyltetracene, commonly known as rubrene (Rub). Again this combination of materials is chosen such that triplet exciton transfer from transmitter to rubrene triplet state (1.14 eV) is energetically downhill.[185] This structure is similar to that used in TTA-UA devices with the highest current yields.[96,146,184]

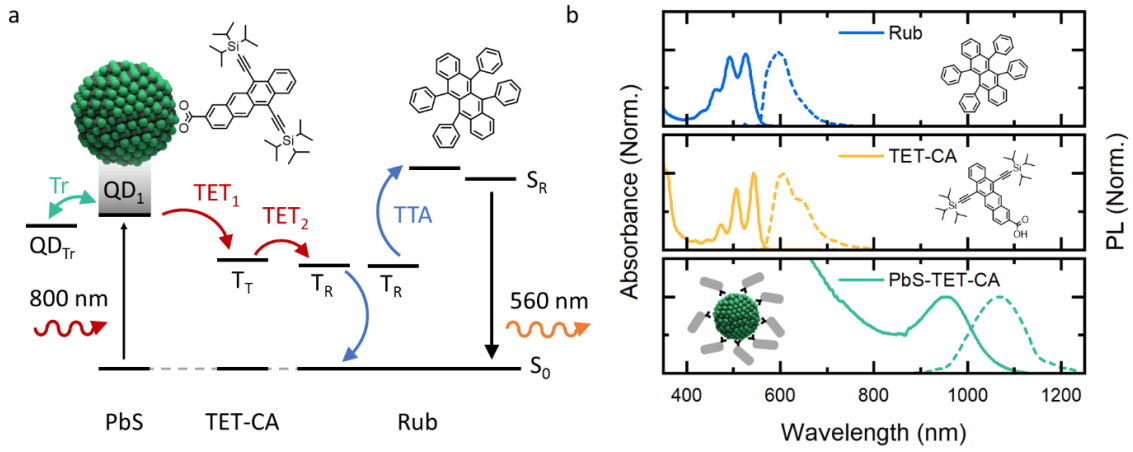

Figure 6.1: Schematic of the PbS-TET-CA:Rub system and its absorbance and photoluminescence. PbS QDs, TET-CA, and rubrene act as the triplet sensitizer, transmitter, and annihilator, respectively, in this hybrid upconversion system. a) Schematics of the triplet-triplet annihilation upconversion process. The PbS QDs absorb low-energy photons, producing a photoexcited exciton QD_1, which then rapidly equilibrates with a trap state on the QD. The TET-CA triplet state, T_T, located on TET-CA molecules bound to the PbS QDs surface, is populated via TET_1 from the QD_1 state. Subsequently, TET_2 occurs to the triplet state of rubrene, T_R, followed by TTA on the collision with another T_R state and the emission of a high energy photon from the rubrene exciton state, S_R. b) The absorbance (solid line) and emission (dashed line) spectra of Rub (blue/top), TET-CA (orange/ mid), and PbS-TET-CA QDs (green/bottom).

6.2 Initial Optical Characterisation

The PbS QDs were synthesised and ligand exchanged using previously reported methods.[137] Solutions of PbS-TET-CA:Rub used here were produced by dispersion of the relevant TTA-UC components in sealed cuvettes in toluene. Figure 6.1b displays the steady-state absorbance and photoluminescence spectra for the individual components of the TTA-UC system. As determined from the excitonic absorption peak, the PbS QDs had an optical bandgap of ~1.3 eV. On exchanging the 'as synthesised' PbS QD's oleic acid ligands (PbS-OA) with TET-CA ligands, a drop in QD IR photoluminescence quantum efficiency (PLQE) from (53 ± 2) % to (2 ± 2) % was observed. This reduction in PLQE is a significant initial indication that energy transfer from the QD excitonic excited state occurs. In Section 6.4 we identify to which states in the PbS-TET-CA QD this energy transfer proceeds to.

An important factor in the TTA-UC process is the efficiency of the photon emission from the singlet state of the annihilator material. Measurement of the pure annihilator,

rubrene at 10 mg/mL in toluene, yields a PLQE of (36 ± 1) % under 515 nm excitation. Rubrene at the same concentration is used in quantum efficiency calculations of the TTA-UC system. It is assumed that this PLQE is an approximation for the annihilator fluorescence efficiency in the TTA-UC blends. This PLQE of the annihilator sets a 36 % upper limit on the upconversion quantum efficiency.

6.3 Identifying Upconversion Photoluminescence

To identify and quantify the upconversion process, photoluminescence (PL) spectra in a 'linear optical' apparatus were measured. Here, excitation of the PbS QDs was achieved with a 785 nm laser diode, while the upconversion photoluminescence from the rubrene was collected using free-space lenses and focused directly onto the slits of a spectrometer. Two visible-pass filters (BG38 Newport) were placed in front of the spectrometer slits to removed scattered light from the excitation source. An important initial consideration is to verify that the 1.3 eV bandgap QDs are sufficiently high in energy for the triplet exciton transfer process to be effective. To check for potential gains in efficiency by using higher bandgap QDs, additional PbS-TET-CA:Rub solutions with 1.4 eV bandgap PbS QDs were produced. Figure 6.2a shows the absorbance of the as synthesised PbS-OA QDs, from which the bandgap is determined by the wavelength of the excitonic peak. To identify the existence of triplet-triplet annihilation upconversion we measure the fluence dependence of the rubrene PL (Figure 6.2b, c). To compare between sample we normalised the PL by the absorption of the samples, at the excitation wavelength. The measured absorption at 785 nm for the PbS(1.3 eV), PbS(1.4 eV), PbS-TET-CA(1.3 eV), and PbS-TET-CA(1.4 eV) QDs were 0.027, 0.057, 0.025, and 0.030, respectively.

PL resulting from TTA has a characteristic squared dependence on the incident fluence.[14] At high enough fluence this relationship reduces to linear, as the efficiency of TTA, η_{TTA}, reaches its maximum for the particular material. In our case, the efficiency of TTA for rubrene has previously been determined to be η_{TTA} = 33 %.[186] The two PbS-TET-CA:Rub solutions show very similar upconversion PL dependences on the incident laser flux (Figure 6.2). When this dependence is fit, in the low and high fluence regime, with a power-law function, $y = Ax^n$, the PL from the PbS-TET-CA:Rub solutions shows the characteristic transition from super-linear (n = 1.82 ± 0.01) to linear (n = 1.01 ± 0.03) expected for a TTA-UC system.[14] The intersection of fits to these two regimes estimates

the threshold excitation flux, G_{Th}, signalling the transition from sub-optimal TTA efficiency to TTA reaching its maximum efficiency. The PbS-TET-CA:Rub systems display a threshold excitation flux of G_{Th} = 5.7 ± 1.0 W/cm^2.

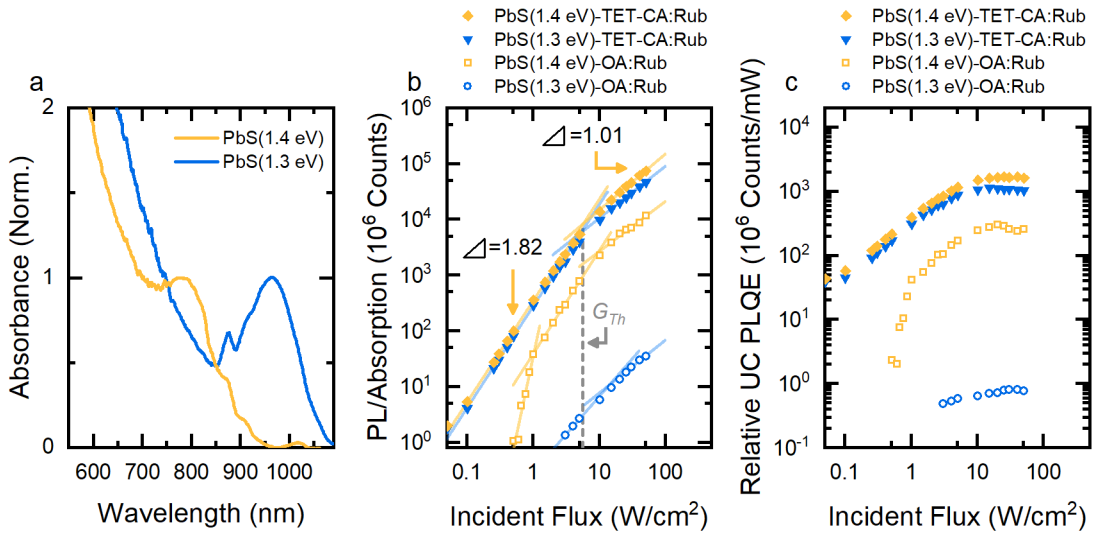

Figure 6.2: Effect of bandgap and triplet transmitter ligand on TTA-UC.
a) Normalised absorbance spectra for the PbS QDs with 1.3 eV and 1.4 eV bandgaps. b,c) Spectrally integrated photon counts generated by upconversion PL in PbS-TET-CA:Rub and PbS-OA:Rub systems under 785 nm excitation of the PbS QDs. Solutions in toluene at QD:Rub concentrations of 1:10 mg/mL. b) PL counts normalised by the sample's absorption at 785 nm. c) Relative upconversion PLQE, calculated by the number of emitted photons per absorbed laser power.

Dividing the absorption-normalised PL counts by the incident laser power yields a measure of the relative upconversion PLQE of the system (Figure 6.2c). Here, we see the effect of the saturation in η_{TTA} by the flattening of the relative upconversion PLQE for incident fluxes above the 5 W/cm^2 threshold.

The threshold flux found here is slightly lower than the values in the range of ~10-50 W/cm^2 in previous reports of PbS and PbSe QDs rubrene systems.[14,100] However, the measured threshold value is significantly lower than the ~0.003 W/cm^2 reported by Mahboub et al. in a system of PbS/CdS core-shell QDs, with a similar tetracene based ligand and rubrene.[187]

Kinetic analysis of the triplet transfer and triplet-triplet annihilation has been carried out by Monguzzi et al.[188] The authors found that the threshold excitation density is given by

$$G_{Th} = \frac{k_R^2 d}{\gamma_{TTA}\alpha_{QD}\eta_{TET}},$$

(6.1)

where k_R is the rubrene triplet intrinsic decay rate, γ_{TTA} is the rubrene bimolecular triplet-triplet annihilation rate, d is the path length of the solution, α_{QD} is the absorption of the QD at the excitation wavelength, and η_{TET} is the triplet exciton transfer efficiency from QD excited state to rubrene triplet exciton. Assuming proper care is taken to minimise contamination with triplet quenching substances such as oxygen, k_R and γ_{TTA} are intrinsic parameters for rubrene. For solutions with low absorption, such as the solutions used here, the QD absorption is effectively linear with sample path length. Thus, d/α_{QD} can be approximated well by a constant. Therefore, the dominant factor affecting the threshold flux is the triplet transfer to the rubrene. The lower G_{Th} value obtained by Muhboub et al. indicates that the PbS-TET-CA:Rub system investigated here has a lower η_{TET} value.

In comparison, the PbS-OA:Rub solutions show significantly lower upconversion PL levels. Additionally, their saturation threshold flux is notably higher, indicating poor triplet exciton transfer efficiencies. This indication of low η_{TET} values is consistent with the lower relative upconversion PLQE values for the PbS-OA system. While the PbS-TET-CA:Rub solutions show little difference with the PbS QD bandgaps above 1.3 eV, the PbS-OA:Rub solutions show a significant dependence on the bandgap. There is a reduction greater than 100 times in upconversion PL for the 1.3 eV PbS-OA system relative to the 1.4 eV system. The similar upconversion PLQE for the PbS-TET-CA QDs indicates that the 1.3 eV PbS QD cores are indeed sufficient for further investigation as TTA-UC systems.

To quantify the photon upconversion quantum efficiency, PLQE measurements using a reference method were undertaken. The comparison of the upconversion PL from the sample and the PL from a reference sample of known PLQE was used to calibrate the PL detection efficiency. A rubrene sample at the same concentration as the upconversion solution (10 mg/mL) was used as the reference. Particular care was taken to ensure as little deviation in the optics between the measurement of the PL spectra for the reference and the sample of interest. In this method, the upconversion quantum efficiency (UCQE) is calculated by

$$\eta_{UC} = 2\eta_{ref} \times \frac{\alpha_{ref}}{\alpha_{UC}} \times \frac{PL_{UC}}{PL_{ref}},$$

(6.2)

where, η_{ref} is the PLQE of the reference sample; α_{ref} and α_{UC} are the absorption at the wavelength of excitation (515 and 785 nm) for the reference and upconversion sample, respectively; finally PL_{ref} and PL_{UC} are the photon counts for the reference and upconversion samples, respectively.[146] Using the previously mentioned absorption values, a rubrene PLQE of (36 ± 1) % and excitation flux above the observed threshold the UCQE for each of the upconversion solutions was calculated (Table 6.1).

We achieve a maximum upconversion efficiency of (1.2 ± 0.2) % for the PbS-TET-CA:Rub system. This efficiency is slightly lower than previous reports for PbS QDs with tetracene based ligands and rubrene upconversion with η_{UC} = (3.5 ± 0.3) %.[146] This indicates a sub-optimal triplet exciton transfer efficiency in the PbS-TET-CA:Rub system. The upconversion quantum efficiency can be expressed as

$$\eta_{UC} = \eta_{Rub}\eta_{TTA}\eta_{TET},$$

(6.3)

where η_{Rub} is the PLQE of the rubrene in the system. Using the previously reported triplet-triplet annihilation efficiency for rubrene (η_{TTA}~33 %) we estimate the triplet exciton transfer efficiencies from PbS QD to the rubrene triplet state for each solution (Table 6.1).[186] By similar measurement techniques Huang et al. have achieved a triplet transfer efficiency of (32 ± 3) %. The comparison of these efficiencies indicates the presence of increased loss pathways in the PbS-TET-CA:Rub system compared to that used by Huang et al. As expected, the PbS-OA:Rub systems have significantly lower UCQE and associated triplet exciton transfer efficiencies. This aligns with previous reports that the oleic acid ligands inhibit triplet exciton transfer.[12,101]

Sample	UCQE (%)	Rub PLQE (%)	η_{TTA} (%)	η_{TET} (%)
PbS(1.3 eV):Rub	$(8 \pm 2)x10^{-4}$	36 ± 1	33	$(7 \pm 1)x10^{-3}$
PbS(1.4 eV):Rub	0.20 ± 0.02	36 ± 1	33	1.8 ± 0.3
PbS(1.3 eV)-TET-CA:Rub	0.68 ± 0.1	36 ± 1	33	5.8 ± 1.2
PbS(1.4 eV)-TET-CA:Rub	1.2 ± 0.2	36 ± 1	33	11 ± 2

Table 6.1: Breakdown of the TTA-UC yields for PbS-TET-CA:Rub and PbS-OA:Rub solutions. UCQE is the upconversion quantum efficiency when the PbS QDs were selectively excited with 785 nm at 53 W/cm^2. η_{TTA} is the triplet-triplet annihilation efficiency used to calculate the overall triplet transfer efficiency from QD to rubrene, η_{TET}.

Before proceeding it is necessary to verify that the reduced efficiency observed in this report, relative to that reported by Huang et al., is not due to a sub-optimal ratio of the TTA-UC components. We achieve this by performing a parameter search across various PbS-TET-CA QD and rubrene concentrations. For each TTA-UC solution, the upconversion PL under ~50 W/cm^2 was measured and the spectrally integrated counts calculated (Figure 6.3). We found that the 1 mg/mL concentration of PbS-TET-CA QDs used is at the peak for upconversion photoluminescence. There is a significant positive relationship between the upconversion efficiency and the rubrene concentration. Figure 6.3c shows that the threshold excitation density is heavily dependent on the concentration of the rubrene triplet acceptor. This dependence is consistent with a reduction in triplet exciton transfer efficiencies at low rubrene concentration. We expand on the triplet exciton transfer efficiencies dependence on the rubrene concentration in Section 6.6.

This modest parameter search indicates that the PbS-TET-CA:Rub concentration of 1:10 mg/mL is close to the optimal. Which in turn suggests that the observed low UCQE is due to loss pathways competing with the triplet transfer to rubrene.

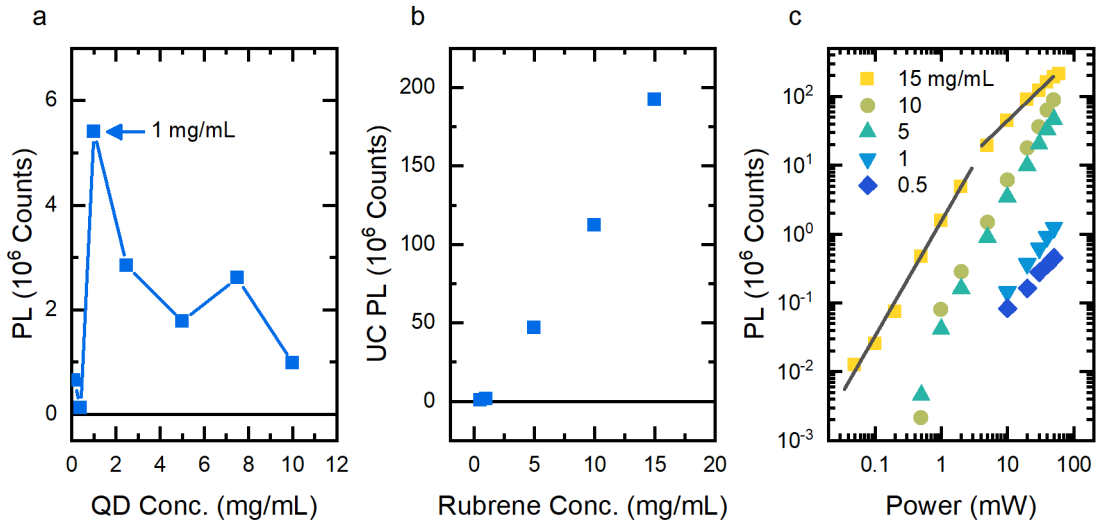

Figure 6.3: Upconversion PL dependence on PbS-TET-CA QD and rubrene concentrations. a,b) Spectrally integrated upconversion PL from solutions of PbS-TET-CA:Rub under 50 W/cm2 excitation at 785 nm. a) Upconversion PL for PbS-TET-CA:Rub solutions with 10 mg/mL of rubrene and varying QD concentrations. b) Upconversion PL for PbS-TET-CA:Rub solutions with 1 mg/mL of PbS-TET-CA QDs and varying Rub concentrations. c) Upconversion PL fluence dependence for PbS-TET-CA:Rub solutions with 1 mg/mL of PbS-TET-CA QDs and varying Rub concentrations. The black lines show power-law fits for the 1:15 mg/mL solution, illustrating the transition from quadratic (n = 1.67 ± 0.02) to linear (n = 0.93 ± 0.05).

6.4 Excited State Trapping

We employ femtosecond transient absorption (fsTA) spectroscopy to investigate the loss pathways competing with triplet exciton transfer. We measured fsTA spectra of the PbS-OA and PbS-TET-CA QDs in toluene solution, with selective excitation (800 nm) of the PbS QDs (Figure 6.4). In both systems, we observe a positive fsTA signal at ~900 nm, characteristic of the QD ground state bleach (GSB). Additionally, we assign the broad negative signals on either side of the GSB to photoinduced absorption (PIA) features due to the QD excitonic excited state. The similarity of the spectral features and strengths at early times (<10 ps) between the PbS-OA and PbS-TET-CA QDs suggests that at these timescales the PbS-TET-CA system is in the PbS excitonic excited state, $[QD_1]$.

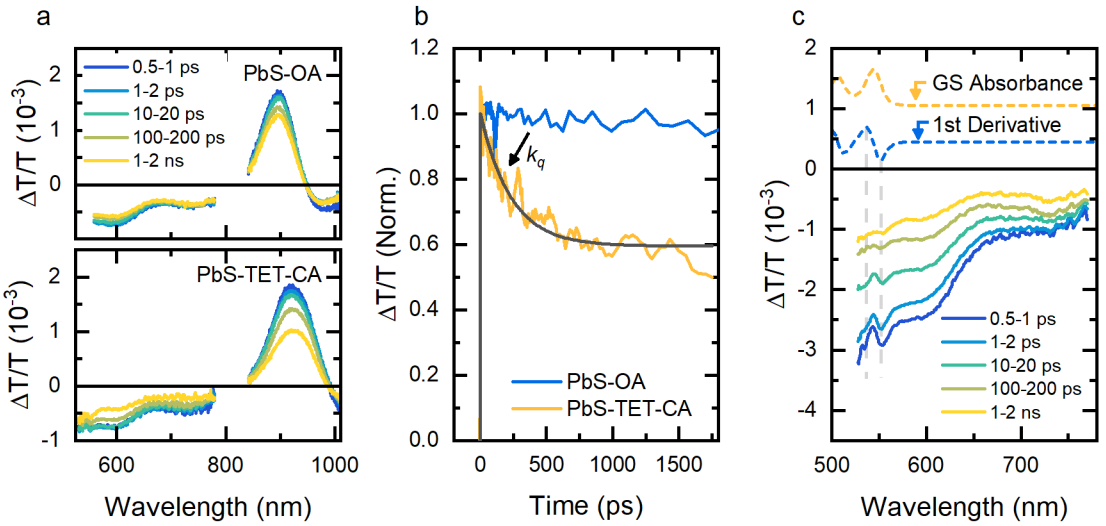

Figure 6.4: Exciting state trapping and quasi-equilibrium in PbS-TET-CA QDs.
a) Temporally averaged fsTA spectra of PbS-OA (top) and PbS-TET-CA (bottom) 4 mg/mL solution solutions, after 800 nm excitation with 120 uJ/cm^{-2}. b) Normalised psTA kinetics at the PbS QD GSB 880-930 nm. The PbS-TET-CA kinetic is fit with equation (6.2). c) Enhanced view of the fsTA spectra for PbS-TET-CA QDs. Dashed lines indicate the spectrally resolved ground state absorption (orange) and its derivative with respect to wavelength (blue) for pristine TET-CA in solution.

Figure 6.4b shows a comparison of the QD GSB of the PbS-OA and PbS-TET-CA QDs over the first ~1.5 ns after photoexcitation. There is a significant decay of the PbS QD excited state population over the first 500 ps. This initial decay component of the PbS QD exciton has been reported previously in relation to our SF-PM projects.[97] In that report, Gray et al. identified this initial decay of the PbS QD GSB as the formation of a quasi-equilibrium between QD excitonic excited state and a trap state. Decay from this trap state was identified as loss pathway competing with photoluminescence from the QD.

Conversely, in this work, we reframe this interpretation as competing with triplet exciton transfer from QD to TET-CA triplet state. Here, we describe the dynamics of the QD excitonic excited state $[QD_1]$ and the trap population $[QD_{Tr}]$ with the following system of equations:

$$\frac{d[QD_1]}{dt} = -k_q[QD_1] + k_{-q}[QD_{Tr}]\,,$$

$$\frac{d[QD_{Tr}]}{dt} = k_q[QD_1] - k_{-q}[QD_{Tr}]\,,$$

(6.4)

where k_q and k_{-q} are the rates for trapping and de-trapping, respectively. This particular system of differential equations is only valid for times much earlier than the timescales for intrinsic decay QD excited state, triplet transfer to the TET-CA ligand, and the decay from the trap state. In the next section, investigating the nanosecond transient absorption dynamics of the PbS-OA and PbS-TET-CA systems, we see that these occur on timescales greater than tens of nanoseconds. Thus, expression (6.4) is a reasonable approximation for the ~100 ps transfer between QD exciton and the trap state. The system of differential equations (6.4), with the initial condition $[QD_{Tr}](0) = 0$, has analytical solutions given by:

$$[QD_1](t) = [QD_1]_0\left(\frac{k_q}{k_q + k_{-q}}e^{-(k_q+k_{-q})t} + \frac{k_{-q}}{k_q + k_{-q}}\right),$$

$$[QD_{Tr}](t) = [QD_1]_0\frac{k_q}{k_q + k_{-q}}\left(1 - e^{-(k_q+k_{-q})t}\right),$$

(6.5)

where $[QD_1]_0$ is the initial photoexcited population of the QD exciton state. Fitting of the equation for $[QD_1](t)$ to the QD GSB for the PbS-TET-CA system yields a trapping rate of k_q ~1.8 ± 0.2 ns^{-1} and a de-trapping rate of k_{-q}~2.6 ± 0.2 ns^{-1}.

Figure 6.4c highlights the fsTA spectra for PbS-TET-CA in the visible region near the TET-CA ground-state absorption. The predominant feature in this range is the broad PIA assigned to the QD exciton excited state. However, superimposed on top of this broad PIA is a narrow positive to negative feature in the range of 540 to 560 nm. Similar photoinduced absorption and bleach signals have been observed in other PbS QDs with acene-based ligands.[189] In a previous report by Bender et al. these induced absorptions and bleach features were assigned to Stark-induced changes in the ligand absorption bands.[189] The Stark-effect describes the transient changes in the bandgap of the TET-CA due to the exposure to an external electric field. The shift in the bandgap of the TET-CA ligand leads to a fsTA feature that is approximated well by the first derivative of its ground-state absorption spectrum. Bender et al. argue that the source of the external electric field is the local field between the electron and hole on the photoexcited QD. The presence of a dipole-like electric field between electron and hole indicates they are spatially separated to some extent. This separation indicates there is a process occurring that is separating the electron and hole in the QD.

Concurrent to the loss of the QD GSB signal over the first 500 ps, we observe a reduction in the Stark-induced features. The combination of decay in combined electron and hole population and the Stark-effect is consistent with the electron and hole separating over this time period. This suggests that as the trap state forms, either the electron, hole, or both, have left the core of the QD and are localised on the surface, or outside the QD.

The presence of a quasi-equilibrium between the QD exciton state and the trap state suggests that the two are relatively close in energy. This motivates the question: what is the Gibbs free energy difference between these states? The equilibrium ratio of QD exciton and trap state can be expressed as

$$\frac{[QD_{Tr}]}{[QD_1]} = \frac{k_q}{k_{-q}} = e^{-\frac{\Delta G}{k_B T}}, \tag{6.6}$$

where ΔG is the Gibbs free energy difference going from QD excitonic state to trap. Substituting the extracted values for k_q and k_{-q}, and taking the room temperature as 300 K, leads to ΔG=10 ± 12 meV. That is, the trap state is ~10 meV higher in energy than the QD exciton for this particular PbS-TET-CA system (Figure 6.5a).

To understand further the energy dependence of the trapping process, we use fsTA data reported by Gray et al. for the same PbS-TET-CA system with multiple bandgaps of PbS QDs.[97] The procedure of fsTA fitting to extract the trapping rates and Gibbs free energy difference was repeated for a range of QD bandgaps (Figure 6.5b). The Gibbs free energy difference from QD exciton excited state to trap state is observed to have a significant dependence on the bandgap of the QD.

At low bandgaps the transfer from QD_1 to QD_{Tr} is endergonic, and exergonic for high bandgap QDs. The lower panel in Figure 6.5b shows the energy of the trap state given the energy of the PbS QD exciton energy, as a function of the QD bandgap. Interestingly the trap energy does not increase at the same rate as the bandgap. In contrast, the trap energy does increase at the same rate as the LUMO of the PbS QD, with respect to changes in the QD bandgap. This relationship can be seen in the parallel nature of the trap energy and QD LUMO values. Values for the PbS QD LUMO were taken from various literature reports.[12,92,146]

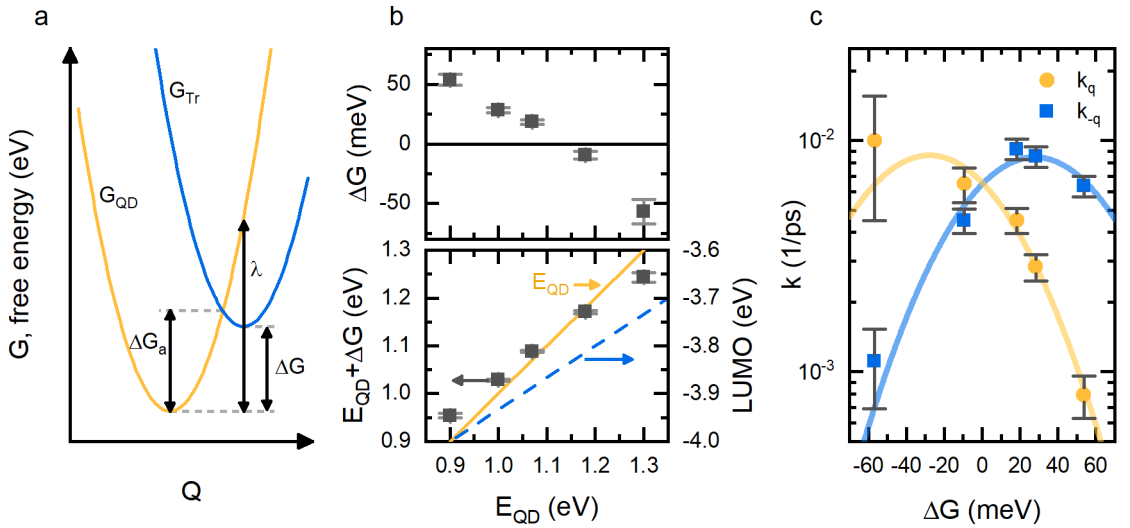

Figure 6.5: Energy dependence of the PbS-TET-CA QD excited state trapping.
The procedure of fitting equation (6.2) is repeated for fsTA data reported for the PbS GSB by Gray et al.[97] *a) Illustration of the relevant parameters in applying Marcus-Hush theory to the QD_1 and QD_{Tr} system. b, top) Gibbs free energy difference between QD_1 and QD_{Tr}, calculated by application of equation (6.6). b, bottom) Energy of the trap state relative to the ground state of the QD, $E_{QD_1} + \Delta G$ (black squares). Bandgap of the PbS QD (solid orange line). Linear fit to the LUMO energy of PbS QDs, relative to the vacuum (dashed blue line). LUMO energies taken from literature.*[12,92,146] *c) Fitted rate constants for trapping, k_q, and de-trapping, k_{-q}. These rates are fitted with equations (6.7) and (6.8), respectively.*

The relationship between the trap energy and the QD LUMO suggests that the trap state has a fixed energy relative to the vacuum. Subtracting the trap energy from the QD LUMO yields an average value of -4.971 ± 0.004 eV, across the QD bandgaps investigated. The uncertainty in this value for the trap energy is representative of the uncertainty and distribution in the trap energy relative to the QD exciton and does not include any uncertainty from the LUMO values. The essentially constant value for the trap state relative to the vacuum indicates that it is not affected by the quantum confinement of the QD and its size dependence. Based on these observations, some possibilities for the origin of the trap state include a fixed energy surface state, or a hole state on the TET-CA ligand.[146,189,190]

Figure 6.5c displays the extracted trapping and de-trapping rates as a function of the Gibbs free energy difference between $[QD_1]$ and $[QD_{Tr}]$ states. Formation of the trap state likely involves the transfer of an electron or hole from the core of the QD, therefore treatment with Marcus-Hush theory is appropriate.[191] Figure 6.5a illustrates the relation between the energy surfaces of QD exciton and the trap state, along with the relative

activation energy for the trapping and de-trapping processes. Consideration for the relevant activation energies for the forward, k_q, and reverse, k_{-q}, process yields

$$k_q = Aexp\left(-\frac{\left(\frac{(\Delta G+\lambda)^2}{4\lambda}\right)}{k_B T}\right), \quad (6.7)$$

$$k_{-q} = Bexp\left(-\frac{\left(\frac{(\Delta G-\lambda)^2}{4\lambda}\right)}{k_B T}\right), \quad (6.8)$$

where λ is referred to as the reorganisation energy, and the pre-exponential factors A and B relate to the probability of transfer between the initial and final state. The fitting of these rate expressions is achieved by least-square fitting. The pre-exponential factors are found to be A = 8.6 ± 0.4 ns^{-1}, and B = 8.9 ± 0.5 ns^{-1}. The extracted reorganisation energy for the transfer is λ = 28 ± 3 meV. This reorganisation energy is relatively low when compared to typical values for organic molecules of a few hundred meV,[192] whereas the reorganisation energy of QDs has been estimated to be 10 meV or less.[193,194] The comparison of the measured reorganisation energy with the typical values for organic molecules and inorganic QDs indicates that the trapping may not involve the electronic states of the ligands. Instead, this points to the trap state being situated on the QD or its surface.

Huang et al. have reported ~100 ps trapping and attributed this to hole transfer from the PbS QD to the HOMO of their tetracene-based ligand.[146] The HOMO energy of non-doped, tetracene-based molecules is typically ~-5.5 eV.[12,146] The difference between this HOMO value and the Gibbs free energy of the traps calculated here is ~500 meV, which can be interpreted as the entropic gain during the hole transfer from PbS QD to TET-CA ligand. If this interpretation is correct, the associated entropic gain is substantial.

Further work should be performed to rule out alternative origins for the trap state. The exact origin of the trap state aside, Huang et al. illustrated the use of PbS/CdS core-shell quantum dots to reduce the trapping rate and increase triplet yields. The reduced trapping with the CdS shelling of the PbS QD can be explained by two hypotheses: improved passivation in the surface states, or by reduced hole transfer due to the energy barrier introduced by the low HOMO CdS shell in the hole transfer. The use of core-shell QDs would be a beneficial research direction to pursue in the future. Additionally,

calculation of the electronic states of the TET-CA ligand while attached to the QDs would be valuable for analysing the origin of such traps.

6.5 Triplet Generation Dynamics

Having investigated the rapid trapping of the QD exciton state, we shift focus to the dynamics of triplet generation on the TET-CA ligand. Nanosecond transient absorption (nsTA) spectra of PbS-OA and PbS-TET-CA solutions were recorded under 920 nm excitation (Figure 6.6). The selective excitation of the PbS QD leads to greatly differing dynamics for the QDs covered in TET-CA compared to OA ligands. In the PbS-OA system a single spectral component is observed, decaying over a microsecond timescale. The PbS-OA nsTA spectrum is similar to that measured on femtosecond timescales. The spectrum comprises of a QD GSB at ~880 nm and broad PIAs across the investigated wavelength range. These spectral features are assigned to the presence of the QD excitonic excited state. Fitting of a mono-exponential decay to the GSB of the QD yields a 2740 ± 40 ns lifetime for the QD exciton.

In contrast, the PbS-TET-CA nsTA data indicates the presence of multiple spectral components. At times earlier than ~100 ns the spectra have a positive signal at ~880 nm, which exhibits bi-exponential decay (Figure 6.6c). We assign this spectral feature to the initial and residual population of the PbS QD excitonic excited state, after reaching quasi-equilibrium with the trap state. Fitting of the PbS-TET-CA QD GSB with a bi-exponential decay yields two distinct lifetimes, 3.7 ± 0.3 ns and 140 ± 5 ns. Given the reduced temporal resolution of the nsTA apparatus, the first component is consistent with the faster than 500 ps decay observed by fsTA. The second component indicates that the decay from the trap state and triplet transfer from the QD exciton to the TET-CA triplet exciton occurs on a ~100 ns timescale.

At 1-10 μs, after the full decay of the QD GSB, a new spectral component is observed in the PbS-TET-CA system. This spectral component has no remnants of the QD GSB, a broad PIA from 520-650 nm, and a positive peak at ~545 nm. In agreement with a previously reported triplet sensitisation spectrum for TET-CA, we assign this spectral component to the TET-CA triplet exciton.[137] The PIA from 520-650 nm is due to the triplet exciton on the TET-CA, and the positive peak at 545 nm is the TET-CA GSB. The TET-CA triplet PIA, when TET-CA is attached to the QD, is less feature-full than the sensitisation spectrum for TET-CA isolated in solution. The lack of a sharp PIA peak at

660 nm, for the TET-CA triplet in the PbS-TET-CA system indicates that the close proximity to the QD alters the high-energy triplet states of TET-CA.

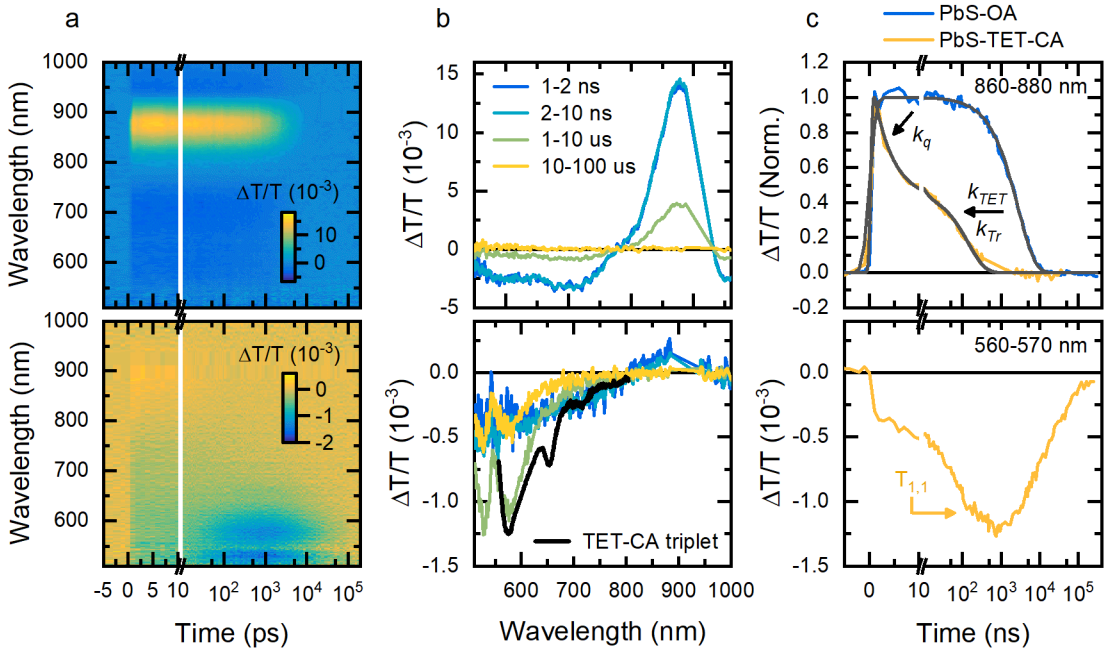

Figure 6.6: Triplet exciton transfer from PbS QDs to TET-CA ligands.
nsTA maps (a) and spectra (b) for 1.3 eV PbS QD with either OA (top) or TET-CA ligands (bottom), under 920 nm excitation at 485 μJ/cm^{-2}. Solutions were prepared to 4 mg/mL QD concentrations in toluene. b) nsTA spectra, integrated over the indicated time ranges. The linearly scaled TET-CA triplet spectrum (black curve) is taken from a previous report by Davis et al.[137] c) nsTA kinetics for PbS-OA and PbS-TET-CA, at the QD GSB, 860-880 nm (top), and the TET-CA triplet PIA, 560-570 nm (bottom). c, top) PbS-OA kinetics fit with a mono-exponential decay, with lifetime 2740 ± 40 ns. PbS-TET-CA kinetics fit with a bi-exponential decay, with lifetimes 3.7 ± 0.3 ns and 140 ± 5 ns.

Monitoring the TET-CA PIA at 560-570 nm shows that the triplet population increases over a ~100 ns timescale (Figure 6.6c). To investigate the yield of triplet generation on the TET-CA ligand we perform an estimate based on the strength of the TET-CA GSB. The absorption of the PbS-TET-CA solution at 920 nm is measured to be 1.28 % by UV-Vis absorption. Based on a pulse flux of 485 μJ cm^{-2}, this relates to 9.5 x 10^{10} photons absorbed per pulse. Combined with a path length of 200 μm, the resultant QD excited state population is

$$[QD_1] = 1.88 \times 10^{-6} \text{ mol L}^{-1}.$$

(6.9)

The peak strength of the TET-CA GSB $\Delta T/T$ signal is

$$\left(\frac{\Delta T}{T}\right)_{GSB} \approx (4 \pm 0.5) \times 10^{-4}.$$

(6.10)

The corresponding change in absorption is given by

$$\Delta A_{GSB} = \log_{10}\left(1 - \left(\frac{\Delta T}{T}\right)_{GSB}\right).$$

(6.11)

Using a previously reported molar attenuation coefficient for the 0-0 vibrionic peak at 545 nm of 18000 L mol^{-1} cm^{-1} and multiplying by the path length of the sample yields a molar absorption coefficient of ϵ_{GSB} = 360 L mol^{-1}.[137] The resultant TET-CA triplet exciton density is given by

$$[T_T] = \frac{\Delta A_{GSB}}{\epsilon_{GSB}} \approx (4.8 \pm 0.6) \times 10^{-7} \text{ mol L}^{-1}.$$

(6.12)

The triplet exciton transfer efficiency from QD to TET-CA is thus

$$\eta_{TET_1} = \frac{[T_T]}{[QD_1]} \approx (26 \pm 3)\ \%.$$

(6.13)

The uncertainty in the calculated triplet exciton transfer efficiency only represents uncertainty in the TET-CA GSB peak strength measured by nsTA and no other possible systematic errors.

The QD exciton and TET-CA triplet features are distinguishable directly in the nsTA spectra. However, the genetic algorithm is needed to clarify the spectral features of the trap state and dynamics of the triplet generation on the TET-CA ligand (Figure 6.7). Here, the nsTA spectra for the PbS-TET-CA QDS is decomposed into three spectral components. Two reference spectra are used in the decomposition: the QD excitonic excited state spectra is based on the average spectra for PbS-OA QDs over the time period 1-500 ns and TET-CA triplet exciton spectrum is taken as the average spectrum for the PbS-TET-CA system between the times 0.6 and 10 µs. The extracted spectrum for

the trap state is void of any positive GSB feature at either the PbS QD or TET-CA GSB regions, or across the entire investigated range. The trap spectrum only consists of a broad PIA from 500 to 800 nm. The resultant decomposed nsTA kinetics were scaled such that their values represent the transient population relative to the initial PbS QD excited state population. The normalised trap kinetic was multiplied by $\frac{k_q}{k_q+k_{-q}}$, the quasi-equilibrium ratio of trap state to initial QD excited state population. The TET-CA triplet population was scaled by the triplet transfer efficiency found above (26 ± 3) %.

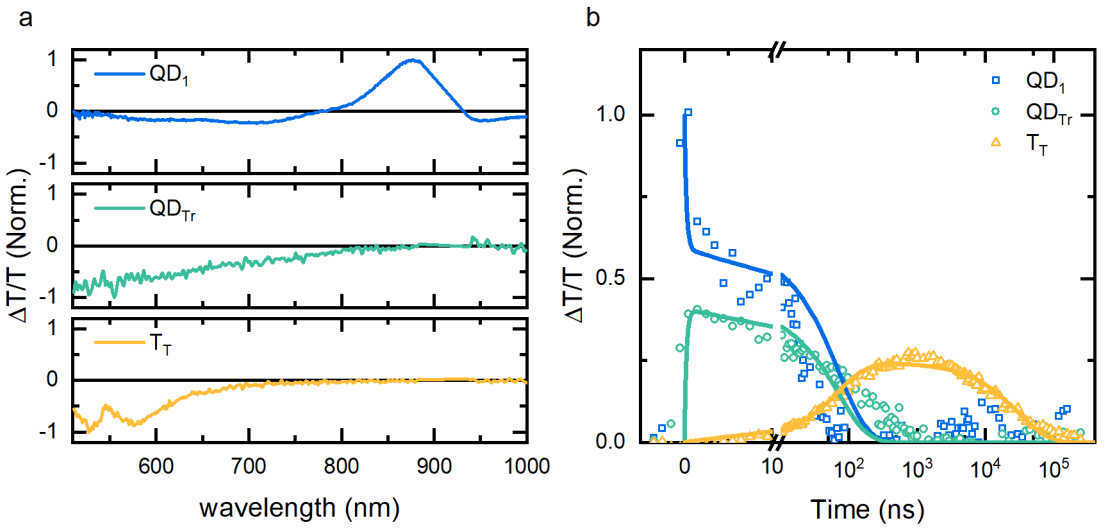

Figure 6.7: Decomposition of triplet exciton transfer dynamics in PbS-TET-CA QDs.
a) Decomposition of the nsTA spectra of PbS-TET-CA into three spectral components, PbS QD excitonic excited state (blue), QD trap state (green) and TET-CA triplet state (orange), is achieved by the genetic algorithm. b) Decomposed kinetics under 920 nm excitation. Kinetics are normalised by the appropriate ratio such that the values present estimate populations relative to the initial QD excited state population. Kinetics are fit with the analytical expression (6.x), see Table 6.2 for obtained fitting parameters.

The decomposed kinetics for the PbS-TET-CA system show a rapidly reached quasi-equilibrium between the $[QD_1]$ and $[QD_{Tr}]$ states. This equilibrium mixture then decays leading to the generation of the TET-CA triplet state, $[T_T]$, which subsequently decays. We model this system with the following system of differential equations

$$\frac{d[QD_1]}{dt} = -\left(k_{QD} + k_q + k_{TET_1}\right)[QD_1] + k_{-q}[QD_{Tr}]\,,$$

$$\frac{d[QD_{Tr}]}{dt} = k_q[QD_1] - \left(k_{-q} + k_{Tr}\right)[QD_{Tr}]\,,$$

$$\frac{d[T_T]}{dt} = k_{TET_1}[QD_1] - k_T[T_T]\,,$$

(6.14)

where, k_{QD}, k_{Tr} and k_T are the decay rates of the QD exciton, trap and TET-CA triplet states, respectively, and k_{TET_1} is the triplet transfer rate from QD excitonic state to TET-CA triplet state. Here, we have assumed that the exothermic nature of the $[QD_1]$ to $[T_T]$ reaction (ΔE ~ -100 meV) means the reverse process is minimal and can be neglected. With the initial condition that all excitation start in the $[QD_1]$ state, the system of ordinary differential equations (6.14) is solved analytically in the symbolic computational package Mathematica. The system of equations is converted to the form

$$\frac{d}{dt}\underline{x}(t) = \boldsymbol{A}\underline{x}(t)\,,$$

(6.15)

where $\underline{x}$ is a vector of the populations. The solution is found by computing the matrix exponential, yielding

$$\begin{bmatrix} [QD_1](t) \\ [QD_{Tr}](t) \\ [T_T](t) \end{bmatrix} = \begin{bmatrix} [QD_1]_0 \\ 0 \\ 0 \end{bmatrix} e^{\boldsymbol{A}t}\,,$$

(6.16)

where $[QD_1]_0$ is the initial QD exciton excited state population. The matrix $e^{\boldsymbol{A}t}$ is found symbolically, although reproducing it here is impractical due to the immense size of the expression. The full analytical expression is then fitted to the decomposed kinetics (Figure 6.7b). The rates k_{Tr}, k_T, and k_{TET_1} are optimised during the fitting procedure. Other variables are fixed at values obtained in earlier experiments (Table 6.2). The obtained triplet transfer rate from PbS QD to the ligand triplet state is considerably slower than in other similar systems.[146] The most apparent difference between the PbS-TET-CA system and these previously reported systems is the geometry of the attachment point. This geometry could be affecting the coupling strength between the QD donor and tetracene chromophore acceptor.

Process	Rate (ns^{-1})	Time constant (ns)
k_{QD} [a]	3.65 x 10^{-4}	2740
k_q [b]	1.8	0.55
k_{-q} [b]	2.6	0.38
k_{TET_1} [f]	(5.8 ± 0.2) x 10^{-3}	172 ± 7
k_{Tr} [f]	(2.6 ± 0.1) x 10^{-2}	38 ± 2
k_T [f]	(3.2 ± 0.3) x 10^{-5}	(31 ± 3) x 10^3

Table 6.2: Fitted triplet generation and decay rates for PbS-TET-CA QDs.
a) Value determined from fitting the mono-exponential decay rate of PbS-OA QDs measured by nsTA and fixed during the fitting of equation (6.16). b) Values determined from fitting the decay of the PbS QD excitonic excited state observed by fsTA and fixed during the fitting of equation (6.16). f) Free varying variables for the fitting of equation (6.16) to the decomposed populations kinetics of triplet transfer in the PbS-TET-CA system.

The decay rate of the trap state found here is two orders of magnitude faster than an equivalent rate determined by fitting for the PbS-TET-CA systems via PLQE measurements by Gray et al.[97] We point to differences in how the model used in this previous report and the current model quantify the energy dependence of the trapping rate as a possible source of discrepancy. Additionally, the trap decay rate may depend on the bandgap of the QDs. In particular, the passivation of the QDs surface could be dependent on the size of the QD, which could lead to a difference between the trap decay rate for low bandgap QDs, as is the focus in the Gray et al. report and the high bandgap QDs investigated here.

Solving the system of equations (6.14) under steady-state conditions leads to efficiencies for the QD PLQE, trap induced decay, and triplet exciton transfer to the TET-CA ligand respectively given by[97]

$$\eta_{QD,r} = \eta_{QD,r,0} \times \frac{k_{QD}}{k_{QD} + k_{TET_1} + k_q - k_{-q}\left(\frac{k_q}{k_{Tr} + k_{-q}}\right)}, \tag{6.17}$$

$$\eta_{Tr} = \frac{k_q - k_{-q}\left(\frac{k_q}{k_{Tr} + k_{-q}}\right)}{k_{QD} + k_{TET_1} + k_q - k_{-q}\left(\frac{k_q}{k_{Tr} + k_{-q}}\right)}, \tag{6.18}$$

$$\eta_{TET} = \frac{k_{TET_1}}{k_{QD} + k_{TET_1} + k_q - k_{-q}\left(\frac{k_q}{k_{Tr} + k_{-q}}\right)}, \tag{6.19}$$

where $\eta_{QD,r,0}$ is the PLQE of the original PbS-OA quantum dots. Substituting the fitted rates yields a QD PLQE of $\eta_{QD,r}$ = (0.8 ± 0.1) %, consistent with the measure PLQE of (2 ± 2) %. The considerable trap decay leads to η_{Tr} = (75 ± 2) %, such that ~75% of excitons decay via the trap state. This leaves ~24 % of excitations from the PbS QDs that make it to the TET-CA triplet state, η_{TET} = (24 ± 2) %.

The trap decay rate quantifies both the intrinsic decay from the trap state and any increase of decay due to non-passivated sites. The passivation dependent quenching is likely dependent on the size of the quantum in relation to the bulk TET-CA ligand.

The sub-optimal triplet transfer efficiency from PbS QD to TET-CA ligand is a significant factor contributing to the low upconversion quantum efficiency. Reduction of the trapping rate, k_q, or the decay rate from the trap, k_{Tr}, are possible methods to improve the upconversion yield. An alternative is to vary the number of the TET-CA ligands on the surface of the PbS QDs. It is commonly found that the triplet transfer rate increases linearly with surface ligand density

$$k_{TET} = n \times k_{TET,0}\,, \tag{6.20}$$

where n is the number of ligands per QD and $k_{TET,0}$ is the triplet transfer rate per ligand. Combining equations (6.19) and (6.20) allows the estimation of the triplet exciton transfer efficiency for any surface density of TET-CA ligands. If the ligand coverage can be increased, for example by a reasonable factor of 2, then the triplet transfer efficiency to the ligand would become ~40%. This would lead to a corresponding increase in the upconversion yield.

6.6 Triplet Transfer Dynamics

Now that the principles governing the generation of triplet excitons on the TET-CA ligands have been explored, we shift attention to the final challenge of investigating the triplet exciton transfer to the rubrene molecules. The dynamics of triplet transfer in solutions of PbS-OA:Rub and PbS-TET-CA:Rub were probed by recording nsTA spectra. The PbS QDs were selectively excited by pumping at 920 nm.

In the PbS-OA:Rub system there is no significant triplet exciton transfer to the rubrene molecules. The intrinsic decay rate of the PbS-OA QDs alone is k_{QD} = 0.365 ± 0.005 μs^{-1}. The decay rate of the QD GSB when 10 mg/mL of rubrene is added, is well fitted with a mono-exponential decay with rate constant 0.37 ± 0.01 μs^{-1} (See appendix D, Figure 7.10 for details). The transfer in this system is expected to be completed in a single step from QD to rubrene. In such a case, the rate of transfer can be expressed as the difference between these two rate constants. Calculation of the difference yields a triplet exciton transfer rate of k_{TET} = 5 ± 15 ms^{-1}. Based on these rates the triplet transfer efficiency is given by

$$\eta_{TET} = \frac{k_{TET}}{k_{TET} + k_{QD}}. \tag{6.21}$$

In the PbS-OA:Rub system we calculate that the triplet transfer rate is η_{TET} = (1 ± 4) %, representing a negligible amount of transfer.

In comparison, the PbS-TET-CA:Rub system shows significant reductions in the TET-CA triplet population which is assigned to triplet exciton transfer to rubrene. Figure 6.8a shows the nsTA kinetics assigned to the combination of the PIA of the $[QD_1]$ and $[QD_{Tr}]$ qausi-equilibrium and the TET-CA triplet exciton, at various concentrations of rubrene. The triplet populations were extracted from these naTA kinetics by subtraction of the spectral components of the $[QD_1]$ and $[QD_{Tr}]$ quasi-equilibrium. Specifically, a mono-exponential decay, with an amplitude equal to the initial $\Delta T/T$ strength at 1 ns, and decay rate $(k_{TET}k_{-q} + k_{Tr}k_q)/(k_q + k_{-q})$, was subtracted from the average nsTA signal strength at 560-570 nm. Figure 6.9c shows the nsTA difference kinetics assigned to the population of the TET-CA triplet exciton at various concentrations of rubrene.

The TET-CA Triplet population shows two components of triplet transfer to the rubrene triplet state. The fast component of triplet transfer results in a reduction in the peak triplet population reached and occurs of timescales faster than 1 μs. This initial

component of triplet transfer appears to proceed with a rate $k_{TET_{2,f}}$, approximately equal to or faster than the triplet generation rate, k_{TET_1}. The second component of triplet transfer to rubrene leads to a reduced lifetime of the TET-CA triplet on ~10 µs timescales. The rate of triplet transfer from the PbS-TET-CA QD to the rubrene triplet state in the slow component, $k_{TET_{2,s}}$, increased with the concentration of the rubrene acceptor.

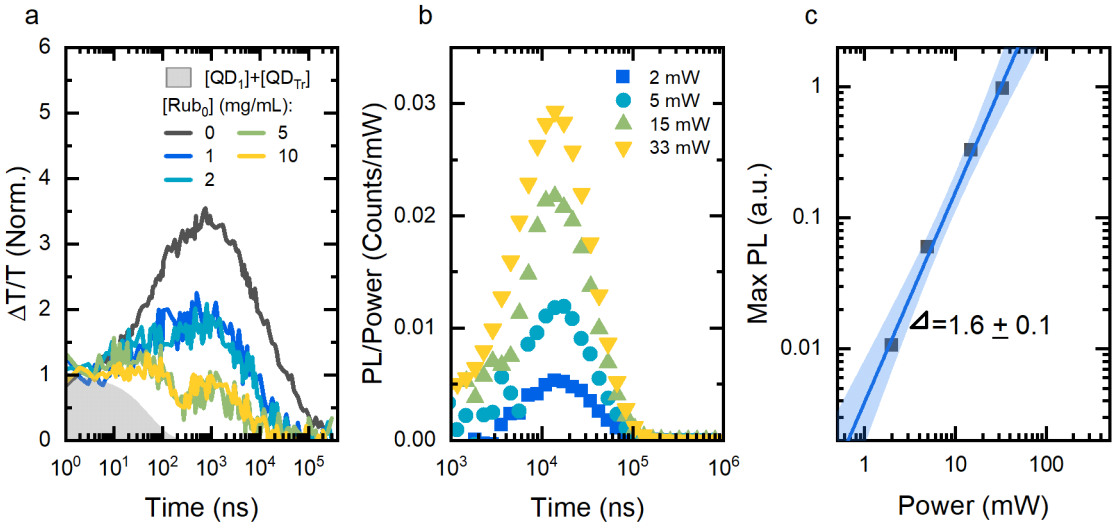

Figure 6.8: Triplet transfer and photoluminescence upconversion in PbS-TET-CA:Rub. a) nsTA kinetics at 560-570 nm for PbS-TET-CA:Rub solutions with various rubrene concentrations, after excitation at 920 nm excitation with 485 µJ/cm^{-2}. Kinetics were normalised to their initial value at 1-2 ns. b) TTA transient PL for PbS-TET-CA (2 mg/mL) and rubrene (10 mg/mL) under 920 nm excitation at various fluences, normalised by the incident laser power. The power normalised PL increases with increasing laser power, indicating a super-linear relationship to excitation density. c) The maximum upconversion PL counts as a function of the incident laser power, showing a non-linear relationship between excitation density and PL.

To complement the nsTA measurements of the TET-CA triplet population, transient photoluminescence spectra were measured under similar conditions with selective excitation of the PbS QDs. Spectral integration over the rubrene emission 550-650 nm allows monitoring of the generation of rubrene triplet population by TTA. Figure 6.8 displays that the upconversion PL from rubrene increases over ~10 µs period after photoexcitation of the PbS QDs. The peak PL intensity reached shows a non-linear dependence on the incident laser power. This non-linear behaviour is consistent with this delayed fluorescence being the result of TTA in the rubrene.[186] The rubrene triplet population can be estimated by plotting the square root of the upconversion PL (Figure 6.9c).[57] For PbS-TET-CA:Rub solutions with rubrene concentrations up to 10 mg/mL, the

rubrene triplet population that undergoes TTA increases microseconds after the initial excitation of the PbS QD.

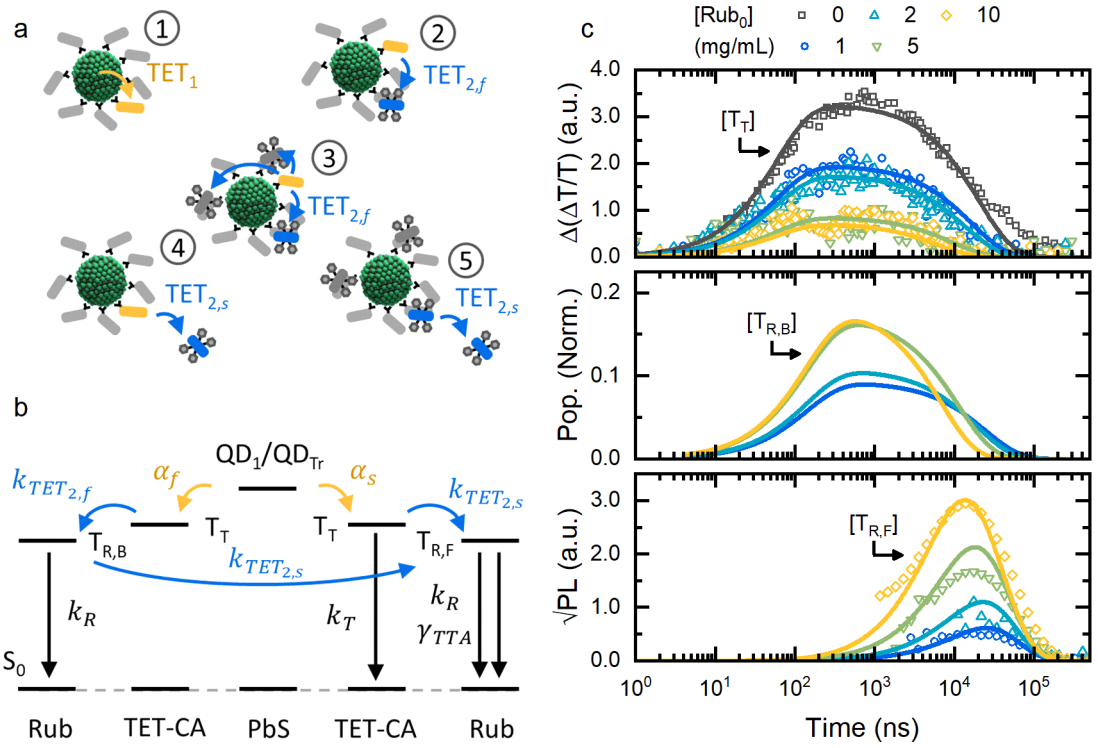

Figure 6.9: Schematic and fits for triplet transfer to bound and free rubrene.
a) Proposed triplet transfer processes occurring in PbS-TET-CA:Rub solutions. (1) Triplet exciton transfer from PbS QD to TET-CA triplet, TET_1. Triplet exciton transfer, $TET_{2,f}$, can occur on fast timescales from TET-CA to one (2) or multiple (3) rubrene molecules bound to the surface of the PbS-TET-CA QD. On slower timescales triplet exciton transfer, $TET_{2,s}$, from QDs without (4) and with (5) adsorbed rubrene molecules, to free-floating rubrene molecules occurs. b) Kinetic model for the multiple triplet transfer and other competing processes. c) Triplet populations for a solution of PbS-TET-CA:Rub. c, top) nsTA difference kinetics for the TET-CA triplet population, $[T_T]$, normalised to the initially population of $([QD_1] + [QD_{Tr}])$. c, bottom) Square root of the transient PL resulting from TTA of the free-floating rubrene triplets, $[T_{R,F}]$. c, mid) Population of the rubrene triplet states bound to the surface of the PbS-TET-CA, $[T_{R,B}]$, inferred from the fitting of equation (6.X).

Figure 6.9a presents the various processes that we consider to explain the observations identified by nsTA and transient PL measurements of the PbS-TET-CA:Rub system. These processes occur as follows:

- Initial triplet exciton transfer from the $[QD_1]$ and $[QD_{Tr}]$ quasi-equilibrium to the TET-CA triplet state (TET_1) occurs on a ~100 ns timescale.
- Rubrene molecules can adsorb to the surface of the QD.

  - If a particular QD has a rubrene adsorbed to its surface, triplet exciton transfer to the triplet state of the adsorbed rubrene, $T_{R,B}$, occurs rapidly.
  - If multiple rubrene molecules are adsorbed to the surface of a single QD, then the triplet transfer occurs at an increased rate. Whether there is one rubrene or many, this fast component of triplet transfer, $TET_{2,f}$, occurs at a rate similar to or faster than TET_1.
  - The sub-population of QDs with no rubrene molecules adsorbed to their surface do not undergo this fast component of triplet transfer.
- On longer timescales, triplet exciton transfer to free-floating rubrene molecules occurs ($TET_{2,s}$). This slower transfer occurs from both the TET-CA triplet state and the rubrene triplets bound to the PbS-TET-CA QDs.

Figure 6.9b illustrates the kinetic model we build to encompass the above processes. The key component of this model is that some fraction α_s of the PbS-TET-CA QDs do not have any rubrene molecules adsorbed to their surface. In comparison, the fraction α_f have at least one rubrene adsorbed. This leads to the following system of differential equations:

$$\frac{d[QD_1]}{dt} = -\left(k_{QD} + k_q + k_{TET_1}\right)[QD_1] + k_{-q}[QD_{Tr}]\,,$$

$$\frac{d[QD_{Tr}]}{dt} = k_q[QD_1] - \left(k_{-q} + k_{Tr}\right)[QD_{Tr}]\,,$$

$$\frac{d[T_T]}{dt} = \alpha_s k_{TET_1}[QD_1] - \left(\gamma_{TET_{2,s}}[Rub_0] + k_T\right)[T_T]\,,$$

$$\frac{d\left[T_{R,B}\right]}{dt} = \alpha_f k_{TET_1}[QD_1] - \left(\gamma_{TET_{2,s}}[Rub_0] + k_R\right)\left[T_{R,B}\right]\,,$$

$$\frac{d\left[T_{R,F}\right]}{dt} = \gamma_{TET_{2,s}}[Rub_0]\left([T_T] + \left[T_{R,B}\right]\right) - k_R\left[T_{R,F}\right]\,, \qquad (6.22)$$

where, $\left[T_{R,B}\right]$ and $\left[T_{R,F}\right]$ are the populations of the rubrene triplet bound and free-floating, respectively. $[Rub_0]$ is the concentration of rubrene molecules in the solution. $\gamma_{TET_{2,s}}$ is the bi-molecular triplet transfer rate from PbS-TET-CA to rubrene. This system of differential equations is solved with the symbolic computation package Mathematica. The analytical solution for the various excited state populations, which is too large to reproduce here, is then fitted to the nsTA kinetics for the TET-CA triplet exciton and the transient PL kinetics for the free-floating rubrene triplet populations. Previously found

rates, such as $[Rub_0]$, k_q, k_{-q}, k_{TET_1}, k_{Tr}, and k_T are fixed during fitting. Whereas, α_s, α_f, $\gamma_{TET_{2,s}}$, and k_R are global fitting parameters. Figure 6.9c shows the fitted kinetics for $[T_T]$, $[T_{R,B}]$ and $[T_{R,F}]$. The rubrene decay rate is found to be k_R = 29 ± 2 ms^{-1}, and is in line with previous reports.[57] The bi-molecular triplet transfer rate is found to be $\gamma_{TET_{2,s}}$ = 12.0 ± 0.5 ms^{-1} mL mg^{-1} or equivalently $\gamma_{TET_{2,s}}$ = (6.4 ± 0.3) x 10^6 M^{-1} s^{-1}. The measured rate for $\gamma_{TET_{2,s}}$ is lower compared to values obtained for triplet transfer to rubrene from organometallic triplet sensitizers, commonly on the order of 10^8 M^{-1} s^{-1}. This indicates there is room for improved triplet transfer, possibly by increasing the Gibbs free driving energy between transmitter and annihilator, or optimising the interaction geometry of rubrene collisions with the QD's ligand shell. For the PbS-TET-CA system with 10 mg/mL of rubrene, the triplet rate given by $k_{TET_{2,s}} = \gamma_{TET_{2,s}}[Rub_0]$ is 120 ± 5 ms^{-1}. This triple transfer rate is ~24 times faster than the equivalent rate for the PbS-OA:Rub system, illustrating the benefits of adopting the TET-CA as a triplet transmitter ligand.

Figure 6.10a displays the fitted values for α_s as a function of the rubrene concentration in the solution. The fraction of PbS-TET-CA QDs without rubrene molecules adsorbed to their surface decreases as the rubrene concentration increases. It is common in the literature to model the distribution of molecules adsorbed to QD by the Poisson distribution.[195] In such frameworks the average number of adsorbed molecules per QD, λ, is given by

$$\lambda = -\ln(\alpha_s)\,. \tag{6.23}$$

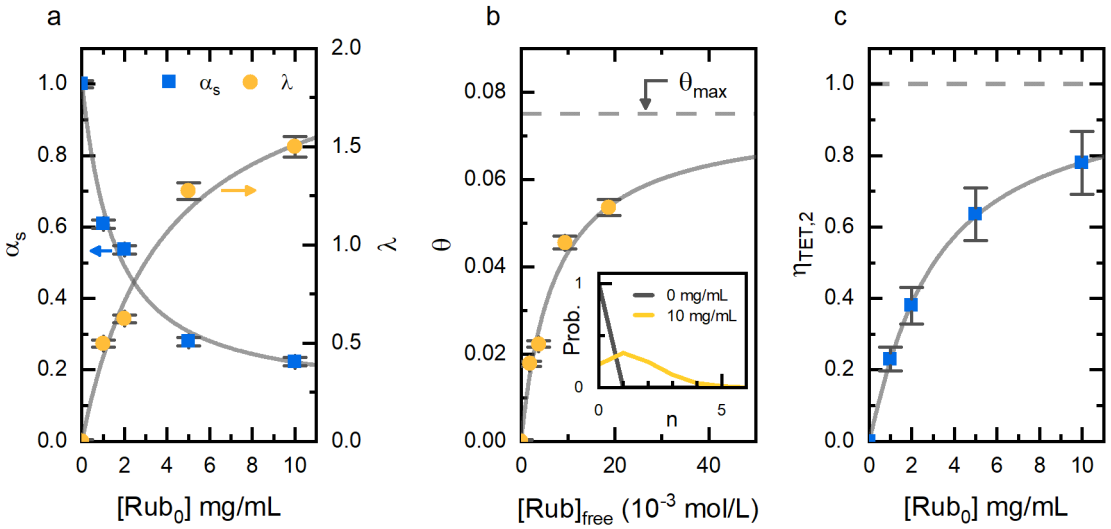

Figure 6.10: Quantification of rubrene adsorption to PbS-TET-CA QDs.
a) The fraction of TET-CA triplet excitons, α_s, remaining after the fast component of triplet transfer as a function of the rubrene concentration in solutions of PbS-TET-CA:Rub (blue squares). The corresponding average number of rubrene molecules per QD based on the Poisson distribution of rubrenes across QDs (orange circles). b) Average site occupancy based on 28 TET-CA ligands for rubrene adsorption per QD. Fitting of a modified Langmuir isotherm is achieved, with a maximum site occupancy of θ_{max} = 0.075 ± 0.014 and adsorption equilibrium constant K_a=140 ± 45 M-1. b, inset) Example of the rubrenes per PbS-TET-CA QD distribution for PbS-TET-CA:Rub solutions with 0 and 10 mg/mL of rubrene. c) Triplet exciton transfer efficiency, η_{TET_2}, from PbS-TET-CA to rubrene free floating triplets.

The rubrene and TET-CA are of similar chemical characteristics. It is reasonable to assume that the adsorption of rubrene molecules to the PbS-TET-CA QDs is facilitated by π-π interactions between the rubrene and TET-CA ligand. Based on previously reported ligand density of ~ 1 nm^{-2}, for a 1.5 nm radius PbS QDs used here, we estimate 28 TET-CA ligands per quantum dot. We take this value as the number of possible adsorption sites per QD, N_{sites}, for the rubrene molecules to adsorb to. Figure 6.10b shows the calculated average site occupancy, $\theta = \lambda / N_{sites}$, fitted with a modified Langmuir isotherm of the form,

$$\theta = \theta_{max} \frac{K_a [Rub_0]_{free}}{1 + K_a [Rub_0]_{free}}, \tag{6.24}$$

where, θ_{max} is the modified occupancy, K_a is the equilibrium constant between adsorption and desorption, and $[Rub_0]_{free} = [Rub_0] - \lambda[QD_0]$, is the concentration of rubrene molecules not attached to the QDs.[196] The observed site occupancy is well fitted with a modified maximum occupancy of θ_{max} = 0.075 ± 0.014 and adsorption

equilibrium constant K_a=140 ± 45 M^{-1}. This θ_{max} value leads to an estimate of ~2.1 sites per QD, which are accessible for rubrene adsorption. This gives an adsorption equilibrium constant lower than previously reported values for chemically bonded ligands on the surface of the QDs. For example, an adsorption constant of K_a = 4.4 x 10^4 M^{-1} had been reported for CdS QDs with a carboxylic acid adsorption.[196] An adsorption constant of only K_a = 5 x 10^2 M^{-1} was reported for the weaker bonding of aminoferrocene to the surface of PbS-OA QDs.[197] The weak adsorption strength is consistent with the hypothesis of weak π-π interactions causing the adsorption. With the knowledge of θ_{max} and K_a, we can now work backwards to find α_s and λ for any value of $[Rub_0]$.

The efficiency of triplet transfer from the TET-CA triplet to the rubrene free-floating triplet states is given by

$$\eta_{TET_2} = \alpha_s \frac{\gamma_{TET_{2,s}}[Rub_0]}{\gamma_{TET_{2,s}}[Rub_0] + k_R} + \alpha_f \frac{\gamma_{TET_{2,s}}[Rub_0]}{\gamma_{TET_{2,s}}[Rub_0] + k_T}. \quad (6.25)$$

From equation (6.25) the triplet transfer efficiencies in Figure 6.10c are calculated for the concentrations of rubrene investigated in nsTA and transient PL. With the use of equation (6.24) η_{TET_2} can be calculated for any concentration of rubrene. The triplet transfer efficiency varies greatly across the investigated range of rubrene concentrations. The maximum value for triplet transfer from TET-CA to rubrene achieved here is η_{TET_2} = (79 ± 9) %. When combined with the transfer efficiency to the TET-CA ligand, η_{TET_1}, the overall triplet transfer efficiency from QD to rubrene can be calculated by $\eta_{TET} = \eta_{TET_1} \times \eta_{TET_2}$. The maximum observed efficiency is η_{TET} = (19 ± 3) %. This sub-optimal efficiency shows that the investigated loss pathways lead to significant reductions in upconversion yields.

6.7 Conclusion and Outlook

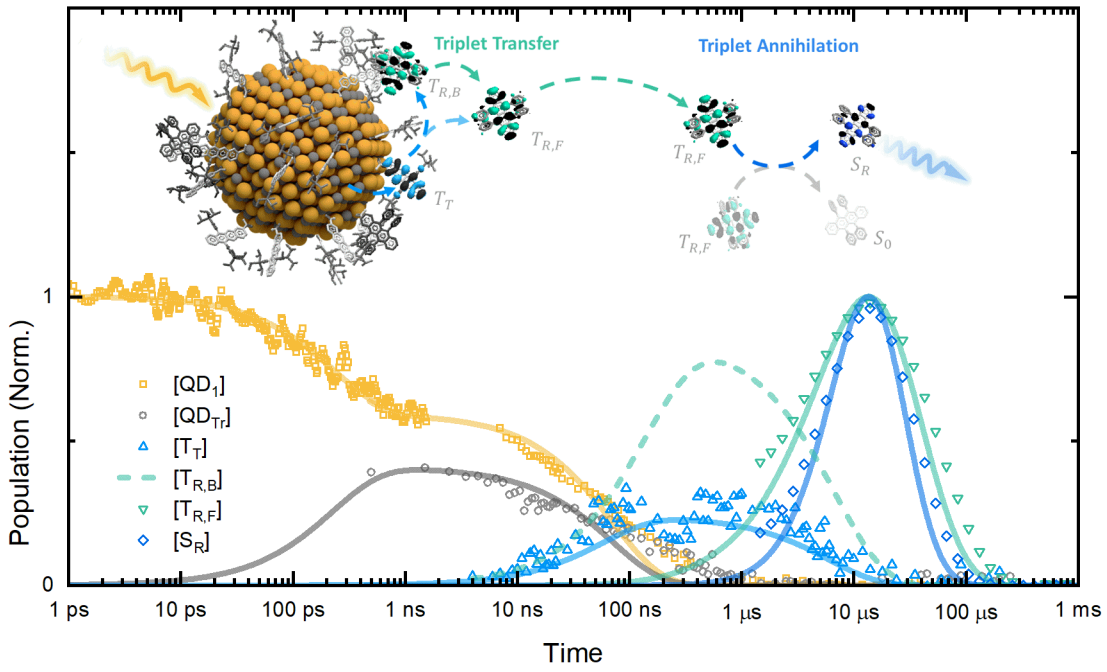

Figure 6.11: Overview of the triplet generation, transfer and triplet-triplet annihilation dynamics. fsTA kinetics shown are for PbS-TET-CA QDs in toluene solution. nsTA and transient PL kinetics shown are for a PbS-TET-CA:Rub solution (2:10 mg/mL).

We have demonstrated a solution-phase TTA-UC system based on the sensitizer-transmitter-annihilator model system. Although the structure is similar to PbS QDs with tetracene-based ligands and rubrene systems used in literature, the performance of the PbS-TET-CA:Rub system is not as high. In particular, the PbS-TET-CA:Rub system achieves a lower UCQE and possesses a higher excitation density threshold. However, this suboptimal system offers a means to study the possible loss pathways which lead to reduced efficiencies in a sensitizer-transmitter-annihilator system. With the application of both femtosecond and nanosecond spectroscopy, multiple loss channels are identified. Rapid loss of the QD excitonic excited state to a trap state is accompanied by the loss of a local electric field in the PbS-TET-CA QD. The dynamics of the trapping and de-trapping are consistent with an electron, hole, or exciton transfer as described by Marcus-Hush theory. The constant energy offset of the trap state with respect to the QD ground state and the PbS QD LUMO indicates that the trap state could be at a fixed energy of ~-4.97 eV relative to the vacuum. The low reorganisation energy for the trapping and de-trapping processes suggest that the trap state is not localised on the

TET-CA ligand. Significantly delayed triplet generation on the TET-CA ligand is observed on ~100 ns timescales. During this time period, decay from the trap state results in a ~75 % loss in the efficiency of TET-CA triplet generation.

There is a dual timescale observed for the triplet exciton transfer to free-floating rubrene molecules. We assign the approximately 100 ns or faster component as transfer from TET-CA triplet excitons to rubrene molecules adsorbed to the surface of the PbS-TET-CA QDs. The later transfer component corresponds to the transfer of triplets to dispersed rubrene molecules. The weak adsorption of rubrene molecules to the surface is consistent with description by a modified Langmuir isotherm. The total triplet transfer efficiency from PbS-TET-CA QDs to dispersed rubrene is dependent on the concentration of rubrene in the solution by both the adsorption of rubrene to the QD surface and the bi-molecular triplet transfer rate. The loss pathways investigated here that compete with both triplet generation and triplet transfer lead to a maximum triplet transfer efficiency of ~20 %, from PbS QD initial excitation to rubrene triplet state. This triplet transfer efficiency is consistent with the low UCQE measured by PLQE measurements.

There are multiple avenues for future investigation that build on developments detailed here. The use of a passivating CdS shell on the PbS core should be studied to reduce the loss of PbS excited states to the trap state or the decay from the trap state. The intrinsic triplet exciton transfer rate from PbS-TET-CA to adjacent rubrene molecules appears to be significantly rapid, investigation of the equivalent triplet transfer process in the thin-films may lead to improved solid-state TTA-UC devices. Such a hypothesis could be tested by applying the lessons learnt from the previous chapter for homogeneously dispersing QDs with an organic host to this system. Such strategies might lead to the first demonstration of a bulk TTA-UC device.

Lastly, it is important to note that the study of the loss pathways in the PbS-TET-CA QD system is applicable to the optimisation of the SF-PM systems presented earlier. With improved understanding of the trap states in PbS-TET-CA QDs, higher PLQEs for use in SF-PM devices could be achieved.

Chapter 7

Conclusions and Future Work

7.1 Conclusions

In summary, this thesis presents multiple advancements in spectral management towards increased photovoltaic power conversion efficiencies. First, we demonstrate a singlet fission photon multiplier system based on a highly tuneable platform that operates sufficiently at solar equivalent fluence. Secondly, we illustrate the use of a novel surface matching methodology to reach ~190 % exciton multiplication in a bulk solid-state device with potential for real-world applications that break the Shockley-Queisser limit. Lastly, we identify how loss pathways and molecular adsorption influences triplet exciton transfer efficiency at the organic-inorganic interface, and its subsequent effect on upconversion yields.

Of particular note, we show how it is possible to achieve efficient harvesting of triplet excitons generated by singlet fission in a bulk system, with minimal loss in efficiency at realistic operational conditions. In our model system, a TIPS-Tc and PbS quantum dot solution, optimal triplet harvesting is approached in the singlet fission photon multiplication by a low concentration of PbS quantum dots. Engineering the quantum dot surface with a triplet transmitter ligands is key to achieving this harvesting, as they act as an intermediate state in the triplet transfer process. Our system operates with such a high triplet transfer rate that it is possible to construct a solution-phase singlet fission photon multiplier that meets two key requirements which had previously not been achieved. Firstly, the system efficiently harvests triplet excitons at solar-equivalent fluence, despite the competition with triplet bi-molecular decay, and secondly, it does this while maintaining a sufficiently low quantum dot parasitic absorption.

In this research we show the potential of singlet fission photon multiplication in a bulk solid-state system, a considerable milestone for the singlet fission community. We are able to demonstrate an exciton multiplication factor of ~190 %, and assign this to near-optimal singlet fission in the organic host and efficient triplet harvesting by a well-dispersed array of quantum dots. The matching of the organic host with a chemically favourable ligand shell on the quantum dots is key to achieving this structure and triplet harvesting. This system illustrates a route to produce singlet fission photon multipliers as a thin film coating which can lead to increased power conversion efficiencies when added to the top of conventional silicon solar cells.

Finally, we identify multiple loss pathways that reduce triplet-triplet annihilation upconversion yields in a model system. In our system, a PbS-TET-CA quantum dot and rubrene solution, the attachment of the transmitter ligand TET-CA is shown to introduce a trap state that competes with triplet transfer to the annihilator molecule. On rapid ~100 ps timescales, excited state transfer to this trap state, indicated to be a surface state on the quantum dots, results in a quasi-equilibrium with the quantum excitonic state. Decay from this trap state is shown to reduce triplet transfer efficiencies by ~75%. Subsequent triplet transfer to the annihilator is found to occur via two mechanisms: on ~100 ns timescales, triplet transfer occurs to annihilators adsorbed to the surface of the quantum. On 10s of μs time periods, triplet transfer occurs to dispersed annihilators. The adsorption is consistent with Langmuir isotherm description and the combination of the two channels controls the upconversion efficiency.

7.2 Future Work

A future goal could be to develop a larger transmitter ligand shell surround the quantum dot. The larger ligand shell could be achieved using a tetracene dimer based ligand. We have pointed to the increased radius and surface area of the ligand shell as factors that may increase the triplet transfer rate from singlet fission host material to quantum dot emitter. An alternative approach that may yield similar effects, could be the investigation of quantum dot materials with larger Bohr radii, such as PbSe. Here, the leakage of quantum dot exciton wavefunction outside the core could increase wavefunction overlap of triplet donor and acceptor resulting in increased transfer rates.

Singlet fission materials with higher triplet exciton energies should be investigated to test coupling of the singlet fission photon multiplier with silicon-based solar cells. With higher triplet exciton energies, quantum dots with bandgap above that of silicon could be viable for triplet exciton transfer. Then finally, investigation of the efficiency gains from a singlet fission photon multiplier optically coupled to a silicon cell could be made. Of particular interest in this scenario, would be the measurement of underlying silicon cell's spectrally resolved quantum efficiency as a means to identify efficiency gains.

The spectral variation of singlet fission photon multiplier efficiency is another research avenue to be pursued. Current architectures show significant absorption in the singlet fission host at its narrow absorption bands, however, a broad absorption band is essential. To overcome this, we propose the integration of a third component in the singlet fission photon multiplier system, a high bandgap singlet sensitizer. The purpose of this sensitizer would be to increase absorption of photons in the film, the resultant photoexcited singlet could then be transferred to the singlet fission host and photon multiplication occurs as before. The identification of a singlet sensitizer with the appropriate chemical interactions with the singlet fission host and absorption in a 'window' of the current absorption is required to pursue this proposal.

Our finding of excited state trapping in the PbS-TET-CA quantum dot system points to the development of core-shell quantum dots. In both the singlet fission photon multiplier and triplet-triplet annihilation upconverter systems developed here, the decay of the excited state within the PbS quantum dot currently limits efficiencies. Such decay channels have been successfully mitigated in similar systems with the use of CdS passivation shell. Therefore, this is possibly a highly advantageous research direction.

Finally, our illustration of morphology control by matching ligand and host chemistry in a solid-state hybrid blend, opens up new device architectures that have previously been hindered by phase separation or quantum dot aggregation. The advantageous triplet exciton transfer offered by this structure will be influential to related fields. For example, we proposed that a solid-state triplet-triplet annihilation upconversion system could be achieved using similar methods, which would surpass the bilayer structures the research community is currently limited to.

7.3 Commercialisation

As an outcome of the work presented here and related projects, authors; Akshay Rao, Nathaniel J. L. K. Davis and the author of this thesis, Jesse Allardice, filed two patents covering the use of photomultiplier films for increased photovoltaic efficiency in collaboration with Cambridge Enterprise. These patents have now been licenced to an industrial partner with the aim of commercialisation. It is the authors' hope that this technology will lead to real-world improvements in photovoltaic efficiency and thus aid the global adoption of sustainable energy sources.

"Whatever you can do, or dream you can, begin it. Boldness has genius, power and magic in it." – Johan Wolfgang von Goethe

References

(1) Powell, D. M.; Fu, R.; Horowitz, K.; Basore, P. A.; Woodhouse, M.; Buonassisi, T. The Capital Intensity of Photovoltaics Manufacturing: Barrier to Scale and Opportunity for Innovation. *Energy Environ. Sci.* **2015**, *8* (12), 3395–3408. https://doi.org/10.1039/c5ee01509j.

(2) Needleman, D. B.; Poindexter, J. R.; Kurchin, R. C.; Marius Peters, I.; Wilson, G.; Buonassisi, T. Economically Sustainable Scaling of Photovoltaics to Meet Climate Targets. *Energy Environ. Sci.* **2016**, *9* (6), 2122–2129. https://doi.org/10.1039/c6ee00484a.

(3) Kamat, P. V. Meeting the Clean Energy Demand: Nanostructure Architectures for Solar Energy Conversion. *J. Phys. Chem. C* **2007**, *111* (7), 2834–2860. https://doi.org/10.1021/jp066952u.

(4) Eisenberg, R.; Nocera, D. G. Preface: Overview of the Forum on Solar and Renewable Energy. *Inorganic Chemistry*. American Chemical Society October 3, 2005, pp 6799–6801. https://doi.org/10.1021/ic058006i.

(5) Deibel, C.; Dyakonov, V. Polymer-Fullerene Bulk Heterojunction Solar Cells. *Reports Prog. Phys.* **2010**, *73* (9). https://doi.org/10.1088/0034-4885/73/9/096401.

(6) International Energy Agency. Data & Statistics - IEA https://www.iea.org/data-and-statistics?country=WORLD&fuel=Renewables and waste&indicator=Solar PV electricity generation (accessed Apr 6, 2020).

(7) Dexter, D. L. Two Ideas on Energy Transfer Phenomena: Ion-Pair Effects Involving the OH Stretching Mode, and Sensitization of Photovoltaic Cells. *J. Lumin.* **1979**, *18–19*, 779–784. https://doi.org/10.1016/0022-2313(79)90235-7.

(8) Tayebjee, M. J. Y.; McCamey, D. R.; Schmidt, T. W. Beyond Shockley-Queisser: Molecular Approaches to High-Efficiency Photovoltaics. *J. Phys. Chem. Lett.* **2015**, *6* (12), 2367–2378. https://doi.org/10.1021/acs.jpclett.5b00716.

(9) Rao, A.; Friend, R. H. Harnessing Singlet Exciton Fission to Break the Shockley-Queisser Limit. *Nature Reviews Materials*. Nature Publishing Group October 4, 2017. https://doi.org/10.1038/natrevmats.2017.63.

(10) Polman, A.; Knight, M.; Garnett, E. C.; Ehrler, B.; Sinke, W. C. Photovoltaic Materials: Present Efficiencies and Future Challenges. *Science*. 2016. https://doi.org/10.1126/science.aad4424.

(11) Futscher, M. H.; Rao, A.; Ehrler, B. The Potential of Singlet Fission Photon Multipliers as an Alternative to Silicon-Based Tandem Solar Cells. *ACS Energy Lett* **2018**, *22*. https://doi.org/10.1021/acsenergylett.8b01322.

(12) Thompson, N. J.; Wilson, M. W. B.; Congreve, D. N.; Brown, P. R.; Scherer, J. M.; Bischof, T. S.; Wu, M.; Geva, N.; Welborn, M.; Voorhis, T. Van; et al. Energy Harvesting of Non-Emissive Triplet Excitons in Tetracene by Emissive PbS Nanocrystals. *Nat. Mater.* **2014**, *13* (October), 1039–1043. https://doi.org/10.1038/nmat4097.

(13) Tabachnyk, M.; Ehrler, B.; Gélinas, S.; Böhm, M. L.; Walker, B. J.; Musselman, K. P.; Greenham, N. C.; Friend, R. H.; Rao, A. Resonant Energy Transfer of Triplet Excitons from Pentacene to PbSe Nanocrystals. **2014**. https://doi.org/10.1038/NMAT4093.

(14) Huang, Z.; Li, X.; Mahboub, M.; Hanson, K. M.; Nichols, V. M.; Le, H.; Tang, M. L.; Bardeen, C. J. Hybrid Molecule − Nanocrystal Photon Upconversion Across the Visible and Near-Infrared. *Nano Lett.* **2015**, *15* (8), 5552–5557. https://doi.org/10.1021/acs.nanolett.5b02130.

(15) Wu, M.; Jean, J.; Bulović, V.; Baldo, M. A. Interference-Enhanced Infrared-to-Visible Upconversion in Solid-State Thin Films Sensitized by Colloidal Nanocrystals. *Appl. Phys. Lett.* **2017**, *110* (21), 211101. https://doi.org/10.1063/1.4984136.

(16) Koehler, A.; Baessler, H. *Electronic Processes in Organic Semiconductors*; 2015. https://doi.org/10.1007/s13398-014-0173-7.2.

(17) Edition, S. *Nanocrystal Quntum Dots*; 2010.

(18) Swenberg, C. E.; Geacintov, N. E. Exciton Interactions in Organic Solids. In *Organic Molecular Photophysics*; 1973.

(19) Barford, W. *Electronic and Optical Properties of Conjugated Polymers*; 2013. https://doi.org/10.1093/acprof:oso/9780199677467.001.0001.

(20) Schwoerer, M.; Wolf, H. C. *Organic Molecular Solids*; 2008. https://doi.org/10.1002/9783527618651.

(21) Pope, M.; Swenberg, C. E. *Electronic Processes in Organic Crystals and Polymers*; 1999. https://doi.org/10.1063/1.327880.

(22) Frenkel, J. On the Transformation of Light into Heat in Solids. I. *Phys. Rev.* **1931**. https://doi.org/10.1103/PhysRev.37.17.

(23) Gregg, B. A.; Hanna, M. C. Comparing Organic to Inorganic Photovoltaic Cells:

Theory, Experiment, and Simulation. *Journal of Applied Physics*. 2003. https://doi.org/10.1063/1.1544413.

(24) Wannier, G. H. The Structure of Electronic Excitation Levels in Insulating Crystals. *Phys. Rev.* **1937**. https://doi.org/10.1103/PhysRev.52.191.

(25) Griffiths, D. J.; Harris, E. G. Introduction to Quantum Mechanics. *Am. J. Phys.* **1995**. https://doi.org/10.1119/1.18098.

(26) Köhler, A.; Beljonne, D. The Singlet–Triplet Exchange Energy in Conjugated Polymers. *Adv. Funct. Mater.* **2004**, *14* (1), 11–18. https://doi.org/10.1002/adfm.200305032.

(27) Smith, M. B.; Michl, J. Singlet Fission. *Chem. Rev.* **2010**, *110* (11), 6891–6936. https://doi.org/10.1021/cr1002613.

(28) Coulson, C. A.; Rushbrooke, G. S. Note on the Method of Molecular Orbitals. *Math. Proc. Cambridge Philos. Soc.* **1940**. https://doi.org/10.1017/S0305004100017163.

(29) Pariser, R. Theory of the Electronic Spectra and Structure of the Polyacenes and of Alternant Hydrocarbons. *J. Chem. Phys.* **1956**. https://doi.org/10.1063/1.1742461.

(30) Dirac, P. A. M. The Quantum Theory of the Emission and Absorption of Radiation Proceedings of the R. Soc. Lond. A March. *Proc. R. Soc. London Ser. A* **1927**.

(31) Brédas, J. L.; Beljonne, D.; Coropceanu, V.; Cornil, J. Charge-Transfer and Energy-Transfer Processes in π-Conjugated Oligomers and Polymers: A Molecular Picture. *Chem. Rev.* **2004**. https://doi.org/10.1021/cr040084k.

(32) Ross, R. T. Some Thermodynamics of Photochemical Systems. *J. Chem. Phys.* **1967**. https://doi.org/10.1063/1.1840606.

(33) Englman, R.; Jortner, J. The Energy Gap Law for Radiationless Transitions in Large Molecules. *Mol. Phys.* **1970**. https://doi.org/10.1080/00268977000100171.

(34) Siebrand, W.; Williams, D. F. Isotope Rule for Radiationless Transitions with an Application to Triplet Decay in Aromatic Hydrocarbons. *The Journal of Chemical Physics*. 1967. https://doi.org/10.1063/1.1840415.

(35) Karabunarliev, S.; Bittner, E. R.; Baumgarten, M. Franck-Condon Spectra and Electron-Libration Coupling in Para-Polyphenyls. *J. Chem. Phys.* **2001**. https://doi.org/10.1063/1.1351853.

(36) Spano, F. C. The Spectral Signatures of Frenkel Polarons in H- And J-Aggregates. *Acc. Chem. Res.* **2010**. https://doi.org/10.1021/ar900233v.

(37) Gadermaier, C.; Cerullo, G.; Sansone, G.; Leising, G.; Scherf, U.; Lanzani, G. Time-Resolved Charge Carrier Generation from Higher Lying Excited States in Conjugated Polymers. *Phys. Rev. Lett.* **2002**. https://doi.org/10.1103/PhysRevLett.89.117402.

(38) Gadermaier, C.; Cerullo, G.; Manzoni, C.; Scherf, U.; List, E. J. W.; Lanzani, G. Dynamics of Higher Photoexcited States in M-LPPP Probed with Sub-20 Fs Time Resolution. *Chem. Phys. Lett.* **2004**. https://doi.org/10.1016/j.cplett.2003.11.092.

(39) Köhler, A.; Beljonne, D. The Singlet-Triplet Exchange Energy in Conjugated Polymers. *Adv. Funct. Mater.* **2004**. https://doi.org/10.1002/adfm.200305032.

(40) Singh, S.; Jones, W. J.; Siebrand, W.; Stoicheff, B. P.; Schneider, W. G. Laser Generation of Excitons and Fluorescence in Anthracene Crystals. *J. Chem. Phys.* **1965**. https://doi.org/10.1063/1.1695695.

(41) Alfano, R. R.; Shapiro, S. L.; Pope, M. Fission Rate of Singlet Excitons in a Tetracene Crystal Measured with Picosecond Laser Pulses. *Opt. Commun.* **1973**, *9* (4), 388–391. https://doi.org/10.1016/0030-4018(73)90278-2.

(42) Pope, M.; Geacintov, N. E.; Vogel, F. Singlet Exciton Fission and Triplet-Triplet Exciton Fusion in Crystalline Tetracene. *Mol. Cryst. Liq. Cryst.* **1969**, *6* (1), 83-. https://doi.org/Doi 10.1080/15421406908082953.

(43) Groff, R. P.; Avakian, P.; Merrifield, R. F.; Station, E. MAGNETIC FIELD DEPENDENCE OF DELAYED FLUORESCENCE FROM TETRACENE CRYSTALS. **1970**, *2* (605), 218–223.

(44) Merrifield, R. E. Diffusion and Mutual Annihilation of Triplet Excitons in Organic Crystals. *Acc. Chem. Res.* **1968**, *1* (5), 129–135. https://doi.org/10.1021/ar50005a001.

(45) Merrifield, R. E. Magnetic Effects on Triplet Exciton Interactions. *Pure Appl. Chem.* **1971**, *27* (3), 481–498. https://doi.org/10.1351/pac197127030481.

(46) Johnson, R. C.; Merrifield, R. E.; Avakian, P.; Flippen, R. B. Effects of Magnetic Fields on the Mutual Annihilation of Triplet Excitons in Molecular Crystals. *Phys. Rev. Lett.* **1967**, *19* (6), 285–287. https://doi.org/10.1103/PhysRevLett.19.285.

(47) Groff, R. P.; Avakian, P.; Merrifield, R. E. Coexistence of Exciton Fission and Fusion in Tetracene Crystals. *Phys. Rev. B* **1970**, *1* (2), 815–817. https://doi.org/10.1103/PhysRevB.1.815.

(48) Burdett, J. J.; Piland, G. B.; Bardeen, C. J. Magnetic Field Effects and the Role of Spin States in Singlet Fission. *Chem. Phys. Lett.* **2013**, *585*, 1–10. https://doi.org/10.1016/j.cplett.2013.08.036.

(49) Rao, A.; Friend, R. H. Harnessing Singlet Exciton Fission to Break the Shockley–Queisser Limit. *Nat. Rev. Mater.* **2017**, *2*, 1–12. https://doi.org/10.1117/2.1201203.004146.

(50) Bayliss, S. L.; Weiss, L. R.; Rao, A.; Friend, R. H.; Chepelianskii, A. D.; Greenham, N. C. Spin Signatures of Exchange-Coupled Triplet Pairs Formed by Singlet Fission. *Phys. Rev. B* **2016**, *94* (4), 045204. https://doi.org/10.1103/PhysRevB.94.045204.

(51) Chan, W.-L.; Ligges, M.; Zhu, X.-Y. The Energy Barrier in Singlet Fission Can Be Overcome through Coherent Coupling and Entropic Gain. *Nat. Chem.* **2012**, *4* (10), 840–845. https://doi.org/10.1038/nchem.1436.

(52) Kolomeisky, A. B.; Feng, X.; Krylov, A. I. A Simple Kinetic Model for Singlet Fission: A Role of Electronic and Entropic Contributions to Macroscopic Rates. *J. Phys. Chem. C* **2014**, *118* (10), 5188–5195. https://doi.org/10.1021/jp4128176.

(53) Gray, V.; Dreos, A.; Erhart, P.; Albinsson, B.; Moth-Poulsen, K.; Abrahamsson, M. Loss Channels in Triplet-Triplet Annihilation Photon Upconversion: Importance of Annihilator Singlet and Triplet Surface Shapes. *Phys. Chem. Chem. Phys.* **2017**, *19* (17), 10931–10939. https://doi.org/10.1039/C7CP01368J.

(54) Smith, M. B.; Michl, J. Recent Advances in Singlet Fission. *Annu. Rev. Phys. Chem.* **2013**, *64*, 361–386. https://doi.org/10.1146/annurev-physchem-040412-110130.

(55) Walker, B. J.; Musser, A. J.; Beljonne, D.; Friend, R. H. Singlet Exciton Fission in Solution. *Nat. Chem.* **2013**, *5* (12), 1019–1024. https://doi.org/10.1038/nchem.1801.

(56) Stern, H. L.; Musser, A. J.; Gelinas, S.; Parkinson, P.; Herz, L. M.; Bruzek, M. J.; Anthony, J.; Friend, R. H.; Walker, B. J. Identification of a Triplet Pair Intermediate in Singlet Exciton Fission in Solution. https://doi.org/10.1073/pnas.1503471112.

(57) Cheng, Y. Y.; Fückel, B.; Khoury, T.; Clady, R. G. C. R.; Tayebjee, M. J. Y.; Ekins-Daukes, N. J.; Crossley, M. J.; Schmidt, T. W. Kinetic Analysis of Photochemical Upconversion by Triplet-Triplet Annihilation: Beyond Any Spin Statistical Limit. *J. Phys. Chem. Lett.* **2010**, *1* (12), 1795–1799. https://doi.org/10.1021/jz100566u.

(58) Stern, H. L.; Cheminal, A.; Yost, S. R.; Broch, K.; Bayliss, S. L.; Chen, K.; Tabachnyk, M.; Thorley, K.; Greenham, N.; Hodgkiss, J. M.; et al. Vibronically Coherent Ultrafast Triplet-Pair Formation and Subsequent Thermally Activated Dissociation Control Efficient Endothermic Singlet Fission. **2017**. https://doi.org/10.1038/NCHEM.2856.

(59) Bakulin, A. A.; Morgan, S. E.; Kehoe, T. B.; Wilson, M. W. B.; Chin, A. W.; Zigmantas, D.; Egorova, D.; Rao, A. Real-Time Observation of Multiexcitonic States in Ultrafast Singlet Fission Using Coherent 2D Electronic Spectroscopy. **2016**.

https://doi.org/10.1038/NCHEM.2371.

(60) Weiss, L. R.; Bayliss, S. L.; Kraffert, F.; Thorley, K. J.; Anthony, J. E.; Bittl, R.; Friend, R. H.; Rao, A.; Greenham, N. C.; Behrends, J. Strongly Exchange-Coupled Triplet Pairs in an Organic Semiconductor. *Nat. Phys.* **2017**, *13* (2), 176–181. https://doi.org/10.1038/nphys3908.

(61) Yong, C. K.; Musser, A. J.; Bayliss, S. L.; Lukman, S.; Tamura, H.; Bubnova, O.; Hallani, R. K.; Meneau, A.; Resel, R.; Maruyama, M.; et al. The Entangled Triplet Pair State in Acene and Heteroacene Materials. *Nat. Commun.* **2017**, *8*. https://doi.org/10.1038/ncomms15953.

(62) Schnedermann, C.; Alvertis, A. M.; Wende, T.; Lukman, S.; Feng, J.; Schröder, F. A. Y. N.; Turban, D. H. P.; Wu, J.; Hine, N. D. M.; Greenham, N. C.; et al. A Molecular Movie of Ultrafast Singlet Fission. *Nat. Commun.* **2019**, *10* (1). https://doi.org/10.1038/s41467-019-12220-7.

(63) Rao, A.; Wilson, M. W. B.; Albert-Seifried, S.; Di Pietro, R.; Friend, R. H. Photophysics of Pentacene Thin Films: The Role of Exciton Fission and Heating Effects. *Phys. Rev. B - Condens. Matter Mater. Phys.* **2011**, *84* (19), 1–8. https://doi.org/10.1103/PhysRevB.84.195411.

(64) Schröder, F. A. Y. N.; Turban, D. H. P.; Musser, A. J.; Hine, N. D. M.; Chin, A. W. Multi-Dimensional Tensor Network Simulation of Open Quantum Dynamics in Singlet Fission. **2017**, 1–8.

(65) Dron, P. I.; Michl, J.; Johnson, J. C. Singlet Fission and Excimer Formation in Disordered Solids of Alkyl-Substituted 1,3-Diphenylisobenzofurans. **2017**. https://doi.org/10.1021/acs.jpca.7b07362.

(66) Dover, C. B.; Gallaher, J. K.; Frazer, L.; Tapping, P. C.; Petty, A. J.; Crossley, M. J.; Anthony, J. E.; Kee, T. W.; Schmidt, T. W. Endothermic Singlet Fission Is Hindered by Excimer Formation. *Nat. Chem.* **2018**, *10* (3), 305–310. https://doi.org/10.1038/nchem.2926.

(67) Birks, J. B.; Srinivasan, B. N.; McGlynn, S. P. The Luminescence of Pyrene in Viscous Solutions. *J. Mol. Spectrosc.* **1968**, *27* (1–4), 266–284. https://doi.org/10.1016/0022-2852(68)90037-4.

(68) Collison, C. J.; Rothberg, L. J.; Treemaneekarn, V.; Li, Y. Conformational Effects on the Photophysics of Conjugated Polymers: A Two Species Model for MEH-PPV Spectroscopy and Dynamics. *Macromolecules* **2001**, *34* (7), 2346–2352. https://doi.org/10.1021/ma001354d.

(69) Law, M.; Luther, J. M.; Song, Q.; Hughes, B. K.; Perkins, C. L.; Nozik, A. J. Structural, Optical, and Electrical Properties of PbSe Nanocrystal Solids Treated Thermally or

with Simple Amines. *J. Am. Chem. Soc.* **2008**. https://doi.org/10.1021/ja800040c.

(70) Tang, J.; Sargent, E. H. Infrared Colloidal Quantum Dots for Photovoltaics: Fundamentals and Recent Progress. *Adv. Mater.* **2011**. https://doi.org/10.1002/adma.201001491.

(71) Guyot-Sionnest, P.; Wehrenberg, B.; Yu, D. Intraband Relaxation in CdSe Nanocrystals and the Strong Influence of the Surface Ligands. *J. Chem. Phys.* **2005**, *123* (7), 074709. https://doi.org/10.1063/1.2004818.

(72) Pandey, A.; Guyot-Sionnest, P. Slow Electron Cooling in Colloidal Quantum Dots. *Science (80-.).* **2008**, *322* (5903), 929–932. https://doi.org/10.1126/science.1159832.

(73) Sauvage, S.; Boucaud, P.; Glotin, F.; Prazeres, R.; Ortega, J. M.; Lemaitre, A.; Gérard, J. M.; Thierry-Flieg, V. Saturation of Intraband Absorption and Electron Relaxation Time in N-Doped InAs/GaAs Self-Assembled Quantum Dots. *Appl. Phys. Lett.* **1998**, *73* (26), 3818–3821. https://doi.org/10.1063/1.122904.

(74) Smith, A. M.; Nie, S. Semiconductor Nanocrystals: Structure, Properties, and Band Gap Engineering. *Acc. Chem. Res.* **2010**. https://doi.org/10.1021/ar9001069.

(75) Gur, I.; Fromer, N. A.; Geier, M. L.; Alivisatos, A. P. Materials Science: Air-Stable All-Inorganic Nanocrystal Solar Cells Processed from Solution. *Science (80-.).* **2005**. https://doi.org/10.1126/science.1117908.

(76) Ip, A. H.; Thon, S. M.; Hoogland, S.; Voznyy, O.; Zhitomirsky, D.; Debnath, R.; Levina, L.; Rollny, L. R.; Carey, G. H.; Fischer, A.; et al. Hybrid Passivated Colloidal Quantum Dot Solids. *Nat. Nanotechnol.* **2012**. https://doi.org/10.1038/nnano.2012.127.

(77) Bae, W. K.; Joo, J.; Padilha, L. A.; Won, J.; Lee, D. C.; Lin, Q.; Koh, W. K.; Luo, H.; Klimov, V. I.; Pietryga, J. M. Highly Effective Surface Passivation of Pbse Quantum Dots through Reaction with Molecular Chlorine. *J. Am. Chem. Soc.* **2012**. https://doi.org/10.1021/ja309783v.

(78) Talapin, D. V. PbSe Nanocrystal Solids for N- and p-Channel Thin Film Field-Effect Transistors. *Science (80-.).* **2005**, *310* (5745), 86–89. https://doi.org/10.1126/science.1116703.

(79) Matvienko, O. O.; Savin, Y. N.; Kryzhanovska, A. S.; Vovk, O. M.; Dobrotvorska, M. V.; Pogorelova, N. V.; Vashchenko, V. V. Dispersion and Aggregation of Quantum Dots in Polymer-Inorganic Hybrid Films. *Thin Solid Films* **2013**, *537*, 226–230. https://doi.org/10.1016/j.tsf.2013.03.046.

(80) Reynolds, L. X.; Lutz, T.; Dowland, S.; MacLachlan, A.; King, S.; Haque, S. A. Charge

Photogeneration in Hybrid Solar Cells: A Comparison between Quantum Dots and in Situ Grown CdS. *Nanoscale* **2012**, *4* (5), 1561–1564. https://doi.org/10.1039/c2nr12081j.

(81) Thompson, N. J.; Wilson, M. W. B.; Congreve, D. N.; Brown, P. R.; Scherer, J. M.; Bischof, T. S.; Wu, M.; Geva, N.; Welborn, M.; Voorhis, T. Van; et al. Energy Harvesting of Non-Emissive Triplet Excitons in Tetracene by Emissive PbS Nanocrystals. *Nat. Mater.* **2014**, *13*, 1039–1043. https://doi.org/10.1038/nmat4097.

(82) Collini, E.; Scholes, G. D. Coherent Intrachain Energy Migration in a Conjugated Polymer at Room Temperature. *Science (80-.).* **2009**. https://doi.org/10.1126/science.1164016.

(83) Förster, T.; Energiewanderung, Z.; Von, F. Zwischenmolekulare Energiewanderung Und Fluoreszenz. *Ann. Phys.* **1939**, *248* (1938), 55–75. https://doi.org/10.1002/andp.19484370105.

(84) Dexter, D. L. A Theory of Sensitized Luminescence in Solids. *J. Chem. Phys.* **1953**, *21* (5), 836. https://doi.org/10.1063/1.1699044.

(85) Laquai, F.; Park, Y.-S. S.; Kim, J.-J. J.; Basché, T. Excitation Energy Transfer in Organic Materials: From Fundamentals to Optoelectronic Devices. TL - 30. *Macromol. Rapid Commun.* **2009**, *30 VN-r* (14), 1203–1231. https://doi.org/10.1002/marc.200900309.

(86) Greenham, N. C.; Peng, X.; Alivisatos, A. P. Charge Separation and Transport in Conjugated Polymer/Cadmium Selenide Nanocrystal Composites Studied by Photoluminescence Quenching and Photoconductivity. *Phys. Rev. B* **1996**, *54* (24), 17628–17637. https://doi.org/10.1103/PhysRevB.54.17628.

(87) Dayal, S.; Kopidakis, N.; Olson, D. C.; Ginley, D. S.; Rumbles, G. Photovoltaic Devices with a Low Band Gap Polymer and CdSe Nanostructures Exceeding 3% Efficiency. https://doi.org/10.1021/nl903406s.

(88) Morgenstern, F. S. F.; Rao, A.; Böhm, M. L.; Kist, R. J. P.; Vaynzof, Y.; Greenham, N. C. Ultrafast Charge-and Energy-Transfer Dynamics in Conjugated Polymer: Cadmium Selenide Nanocrystal Blends. *ACS Nano* **2014**, *8* (2), 1647–1654. https://doi.org/10.1021/nn405978f.

(89) Lee, J.; Jadhav, P.; Baldo, M. A. High Efficiency Organic Multilayer Photodetectors Based on Singlet Exciton Fission. *Cit. Appl. Phys. Lett. J. Appl. Phys. J. Appl. Phys. J. Chem. Phys. J. Chem. Phys. Appl. Phys. Lett. J. Appl. Phys.* **2009**, *95* (3693), 33301–114102. https://doi.org/10.1063/1.3182787.

(90) Rao, A.; Wilson, M. W. B.; Hodgkiss, J. M.; Albert-Seifried, S.; Bässler, H.; Friend,

R. H. Exciton Fission and Charge Generation via Triplet Excitons in Pentacene/C 60 Bilayers. *J. Am. Chem. Soc.* **2010**, *132* (36), 12698–12703. https://doi.org/10.1021/ja1042462.

(91) Jacobson, M. Z.; Delucchi, M. A.; Bazouin, G.; Bauer, Z. A. F.; Heavey, C. C.; Fisher, E.; Morris, S. B.; Piekutowski, D. J. Y.; Vencill, T. A.; Yeskoo, T. W. Singlet Exciton Fission-Sensitized Infrared Quantum Dot Solar Cells. *Energy Environ. Sci.* **2015**, *8* (7), 2093–2117. https://doi.org/0.1021/nl204297u.

(92) Jadhav, P. J.; Brown, P. R.; Thompson, N.; Wunsch, B.; Mohanty, A.; Yost, S. R.; Hontz, E.; Van Voorhis, T.; Bawendi, M. G.; Bulovi??, V.; et al. Triplet Exciton Dissociation in Singlet Exciton Fission Photovoltaics. *Adv. Mater.* **2012**, *24* (46), 6169–6174. https://doi.org/10.1002/adma.201202397.

(93) Congreve, D. N.; Lee, J.; Thompson, N. J.; Hontz, E.; Yost, S. R.; Reusswig, P. D.; Bahlke, M. E.; Reineke, S.; Van Voorhis, T.; Baldo, M. A. External Quantum Efficiency Above 100% in a Singlet-Exciton-Fission-Based Organic Photovoltaic Cell. *Science (80-.).* **2013**, *340* (6130), 334–337. https://doi.org/10.1126/science.1232994.

(94) Tabachnyk, M.; Ehrler, B.; Gélinas, S.; Böhm, M. L.; Walker, B. J.; Musselman, K. P.; Greenham, N. C.; Friend, R. H.; Rao, A. Resonant Energy Transfer of Triplet Excitons from Pentacene to PbSe Nanocrystals. *Nat. Mater.* **2014**, *13* (October), 1033–1038. https://doi.org/10.1038/nmat4093.

(95) Mahboub, M.; Maghsoudiganjeh, H.; Pham, A. M.; Huang, Z.; Tang, M. L. Triplet Energy Transfer from PbS(Se) Nanocrystals to Rubrene: The Relationship between the Upconversion Quantum Yield and Size. *Adv. Funct. Mater.* **2016**, *26* (33), 6091–6097. https://doi.org/10.1002/adfm.201505623.

(96) Huang, Z.; Tang, M. L. Designing Transmitter Ligands That Mediate Energy Transfer between Semiconductor Nanocrystals and Molecules. *J. Am. Chem. Soc.* **2017**, *139* (28), 9412–9418. https://doi.org/10.1021/jacs.6b08783.

(97) Gray, V.; Allardice, J. R.; Zhang, Z.; Dowland, S.; Xiao, J.; Petty, A. J.; Anthony, J. E.; Greenham, N. C.; Rao, A. Direct vs Delayed Triplet Energy Transfer from Organic Semiconductors to Quantum Dots and Implications for Luminescent Harvesting of Triplet Excitons. *ACS Nano* **2020**, *14* (4), 4224–4234. https://doi.org/10.1021/acsnano.9b09339.

(98) Garakyaraghi, S.; Mongin, C.; Granger, D. B.; Anthony, J. E.; Castellano, F. N. Delayed Molecular Triplet Generation from Energized Lead Sulfide Quantum Dots. *J. Phys. Chem. Lett.* **2017**, *8* (7), 1458–1463. https://doi.org/10.1021/acs.jpclett.7b00546.

(99) Bender, J. A.; Raulerson, E. K.; Li, X.; Goldzak, T.; Xia, P.; Troy, ‖; Voorhis, V.; Tang, M. L.; Roberts, S. T. Surface States Mediate Triplet Energy Transfer in Nanocrystal−Acene Composite Systems. **2018**. https://doi.org/10.1021/jacs.8b01966.

(100) Wu, M.; Congreve, D. N.; Wilson, M. W. B.; Jean, J.; Geva, N.; Welborn, M.; Voorhis, T. Van; Bulovi, V.; Bawendi, M. G.; Baldo, M. A. Solid-State Infrared-to-Visible Upconversion Sensitized by Colloidal Nanocrystals. *Nat. Photonics* **2015**, *10* (1), 31–34. https://doi.org/10.1038/NPHOTON.2015.226.

(101) Nienhaus, L.; Wu, M.; Geva, N.; Shepherd, J. J.; Wilson, M. W. B.; Bulović, V.; Van Voorhis, T.; Baldo, M. A.; Bawendi, M. G. Speed Limit for Triplet-Exciton Transfer in Solid-State PbS Nanocrystal-Sensitized Photon Upconversion. *ACS Nano* **2017**, *11* (8), 7848–7857. https://doi.org/10.1021/acsnano.7b02024.

(102) Collins, F. C.; Kimball, G. E. Diffusion-Controlled Reaction Rates. *J. Colloid Sci.* **1949**, *4* (4), 425–437. https://doi.org/10.1016/0095-8522(49)90023-9.

(103) W. Zur Kinetischen Theorie Der Brown'schen Molekularbewegungen Und Der Suspensionen - Smoluchowski, M. v., (Ann. d. Physik 21, 756-80.). *Zeitschrift für Chemie und Ind. der Kolloide* **1907**. https://doi.org/10.1007/BF01813736.

(104) Smoluchowski, M. Attempt for a Mathematical Theory of Kinetic Coagulation of Colloid Solutions. *Z. Phys. Chem* **1917**.

(105) URSS, B. S.-A. P.; 1935, undefined. On the Theory of Photochemical Reactions and Chemiluminescence in Solutions.

(106) Schulten, K. Rates of Diffusion-Controlled Reactions https://www.ks.uiuc.edu/Services/Class/PHYS498/LectureNotes/chp8.pdf (accessed Oct 22, 2018).

(107) Shockley, W.; Queisser, H. J. Detailed Balance Limit of Efficiency of P-n Junction Solar Cells. *J. Appl. Phys.* **1961**, *32* (3), 510–519. https://doi.org/10.1063/1.1736034.

(108) NREL. Best Research-Cell Efficiencies https://www.nrel.gov/pv/assets/pdfs/best-research-cell-efficiencies-190416.pdf (accessed May 15, 2019).

(109) NREL. Reference Air Mass 1.5 Spectra https://www.nrel.gov/grid/solar-resource/spectra-am1.5.html (accessed Jun 5, 2019).

(110) Multiple exciton generation in a quantum dot solar cell https://spie.org/news/4146-multiple-exciton-generation-in-a-quantum-dot-solar-cell?SSO=1 (accessed Apr 12, 2020).

(111) Green, M. A.; Emery, K.; Hishikawa, Y.; Warta, W.; Dunlop, E. D. Solar Cell Efficiency Tables (Version 45). *Prog. Photovoltaics Res. Appl.* **2015**, *23* (1), 1–9. https://doi.org/10.1002/pip.2573.

(112) Kosten, E. D.; Atwater, J. H.; Parsons, J.; Polman, A.; Atwater, H. A. Highly Efficient GaAs Solar Cells by Limiting Light Emission Angle. *Light Sci. Appl.* **2013**. https://doi.org/10.1038/lsa.2013.1.

(113) Einzinger, M.; Wu, T.; Kompalla, J. F.; Smith, H. L.; Perkinson, C. F.; Nienhaus, L.; Wieghold, S.; Congreve, D. N.; Kahn, A.; Bawendi, M. G.; et al. Sensitization of Silicon by Singlet Exciton Fission in Tetracene. *Nature* **2019**, *571* (7763), 90–94. https://doi.org/10.1038/s41586-019-1339-4.

(114) Bludau, W.; Onton, A.; Heinke, W. Temperature Dependence of the Band Gap of Silicon. *J. Appl. Phys.* **1974**, *45* (4), 1846–1848. https://doi.org/10.1063/1.1663501.

(115) Wen, S.; Zhou, J.; Schuck, P. J.; Suh, Y. D.; Schmidt, T. W.; Jin, D. Future and Challenges for Hybrid Upconversion Nanosystems. *Nat. Photonics* **2019**, *13* (12), 828–838. https://doi.org/10.1038/s41566-019-0528-x.

(116) Hines, M. A.; Scholes, G. D. Colloidal PbS Nanocrystals with Size-Tunable Near-Infrared Emission: Observation of Post-Synthesis Self-Narrowing of the Particle Size Distribution. *Adv. Mater.* **2003**, *15* (21), 1844–1849. https://doi.org/10.1002/adma.200305395.

(117) Mello, J. de; Wittmann, H.; Friend, R. An Improved Experimental Determination of External Photoluminescence Quantum Efficiency. *Adv. Mater.* **1997**, *9* (3), 230–232.

(118) Tabachnyk, M.; Ehrler, B.; Gélinas, S.; Böhm, M. L.; Walker, B. J.; Musselman, K. P.; Greenham, N. C.; Friend, R. H.; Rao, A. Resonant Energy Transfer of Triplet Excitons from Pentacene to PbSe Nanocrystals-Supplementary Information. *Nat. Mater.* **2014**, *13*, 1033–1038. https://doi.org/10.1038/nmat4093.

(119) Wilson, M. W. B. Ultrafast Triplet Generation in Organic Semiconductors, University of Cambridge, 2012.

(120) Rao, A.; Chow, P. C. Y.; Gélinas, S.; Schlenker, C. W.; Li, C.-Z.; Yip, H.-L.; Jen, A. K.-Y.; Ginger, D. S.; Friend, R. H. The Role of Spin in the Kinetic Control of Recombination in Organic Photovoltaics. *Nature* **2013**, *500* (7463), 435–439. https://doi.org/10.1038/nature12339.

(121) Gelinas, S.; Rao, a.; Kumar, a.; Smith, S. L.; Chin, a. W.; Clark, J.; van der Poll, T. S.; Bazan, G. C.; Friend, R. H. Ultrafast Long-Range Charge Separation in Organic Semiconductor Photovoltaic Diodes. *Science (80-.).* **2014**, *343* (6170), 512–516.

https://doi.org/10.1126/science.1246249.

(122) Allardice, J. R.; Thampi, A.; Dowland, S.; Xiao, J.; Gray, V.; Zhang, Z.; Budden, P.; Petty, A. J.; Davis, N. J. L. K.; Greenham, N. C.; et al. Engineering Molecular Ligand Shells on Quantum Dots for Quantitative Harvesting of Triplet Excitons Generated by Singlet Fission. *J. Am. Chem. Soc.* **2019**, *141*, 12907–12915. https://doi.org/10.1021/jacs.9b06584.

(123) Stern, H. L.; Musser, A. J.; Gelinas, S.; Parkinson, P.; Herz, L. M.; Bruzek, M. J.; Anthony, J.; Friend, R. H.; Walker, B. J. Identification of a Triplet Pair Intermediate in Singlet Exciton Fission in Solution. *Proc. Natl. Acad. Sci.* **2015**, *112* (25), 7656–7661. https://doi.org/10.1073/pnas.1503471112.

(124) Nelson, J. *The Physics of Solar Cells*; World Scientific Publishing Company, 2003.

(125) Xia, J.; Sanders, S. N.; Cheng, W.; Low, J. Z.; Liu, J.; Campos, L. M.; Sun, T. Singlet Fission: Progress and Prospects in Solar Cells. *Adv. Mater.* **2017**, *29* (20). https://doi.org/10.1002/adma.201601652.

(126) Merrifield, R. E. (Triplet Annihilation, Simple) Theory of Magnetic Field Effects on the Mutual Annihilation of Triplet Excitons. *J. Chem. Phys.* **1968**, *48* (9), 4318. https://doi.org/10.1063/1.1669777.

(127) Merrifield, R. E.; Avakian, P.; Groff, R. P. Fission of Singlet Excitons into Pairs of Triplet Excitons in Tetracene Crystals. *Chem. Phys. Lett.* **1969**, *3* (6), 386–388. https://doi.org/10.1016/0009-2614(69)80144-2.

(128) Geacintov, N.; Pope, M.; Vogel, F. Effect of Magnetic Field on the Fluorescence of Tetracene Crystals: Exciton Fission. *Phys. Rev. Lett.* **1969**, *22* (12), 593–596. https://doi.org/10.1103/PhysRevLett.22.593.

(129) MacQueen, R. W.; Liebhaber, M.; Niederhausen, J.; Mews, M.; Gersmann, C.; Jäckle, S.; Jäger, K.; Tayebjee, M. J. Y.; Schmidt, T. W.; Rech, B.; et al. Crystalline Silicon Solar Cells with Tetracene Interlayers: The Path to Silicon-Singlet Fission Heterojunction Devices. *Mater. Horizons* **2018**, *5* (6), 1065–1075. https://doi.org/10.1039/C8MH00853A.

(130) Ehrler, B.; Wilson, M. W. B.; Rao, A.; Friend, R. H.; Greenham, N. C. Singlet Exciton Fission-Sensitized Infrared Quantum Dot Solar Cells. *Nano Lett.* **2012**, *12* (2), 1053–1057. https://doi.org/10.1021/nl204297u.

(131) Congreve, D. N.; Lee, J.; Thompson, N. J.; Hontz, E.; Yost, S. R.; Reusswig, P. D.; Bahlke, M. E.; Reineke, S.; Van Voorhis, T.; Baldo, M. a. External Quantum Efficiency above 100% in a Singlet-Exciton-Fission-Based Organic Photovoltaic Cell. *Science* **2013**, *340* (6130), 334–337. https://doi.org/10.1126/science.1232994.

(132) Pazos-Outo, L. M.; Min Lee, J.; Futscher, M. H.; Kirch, A.; Tabachnyk, M.; Friend, R. H.; Ehrler, B. A Silicon−Singlet Fission Tandem Solar Cell Exceeding 100% External Quantum Efficiency with High Spectral Stability. **2019**, *08*, 7. https://doi.org/10.1021/acsenergylett.6b00678.

(133) Zhang, B.; Liu, Y.; State, B. G.; Green, B. Direct Observation of Triplet Energy Transfer from Semiconductor Nanocrystals. *Science (80-.).* **2016**, *351* (6271), 369–372. https://doi.org/10.1126/science.aad6378.

(134) Mahboub, M.; Maghsoudiganjeh, H.; Pham, A. M.; Huang, Z.; Tang, M. L. Triplet Energy Transfer from PbS(Se) Nanocrystals to Rubrene: The Relationship between the Upconversion Quantum Yield and Size. *Adv. Funct. Mater.* **2016**, *26* (33), 6091–6097. https://doi.org/10.1002/adfm.201505623.

(135) Nishimura, N.; Allardice, J. R.; Xiao, J.; Gu, Q.; Gray, V.; Rao, A. Photon Upconversion Utilizing Energy beyond the Band Gap of Crystalline Silicon with a Hybrid TES-ADT/PbS Quantum Dots System. *Chem. Sci.* **2019**, *10*, 4717–4932. https://doi.org/10.1039/c9sc00821g.

(136) Li, X.; Huang, Z.; Zavala, R.; Tang, M. L. Distance-Dependent Triplet Energy Transfer between CdSe Nanocrystals and Surface Bound Anthracene. *J. Phys. Chem. Lett* **2016**, *7*, 28. https://doi.org/10.1021/acs.jpclett.6b00761.

(137) Davis, N. J. L. K.; Allardice, J. R.; Xiao, J.; Petty, A. J.; Greenham, N. C.; Anthony, J. E.; Rao, A. Singlet Fission and Triplet Transfer to PbS Quantum Dots in TIPS-Tetracene Carboxylic Acid Ligands. *J. Phys. Chem. Lett.* **2018**, *9* (6), 1454–1460. https://doi.org/10.1021/acs.jpclett.8b00099.

(138) Zeng, B.; Palui, G.; Zhang, C.; Zhan, N.; Wang, W.; Ji, X.; Chen, B.; Mattoussi, H. Characterization of the Ligand Capping of Hydrophobic CdSe–ZnS Quantum Dots Using NMR Spectroscopy. *Chem. Mater.* **2018**, *30* (1), 225–238. https://doi.org/10.1021/acs.chemmater.7b04204.

(139) Hines, M. A.; Scholes, G. D. Colloidal PbS Nanocrystals with Size-Tunable Near-Infrared Emission: Observation of Post-Synthesis Self-Narrowing of the Particle Size Distribution. *Adv. Mater.* **2003**, *15* (21), 1844–1849. https://doi.org/10.1002/adma.200305395.

(140) Patnaik, P. *Handbook of Inorganic Chemicals*; McGraw-Hill, 2003.

(141) Moreels, I.; Lambert, K.; Smeets, D.; De Muynck, D.; Nollet, T.; Martins, J. C.; Vanhaecke, F.; Vantomme, A.; Delerue, C.; Allan, G.; et al. Size-Dependent Optical Properties of Colloidal PbS Quantum Dots. *ACS Nano* **2009**, *3* (10), 3023–3030. https://doi.org/10.1021/nn900863a.

(142) Jafari, S. M.; He, Y.; Bhandari, B. Production of Sub-Micron Emulsions by

Ultrasound and Microfluidization Techniques. *J. Food Eng.* **2007**, *82* (4), 478–488. https://doi.org/10.1016/j.jfoodeng.2007.03.007.

(143) Patel, C. K. N.; Tam, A. C. Quantitative Spectroscopy of Micron-thick Liquid Films. *Appl. Phys. Lett.* **1980**, *36* (1), 7–9. https://doi.org/10.1063/1.91282.

(144) Xu, S.; Wang, C.; Xu, Q.; Li, R.; Shao, H.; Zhang, H.; Fang, M.; Lei, W.; Cui, Y. What Is a Convincing Photoluminescence Quantum Yield of Fluorescent Nanocrystals. *J. Phys. Chem. C* **2010**, *114* (34), 14319–14326. https://doi.org/10.1021/jp100696e.

(145) Cheng, Y. Y.; Fückel, B.; Khoury, T.; Clady, R. G. C. R.; Tayebjee, M. J. Y.; Ekins-Daukes, N. J.; Crossley, M. J.; Schmidt, T. W. Kinetic Analysis of Photochemical Upconversion by Triplet−Triplet Annihilation: Beyond Any Spin Statistical Limit. *J. Phys. Chem. Lett.* **2010**, *1* (12), 1795–1799. https://doi.org/10.1021/jz100566u.

(146) Huang, Z.; Xu, Z.; Mahboub, M.; Li, X.; Taylor, J. W.; Harman, W. H.; Lian, T.; Tang, M. L. PbS/CdS Core-Shell Quantum Dots Suppress Charge Transfer and Enhance Triplet Transfer. *Angew. Chemie Int. Ed.* **2017**, *56* (52), 16583–16587. https://doi.org/10.1002/anie.201710224.

(147) Laidler, K. J. (Keith J.; Meiser, J. H. *Physical Chemistry*; Benjamin/Cummings Pub. Co: Menlo Park Calif., 1982.

(148) Shoup, D.; Lipari, G.; Szabo, A. Diffusion-Controlled Bimolecular Reaction Rates. The Effect of Rotational Diffusion and Orientation Constraints. *Biophys. J.* **1981**, *36* (3), 697–714. https://doi.org/10.1016/S0006-3495(81)84759-5.

(149) Nakamura, S.; Sakai, H.; Nagashima, H.; Kobori, Y.; Tkachenko, N. V.; Hasobe, T. Quantitative Sequential Photoenergy Conversion Process from Singlet Fission to Intermolecular Two-Electron Transfers Utilizing Tetracene Dimer. *ACS Energy Lett.* **2019**, *4* (1), 26–31. https://doi.org/10.1021/acsenergylett.8b01964.

(150) Pun, A. B.; Sanders, S. N.; Kumarasamy, E.; Sfeir, M. Y.; Congreve, D. N.; Campos, L. M. Triplet Harvesting from Intramolecular Singlet Fission in Polytetracene. *Adv. Mater.* **2017**. https://doi.org/10.1002/adma.201701416.

(151) Pace, N. A.; Korovina, N. V.; Clikeman, T. T.; Holliday, S.; Granger, D. B.; Carroll, G. M.; Nanayakkara, S. U.; Anthony, J. E.; McCulloch, I.; Strauss, S. H.; et al. Slow Charge Transfer from Pentacene Triplet States at the Marcus Optimum. *Nat. Chem.* **2019**, 1–8. https://doi.org/10.1038/s41557-019-0367-x.

(152) Huggins, M. L. Solutions of Long Chain Compounds. *J. Chem. Phys.* **1941**, *9* (5), 440. https://doi.org/10.1063/1.1750930.

(153) Flory, P. J. Themodynamics of High Polymer Solutions. *J. Chem. Phys.* **1941**, *9*, 660.

https://doi.org/10.1063/1.1723621.

(154) Gray, V.; Moth-Poulsen, K.; Albinsson, B.; Abrahamsson, M. Towards Efficient Solid-State Triplet–Triplet Annihilation Based Photon Upconversion: Supramolecular, Macromolecular and Self-Assembled Systems. *Coordination Chemistry Reviews*. Elsevier B.V. May 1, 2018, pp 54–71. https://doi.org/10.1016/j.ccr.2018.02.011.

(155) Crisp, R. W.; Schrauben, J. N.; Beard, M. C.; Luther, J. M.; Johnson, J. C. Coherent Exciton Delocalization in Strongly Coupled Quantum Dot Arrays. *Nano Lett.* **2013**, *13* (10), 4862–4869. https://doi.org/10.1021/nl402725m.

(156) Weidman, M. C.; Yager, K. G.; Tisdale, W. A. Interparticle Spacing and Structural Ordering in Superlattice Pbs Nanocrystal Solids Undergoing Ligand Exchange. *Chem. Mater.* **2015**, *27* (2), 474–482. https://doi.org/10.1021/cm503626s.

(157) Ip, A. H.; Kiani, A.; Kramer, I. J.; Voznyy, O.; Movahed, H. F.; Levina, L.; Adachi, M. M.; Hoogland, S.; Sargent, E. H. Infrared Colloidal Quantum Dot Photovoltaics via Coupling Enhancement and Agglomeration Suppression. *ACS Nano* **2015**, *9* (9), 8833–8842. https://doi.org/10.1021/acsnano.5b02164.

(158) Gilmore, R. H.; Lee, E. M. Y.; Weidman, M. C.; Willard, A. P.; Tisdale, W. A. Charge Carrier Hopping Dynamics in Homogeneously Broadened PbS Quantum Dot Solids. *Nano Lett.* **2017**, *17* (2), 893–901. https://doi.org/10.1021/acs.nanolett.6b04201.

(159) Ginger, D. S.; Greenham, N. C. Photoinduced Electron Transfer from Conjugated Polymers to Cdse Nanocrystals. *Phys. Rev. B* **1999**, *59* (16), 10622–10629. https://doi.org/10.1103/PhysRevB.59.10622.

(160) Kwak, J.; Bae, W. K.; Zorn, M.; Woo, H.; Yoon, H.; Lim, J.; Kang, S. W.; Weber, S.; Butt, H. J.; Zentel, R.; et al. Characterization of Quantum Dot/Conducting Polymer Hybrid Films and Their Application in Light-Emitting Diodes. *Adv. Mater.* **2009**, *21* (48), 5022–5026. https://doi.org/10.1002/adma.200902072.

(161) Martínez-Ferrero, E.; Albero, J.; Palomares, E. Materials, Nanomorphology, and Interfacial Charge Transfer Reactions in Quantum Dot/Polymer Solar Cell Devices. *J. Phys. Chem. Lett.* **2010**, *1* (20), 3039–3045. https://doi.org/10.1021/jz101228z.

(162) Nann, T.; Skinner, W. M. Quantum Dots for Electro-Optic Devices. *ACS Nano* **2011**, *5* (7), 5291–5295. https://doi.org/10.1021/nn2022974.

(163) Freitas, J. N.; Gonçalves, A. S.; Nogueira, A. F. A Comprehensive Review of the Application of Chalcogenide Nanoparticles in Polymer Solar Cells. *Nanoscale* **2014**, *6* (12), 6371–6397. https://doi.org/10.1039/c4nr00868e.

(164) Stern, H. L.; Cheminal, A.; Yost, S. R.; Broch, K.; Bayliss, S. L.; Chen, K.; Tabachnyk, M.; Thorley, K.; Greenham, N.; Hodgkiss, J. M.; et al. SI: Vibronically Coherent Ultrafast Triplet-Pair Formation and Subsequent Thermally Activated Dissociation Control Efficient Endothermic Singlet Fission. *Nat. Chem.* **2017**, *9* (12), 1205–1212. https://doi.org/10.1038/nchem.2856.

(165) Wang, L.; Olivier, Y.; Prezhdo, O. V.; Beljonne, D. Maximizing Singlet Fission by Intermolecular Packing. *J. Phys. Chem. Lett.* **2014**, *5* (19), 3345–3353. https://doi.org/10.1021/jz5015955.

(166) Spano, F. C.; Silva, C. H-and J-Aggregate Behavior in Polymeric Semiconductors. *Annu. Rev. Phys. Chem* **2014**, *65*, 477–500. https://doi.org/10.1146/annurev-physchem-040513-103639.

(167) Arias, D. H.; Ryerson, J. L.; Cook, J. D.; Damrauer, N. H.; Johnson, J. C. Polymorphism Influences Singlet Fission Rates in Tetracene Thin Films. *Chem. Sci.* **2016**, *7* (2), 1185–1191. https://doi.org/10.1039/C5SC03535J.

(168) Kolata, K.; Breuer, T.; Witte, G.; Chatterjee, S. Molecular Packing Determines Singlet Exciton Fission in Organic Semiconductors. *ACS Nano* **2014**, *8* (7), 7377–7383. https://doi.org/10.1021/nn502544d.

(169) Roberts, S. T.; Mcanally, R. E.; Mastron, J. N.; Webber, D. H.; Whited, M. T.; Brutchey, R. L.; Thompson, M. E.; Bradforth, S. E. Efficient Singlet Fission Discovered in a Disordered Acene Film. https://doi.org/10.1021/ja300504t.

(170) Piland, G. B.; Bardeen, C. J. How Morphology Affects Singlet Fission in Crystalline Tetracene. *J. Phys. Chem. Lett.* **2015**, *6* (10), 1841–1846. https://doi.org/10.1021/acs.jpclett.5b00569.

(171) Wan, Y.; Wiederrecht, G. P.; Schaller, R. D.; Johnson, J. C.; Huang, L. Transport of Spin-Entangled Triplet Excitons Generated by Singlet Fission. *J. Phys. Chem. Lett.* **2018**, *9*, 6731–6738. https://doi.org/10.1021/acs.jpclett.8b02944.

(172) Piland, G. B.; Burdett, J. J.; Kurunthu, D.; Bardeen, C. J. Magnetic Field Effects on Singlet Fission and Fluroescence Decay Dynamics in Amorphous Rubrene. *J. Phys. Chem. C* **2013**, *117*, 1224–1236.

(173) Thampi, A.; Stern, H. L.; Anthony, J. E.; Rao, A. Elucidation of Excitation Energy Dependent Correlated Triplet Pair Formation Pathways in an Endothermic Singlet Fission System. https://doi.org/10.1021/jacs.7b06274.

(174) Liu, M.; Voznyy, O.; Sabatini, R.; García de Arquer, F. P.; Munir, R.; Balawi, A. H.; Lan, X.; Fan, F.; Walters, G.; Kirmani, A. R.; et al. Hybrid Organic–Inorganic Inks Flatten the Energy Landscape in Colloidal Quantum Dot Solids. *Nat. Mater.* **2016**, *1* (November), 1–21. https://doi.org/10.1038/nmat4800.

(175) Sajjad, M. T.; Blaszczyk, O.; Jagadamma, L. K.; Roland, T. J.; Chowdhury, M.; Ruseckas, A.; Samuel, I. D. W. Engineered Exciton Diffusion Length Enhances Device Efficiency in Small Molecule Photovoltaics. *J. Mater. Chem. A* **2018**, *6* (20), 9445–9450. https://doi.org/10.1039/c8ta01226a.

(176) Zhu, T.; Wan, Y.; Guo, Z.; Johnson, J.; Huang, L. Two Birds with One Stone: Tailoring Singlet Fission for Both Triplet Yield and Exciton Diffusion Length. *Adv. Mater.* **2016**, *28* (34), 7539–7547. https://doi.org/10.1002/adma.201600968.

(177) Hedley, G. J.; Ruseckas, A.; Samuel, I. D. W. Light Harvesting for Organic Photovoltaics. *Chem. Rev.* **2017**, *117* (2), 796–837. https://doi.org/10.1021/acs.chemrev.6b00215.

(178) Ruseckas, A.; Shaw, P. E.; Samuel, I. D. W. Probing the Nanoscale Phase Separation in Binary Photovoltaic Blends of Poly(3-Hexylthiophene) and Methanofullerene by Energy Transfer. *J. Chem. Soc. Dalt. Trans.* **2009**, No. 45, 10040–10043. https://doi.org/10.1039/b912198f.

(179) Gray, V.; Allardice, J. R.; Zhang, Z.; Dowland, S.; Xiao, J.; Petty, A. J.; Anthony, J. E.; Greenham, N. C.; Rao, A. Energetic Dependence of Triplet Energy Transfer to PbS Quantum Dots for Singlet-Fission Based Photon Multiplication. *Submitted* **2019**.

(180) Najafov, H.; Lee, B.; Zhou, Q.; Feldman, L. C.; Podzorov, V. Observation of Long-Range Exciton Diffusion in Highly Ordered Organic Semiconductors. *Nat. Mater.* **2010**, *9* (11), 938–943. https://doi.org/10.1038/nmat2872.

(181) Di, D.; Yang, L.; Richter, J. M.; Meraldi, L.; Altamimi, R. M.; Alyamani, A. Y.; Credgington, D.; Musselman, K. P.; MacManus-Driscoll, J. L.; Friend, R. H. Efficient Triplet Exciton Fusion in Molecularly Doped Polymer Light-Emitting Diodes. *Adv. Mater.* **2017**, *29* (13), 1605987. https://doi.org/10.1002/adma.201605987.

(182) Hoseinkhani, S.; Tubino, R.; Meinardi, F.; Monguzzi, A. Achieving the Photon Up-Conversion Thermodynamic Yield Upper Limit by Sensitized Triplet-Triplet Annihilation. *Phys. Chem. Chem. Phys.* **2015**, *17* (6), 4020–4024. https://doi.org/10.1039/c4cp03936j.

(183) Pope, M.; Geacintov, N. E.; Saperstein, D.; Vogel, F. Calculation of the Diffusion Length, Diffusion Coefficient and Lifetime of Triplet Excitons in Crystalline Tetracene. *J. Lumin.* **1970**, *1–2* (C), 224–230. https://doi.org/10.1016/0022-2313(70)90037-2.

(184) Mahboub, M.; Huang, Z.; Tang, M. L. Efficient Infrared-to-Visible Upconversion with Subsolar Irradiance. https://doi.org/10.1021/acs.nanolett.6b03503.

(185) Ma, L.; Zhang, K.; Kloc, C.; Sun, H.; Michel-Beyerle, M. E.; Gurzadyan, G. G. Singlet Fission in Rubrene Single Crystal: Direct Observation by Femtosecond Pump–

Probe Spectroscopy. *Phys. Chem. Chem. Phys.* **2012**, *14* (23), 8307. https://doi.org/10.1039/c2cp40449d.

(186) Cheng, Y. Y.; Khoury, T.; Clady, R. G. C. R.; Tayebjee, M. J. Y.; Ekins-Daukes, N. J.; Crossley, M. J.; Schmidt, T. W. On the Efficiency Limit of Triplet-Triplet Annihilation for Photochemical Upconversion. *Phys. Chem. Chem. Phys.* **2010**, *12* (1), 66–71. https://doi.org/10.1039/b913243k.

(187) Mahboub, M.; Huang, Z.; Tang, M. L. Efficient Infrared-to-Visible Upconversion with Subsolar Irradiance. *Nano Lett.* **2016**, *16* (11), 7169–7175. https://doi.org/10.1021/acs.nanolett.6b03503.

(188) Monguzzi, A.; Braga, D.; Gandini, M.; Holmberg, V. C.; Kim, D. K.; Sahu, A.; Norris, D. J.; Meinardi, F. Broadband Up-Conversion at Subsolar Irradiance: Triplet−Triplet Annihilation Boosted by Fluorescent Semiconductor Nanocrystals. **2014**. https://doi.org/10.1021/nl503322a.

(189) Bender, J. A.; Raulerson, E. K.; Li, X.; Goldzak, T.; Xia, P.; Van Voorhis, T.; Tang, M. L.; Roberts, S. T. Surface States Mediate Triplet Energy Transfer in Nanocrystal-Acene Composite Systems. *J. Am. Chem. Soc.* **2018**, *140* (24), 7543–7553. https://doi.org/10.1021/jacs.8b01966.

(190) Caram, J. R.; Bertram, S. N.; Utzat, H.; Hess, W. R.; Carr, J. A.; Bischof, T. S.; Beyler, A. P.; Wilson, M. W. B.; Bawendi, M. G. PbS Nanocrystal Emission Is Governed by Multiple Emissive States. *Nano Lett.* **2016**, *16* (10), 6070–6077. https://doi.org/10.1021/acs.nanolett.6b02147.

(191) Zhu, H.; Yang, Y.; Wu, K.; Lian, T. Charge Transfer Dynamics from Photoexcited Semiconductor Quantum Dots. **2016**. https://doi.org/10.1146/annurev-physchem-040215-112128.

(192) Kaledin, A. L.; Lian, T.; Hill, C. L.; Musaev, D. G. A Hybrid Quantum Mechanical Approach: Intimate Details of Electron Transfer between Type-I CdSe/ZnS Quantum Dots and an Anthraquinone Molecule. *J. Phys. Chem. B* **2015**, *119* (24), 7651–7658. https://doi.org/10.1021/jp511935z.

(193) Tvrdy, K.; Frantsuzov, P. A.; Kamat, P. V. Photoinduced Electron Transfer from Semiconductor Quantum Dots to Metal Oxide Nanoparticles. *Proc. Natl. Acad. Sci. U. S. A.* **2011**, *108* (1), 29–34. https://doi.org/10.1073/pnas.1011972107.

(194) Cánovas, E.; Moll, P.; Jensen, S. A.; Gao, Y.; Houtepen, A. J.; Siebbeles, L. D. A.; Kinge, S.; Bonn, M. Size-Dependent Electron Transfer from PbSe Quantum Dots to SnO 2 Monitored by Picosecond Terahertz Spectroscopy. *Nano Lett.* **2011**, *11* (12), 5234–5239. https://doi.org/10.1021/nl202550v.

(195) Knowles, K. E.; Malicki, M.; Weiss, E. A. Dual-Time Scale Photoinduced Electron

Transfer from PbS Quantum Dots to a Molecular Acceptor. *J. Am. Chem. Soc* **2012**, *134*, 12470–12473. https://doi.org/10.1021/ja3060222.

(196) Morris-Cohen, A. J.; Frederick, M. T.; Cass, L. C.; Weiss, E. A. Simultaneous Determination of the Adsorption Constant and the Photoinduced Electron Transfer Rate for a Cds Quantum Dot-Viologen Complex. *J. Am. Chem. Soc* **2011**, *133*, 10146–10154. https://doi.org/10.1021/ja2010237.

(197) Malicki, M.; Knowles, K. E.; Weiss, E. A. Gating of Hole Transfer from Photoexcited PbS Quantum Dots to Aminoferrocene by the Ligand Shell of the Dots. *Chem. Commun.* **2013**. https://doi.org/10.1039/c2cc32895j.

Appendix A

Supporting Data for Solution Phase SF-PM

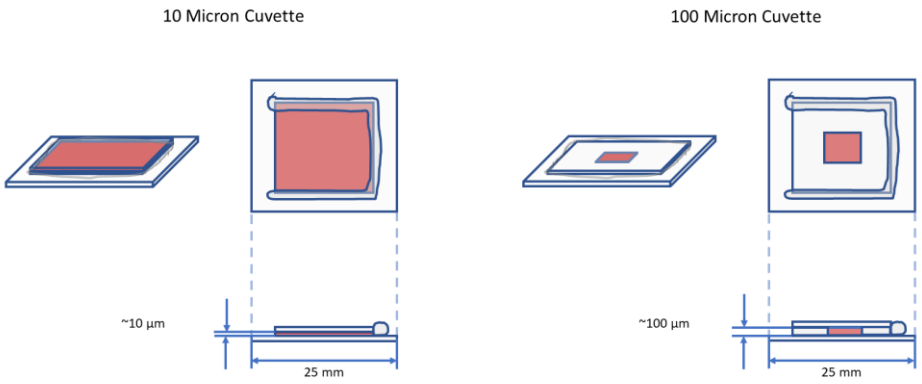

Figure 7.1: Schematic of the in-house made cuvettes.
Either size were filled with roughly 10 µL of solution. The low volumes needed for these cuvettes allows the exploration of a wider range of concentration, particularly for higher concentrations of TIPS-Tc and QDs where material constraints must be considered. After filling the cavity with the desired solution, epoxy was applied to seal the remaining edge.

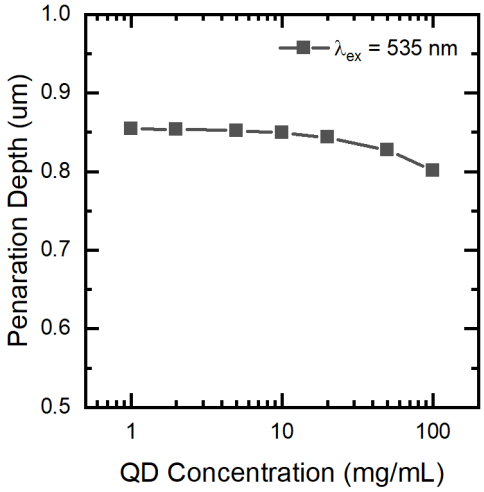

Figure 7.2: Light penetration depth for SF-PM solutions.
Calculated light penetration depth (535nm) for solutions of PbS-TET-CA QDs and TIPS-Tc (200 mg/mL). The values are calculated from the measured attenuation coefficients.

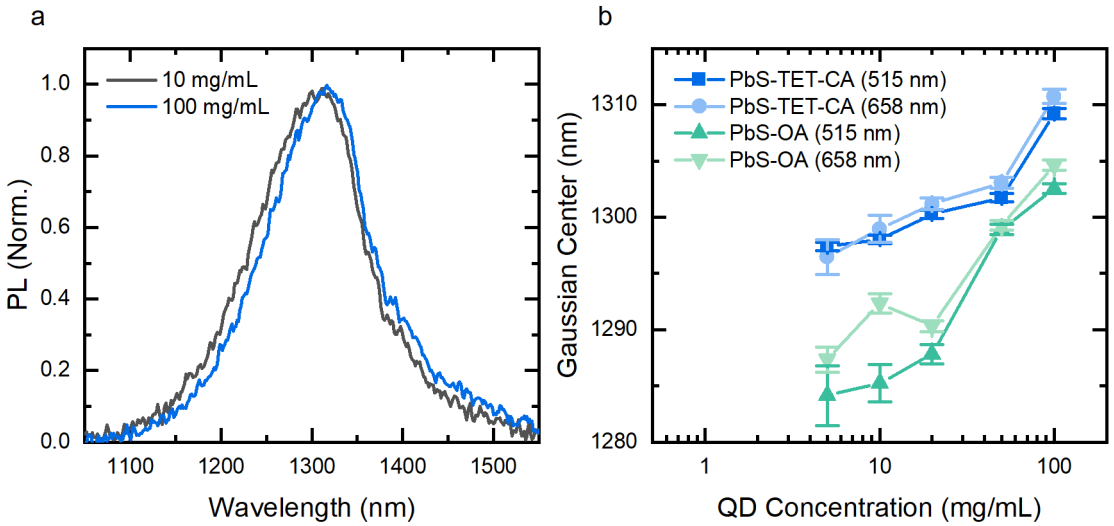

Figure 7.3: PbS quantum dot self-absorption.
a) IR PL spectra of 10 (black) and 100 mg/mL (blue) PbS-TET-CA QDs with TIPS-Tc (200 mg/mL), under 515 nm excitation, showing a red-shift in the PL for higher concentration of QDs. b) PL peak wavelength, with uncertainty, as measured by a Gaussian fit to the IR PL, for both 515 and 658 nm excitation of solution of QDs with TIPS-Tc (200 mg/mL).

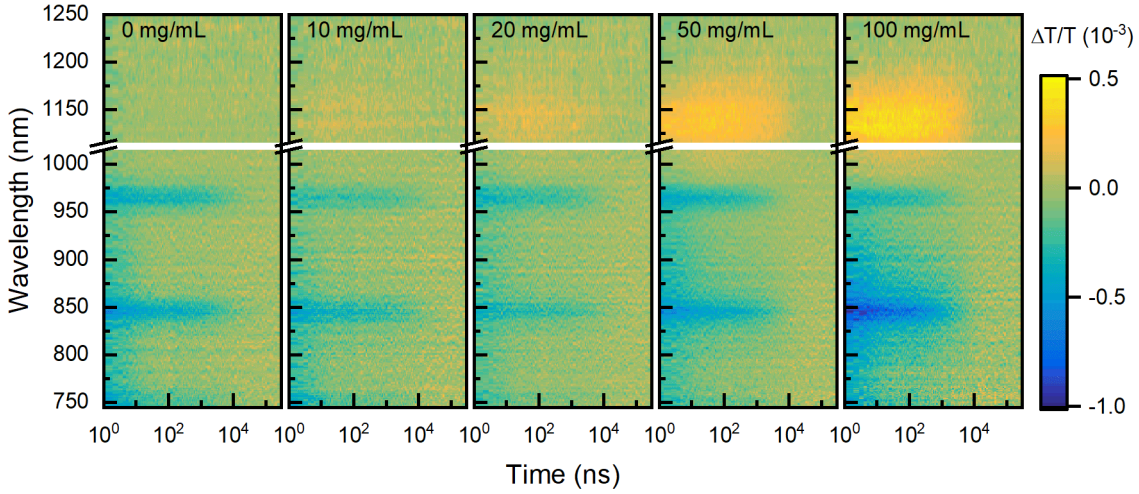

Figure 7.4: TIPS-Tc:PbS-TET-CA solution nsTA maps.
Nanosecond transient absorption maps for solutions of concentrated TIPS-Tc (200 mg/mL), with varying concentrations of PbS-TET-CA QDs (0-100 mg/mL), with a 535 nm pump at 50 µW (42 µJ/cm^2).

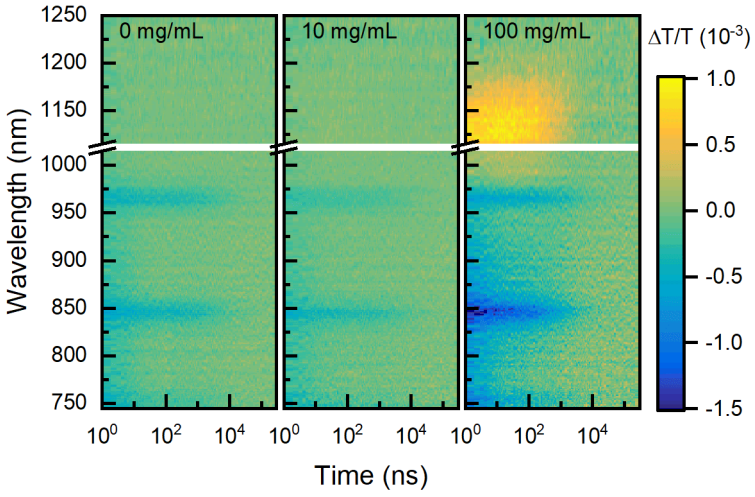

Figure 7.5: TIPS-Tc:PbS-OA solution nsTA maps.
Nanosecond transient absorption maps for solutions of concentrated TIPS-Tc (200 mg/mL), with varying concentrations of PbS-OA QDs (0-100 mg/mL), with a 535 nm pump at 50 µW (42 µJ/cm^2).

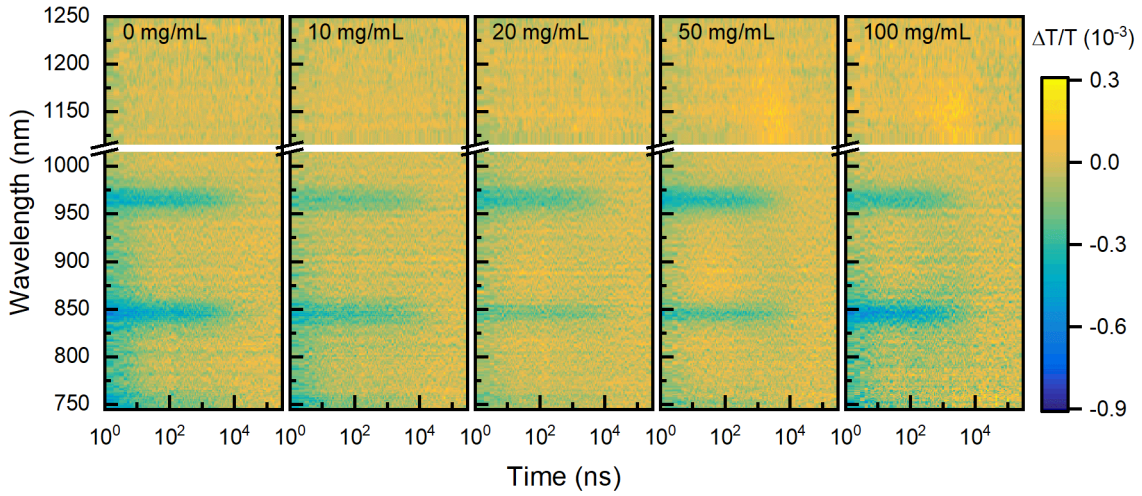

Figure 7.6: TIPS-Tc:PbS-TET-CA solution nsTA difference maps.
Nanosecond transient absorption difference maps (relative to PbS-TET-CA QDs) for solutions of concentrated TIPS-Tc (200 mg/mL), with varying concentrations of PbS-TET-CA QDs (0-100 mg/mL), with a 535 nm pump at 42 µJ/cm^2.

Excitation wavelength	515 nm						658 nm
QD Conc (mg/mL)	1	5	10	20	50	100	20
PbS-OA	0.0	1.1	2.0	3.1	10.1	9.9	19.2
PbS-TET-CA	0.6	12.0	13.8	16.7	18.2	16.0	14.6

Table 7.1: IR PLQE values for solution SF-PM samples.
solutions of TIPS-Tc (200 mg/mL) and QD's of varying concentration, under 515 and 658 nm laser excitation. The intrinsic QDs PLQE is taken as the IR PLQE under 658 nm excitation, in a solution of TIPS-Tc (200 mg/mL) and QDs (20 mg/mL). 515 and 658 nm IR PLQE values were measured under 5 mW/cm^2 fluence.

Pulse Power ($\mu J/cm^2$)	k_1 (1/ms)	$\Delta T/T$ (0)	[T](0) ($1/cm^3$)	k_2 (10^{-23} cm^3/ns)	f2
21	5.6 ± 5.1	(2.2 ± 0.1)x10^{-4}	0.9x10^{18}	(7.6 ± 0.3)	0.83 ± 0.36
42	5.6 ± 5.1	(3.4 ± 0.1)x10^{-4}	1.8x10^{18}	(7.6 ± 0.3)	0.88 ± 0.34
168	5.6 ± 5.1	(12 ± 0.1)x10^{-4}	7.2x10^{18}	(7.6 ± 0.3)	0.95 ± 0.35

Table 7.2: TIPS-Tc triplet bi-molecular decay parameters.
Nanosecond transient absorption fitting parameters for the TIPS-Tc triplet PIA (840-850 nm) of TIPS-Tc at 200 mg/mL. Transient absorption bi-molecular decay rates are converted to triplet density bi-molecular decay rates by estimation of the initial triplet density.

Appendix B

Excited State Decay Under Periodic Excitation

We consider a process that instantaneously produces B excited states at periodic interval T, which then exponentially decay with time constant τ, the population of total excited states at time t can be expressed as,

$$y(t) = Be^{-t/\tau} + Be^{-\frac{T}{\tau}} + Be^{-\frac{2T}{\tau}} + Be^{-\frac{3T}{\tau}} + \cdots$$

Collecting the summation we find,

$$y(t) = Be^{-t/\tau}\left(1 + \sum_{n=1}^{\infty} exp\left(-\frac{nT}{\tau}\right)\right).$$

The summation is of geometric form and so the converges to,

$$\sum_{n=1}^{\infty}(e^{-x})^n = \frac{e^{-x}}{1-e^{-x}} = \frac{1}{e^x - 1},$$

for $x > 0$. Thus the population is given by,

$$y(t) = Be^{-t/\tau} + \frac{B}{e^{T/\tau} - 1}.$$

Extending this to a bi-exponential decay process with times constants τ_1 and τ_2 gives,

$$y(t) = Ae^{-t/\tau_1} + \frac{A}{e^{T/\tau_1} - 1} + Be^{-t/\tau_2} + \frac{B}{e^{T/\tau_2} - 1}.$$

In the case that τ_1 is very fast, the limit $T/\tau_1 \rightarrow \infty$, we finally arrive at,

$$y(t) \approx Ae^{-t/\tau_1} + Be^{-t/\tau_2} + \frac{B}{e^{T/\tau_2} - 1}.$$

We use this function was used to describe the QD IR transient PL. The τ_1 rate parameterise a fast decay of PL, due possibly to auger recombination, while the longer τ_2 decay represents the PL decay of the QD including population after triplet transfer.

Appendix C

Supporting Data for Solid State SF-PM

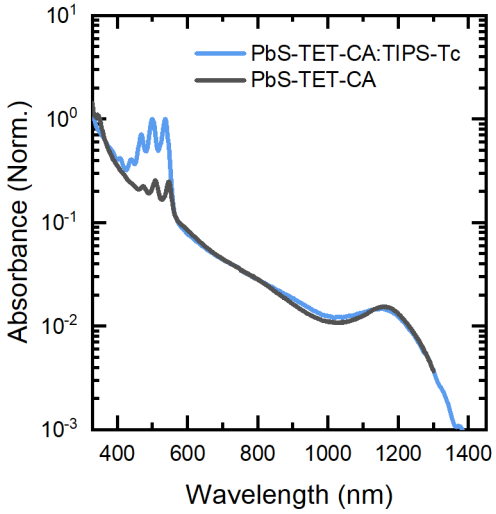

Figure 7.7: Normalised absorbance spectra of a solid state SF-PM. PbS-TET-CA:TIPS-Tc film (blue) and a solution of PbS-TET-CA QDs in toluene. Absorption spectrum were measured by Dr Simon Dowland.

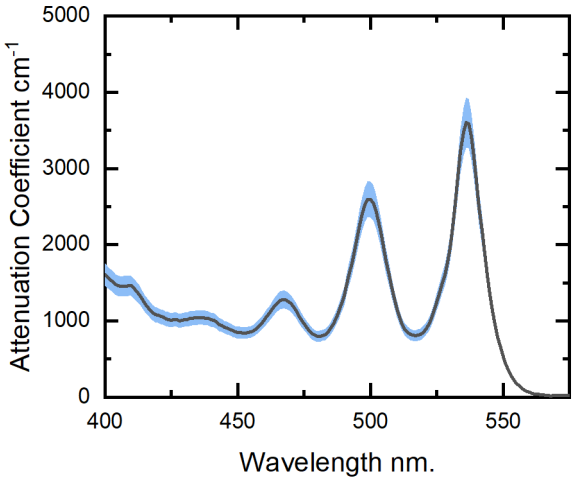

Figure 7.8: Thin-film TIPS-Tc attenuation coefficient spectrum (black curve).
Calculated from the absorbance spectrum of a 220 ± 20 nm thick film of TIPS-Tc. The uncertainty in the attenuation coefficient is calculated from the uncertainty in the film thickness (light blue). Absorption spectrum and TEM measurements of film thickness were measured by Dr James Xiao.

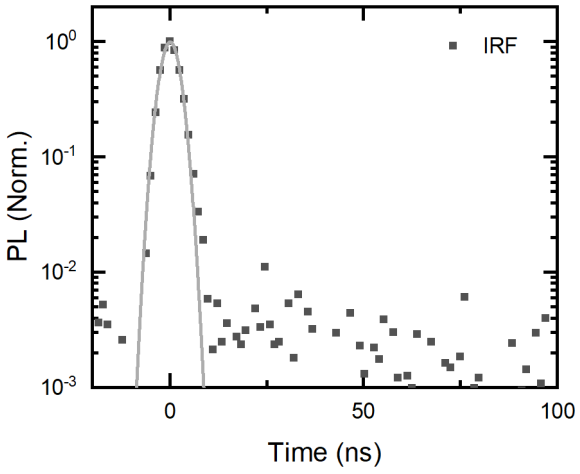

Figure 7.9: IR TCSPC instrument response function (IRF).
Collected using a scattering glass substrate with 650 nm laser scatter. Fitting the IRF with a gaussian peak function is obtained with a full width half maximum of 5.5 ± 0.5 ns.

Appendix D

Supporting Figures for PbS-TET-CA:Rub

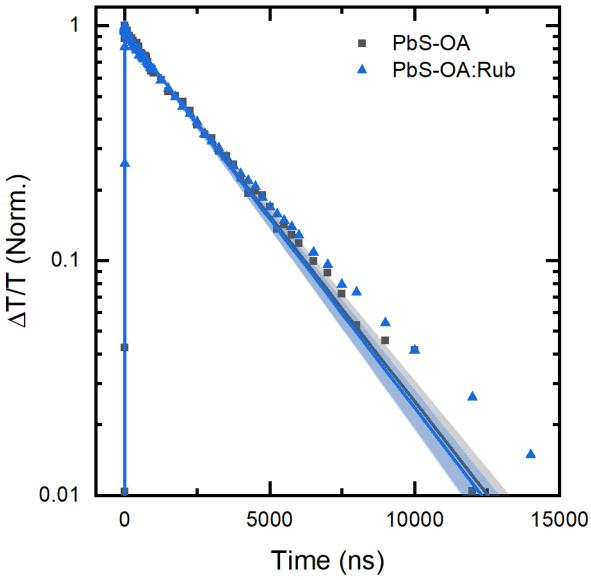

Figure 7.10: Excited state decay for PbS-OA and rubrene solutions.
nsTA kinetics in the region of the PbS GSB (890-910 nm), showing the us timescale decay of the PbS excited state exciton. The decays of the PbS GSB feature are well described by mono-exponential decays with lifetimes 2740 ± 40 ns (PbS-OA) and 2700 ± 70 ns (PbS-OA:Rub). The addition of Rubrene (10 mg/mL) shows insignificant effect, within certainty, on the exciton lifetime of the PbS-OA QD. Indicating a low triplet transfer rate relative to the PbS exciton lifetime.